VRIJE UNIVERSITEIT BRUSSEL
FACULTY OF APPLIED SCIENCES
DEPARTMENT OF ELECTRONICS AND INFORMATION PROCESSING

A Multidisciplinary Analysis of Frequency Domain Metal Detectors for Humanitarian Demining

Claudio Bruschini

Brussels, September 2002

Promoter: Prof. Hichem Sahli

Thesis submitted to the Faculty of Applied Sciences of the
Vrije Universiteit Brussel to obtain the degree of
Doctor in Applied Sciences

Examining Committee

Prof. Hichem Sahli – Vrije Universiteit Brussel – Promoter

Prof. Ronald Van Loon – Vrije Universiteit Brussel – Committee Chair

Prof. Jan Cornelis – Vrije Universiteit Brussel – Committee Secretary

Prof. hon. Jean-Daniel Nicoud – Ecole Polytechnique Fédérale de Lausanne – Member

Dr. Axel Melsheimer – Institut Dr. Förster, Reutlingen (D) – Member

A Marinella, magnifica sorpresa
di una vita che non finisce di sorprendere,
per il suo amore profondo ed il suo sorriso

Ai miei Genitori,
per il loro sostegno continuo e la loro pazienza

Summary

This thesis details an analysis of **metal detectors** (low frequency electromagnetic induction devices) with emphasis on Frequency Domain (FD) systems and the operational conditions of interest to **humanitarian demining**.

After an initial look at humanitarian demining and a review of their basic principles we turn our attention to **electromagnetic induction modelling** and to **analytical solutions** to some basic FD direct (forward) problems. The second half of the thesis focuses then on the **analysis of an extensive amount of experimental data**. The possibility of target classification is first discussed on a qualitative basis, then quantitatively. Finally, we discuss shape and size determination via near field imaging.

On the **theoretical side** we confirm the possibility of *distinguishing* between different objects and of *identifying* some targets based on their characteristic phase response. In addition, we indicate the possibility of exploiting the phase shift dependence on the object size to reduce the amount of detected clutter. **Soil effects**, which are often not sufficiently considered, are taken into account by using a homogenous half-space model and by analysing some frequency differencing methods and features which are more robust to variations in ground conditions. Fluctuations in the soil signal are also clearly documented in the experimental data.

On the **experimental side** we analyse in detail the response from reference objects, targets (mostly mines), and clutter (debris). A number of theoretical elements of the basic models are confirmed, in particular the trends in the phase response and important demagnetization effects. In addition a number of effects, such as orientation dependencies, changes due to axial offsets, and the response of composite objects and their variability, are also highlighted.

On the **qualitative side** (signal trajectories in the **complex plane**) we show that it is possible to distinguish smaller clutter items from larger objects, and that some mines have quite characteristic responses. A "qualitative" (coarse) target classification is therefore possible.

On the **quantitative side** we simplify the complex plane curves by extracting a corresponding set of features, resulting in a **combined, simplified user interface**. Most of the information turns out to be contained in the phase response. The resulting **classification opportunities** are then discussed along three main lines:

- A **coarse target classification** according to the ***object size*** (actually the response parameter), and permeability (ferromagnetic or not), seems indeed to be possible, at least for scenarios with a sufficient S/N ratio. In the low S/N case it should however still be possible to exploit some of the additional features which are more robust to background (soil) fluctuations.
- The results for some **large metallic objects** confirm that it is possible to discriminate them for smaller clutter relying on their phase response. This seems true to a limited extent only for mines with an average metallic content (e.g. **PMN**, **PMN2**).
- **Discriminating mines from clutter** or among themselves depends in the end on i) which and how many types of mines are present (*a priori* knowledge), ii) how much one can rely on stable mine signatures, iii) how representative the debris we had available is, and in particular on iv) how many clutter objects have a sufficient S/N ratio to allow discrimination.

  Indeed, *the actual system effectiveness will depend on how much the* ***false alarm rate*** *can be reduced,* i.e. *how many times a clutter item has a sufficient S/N to be identified as such*.

Finally, we show, to the best of our knowledge, the first high resolution (R=2-3 cm for a flush object) 2D near real-time "**images**" of shallowly buried (ferromagnetic) metallic components of mines with relevant metal content and UXO. First deconvolved MD images of minelike objects are also obtained, demonstrating that image resolution can be enhanced with deblurring (deconvolution) techniques. The limits of both approaches are also detailed.

Although some of these results were already known to the metal detector community, their diffusion has rarely happened, to the best of our knowledge, in a public document and in a coherent way, with the necessary scientific rigour.

Acknowledgements

I do remember only vaguely the first time I heard of the "celebrations" accompanying the end of a doctorate, somewhere up in the Nordic countries, with people in their thirties, possibly married and even with children. Now I know what it is all about – a thesis, I mean.

I do on the other hand remember well one of my field visits to Croatia, when the deminer in front of me took me to see a mini-flail which had finished cutting vegetation, suggesting to "walk in the tracks". I did, but what an eerie feeling: you stare at the ground, trying to see below the surface, but it is basically a hopeless task.

Strange as it may seem, these two things go together – an unusual subject, humanitarian demining, led to an usual thesis: a member of the jury remarked that "It needs courage to take up a metal detector as a subject for a thesis" (although probably less than walking in the tracks), another said that "A few years ago I did not think that it would be possible to carry out a thesis on metal detectors"...

Everything started with the DeTeC project at the LAMI (Laboratoire de Microinformatique) of the EPFL in Lausanne, Switzerland, which is why I would like to start by thanking Prof. Jean-Daniel Nicoud. His pioneering activities have certainly influenced the European academic R&D work on the subject, and without him I would not have been able to continue my work. With Jean-Daniel I learnt in particular how to improvise and take initiatives.

The members of the former DeTeC team, in particular Frédéric Guerne and Bertrand Gros, built the gantry and data acquisition electronics and thus made data acquisition and collection possible. From them I learnt how real engineers work. Marie-Jo, the LAMI's secretary and soul, has been very kind and helpful on a number of occasions, and taught me than "indispensable persons" do not exist. One way to take one's role and importance a bit less seriously.

Everything continued at the VUB with Profs. Hichem Sahli and Jan Cornelis, who offered me the opportunity to carry out this work. I would like to thank Hichem in particular for his patience, for his encouragement and for his trust, which went way beyond mere professional matters. If I arrived at the end of this work believing in what I did it is also because he provided me with the freedom to analyse the problem in depth from different perspectives.

Very special thanks go to Karin de Bryun, with whom I worked on EUDEM and am working on EUDEM2 – merci Karin for your friendship and assistance during these years! I also received precious help and support from Luc van Kempen on a large number of occasions, again well beyond professional matters, as well as from Hermine, Lixin, Timofei, Valentin, and many others at ETRO. Joris Lochy carried out a "Werkkollege" (semester project) which was instrumental in wrapping up data acquisition and analysis.

Many thanks go also to John Alldred of Protovale for a number of discussions and always precise answers, Olivier Burdet (EPFL) for a couple of discussions and especially for the Ferroscan reference, Hansjörg Nipp of the HILTI Corporation for its very positive and cooperative attitude, Patrick Gaydecki and Werner Ricken for information on research on imaging metal detectors, Beat Diem of PROCEQ SA for the Profometer 4 documentation, and Gloria Menegaz (EPFL) for her advice on wavelets. Special thanks go to the staff of the Institut Dr. Förster in Reutlingen, Klaus Ausländer, Thomas Himmler and Axel Melsheimer, whose cooperative attitude was greatly appreciated; their Minex detector was instrumental in delivering most of the experimental data on which this work is relying. Many interesting e-mail exchanges have taken place with Piotr Szyngiera (Silesian Technical University, Poland); his help on the Patent Study was also most welcome.

Finally, when working on a thesis one sometimes fears that it will never finish– a "mid-thesis" crisis, so to speak. I would therefore like to sincerely thank all those who helped me with their friendship, love and encouragement over all these years. This is also your work.

Contents

1.
Introduction and Thesis Framework

In this chapter we are setting the scene for the following work, starting with an introduction to the current situation in Humanitarian Demining and to the different approaches to the landmine detection problem, as well as to the resulting research avenues. The role of metal detectors and its limitations, and the current research activity more specifically linked to metal detectors are then highlighted. This sets the framework for the research carried out in this thesis, whose main directions are analysed and motivated.

1.1. The Current Situation in Humanitarian Demining

The world's attention has been often captured, during these last years, by the landmine problem and its devastating effects on the civilian population. The latter can very well be indirect, in terms of denying access to arable land, infrastructure and housing for example.

These "weapons of terror", especially the antipersonnel (AP) mines, are indeed often cheap, easy to manufacture and exceedingly often used by the warring factions without keeping detailed records. Ordinary ("dumb") landmines can stay active for decades and, even if normally placed close to the surface (flush to some cm deep), can be displaced from their original position as a consequence of natural events such as floods or drifting sands. Unexploded Ordnance (UXO), i.e. munition which has not detonated (usually due to failure), has very often to be cleared as well before being able to declare an area as safe. Needless to say, for humanitarian demining a detection rate approaching perfection, i.e. 100%, must be obtained. Time is less important than accuracy.

The *ensemble* of activities dealing with the mine problem is known as *Mine Action*, and includes tasks such as mine awareness, victim rehabilitation, advocacy, etc., in addition to detection and clearance on which we will focus. We will also not cover military demining.

Detection and clearance are still being very often carried out in humanitarian demining using manual methods as the *primary procedure*. Once a mine has been found, deminers know well how to remove it or blow it up. *When operating in this way* the detection phase still relies heavily on metal detectors (see Figure 1.1), whereby each alarm needs to be carefully checked until it has been fully understood and/or its source removed [BRO98, KIN96]. This is normally done visually, and by prodding and/or excavating the ground. Sometimes this is the only way to explore the ground, for example when the area is saturated with metallic debris. Metal detectors are still to the best of our knowledge, apart from dogs*, the only detectors really being used in the field*, and are probably going to remain in use for quite some time.

Prodding consists in scanning the soil at a shallow angle of maximum 30° using long rigid sticks of metal. Each time the deminers feel something, they must check the contour of the object to determine if it is a mine. This is dangerous because the mine could have moved and the sensitive surface turned towards the operator.

Figure 1.1: HALO Trust deminer in Cambodia, checking the ground with an Ebinger 420SI metal detector

[Images' Source: EPFL/DeTeC]

Figure 1.2: (Top) Example of metallic debris (ruler: 25 cm long):

Figure 1.3: (Bottom) Chinese Type 72 minimum-metal AP mine (78 mm large, 38 mm high)

The clearance rate achieved in this careful, thorough but slow way does not usually exceed 100 m^2 per deminer per day. Indeed, metal detectors cannot unfortunately differentiate a mine (see Figure 1.3) or UXO from metallic debris (an example is shown in Figure 1.2). In most battlefields, but not only there, the soil is contaminated by large quantities of shrapnel, metal scraps, cartridge cases, etc., leading to between 100 and 1,000 false alarms for each real mine. Each alarm means a waste of time and induces a loss of concentration [EBL96]. Note that when manual methods follow other procedures, such as mechanical clearance, constraints on the need to check each alarm are often somewhat relaxed.

Other types of mines will be shown in Chapter 5, along with an extensive analysis of the metallic debris, of which Figure 1.2 represents but one example.

Information Sources

The following organisations and the corresponding Websites provide a good overview of mine action and constitute a good starting point for further research:

- **International organisations** dealing with the mine problem, such as the United Nations Mine Action Service (`www.mineaction.org`), the Geneva International Centre for Humanitarian Demining (GICHD, `www.gichd.ch`), and the national Mine Action Centres (MAC), for example in Afghanistan, Cambodia, Croatia, etc.
- Organisations or projects dedicated to the diffusion of information, in particular of technical nature, such as the Mine Action Information Center (MAIC) at the James Madison University (`maic.jmu.edu`), the European ARIS Network of Excellence (`demining.jrc.it/aris/`) and the European EUDEM2 support measure (`www.eudem.vub.ac.be`).

- Non Governmental Organisations (**NGO**), some of which have been involved in demining for the last 10 years or so. The largest ones are the Halo Trust (`www.halotrust.org`), Mines Advisory Group (MAG, `www.mag.org.uk`), Norwegian People's Aid (NPA, `www.npaid.org`), and Handicap International (HI, `www.handicap-international.org`). "Menschen gegen Minen" (MgM, `www.mgm.org`) is a smaller but very active and well known organisation, in particular for its online "Forum".
- Academic organisations such as the University of Western Australia (UWA, Prof. James Trevelyan, `www.mech.uwa.edu.au/jpt/demining/`), known for its emphasis of practical problems and incremental approach, and the VUB (`www.demining.vub.ac.be`). The EPFL/ DeTeC Website (`diwww.epfl.ch/lami/detec/`) is also a good source of information, although it is not regularly updated any more.

The EUDEM report can also be a good starting point [BRU99a]. Among the many sources for a description of existing mines we can recommend [JAN02] by Colin King, and for example the list contained in the [MIM01] study.

1.2. Landmine Detection and Current Research Avenues

Humanitarian demining is carried out in a large number of diverse scenarios (agricultural fields, urban environments, infrastructure, road and rail networks, forests, etc.), on targets which vary in size from tiny AP mines to large antitank mines or even larger improvised explosive devices or UXO, buried or on the surface. Some minefields are laid out in military fashion along precise patterns, most are not, and a sizeable fraction contains only a few mines (and are probably the most difficult ones to tackle).

In order to make the problem tractable and indicate the areas of research where we feel that the scientific community, in particular its component dealing with sensor systems, can be of help we will focus on the landmine detection aspects. It is recognised that this will however represent only part of an overall solution: for example, any improved sensor will constitute only a marginal improvement if the deminer still has to cut the vegetation by hand prior to its use, an operation which can take up more than half of his time.

Researchers vs. End Users

In research into sensors for demining it is often far from easy to keep a reasonably close contact to the field, which is however warmly recommended in order to avoid "reinventing the wheel" or devising systems which are of little practical use. Conversely, demining organisations are not always aware of the scientific and industrial R&D cycles and tend to put too much expectations on early developments. It can therefore happen that when a prototype is tested the end users focus too much on the system's characteristics, missing the fact that it is much more likely that a system, which gets the physics right, can be engineered into a user friendly device, than vice versa.

This leads to the question of which are the precise requirements coming from the field. Up to a short time ago the reply did often depend on the demining organisation and the situation it was operating in. Recent efforts by the UN are addressing this issue, trying to coming up with a list of precise requirements on which the scientific community and commercial organisations can build upon. Concerning the detection aspects the requirements are obviously linked to the question of "what is a mine" and how much *a priori* knowledge can be assumed (the maximum possible for the researcher, usually the minimum necessary for the deminer).

Wide Area vs. Close-in Detection

Broadly speaking there are two main approaches to the landmine detection problem, which correspond to two distinct needs:

- **Wide area** detection, which does ideally precede close-in detection and consists in establishing if a given area is mined at all and establishing the boundaries of a mined area. There are indeed numerous instances in which a given area is suspected to be mined but no precise records are available, especially in situations which have involved irregular warring factions or poorly trained ones. In these cases local information sources are exploited whenever possible, but it still happens quite often that a field or an area are demined without finding at the end a single dangerous objects, losing time instead of concentrating on areas which really need to be demined.

  Wide area detection includes the use of trace explosive detection systems – dogs at present, with ongoing work on "artificial noses" to complement them – as well as research into airborne or vehicle based multi-sensor systems, to be used to locate *minefield indicators* and when possible to detect individual mines.
- **Detection of individual mines**, which deals with the precise location of single mines, an operation which is up to now carried out mostly using manual methods as previously discussed.

  Much of the R&D effort for humanitarian demining has in fact gone towards the **close-in detection** of mines, mainly the blast ones, rather than towards stand-off techniques for fragmentation or bounding mines.

Both detection methods can be strongly influenced, when looking at buried objects, by the fact that soil parameters are very variable.

Stand Alone vs. Multi-sensor Systems

Different sensor systems can in turn be used individually or in combination, and can be categorised as follows:

- **Stand alone** sensors, meant to be used by themselves, either as enhancements of existing ones such as metal detectors, or as completely new approaches (e.g. acoustics).
- **Multi-sensor** systems in which several sensors are combined in order to exploit complementary information[1], and to enhance detection and even classification. Sensor fusion should guarantee that the multi-sensor system at least retains the probability of detection of each single sensor, and moreover reduces the false alarm rate. Multi-sensor systems have been in part introduced as no alternative to metal detectors has emerged during the years.

  The ultimate goal would be to fully integrate individual sensors, physically as well as from the point of view of data fusion. Physical integration requires close collaboration between the manufacturers of individual pieces of equipment, to ensure technical compatibility and to avoid cross talk and measurement ambiguity due to spatio-temporal misalignment. This is probably easier to achieve than full data fusion [BRU99a].

  The idea of combining different sensors to increase their individual strengths is indeed attractive, at least at first sight; it comes however at the price of increased system complexity, which might or might not be acceptable depending on the target application[2], and probably with increased performance evaluation complexity as well.
- Easier solutions are investigated as well, such as using two detectors in sequence, typically the first sensor as **primary detector** (quite often the metal detector), the second as **confirmation sensor** (e.g. a GPR or explosive detection systems such as neutron based ones or Nuclear Quadrupole Resonance), possibly leaving the final decision to the operator. In these combinations the basic idea is to use a well known and accepted sensor in the primary role, and reduce its false alarm rate with the second sensor.

1. In a ideal case each sensor measures different physical characteristics
2. A more complex airborne system might for example be more acceptable than a more complex hand-held device.

> This can simplify to a great extent system design and analysis, and in a certain sense comes closer to current operational procedures, where "sensors" (metal detectors, manual prodding, sniffing dogs) are used sequentially. Generally speaking, in all systems an experienced operator is crucial for overall performance [BRU99a].

The underlying rationale behind the interest in multi-sensor system design and data fusion is that the exploitation of different sensing principles leads to more reliable detection/classification results by combining different pieces of incomplete or imperfect information. *The risk of this approach is that combining insufficiently mature sensors yields an even more complicated problem than pushing individual sensor technologies to their intrinsic physical detection limits.* This implies that research and development of single-sensor data processing and pattern recognition techniques for mine detection/classification should be continued [BRU99a], an approach which we have indeed pursued by looking in-depth at the response of metal detectors.

When using the second sensor in a confirmatory role one should not forget that we are basically asking for two sensors with an individual detection performance close to 100%, although this combination could be easier to validate than an integrated multi-sensor system. Also, the confirmation sensor has to be reasonably fast, the reference being represented for example by the time currently spent by deminers in investigating each metal detector alarm. From the purely financial point of view, which is unfortunately quite often determinant, it might indeed make little sense to acquire an expensive detector which is overall only slightly faster than what a deminer is already able to do.

Hand-held Systems vs. Vehicle Based Platforms

Multi-sensor systems can be made **portable**, similarly to currently used metal detectors. The human operator is indeed still difficult to surpass when it comes to taking analytical decisions in a complex environment, and there will always be situations where portable equipment is needed. Problems lie in producing affordable (5-10 times the cost of an individual high-end metal detector?), compact and lightweight systems, with sufficient autonomy, improved productivity (reduced false alarm rate), ease of use (ergonomics), and overall performances justifying the price.

Vehicle based platforms are typically used for rapid surveying of large areas, in particular roads or moderately off-road areas. Sensor choice as well as sensor performance are usually not constrained by power and computational requirements. Sensor arrays are usually employed. Position tracking equipment and platform stability control systems are also extremely important. Usually a combination of forward looking (e.g. infrared, visual, multispectral cameras, Ultra Wide Band radar) and downward looking sensors (e.g. GPR array, MD array) are used. Near "real-time" processing and decision taking might be necessary at high vehicle speeds. In some cases remotely controlled vehicles are used [BRU99a].

Detector Validation

We will not enter here into the details of the procedures necessary to validate a new sensor system, which does in principle involve testing on a very large number of targets, probably in the thousands, if the required detection rate[3] levels of the order of 99.6% or more are really to be documented. It is however interesting to note that to the best of our knowledge no rigorous analysis of the performance of existing fielded systems has been carried out either, in field conditions and at the previously indicated levels, at least before starting to use such a system[4]. In this respect the [IPPTC01] evaluation presents some quite interesting and sobering results, in particular for difficult field conditions and targets (deep and/or minimum-metal mines).

3. The detection rate will actually depend on different parameters, for example the target depth.
4. Some extensive *a priori* evaluation have definitely taken place in house for metal detectors using metallic targets, and some *a posteriori* field evaluation probably as well based on their widespread use.

Detector validation is actually more complex when different sensors and tools are used in a combined procedure, for example dogs to verify land cleared with manual methods or vehicle-based sensors. In this case it might well be possible that an individual sensor misses some mines which are then detected during the following step(s) of the procedure. One can however imagine that certifying such a combined approach in a rigorous way would even be more complex than certifying an individual sensor.

In the end one might therefore well have to reduce the problem complexity and be pragmatic, as already done in some countries, by certifying (actually simply accepting...) a demining procedure if it involves for example the use of at least two different detection methodologies, if possible individually validated up to a level judged to be satisfactory, combined with appropriate Quality Assurance/Quality Control procedures (which typically include a final partial check of the demined area).

Bibliography and Resources

Amongst the recent scientific publications dealing with sensors for landmine detection we can point to the [IEEE01] and [SSTA01] Special Issues. Previous review articles on mine and UXO detection sensors include [McF80, McF91, JPL95], and [JAS96, MIT96] for early reviews and interesting emerging ideas. An overview of the different sensing methodologies has also been provided in the EUDEM report [BRU99a] and ExploStudy[5] [BRU01], as well as the early papers [GRO96, BRU97a] (and the references contained therein), in which the author has been involved. Ongoing efforts include the information collection ongoing at the EUDEM Website (**`www.eudem.vub.ac.be`**).

International conferences covering the topic include specialised workshops such as those organised by the European ARIS Network of Excellence, the Edinburgh 1996 and 1998 EUREL International Conferences on “The Detection of Abandoned Land Mines”, the annual SPIE AeroSense and UXO Forum (US), and the Monterey Symposia (US, every 18 months). with the European ones in general more focused on the humanitarian demining needs and specificities than their US counterparts.

A number of multi national R&D projects in humanitarian demining have been launched during the past years with the financial help of the European Community, aimed at civilian applications. They have been detailed in the EUDEM report [BRU99a], with recent developments being covered in the EUDEM Website, amongst others.

5. Although aimed at the detection of explosives for Explosive Ordnance Disposal tasks a large part of the contents are of interest to landmine detection too.

1.3. The Role of Metal Detectors

Although the integration of mine detection dogs and mechanical systems (for *mechanically assisted demining* rather than mechanical demining) into humanitarian demining activities has considerably progressed in the last years, metal detectors do still play a considerable role and are present in nearly every multi-sensor system being researched (which should also ease system acceptance). Their weakness is in the detection of "only" metal, but at least one knows precisely what the detector is looking for.

The vast majority of all deployed mines do indeed contain some amount of metal[6] – the problem is in the high false alarm rate (see for example [JOY98] for some impressive statistics on the fragmentation of a grenade or a mortar bomb) rather than in the detection capability, with the exception of difficult ground conditions such as magnetic soils, where the present detectors do show their limits as clearly documented in [IPPTC01].

Research into metal detectors – pushing the full single sensor systems towards their intrinsic physical detection limits – *can therefore be beneficial for existing systems, not the least to better understand how they work, as well as for future ones, and this is where we have seen room for improvement.*

Also, although as discussed most users do basically investigate every alarm, we have come across a few situations in which the end user was implementing some response selection scheme:

- The **VAMIDS metal detector array** has been used in a stand alone application by Mechem, a South African demining company, which has carried out tests with the array mounted on a mine protected vehicle (MPV) to flag metal detector alarms using spray marks. The latter were then analysed by manual deminers who recleared the area, with a considerable reduction in false alarm rate with respect to the use of an ordinary metal detector (30 mines found by the array and then confirmed by the deminers on a 20,000 m^2 field, plus 107 false alarms for the array vs. 1640 additional metal signals for the deminers) [JOY02].

  The array was lifted from the ground in order to reduce sensitivity to near surface clutter, whilst still keeping sufficient sensitivity to detect the targets known to be present, i.e. PMN, PMN2 and PMD6 AP mines, which are not minimum-metal. A different test along similar lines has been reported in [JOY98].
- In a scenario in which the **target was UXO** rather than mines (a situation which occurs for example in Laos and some areas of Vietnam) the sensitivity of metal detectors was calibrated to the smallest target of interest at the maximum depth of about 50 cm[7].
- In demining operations were **multiple systems were used sequentially** – mechanical flails followed by dogs and finally men with metal detectors – the metal detectors were not used to check every alarm, rather to look only for larger metallic pieces such as detonators or UXO, with a consequent important gain in time[8] (the deminers were discriminating in some sort themselves on the basis of the detector signals).

These examples do not represent common practice, but they raise the hope that an intelligent system can be effectively used in the field, and that it might be possible to move beyond "mere" detection.

6. Albeit in some cases only at the level of the detonator capsule or striker pin (minimum-metal mines).
7. Roger Hess, UXB International, *private comm.* and communications to the online MgM Forum (2000).
8. Mario Sepe, ABC, Croatia, field visit (1999).

1.4. Metal Detectors R&D

It is in a certain sense amazing that more than a century after Maxwell put down his famous equations there are still a number of problems in electromagnetism looking for a satisfactory solution. In the case of metal detectors (actually eddy current devices) research and development of applications is additionally complicated by the following factors:

- **Lack of scientific information**: The metal detector industry is mostly composed of small manufacturers which have to protect their investment and have no particular incentive to publish the technical details of their systems or approaches (with the exception of patents, which have been the subject of a separate study [SIG02]).
- **Target and clutter variability**: In humanitarian demining there is a quite large number of target objects. Although it is true that these can mostly be grouped in a few categories (rings, spheres, cylinders, spheroids), the clutter items can basically have any shape. In addition there are composite objects as well.
- **Soil properties**: The soil is often assumed to be "transparent", for example in UXO detection, but it has to be clear that this is only a first order approximation, which gets worse as the target object gets less conductive or permeable, smaller or deeper, and as the soil becomes more conductive, permeable or inhomogeneous. As discussed the situation in magnetic soils (e.g. laterite) can be particularly difficult for metal detectors.

As a result of these factors and of the problem's complexity, to the best of our knowledge no current metal detector for humanitarian demining applications dares to deliver some quantitative information on the object under analysis. This is astonishing at first view, since the metal detectors' internal signals do depend, both spatially and temporally, on the nature of the object under study, its depth and size, an information which is exploited in other disciplines such as Non-Destructive Testing (see §3.2.2).

The apparent lack of quantitative output is probably linked to the fact that it is in general much easier to detect an anomaly than to classify it (i.e. saying that "there is something" rather than saying "there is an object of a given type"), and that in addition classification results get usually worse with decreasing signal to noise ratio. The fact that a deminer working in a traditional way with a portable detector has usually to walk in the area he clears, and therefore would pay dearly a mistake, has certainly also played a role in shaping research directions.

Things have however started to change in the last few years, as more effort has gone into understanding the basics of metal detectors for demining as well as UXO detection applications. Advances have been reported in areas such as:

- **Hardware**: Enhancements to existing hardware such as multifrequency systems or advanced pulse detectors, possibly deployed as arrays, or the use of new sensors such as magnetoresistive elements (see Chapters 2, 3 and 7).
- **Modelling** (physics understanding): Use of the dipole model and of enhanced target models for specific applications, to analyse the spatial characteristics of the induced magnetic field and/or its frequency/time dependence (see Chapters 2 and 3). Better understanding of soil properties and of their frequency/time dependence (see Chapter 4).
- **Algorithms**: Enhanced background suppression for example, or pole extraction from time domain data.

1.5. Thesis Framework

The aim of this thesis is to focus on metal detectors, analyse them from the theoretical and experimental point of view, and understand how their use in humanitarian demining could be improved. While staying as close as possible to practical aspects, we have chosen to emphasize the following research directions:

- **Multidisciplinary approach**: Other fields in which similar devices are used with profit have been analysed, in particular Geophysics and Non-Destructive Testing (NdT), and to a lesser extent Electrical Engineering, security applications (detection of concealed weapons for example) and Image Processing in Optics/Astronomy (for Chapter 7). Scales and geometries are however different in most cases, and care has been taken in transposing results.

  Examples of input from these fields include diverse topics such as basic target models, frequency differencing techniques, or the effect of superparamagnetic ground.

- **Patent analysis**: Due to the somewhat peculiar nature of the metal detector manufacturing community, quite some practical technical information is published only in the form of patents. This is particularly true for detectors build for hobbyists (e.g. treasure hunting), which use in some cases interesting technical innovations such as multifrequency operation or multi-period pulses.

  Patents have been analysed in a separate study [SIG02] carried out within the framework of the EUDEM2 survey.

- **Use of analytical models**: Some basic existing analytical models have been looked at in detail taking into account the parameters of interest to humanitarian demining. The soil response has been calculated as well, using a homogenous half-space model. Frequency differencing and ratioing techniques have also been considered, to help in background suppression.

  The analytical models provide an understanding of the direct, or forward, problem (obtaining the induced fields or voltages knowing the target and the operating conditions), and have been complemented in a semi-quantitative way in the case of elongated ferromagnetic objects such as short cylinders, for which demagnetization effects can be and are relevant.

- **Analysis of internal signals**: Internal raw (unprocessed) signals, rather than already processed ones (e.g. audio output), have been acquired under laboratory conditions with a commercial two-frequency metal detector, as a function of position and of a number of parameters. The use of internal signals makes it possible to fully characterise an object's response.

  The use of an existing and precise sensor has the additional advantage of not having to be burdened by sensor development issues.

- **Use of realistic targets**: Apart from reference objects, data taking concentrated on debris collected during a previous data taking campaign in Cambodia, and on real mines and their components.

- **Pattern recognition approach**: We have opted for a pattern recognition approach, rather than model fitting, in order to estimate the target parameters from measurements (see A1.1 for a short discussion). This has arisen in a natural way from the analysis of the response curves in the complex plane, their simplification by extracting a corresponding set of features, and the addition of supplementary features. It is also motivated by the large number of possible clutter shapes and by the number of clutter items usually overwhelming the number of mines.

- **Near field "imaging"**: As a complementary approach the possibility of generating images with a metal detector is also considered.

The link between the modelling aspects and the available experimental data is the main reason behind the choice to concentrate on frequency domain operation (FD results are also somewhat easier to understand as a first approach), and is in no way to interpreted as a negative judgement of time domain (pulse) systems. The FD results can obviously be extended to the time domain by using Fourier transformation. Each approach retains however its peculiarities, and we have therefore preferred to concentrate on one of them.

While it is true that analytical solutions exist only for a few basic geometries and analytical models are thus less flexible than numerical techniques, they are an excellent tool when it comes to providing general insight into the physics of the scattering process and its dependence on the model's parameters. The modelling has also been very important in the feature definition process.

Some of the target and soil modelling results, and methods to reduce soil effects, have already been known for a certain time, but to the best of our knowledge not necessarily in the form presented here by those involved with metal detection systems applied to humanitarian demining needs. We therefore see added value in having put together this information in a coherent way, with emphasis on humanitarian demining specificities.

On the experimental side, relying on two frequencies does obviously provide limited information with respect to a multifrequency system; this is however partially compensated by the two frequencies being placed towards the limits of the frequency band of interest.

Thesis Outline

Chapter 1 provides an **introduction** to the current situation in Humanitarian Demining and to the different approaches to the landmine detection problem, as well as to the resulting research avenues. The role of metal detectors and its limitations, and the current research activity more specifically linked to metal detectors are then highlighted. This sets the framework for the research carried out in this thesis, whose main directions are analysed and motivated.

Chapter 2 reviews the **basic principles** of low frequency electromagnetic induction devices ("metal detectors"), from the physics as well as from the technology point of view, and their application to Humanitarian Demining. It also looks at present-day commercial systems and at the generalities of some advanced developments.

Chapter 3 and **4** set the **theoretical framework**. They are dedicated to electromagnetic induction modelling aspects and focus on analytical solutions to some basic Frequency Domain problems, with the aim of understanding the direct (forward) problem.

Chapter 3 looks in detail at the response of a simple circuit model and at the general form of a target's EM induction response, before specializing on **representative basic targets** such as spheres and cylinders, with emphasis on the operating conditions prevailing in humanitarian demining and on frequency domain systems and their *phase response* in particular.

Chapter 4 deals with the **response of the ground** itself, calculated using known frequency domain analytical solutions in integral form for a (homogenous) half-space in Geophysics, or equivalently for a semi-infinite medium in NdT, in the case of a loop of finite size. Emphasis is again put on the operating conditions prevailing in humanitarian demining. Magnetic soil conditions are also considered, together with some frequency differencing methods to reduce soil effects.

Chapter 5 is dedicated to the acquisition and analysis of an extensive amount of metal detector raw data. The **experimental data** is compared with theoretical expectations, and the possibility of identifying targets of interest, or at least discriminating some metallic objects based on the characteristics of their response (in particular the phase), is analyzed relying mostly on complex plane plots. Results are reported for reference objects, for debris collected during a previous data taking campaign in Cambodia, and for a number of mines and their components, varying different experimental parameters (target distance, orientation, etc.).

Chapter 6 extends the results detailed in Chapter 5 providing a more **quantitative analysis** of the acquired data. The aim is to provide information complementary to the "complex plane" user interface, to address situations in which an object-by-object analysis by a human operator is not possible (automated interpretation), and to study classification opportunities.

After a preprocessing step a number of features are defined and ways to calculate them in practice from the available experimental data sets are proposed. The resulting feature distributions are then analysed and object classification opportunities discussed.

Chapter 7 tackles a complementary approach, looking at ways to provide information on the object's size and shape via near field **imaging**. This could be useful in discriminating in certain circumstances mines and/or UXO from clutter. It concentrates in particular on two portable high resolution applications, the first featuring a commercial multisensor systems designed for NdT applications in civil engineering, the second concentrating on the application of image deblurring techniques (deconvolution) to bidimensional data obtained with the Förster Minex metal detector.

Chapter 8 draws the main conclusions, emphasizes the thesis' original contribution and provides a brief outlook of how this work could be continued, or which other directions could be taken.

Bibliography

[BRO98] Brooks, J.; Nicoud, J.D. *Applications of GPR Technology to Humanitarian Demining Operations in Cambodia: Some Lessons Learned*. Proceedings of the Third Annual Symposium on Technology and the Mine Problem, Naval Postgraduate School, Monterey, CA, USA, 6-9 Apr. 1998. Available online as ref. Brooks98a at http://diwww.epfl.ch/lami/detec/

[BRU97a] C. Bruschini, B. Gros, "*A Survey of Current Sensor Technology Research for the Detection of Landmines*", SusDem'97 (International Workshop on Sustainable Humanitarian Demining) conference proceedings, Zagreb (Croatia), 29 Sept.-1 Oct. 1997, pp. 6.18/6.27.

Published in Sustainable Humanitarian Demining: Trends, Techniques and Technologies, Mid Valley Press, Verona, VA, USA, Dec. 1998, pp. 172-187, and as *"A Survey on Sensor Technology for Landmine Detection"* in the Journal of Humanitarian Demining, Issue 2.1, Feb. 1998. Available online at http://www.hdic.jmu.edu/hdic/journal/2.1/home.htm.

[BRU99a] C. Bruschini, K. de Bruyn, H. Sahli, J. Cornelis, and J.-D. Nicoud, "EUDEM: The EU in Humanitarian DEMining – Final Report (Study on the State of the Art in the EU related to humanitarian demining technology, products and practice)", EPFL-LAMI and VUB-ETRO, Brussels, Belgium, July 1999. Available from http://www.eudem.vub.ac.be/ and http://diwww.epfl.ch/lami/detec/.

[BRU01] "Commercial Systems for the Direct Detection of Explosives (for Explosive Ordnance Disposal Tasks)" (ExploStudy), Internal Note, Feb. 2001, 68 pp. Available from http://diwww.epfl.ch/lami/detec/. Published in modified form as:

"Commercial Systems for the Direct Detection of Explosives for Explosive Ordnance Disposal Tasks", Subsurface Sensing Technologies and Applications (SSTA), Vol. 2 No. 3, July 2001, pp. 299-336.

[EBL96] K. Eblagh, "Practical Problems in Demining and Their Solutions", *Proceedings of the EUREL Int. Conference on The Detection of Abandoned Landmines*, Edinburgh, UK, pp. 1-5, 7-9 Oct. 1996.

[GRO96] B. Gros, C. Bruschini, "Sensor Technologies for the Detection of Antipersonnel mines. A survey of current research and system developments", ISMCR'96 (Measurement and Control in Robotics), Brussels, Belgium, May 1996, pp. 564-569.

[IEEE01] Carin, L. (Ed.): *Special Issue on Landmine and UXO Detection*, IEEE Transactions on Geoscience and Remote Sensing, Vol. 39 No 6 (2001)

[IPPTC01] Das, Y., Dean, J. T., Lewis, D., Roosenboom, J. H. J., and Zahaczewsky, G. (Eds.), International Pilot Project for Technology Co-operation – Final Report (A multi-national technical evaluation of performance of commercial off the shelf metal detectors in the context of humanitarian demining), publication EUR 19719 EN, published by the European Commission, Joint Research Centre, Ispra, Italy, July 2001. Available from http://demining.jrc.it/ipptc/

[JAN02] King, C. (Ed.), Janes's Mine and Mine Clearance 2001-2002, Jane's Information Group Limited, London, 6th Edition, Jan. 2002. ISBN: 0 7106 2324 0.

[JAS96] Horowitz P., et al., "New Technological Approaches to Humanitarian Demining", Report JSR-96-115, JASON, The MITRE Corporation, McLean, Virginia, Nov. 96.

[JOY98] Joynt, V., "Mobile mine detection: a field perspective", *Proceedings of the 2nd EUREL Int. Conference on The Detection of Abandoned Landmines*, Edinburgh, UK, pp. 14-18, 12-14 Oct. 1998.

[JOY02] Joynt, V. "National Mine Action: Problems and Predictions", Journal of Mine Action, Mine Action Information Center at the James Madison University, Issue 6.1, 2002, pp. 37-41. Available from http://maic.jmu.edu/journal/6.1/index.htm

[JPL95] "Sensor Technology Assessment for Ordnance and Explosive Waste Detection and Location", Jet Propulsion Laboratory, JPL D-11367 Rev. B, Pasadena, California, Mar. 95, 293 pp.

[KIN96] King, C. *Mine Clearance…in the Real World*. Proceedings of the Technology and the Mine Problem Symposium, Naval Postgraduate School, Monterey, CA, USA, 18-21 Nov. 1996, pp. 3-3/3-9.

[McF80] J.E. McFee and Y. Das, "The Detection of Buried Explosive Objects", DRES, Ralston, Canada, Canadian Journal of Remote Sensing, Vol. 6, No. 2, December 1980, pp. 104-121.

[McF89] J.E. McFee, "Electromagnetic Remote Sensing; Low Frequency Electromagnetics", Defence Research Establishment Suffield, Ralston, Alberta, Canada, Suffield Special Publication No. 124 (report DRES-SP-124), January 1989.

[McF91] J.E. McFee and Y. Das, "Advances in the location and identification of hidden explosive munitions", DRES Report SR 548, Suffield, Canada, February 1991, 83 pp.

[MIM01] Dean, J. T. (Ed.), Project MIMEVA – Study of Generic Mine-like Objects for R&D in Systems for Humanitarian Demining, Final Report, contract ref. AA 501852, European Commission, DG Joint Research Centre, Institute for Systems, Informatics and Safety, Technologies for Detection and Positioning Unit, Ispra, Italy, July 2001. Available from http://humanitarian-security.jrc.it/demining/final_reports/mimeva/report.htm

[MIT96] Tsipis K., "Report on the Landmine Brainstorming Workshop of Aug. 25-30, Nov. 96", Report #27, Program in Science & Technology for International Security, MIT, Cambridge, MA, USA, 1996.

[SIG02] Sigrist, C., and Bruschini, C., "Metal Detectors for Humanitarian Demining: a Patent Search and Analysis", EUDEM2 report, May 2002. Available from http://www.eudem.vub.ac.be/

[SSTA01] Daniels, D.; Cespedes E. (Eds.): *Special Issue UXO and Mine Detection,* Subsurface Sensing Technologies and Applications (SSTA), Vol. 2 Issue 3 (2001)

Appendix A1.

A1.1. Inverse EM Induction Problems: Pattern Recognition vs. Modelling

The problems in which field measurements are used to infer properties of the source of the field are usually called "inverse problems" [McF89]. In the particular case of **inverse electromagnetic induction problems** we are dealing with, the aim is to recover the position (x,y coordinates and depth), shape, size and electrical material properties (conductivity and permeability) of a hidden compact object of finite size, plus possibly its orientation. In practice we are usually looking at a subset of these parameters.

There are two general techniques that may be used to estimate the target parameters from measurements, namely "model fitting" and "pattern recognition" [McF89]:

- **Model fitting** involves devising a mathematical model to describe the secondary (induced) fields as a function of source parameters, and then performing maximum-likelihood estimation (MLE, such as least squares fitting) to determine the parameter values that best fit the measurements. It is also possible to use a numerical model in the MLE procedure in place of an analytic equation, at the price of increased computational complexity.

  Model fitting is obviously limited by there being an applicable model (and most geometries do not have simple models).

- **Pattern recognition** involves comparing characteristics of a set of EM data from an unknown object with that from a known one, to determine if the two objects are the same. Some form of data reduction or compression ("feature extraction") might be necessary to make pattern recognition feasible. In some cases large libraries of feature vectors can be required.

  The problem becomes usually less tractable as the number of possible object shapes and sizes increases.

2.

Metal Detectors Basics

"Immediately upon the announcement of Arago's discovery of the influence of rotating plates of metal upon a magnetic needle (1824), and Faraday's important discovery of voltaic and magneto-induction (1831), it became evident that the induced currents circulating in a metallic mass might be so acted upon either by voltaic or induced currents circulating in a metallic mass as to bring some new light to bear on the molecular construction of metallic bodies.

The question was particularly studied by Babbage, Sir John Herschell, and M. Dove, who constructed an induction-balance, [...,] to which he gave the name of "differential inductors". " [HUG1879]

In this chapter we will focus on the low frequency electromagnetic detection of metallic objects, concentrating in particular on induction devices ("metal detectors") and their application to Humanitarian Demining. We will begin by reviewing the *basic principles* of such systems, from the physics as well as from the technology point of view (§2.2), having a first look at some features of the primary and secondary magnetic field and of the induction mechanism, and at the general operating principles of metal detectors. *Quantitative* details on these aspects will be provided in the next chapter.

The introductory part will be followed by a description of present-day commercial systems (§2.3), which are the result of many years' efforts in increasing sensitivity and autonomy, and mastering background rejection and ergonomics. The last section (§2.4) will then focus on the generalities of advanced developments and provide ideas of how they could be used with profit in humanitarian demining, possibly in selected scenarios. Some of the corresponding improvements will be tackled in the following chapters, with the aim of providing target information which is nowadays mostly missing.

2.1. Electromagnetic Detection of Metallic Objects

The detectors we will consider are electromagnetic sensors which usually either exploit static magnetic fields, or low frequency electromagnetic fields up to some hundred kHz roughly. These sensors are capable of detecting metallic objects buried in the ground at usually shallow depth (tens of centimetres to some meters), whilst providing "limited" information on their nature (depth, shape, size, material, etc.). Direct contact with the surface is not necessarily required, but proximity might well be [BRU00a]. For an overview of detection systems see also [ROC99].

2.1.1. Magnetic Devices

Magnetic devices rely on the influence of nearby ferromagnetic objects, either via induced or via residual magnetization, on a magnetic field which they can generate themselves, or which can be naturally occurring.

Instruments of the first kind are active; they can for example measure changes in the magnetic circuit's properties, such as its magnetic reluctance, or directly map the deformation ("flux leakage") of the static magnetic field they produce [ALL97]. They are for instance being used or proposed for civil engineering applications (rebar locators, cover meters) [BUN96].

Instruments of the second kind are passive, not radiating any energy, and typically measure tiny disturbances of the earth's natural magnetic field; they are called magnetometers, or gradiometers when used in a differential arrangement. These very sensitive devices are usually employed to detect large ferromagnetic objects such as UXO and can be effective to depths of several meters [JPL95], but do not react to non-ferromagnetic targets. They are only used in humanitarian demining when a real need exists (e.g. deeply buried UXO).

In the following we will therefore concentrate our attention on electromagnetic induction devices, which are routinely being used in a number of different fields (civil engineering, humanitarian demining, geophysics, security applications, etc.).

2.1.2. Metal Detectors (Electromagnetic Induction Devices)

Electromagnetic induction devices, which are the ones often referred to when speaking of "metal detectors", are active, low frequency inductive systems. They are usually composed of a search head, containing one or more coils carrying a time-varying electric current[9] $I_{\mathrm{prim}}(t)$. The latter generates a corresponding time-varying magnetic field[10] $\boldsymbol{B}_{\mathrm{prim}}(\boldsymbol{r}, t)$ which "propagates" towards the metallic target (and in other directions as well). This primary (or incident) field reacts with the electric and/or magnetic properties of the target, usually the soil itself or a solid structure, and any metallic object contained in it. The target responds to it by modifying the primary field or, as a more accurate description, by generating a secondary (or scattered) magnetic field $\boldsymbol{B}_{\mathrm{sec}}(\boldsymbol{r}, t)$. This effect links back into the receiver coil(s) in the search head, where it induces an electrical voltage which is detected and converted, for example, into an audio signal [ALL92]. These processes are summarised in Eq. (2.1) below and shown schematically in Figure 2.1.

$$\mathrm{I}_{\mathrm{Prim}}(\mathrm{t}) \rightarrow \mathbf{B}_{\mathrm{Prim}}(\mathbf{r}, \mathrm{t}) \rightarrow \mathbf{J}_{\mathrm{eddy}}(\mathbf{r}, \mathrm{t}) \rightarrow \mathbf{B}_{\mathrm{sec}}(\mathbf{r}, \mathrm{t}) \rightarrow \mathrm{I}_{\mathrm{sec}}(\mathrm{t}) \tag{2.1}$$

The secondary field $\boldsymbol{B}_{\mathrm{sec}}(\boldsymbol{r}, t)$ depends, both temporally and spatially, on a large number of parameters (see also [CHE84]): the problem's *geometry* (object distance and orientation), the object's *properties* (shape, size, conductivity and permeability), the temporal and spatial distribution of the *primary field* and, last but absolutely not least, the presence of any *background*

9. These devices are usually working in the VLF (Very Low Frequency) part of the electromagnetic spectrum, up to a maximum of some hundred kHz.
10. **B** [Tesla], with $\mathbf{B}=\mu_0\mu_r\mathbf{H}$, is also called "magnetic induction", in which case **H** [A/m] is called "magnetic field".

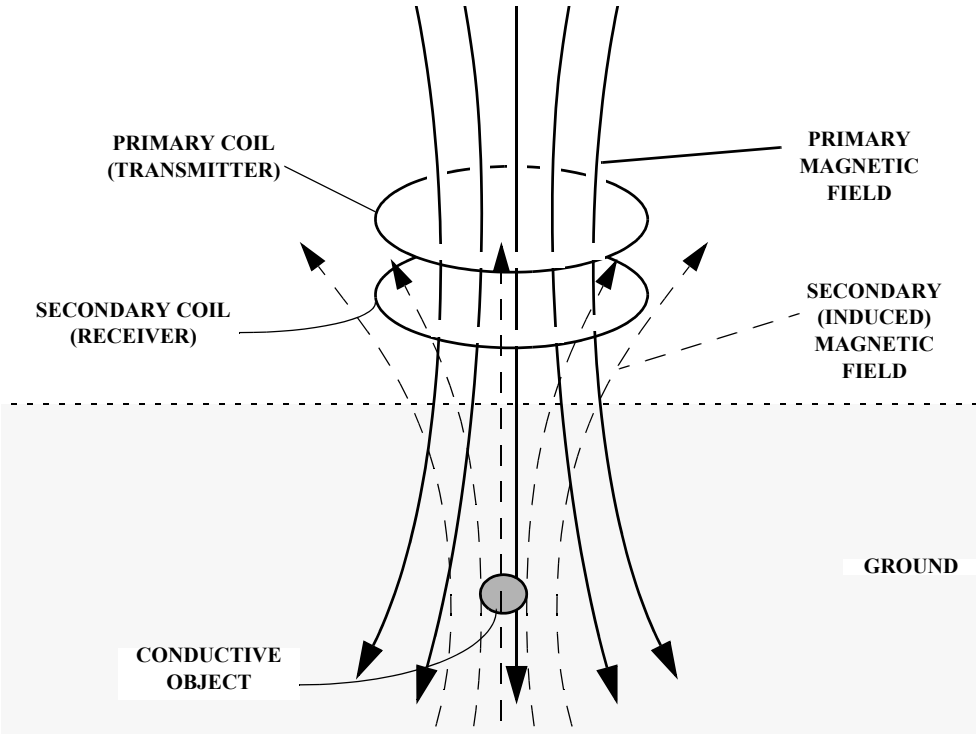

Figure 2.1: Schematic Primary/Secondary field plot (continuous wave system, non-ferromagnetic object)

signal (in particular *the ground itself!*). This is schematically represented in Figure 2.2 referring as an example to a spheroid with semi-axes of length R_1 and R_2, oriented at angles Θ, Φ. Note that at the frequency range of interest we are basically insensitive to the target's dielectric properties (ε), as will be demonstrated in §3.4.2. Target characterization is very difficult in the general case, but there are a number of situations where some (limited) statements on its nature can be issued.

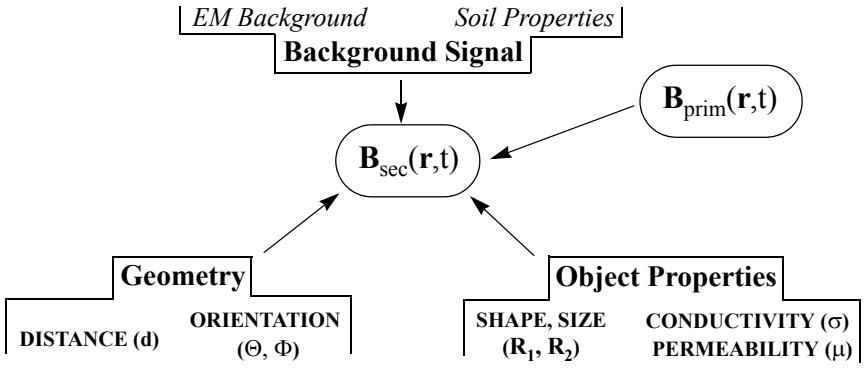

Figure 2.2: Parameters influencing the secondary (induced) magnetic field

2.2. Theoretical Background: Basic Principles

In this paragraph we review the *basic principles* of metal detectors, from the point of view of the basic physics, having a first look at some features of the primary and secondary magnetic field and of the induction mechanism, and of the general operating principles.

2.2.1. Induction

The secondary field is due to eddy currents[11], which are induced by the primary field in nearby conductive objects (see the $\mathbf{J}_{eddy}(\mathbf{r},t)$ in Eq. (2.1)). Low conductivity metals, such as some alloys and stainless steel, are in general more difficult to detect, whereas the detector's response is magnified for ferromagnetic objects due to the high value of their relative permeability μ_r (induced magnetization). Magnetic effects can play a substantial role, in particular for ferromagnetic objects at the lower frequency range, as will be detailed in the next chapter.

Eddy currents are due to time-varying magnetic fields and are basically governed by the law of induction (Faraday's Law). They circulate mostly on the surface of the metallic target ("skin effect"), which explains why metal detectors are mostly surface area detectors. As a rule of thumb, larger objects will generate more eddy currents, but an object with twice the surface will not be found twice as deep; indeed, the field decreases very rapidly with distance (§2.2.2). The strength of eddy currents will also increase in objects with higher conductivity.

The skin effect states that an electromagnetic field decays in a conducting medium as $e^{-r/\delta}$, where r is the distance from the surface and δ is a characteristic depth of penetration, the *skin depth*. Eddy currents generate magnetic fields opposed to the primary field (Lenz's Law); the current flow will therefore decrease for increasing depth within the object. The skin depth depends on the frequency f, on the permeability μ and conductivity σ of the material as follows:

$$\delta = \sqrt{\frac{1}{\pi f \mu \sigma}} = \sqrt{\frac{2}{\omega \mu \sigma}} \cong \frac{500}{\sqrt{\sigma f}} \text{ when } \mu = \mu_0 \qquad (2.2)$$

In the case of copper, for example, we have that $\sigma=1/\rho=5.8\times10^7$ S/m, and $\mu=\mu_0=4\pi\times10^{-7}$ H/m = 1.26×10^{-6} H/m. This translates into a penetration depth at 2 and 20 kHz of, respectively, 1.5 mm and 0.47 mm. Other values are listed in Table 2.1, but as a rule of thumb we can say that the skin depth is of the order of one mm, at 10 kHz, for most metals. Table 2.1 lists some conductivity and permeability figures for the most common conductors, especially useful to calculate the skin depth at a given frequency. The conductivity is given in Siemens/m (or mhos/m, remembering that $\sigma=1/\rho$ where ρ is the resistivity in Ohm·m), the permeability in units of $\mu_0=4\pi\times10^{-7}$ Henry/m.

Material	*Conductivity σ (10^7 S/m)*	*Permeability μ_r (in units of μ_0)*	*Skin Depth δ (@2 kHz, in mm)*	*Skin Depth δ (@20 kHz, in mm)*
Copper	5.8	1	1.5	0.47
Aluminium	3.54	1	1.9	0.60
Brass (yellow)	1.5	1	2.9	0.92
Steel (typical)	0.63	150 (300)	0.37 (0.26)	0.12 (0.082)

Table 2.1: Conductivity, Permeability and Skin Depth values for some conductors at 20°C

11. Also known as "Foucault currents" in some countries (especially French speaking ones).

As we said, eddy currents circulate mostly on the surface of the metallic target. Metal detectors are therefore mostly surface area detectors, and what counts is the portion of surface area which is "looking" towards the bottom of the detector. This can be intuitively explained by thinking of a small coil of area S, at an angle α with respect to a time varying, uniform primary magnetic field of magnitude B. At its ends a voltage V will be induced, which is, according to Faraday's law, proportional to the change of magnetic flux Φ passing through the coil, and therefore to cosα:

$$V = -\partial\Phi/\partial t \quad \text{with} \quad \Phi = \int_S \boldsymbol{B}_{\text{sec}} \cdot \boldsymbol{dS} \tag{2.3}$$

This is graphically depicted in Figure 2.3. In practice even for α=90° (vertical object) there might be a response by scanning over the object because the field itself is not necessarily vertical at the object's position.

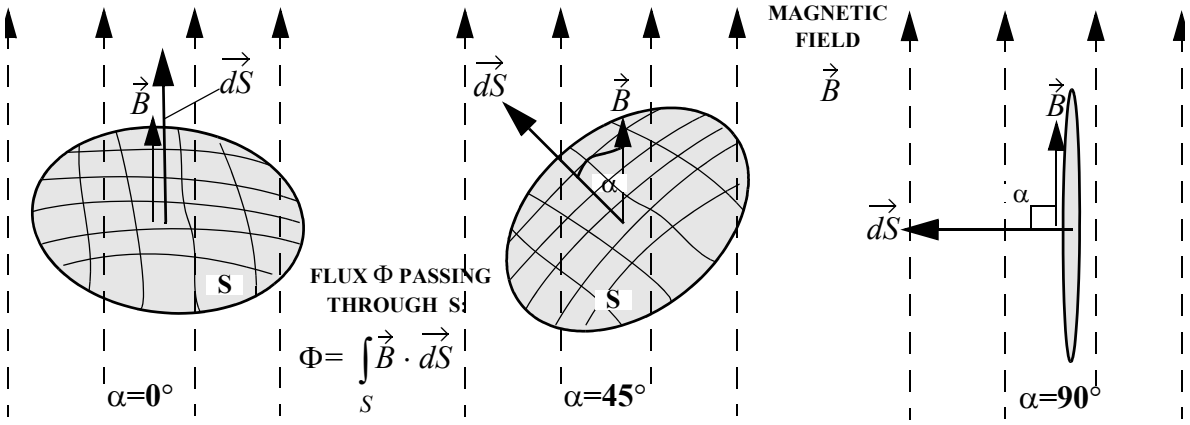

Figure 2.3: Target orientation effects

2.2.2. Magnetic Field Behaviour

Metal Detectors are *proximity sensors*. Indeed, in the case of a circular coil of radius *R*, carrying a current *I* and having *N* turns, the primary field B_z at a distance *d* on the coil axis behaves as:

$$B_z(d) = \frac{N\mu_0 I}{2}\frac{R^2}{(R^2+d^2)^{3/2}} = \frac{\mu_0 M}{2\pi(R^2+d^2)^{3/2}} \quad \text{with} \quad M = NI\pi R^2 \tag{2.4}$$

where *M* is the coil's magnetic moment (in general: *M=NIS*, with *S* being the coil surface). We have in particular:

$$B_z(0) = \frac{N\mu_0 I}{2R}, \quad B_z(2R) \approx \frac{1}{11}B_z(0) \quad \text{and} \quad B_z(d) \approx \frac{\mu_0 M}{2\pi d^3} \quad \text{for } d \gg R \tag{2.5}$$

The field decreases therefore with the cube of the distance *d* far away from the coil. Given that the secondary magnetic field has to "propagate" all the way back to the receiver coil(s) it is not surprising that the "art" of building metal detectors consists, in a certain sense, in discriminating small target signals from background signals.

Note that the actual *far field* behaviour does in fact not depend on the exact coil shape but only on its dipole moment *M*, a magnetic dipole model being applicable. Analytic expressions are therefore available.

Note also that the primary magnetic field generated at the surface (*d*=0) by a coil carrying a given current I and having a fixed number of turns N (i.e. *NI*=constant) gets smaller as the coil gets larger (Eq. (2.5)), but decreases less rapidly with distance as shown in Figure 2.4, and that smaller receiving coils pick up a correspondingly smaller fraction of the secondary field[12]. Smaller coils

provide therefore better sensitivity (at closer ranges) and spatial resolution, but do not allow to go as deep, and scan as fast, as the larger ones.

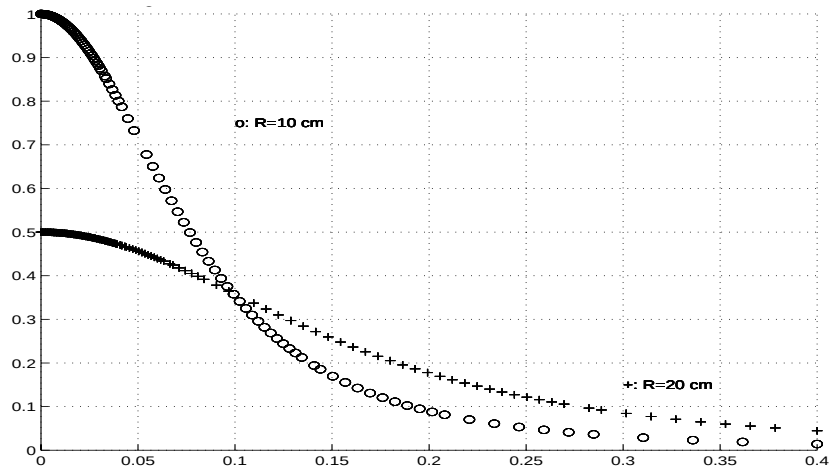

Figure 2.4: Magnetic field behaviour with distance (in m) for coils of different sizes (*NI* constant; field normalized to the field of the smallest coil at d=0)

Expressions for the magnetic field of a circular and a rectangular coil are quoted in A2.2.

Finally, let us point out that these considerations are strictly speaking valid only in the static case; they retain however their validity for low frequency electromagnetic fields, as will be demonstrated in §3.4.2.

2.2.3. Coil Configurations

Figure 2.5 shows some of the most frequently encountered coil configurations. Most metal detectors for landmine detection are of the coplanar type (left); the coils are in the same plane and can be concentric as for example in the well-known Schiebel metal detector, or shaped like a "double-D" as in the Förster Minex 2FD which will be discussed later on. Oval shapes, which somewhat concentrate the field towards the centre, are also proposed by a number of manufacturers, as well as square coils, or differential setups (see also Figure 2.6). The "4B" design achieves good pinpointing (accurate object location), at the expense of a reduced sensitivity due to a small effective area (the overlap region near the middle; the receive coil is the smaller one in the centre). The resulting field pattern is rather complex.

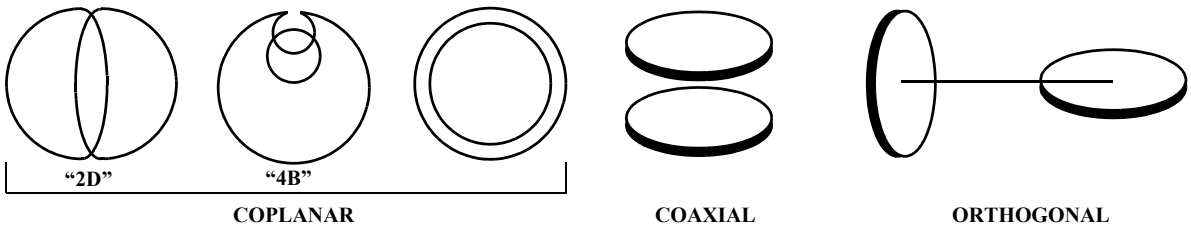

Figure 2.5: Some of the most frequently employed coil configurations (transmit-receive systems) (Adapted from [LAG79]).

The orthogonal setup is often used in combination with larger coils for deep-seeking devices (transmit vertical, receive horizontal). The coaxial setup can be more complex, with several receive coils for example as in the case of some MD arrays, and/or for systems targeted at UXO detection.

12. This is rigorously valid only for a uniform magnetic field

Differential (receive) setups are also used by several manufacturers. The corresponding signals are typically left-right symmetric and show a sharp transition, instead of a maximum, when passing over the object (see Figure 2.6); this setup eases pinpointing (localization of the object's centre), helps in background suppression and enhances the separation power (localizing nearby objects). On the other hand mechanical tolerances are stricter, and sensitivity is probably somewhat decreased, given that the receiving coil has been split into two, effectively halving the sensitive area.

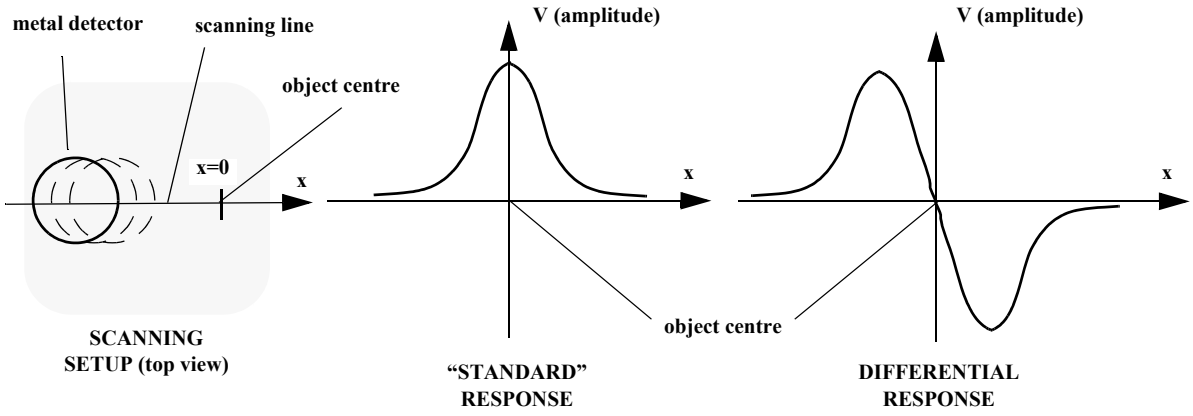

Figure 2.6: Differential response vs. standard response (qualitatively) for a linear scan

2.2.4. Frequency Domain Metal Detectors

Metal detectors can be schematically subdivided in Frequency Domain (FD) (or Continuous Wave, CW), and Time Domain (TD) systems [ALL92, RIG99, SZY99].

Frequency Domain instruments make use of a discrete number of sinusoidal signals, very often just one. Single coil and separate transmit/receive circuits are possible, as will be described below.

Information on the target's nature is contained in the *amplitude and phase* of the received signal, or equivalently in the real and imaginary part of the probe's complex impedance change (ΔZ), as the detector approaches the target. Their measurement in *background conditions* can be used to reject part of the background signal itself, especially in areas in which the detector's performance would otherwise be seriously degraded, such as sea beaches (salt water is conductive) or strongly mineralized regions (containing for example bauxite, laterite, magnetite or magmatite), which can be conductive or iron rich, as found in parts of Cambodia, Mozambique and Angola. Generally speaking, background rejection is more difficult in nonhomogeneous areas.

From the point of view of sensitivity there is a tendency to move towards higher operating frequencies, which can be probably explained by thinking of the quality factor Q improvement of a resonant (LC) circuit, and also by the fact that the induced voltage V is proportional, according to Faraday's law, to the rate of change of the magnetic flux Φ passing through the receiver coil (Eq. (2.3)). Indeed, $\boldsymbol{B}_{sec}$ varies as $e^{i\omega t}$, and the same is true for Φ. Therefore[13] $V \propto \omega e^{i\omega t}$.

On the other hand lower frequencies penetrate better, appear to be less affected by ground mineralisation and the skin effect in metal is reduced, so that a comprise solution has to be found as usual. In the Förster Minex 2FD system an interesting strategy has been adopted, which consists in employing one frequency (2.4 kHz) towards the lower bound and one (19.2 kHz) towards the upper bound of the frequency range of interest. Other characteristics of higher and

13. We are simplifying here, in reality $\boldsymbol{B}_{sec}$ obviously depends on ω too.

lower operating frequencies will be discussed when looking at the response predicted by the theoretical models (Chapter 3).

As an example of Frequency Domain detectors we can quote the Förster Minex 2FD, quite a few models from the Ebinger line and most treasure hunting devices. Frequency Domain systems have often been the choice for mine detection because they seem to work well especially for very small and close objects, except where ground conditions are severe and request the use of pulsed systems. The possibility of using an array of frequency domain detectors is somewhat complicated by interference effects between neighbouring systems.

We will now discuss different ways of implementing Frequency Domain metal detectors.

2.2.4.1. Single Coil Frequency Domain Metal Detectors

A single coil can be used, whereby there are basically two ways of working.

In a first scheme the coil's change in impedance ΔZ is detected by measuring for example the damping of a (fixed frequency) resonant circuit, as shown schematically in the upper half of Figure 2.7. In this simplified transformer model the coil acts as the primary winding of a transformer, the object as a "single turn" secondary winding (N_S=1), representing the load on the transformer. In practice one could measure the amplitude and/or phase of the voltage change across the primary coil (V_P=$I_P Z_P$), assuming a constant current I_P.

When approaching a metallic object there would be a decrease in the probe's impedance. For ferromagnetic objects the magnetic flux would however be strengthened[14] and ΔZ increases.

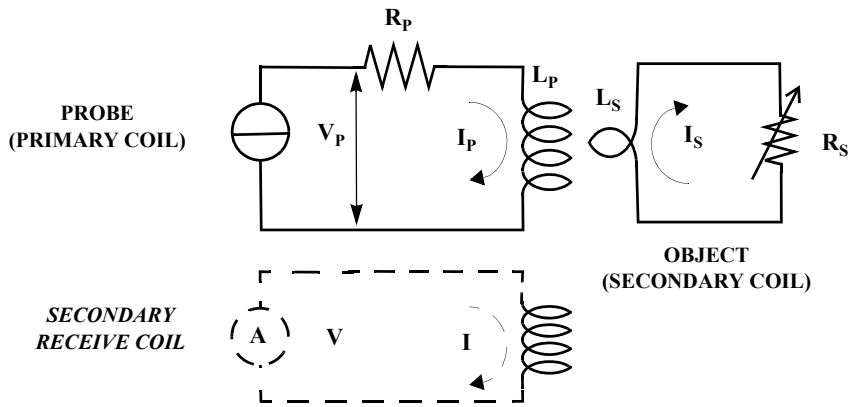

Figure 2.7: Simplified transformer model of a metal detector in presence of test material (buried object)

In a second scheme the change in self-inductance of a single coil is measured by looking at the frequency shift Δf_{res} of an oscillator in which the coil acts as the inductive element (with for example $f_{res} = \sqrt{1/(LC)}$ for an LC oscillating circuit). One of the simplest methods is the Beat Frequency Oscillator (BFO), which was one of the earliest types of metal detectors and is still used in some simple applications, such as for traffic light controls via a loop buried under the surface. A schematic BFO implementation, which directly produces an audio signal, is shown in Figure 2.8. No ground balancing was possible with BFO systems.

Other implementations based on the modifications of the properties of a resonant circuit are also proposed by some manufacturers.

14. We can think for example of a coil whose inductance L will increase introducing into it a ferromagnetic core.

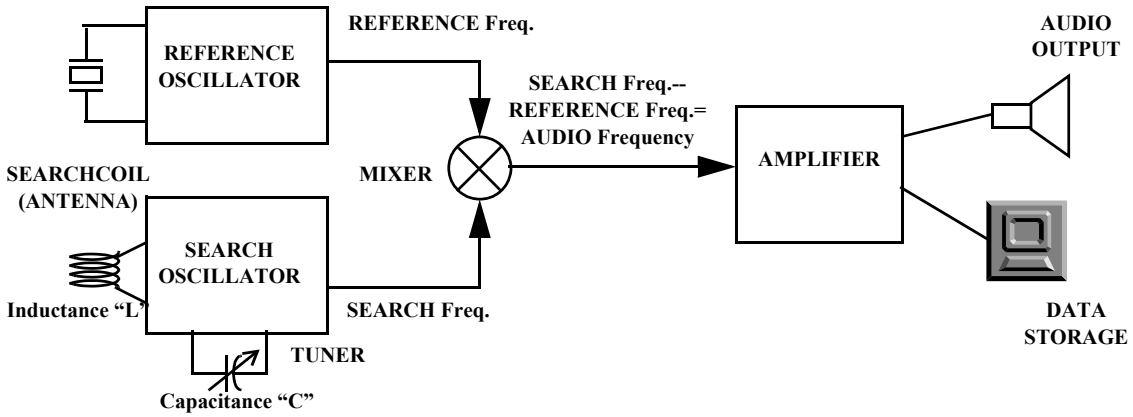

Figure 2.8: The Beat Frequency Oscillator (a type of single coil Frequency Domain MD) (Adapted from [GAR95])

2.2.4.2. Frequency Domain Metal Detectors with Separate Transmit/Receive Circuits

Most modern Frequency Domain metal detectors do in fact use separate transmit/receive circuits and operate in the VLF region of the spectrum, typically between a few kHz and a few tens of kHz (say 1-50 kHz). If we denote the voltage in the transmitter coil with V_1 and in the receiver coil with V_2, and M_{12} is the mutual inductance between the two coils, then we have that (operating at a single frequency ω):

$$V_1 = I_1 e^{i\omega t} \text{ and } V_2 = -i\omega M_{12} I_1 e^{i\omega t} \tag{2.6}$$

with $M_{12} = M_{21}$ (reciprocity theorem). Any change in the voltage V_2 induced in the receiver coils caused by the presence of metallic or magnetic objects can therefore be interpreted as a (usually small) change in the mutual inductance M_{12} between the transmit and receive coil(s)[15] (see again Figure 2.7). In fact, for this type of detectors the coils are often arranged to have as low a mutual inductance as possible when no object is present (i.e. minimize direct coupling of transmitted and received field), in order to enhance the contrast between the situation with presence and with absence of signal. In such a setup the position of the coils can therefore be critical, for instance in presence of large temperature gradients and/or of mechanical stress (coil flexing) which can influence the coil coupling.

In the case of single frequency FD instruments the secondary (or received) signal:

$$V_{sec}(t) = A_{sec} \sin(\omega t + \varphi) \tag{2.7}$$

will vary sinusoidally as a function of time at the angular frequency ω of the transmitted signal, but in general phase shifted (i.e. time delayed) by φ with respect to the latter (for details see [VUI94]). The received signal can also be written as:

$$V_{sec}(t) = A_{sec} \sin(\omega t + \varphi) = V_R \sin\omega t + V_X \cos\omega t \quad \text{where} \quad V_R = A_{sec} \cos\varphi \quad \text{and} \quad V_X = A_{sec} \sin\varphi \tag{2.8}$$

The first quantity, V_R, is the component of the received signal in phase with the transmitted one ("**in-phase**" or **resistive** component), the second, V_X, is the component of the received signal dephased by 90 degrees with respect to the transmitted signal ("**quadrature-phase**" or **reactive** component); both representations are clearly equivalent.

It is therefore customary to represent the received signal V_{sec} as the complex quantity:

$$V_{sec} = V_R + iV_X \ , \ i=\sqrt{-1} \tag{2.9}$$

15. Metal detectors of this type are also called **Induction-Balance** systems.

bidimensionally in a complex plane (or impedance plane) as a point of coordinates $V_{sec}=(V_R,V_X)$, as schematically shown in Figure 2.9.

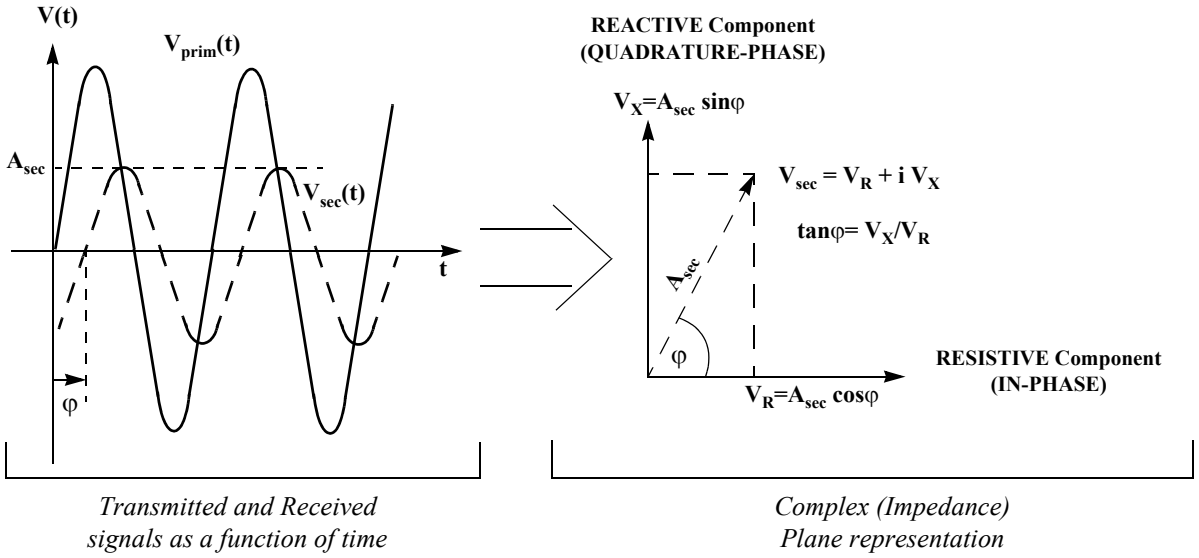

Figure 2.9: Representation of the received signal as phase vector in the complex (impedance) plane

Note that the separation in in-phase and quadrature-phase component, which can be achieved electronically for example by means of a synchronous demodulator[16], requires a quite precise control of the reference phase. For example, the accuracy of the reference phase regulation of the Förster Minex detector is of about 0.01° (about 0.17 mrad), necessary in particular to keep track of tiny variations in the target output signals (especially when their difference is used for detection, as we will see later) compared with often much larger background signal levels. In addition the reference phase regulation needs to be continuous in order to provide sufficient (thermal) stability and counteract drifts.

The amplitude A_{sec}, and often the phase shift φ too (or equivalently V_R and V_X), will in fact vary when the detector and the target object are moved with respect to each other, containing information on the target's nature:

$$A_{sec} = A_{sec}(t)\ ,\ \varphi = \varphi(t) \ \text{ or equivalently } \ V_R = V_R(t)\ ,\ V_X = V_X(t) \qquad (2.10)$$

These are the quantities we are interested in and we will not be surprised by seeing later on the point corresponding to $V_{sec}=(V_R,V_X)$ move in the complex plane along characteristic lines as the detector or the target are displaced.

2.2.5. Time Domain Metal Detectors

Time Domain, or "pulse", instruments work by passing pulses of current through a coil (typical repetition rate of the order of 1 kHz), taking care to minimise the current switch-off time (a few μsec). Eddy currents are thus induced in nearby conductive objects; the exponential decay of the corresponding secondary magnetic field, which is slower than the primary one, is observed with time. A Time Domain metal detector measures in other words how quickly the momentarily generated magnetic field breaks down, which happens to be slower in presence of metal [ALL92].

16. By sampling, for example, the sinusoidal signal at two positions 90° apart on the waveform.

A practical example, referring to the Protovale pulse induction sensor for rebar location, is shown in Figure 2.10. The current in the coil starts up fairly gently (a), and is then turned off very rapidly at the end of the pulse (a few μsec); this induces a very large voltage spike ("back e.m.f.") (b). The cycle is repeated after about 1 msec. The eddy currents induced in a conductive target try to recreate the field that has just disappeared, and also decade graciously away (c). These eddy currents generate a secondary magnetic field that induces a (small) voltage in the coil head, which decays at the same rate (actually as its time derivative) (d). The signal is sampled only after a short delay, which ensures that the switch-off transient is over (e) [ALL92].

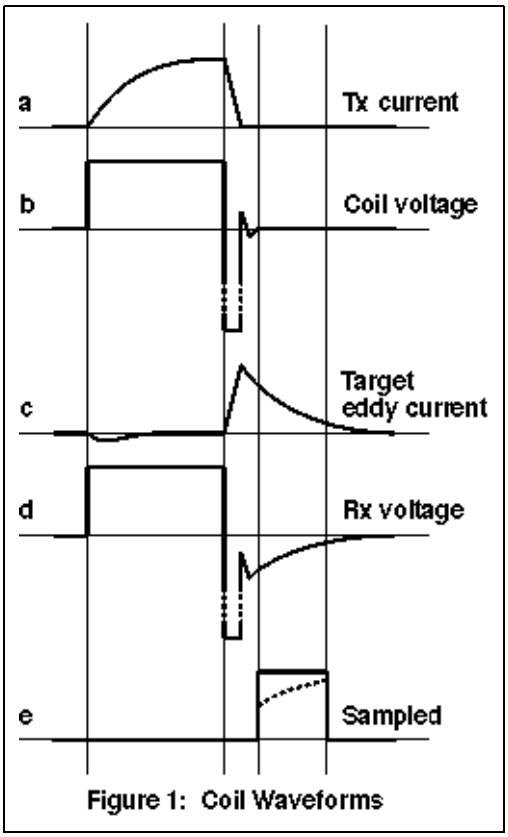

Figure 2.10: Typical pulse induction detector timing (Source: [ALL92])

The eddy current decay time constant itself, some tens (short) to hundred μsec, depends (predominantly) on the target's conductivity, permeability and size. Low conductivity background and nuisance items, such as sea water and thin foils for example, have a very short decay time. A pulse detector, which is tuned to sample only a specific portion of the received signal, can therefore be "easily" made insensitive to them by an appropriate choice of the delay (some tens of μsec[17]) between switch-off and sample. A similar argument applies to purely magnetic but non-conductive targets, which are magnetised by the transmit pulse but demagnetise just as promptly after switch-off. On the other hand it was true until a few years ago that overall sensitivity is reduced in comparison with Frequency Domain detectors, and there can be problems in finding low conductivity metallic objects such as those made of stainless steel. Figure 2.11 summarizes the situation and stresses the difference between the "good" and the "poor" conductor case.

17. [ROW] quotes 20 μsec, ideally, and realistically 30 to 40 μsec. Improved systems tend however to sample the entire waveform and/or start at earlier sampling times, as in [NEL01].

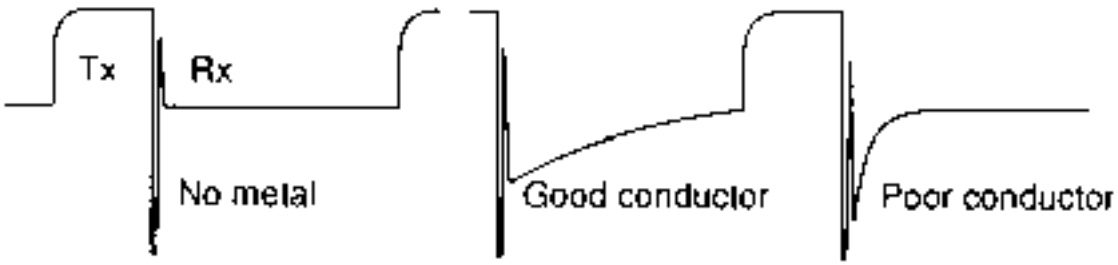

Figure 2.11: Decay of the induced pulse in the no metal, good and poor conductor case (Source: Protovale)

Given that the transmit and receive phase are temporally separated – the received waveform is usually[18] sampled during the time in which the transmitter is off – pulse detectors can use one and the same coil for transmitting and receiving; the decoupling of the two phases also allows to work with high power, and therefore in practice to go deeper (increased sensitivity due to higher field strength). Power consumption might obviously become an issue, and the presence of a large inductance (due for instance to a large number of turns and/or a large area of the transmitter coil) can cause switch-off problems.

Pulse systems are the detector of choice when it comes to working in salt water or strongly mineralised soils. They are however increasingly often challenging Frequency Domain systems, and not only where conditions are severe.

Time Domain systems are inherently broadband and sample therefore a larger portion of the VLF electromagnetic spectrum. This information is however often not used directly, e.g. when the received signal is sampled only in a few points, or when its integral over a time window is used.

The interested reader will find a more detailed description of the different stages of the pulse response in [KAC98] and in general in the geophysical literature dealing with Time Domain systems. Detailed time-decay data is shown for a variety of mines in [NEL01], which does also take into account soil effects, in particular on the response of minimum-metal mines.

18. Recording before the transmission phase is finished is in principle also possible.

2.3. Modern Tools

We will describe in this section present-day commercial systems, which are the result of many years' efforts in increasing sensitivity and autonomy, and mastering background rejection and ergonomics. The interested reader can look as a complement at the [SIG02] **patent study**, in particular at the *reference patents* mentioned therein, of which we have incorporated here the most interesting elements.

2.3.1. Background Signal

As already hinted at in Figure 2.2, the target signal is accompanied by an omnipresent background signal. The latter is made up of contributions due to electromagnetic (EM) background (e.g. due to power lines or other forms of interference), to drift effects (e.g. due to thermal and/or mechanical variations) and to the soil signal itself. It should be possible to mitigate the first two effects by a careful design of the hardware (coils, electronics) and of the signal processing (e.g. bandpass filtering). A differential setup should also be helpful.

We already discussed in §2.2.4 the importance of the soil signal itself, in particular in areas such as sea beaches or strongly mineralized regions, which can be conductive or iron rich [MIL96] (see also Table 3.3), as found in parts of Cambodia[19], Mozambique and Angola for example. An iron rich ground would result in a reactive component, a conductive ground in a resistive signal, which seems to be the prevalent condition in most parts of the world (with the notable exception of Australia).

The soil's conductivity is indeed small compared to that of metals, but is distributed over a much larger volume. The resulting signal, V_{soil}, can therefore be far from negligible. In such regions the detector's performance can be seriously degraded, especially when looking for small signals, resulting from small and/or deep objects, which can be completely masked by the ground signal. In reality, therefore (all quantities being complex):

$$V_{sec} = V_{soil} + V_{target} \tag{2.11}$$

In addition the magnetic susceptibility of certain soils can vary with frequency (or time) [DAS98, and refs. [10]-[20] therein mentioned], as will be discussed in Chapter 4.

In these cases some form of background rejection is essential and often relies on measuring the ground signal when no metallic object is present, to then "follow" and suppress it as well as possible. One "classical" way of implementing this in a frequency domain system with separated transmit/receive circuits consists in measuring the phase shift due to the ground signal alone, and providing the received signal relative to it by means of a synchronous demodulator, as depicted in Figure 2.12.

Generally speaking, background rejection, also called "ground balancing", is more difficult in nonhomogeneous areas. Metal detectors can perform the ground balancing function automatically or manually, for example via a multiturn knob in FD systems, the latter option being preferred by experts when a high degree of precision and total control of the instrument is required. Ground balancing can in fact be extremely delicate, given that situations where one component is much larger than the other, up to a ratio of 1000:1 corresponding to an angle of 0.057 degrees in the phase plane, are not infrequent ([ROW] mentions "a resolution of better than 500 to 1"). Automatic ground balancing is usually preferred in systems for humanitarian demining. Sensitivity will nevertheless usually be reduced, partly because the magnetic field penetrates less well in the ground, and partly due to possible problems with localized soil inhomogeneities such as voids, roots, or "hot rocks" (magnetic rocks), which would cause too many "false alarms".

19. Mineralised (lateritic) soil was estimated to be present in 40% of the minefields in Cambodia [DAS98].

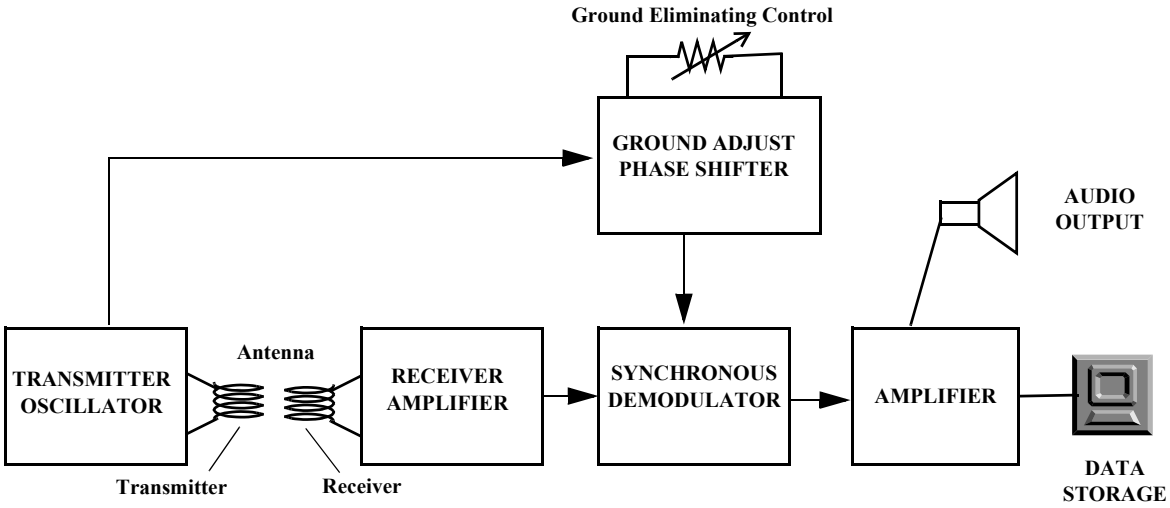

Figure 2.12: Ground balancing in Frequency Domain transmit/receive detectors (Adapted from [GAR95])

Notice that certain detectors have to be moved continuously to work properly (also called *motion* or *dynamic systems)*, whilst others are capable of static operation *(non-motion* systems*)*.

The effect of soil on the performance of metal detectors used for landmine detection was in fact already recognized during WWII, and some models were fitted to reduce the "pavé effect" due to road stones containing particles of magnetic iron oxides (discrimination against low conductivity magnetic bodies) [ROS48, DAS98]. In more recent scientific publications the subject seems however not to have been considered all too often, partly due to the focus on in-air measurements or on UXO, whose signal is often large enough, especially for shallowly buried ordnance, to allow ignoring any soil contribution. This is usually not the case for landmine detection, in particular when minimum-metal mines are present, and has been clearly demonstrated in recent evaluations [IPPTC01]. We will therefore dedicate a full chapter to the quantitative analysis of the soil's response.

There is therefore quite a lot to learn from other applications of metal detection, in particular treasure hunting, where soil effects have been a subject of interest for the last decades (we are thinking for example of the successful marketing of the Australian Minelab F1A4 detector for landmine detection).

2.3.2. Metal Detectors for Humanitarian Demining

The following paragraphs will be dedicated to an overview of the systems currently used or developed for humanitarian demining applications, and their most important current limitations. Their role has already been described in §1.3.

2.3.2.1. Manufacturer Overview

Most of the companies producing metal detectors for landmine detection are small and jealously guard the secrets of the trade (see §1.4); technical and scientific documentation has unfortunately been rather rare up to now, with the possible exception of patents. Production has been in general mostly geared towards the military market. Recently several systems that take into account the humanitarian demining needs have seen the light [BRU99a]. Most of the companies do also produce systems geared towards other applications of inductive sensors, such as security or Non-Destructive Testing (in particular Förster, whose main activities are in fact in this field), and magnetometers for the detection of UXO. We will see if the recent R&D activities in the sector, in particular in the US, will bring innovation to the field and change its shape.

European metal detector manufacturers are well established at international level and include Ebinger, Förster and Vallon in Germany, Schiebel in Austria, Guartel in the UK and CEIA in Italy. The other major international player is Minelab (Australia), which has entered the market a few years ago.

The total installed base in humanitarian demining is probably in the 10000 to 20000 units range, counting slightly less than one metal detector per deminer. The corresponding figure for the military market might be, very indicatively, double as much (the US Army has acquired from Schiebel about this many detectors at the beginning of the '90s). The total number of units sold each year for humanitarian demining does probably not exceed a few thousand, which would imply yearly sales in the order of a few tens of millions of Euro. This gives an idea of the market involved, although the importance of related markets should not be underestimated, in particular the detection of UXO for site remediation. Summarizing

- Mostly specialized SME (Small to Medium Enterprises). Little technical/scientific literature (Intellectual Property Rights issues!).
- Strong European position. Installed base ~ 10000-20000.
- Some increase in R&D outside the traditional manufacturer area
- Strong similarities between military and humanitarian demining systems

2.3.2.2. Man Portable Systems

Metal detectors for humanitarian demining are remarkable active sensors capable of detecting tiny amounts of metal, from a fraction of a gram onwards, at shallow depths. Frequency Domain systems have often been the choice because they seem to work well especially for very small and close objects, but they are being more and more challenged by pulse systems, and not only where ground conditions are severe. Portable systems share the following characteristics (true for most models):

- **Weight**: less than 2 kg. **Price**: in the 2000-4000 Euro range.
- **Size**: round, oval or rectangular head. In the former case the diameter is between 20 and 30 cm, to achieve sufficient depth and a reasonable scanning surface and speed; the thickness is of about a couple of cm.
- **Operating depth**: shallow, i.e. from flush (even with the surface) down to about 10-15 cm for minimum-metal mines, 20-30 cm for mines with an appreciable metallic content, and about 50-70 cm for large metallic objects such as UXO or metallic mines. Can reach deeper using *large loop* detectors, as alternative/complement to magnetometers.
- **Electrical/Mechanical**: capable of working with standard cell batteries for a long time (tens of hours), and usually simple to use. Many demining teams pay more attention to the ergonomics rather than to the pure performances of the detector itself.
- **Output**: normally an audio signal, usually already the result of extensive internal data processing**,** from which an experienced operator can make some qualitative statement on the target type and position/depth. When using manual methods as the *primary procedure*, **each** alarm is carefully checked until it has been fully understood and/or its source removed.

To the best of our knowledge no current metal detector for humanitarian demining applications delivers some quantitative information on the object under analysis. This is astonishing at first view, since there are other disciplines like Non-Destructive Testing where this is the case. It can probably be explained by the urgent priority to enhance detection performance through better background rejection (i.e. reduction of the metal detector false alarm rate) and achieving higher sensitivity, as well as by the need of being very precise whilst usually not having any a priori information on the object under analysis. Additional comments have been provided in §1.4.

A few large coil metal detectors, such as those by Ebinger and Vallon, have been manufactured for the detection of larger metallic objects such as metallic mines or UXO. They can be employed as an alternative to magnetometers for the detection of ordnance that is not too deeply buried, or in cases where magnetometers can not be used (magnetic soil).

A number of issues, in particular technical ones, that should be considered in comparing the performance of different detectors for humanitarian demining are discussed in detail in [DAS98, IPPTC01].

2.3.2.3. Vehicle Based Systems (Arrays)

Most metal detector arrays, normally one to several meters wide, are derived from commercially available metal detector technology and are *usually employed for vehicle platforms to rapidly scan large areas*. Some of them can deliver information not only on the location of metallic objects but also on their depth and their approximate size, e.g. in the form of an "equivalent object volume" (which can be used to reduce the number of false alarms when looking for UXO). Some systems do also employ special suspension devices to make sure that the detectors are always parallel to the surface, and that a constant height is maintained [BRU99a].

European manufacturers include Förster, TZN and Vallon in Germany, as well as Schiebel in Austria and Guartel in the UK. Förster is working on an extension of its portable Minex 2FD two frequency continuous wave technology, using one large rectangular transmitter coil and 7 staggered (i.e. partially overlapping) differential receiver coil pairs; the final system should not be too expensive. TZN is a relative newcomer to the field, and is now commercialising the AMOS Unexploded Ordnance Detection System, which uses pulse induction and features a double layer coil system. Vallon and Schiebel arrays have been on the market for some time, whereby the Schiebel VAMIDS (Vehicular Array Mine Detection System) has been used in a number of projects; it employs combinations of 1 m wide flexible or rigid segmented arrays containing eight individual sensors [BRU99a].

Apart from the use in combination with other sensors, metal detector arrays can be used on their own, possibly for *Quality Control applications*, and the set-up/maintenance of a *data archive* in order to compare previously executed searches with new searches[20] (suggestions by TZN). Applications on road and road verge, or in combination with a magnetometer for the detection of UXO are also feasible (suggestions by Förster). They obviously strongly depend on the end user and its Standard Operating Procedures (SOP) [BRU99a].

In general the importance of metal detector arrays for *UXO detection* (e.g. for site remediation), typically as complement to magnetometers, as well as an element in multisensor platforms, seems to be growing. Additional information on metal detector arrays or scanning systems is provided in §7.2, which analyses their use in the context of imaging applications.

2.3.2.4. Summary of Present Limitations

Some of the most important present limitations of metal detectors can be summarized as follows:

- High "**False Alarm**" rate (100:1 to 1000:1) due to metallic debris (ex. former battlefields, urban areas).
- Reduced sensitivity in **mineralized soils**, sea water.
- **Quantitative indications** on metallic target object **missing** (can obviously be very difficult due to background signal, unknown target, need not to fail).
- Development of **arrays** (for vehicles) is rather recent, still room for improvement.

20. Recording the data might in fact be useful in case of controversy at a later stage, i.e. after clearance, for "going over the books" easily.

2.3.3. Metal Detectors for Hobbyists

Metal detectors designed for hobbyists are mostly simpler and less expensive than their humanitarian demining counterparts, but make use in some cases of interesting innovations and are supposed to possess some target classification capabilities. As such they deserve a closer look.

We will comment in the following mostly on FD systems. Some additional information can be found for example in [ROW], in the [SIG02] patent study, and to a lesser extent for what concerns scientific details in publications which are more application oriented and intended for a wide audience such as [GAR95, LAG79]. An exception was [LeG69], which started from basic electronics and managed to achieve, without using a single (explicit) formula, a remarkable and in-depth review of the physics/technology of the subject.

2.3.3.1. VLF Transmitter/Receiver (Induction Balance) Systems

Although Frequency Domain metal detectors for hobbyists, e.g. for "treasure hunting" might not meet some of the standards of humanitarian demining in terms of ease of use, robustness, or reproducibility, it is true that they have incorporated target classification capabilities ("discrimination") for quite some time. This discrimination is basically a sorting of metallic objects based primarily on their phase angle response[21] (the signal strength can also play a role).

Indeed, as we will also see in the theoretical analysis of a Simple Circuit Model (§3.1), the largest phase shift will occur for metal objects which are primarily inductive; large, thick objects made from excellent conductors like gold, silver, and copper. Smaller phase shifts are typical for objects which are primarily resistive; smaller, thinner objects, or those composed of less conductive materials. Purely ferromagnetic materials, including most soils and sands, are on the other hand reported as having little or no phase shift [ROW].

Target discrimination also takes advantage from the fact that in some instances the target objects are known a priori, as is for example the case with coins (all US coinage is apparently consistently minted). A calibration is therefore possible and pattern of responses can be stored in a small database for the most advanced (microprocessor based) detectors, preanalysing the soil and all detected target responses (phase shift and signal strength). In this case the object's approximate depth can also be indicated once it has been identified, using the measured signal strength and knowing the detector's parameters (coil size, transmit current). Iron targets are characterised as "orientation sensitive", as we will confirm in Chapters 5 and 6, and the measured phase may change dramatically when moving the coil over them [ROW].

The discrimination can consist in a simple threshold on the phase shift, or "notch discrimination" in which only targets within a given phase angle range are considered. The metal detector may provide a numeric read-out, meter indication or another type of visual display. An example is provided in Figure 2.13: a number based on the measured phase is displayed on the horizontal axis, the signal strength on the vertical axis. This type of display is apparently very useful in distinguishing trash from more valuable objects. The distinction between ferrous and non-ferrous objects is evident, as well as the sorting of the latter into metal type (nickel and aluminium, US pennies and quarters, etc.).

Some practical problems to such a classification approach have been reported with some object types such as aluminium foil, or pull-tabs, possibly bent or broken, because of their large surface to volume ratio. *How good discrimination is in general also remains an open question, and one can expect that target identification will be more problematic with targets delivering weak responses, and/or being deep*[22]. Herein lies the question to be answered when thinking of transposing it to humanitarian demining applications.

21. White's Electronics, *Private Communication*, 1997.

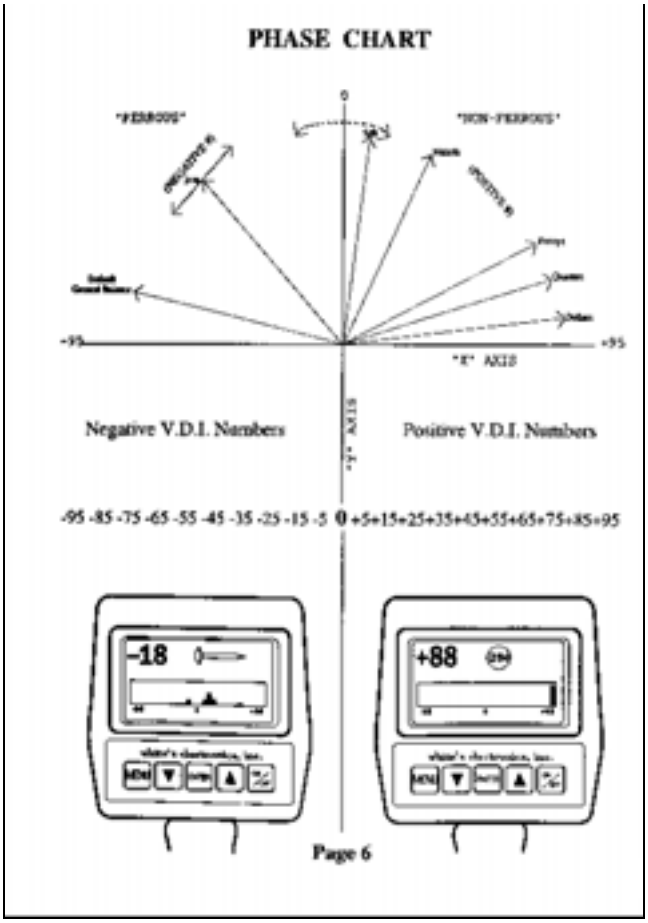

Figure 2.13: White's Electronics "SignaGraph"™ display [ROW]

The possibility also exists that a detector, passing over (or near) a rejected target and then over a good one, will not detect (i.e. mask) the latter [CON96].

2.3.3.2. Ground Balance

As already indicated, in any practical scheme it will be of fundamental importance to separate the signal due to the target from the soil signal itself, which can be much stronger. What can be exploited is the fact that the phase shift due to the ground tends to remain fairly constant over a limited area [ROW], whereas the target response changes quickly when moving over it. Some ground balancing schemes have already been described in §2.3.1, and additional information can be found in [ROW] and [SIG02] in particular.

2.3.3.3. Advanced Systems

The use of **multiple frequencies** should enhance target discrimination capabilities, as well as ease background rejection. A number of manufacturers are proposing multifrequency systems, e.g. Minelab (Australia) using a technique termed Broad Band Spectrum (17 separate frequencies from 1.5 kHz to 22.5 kHz transmitted together), and probably White's (US) with its Spectrum XLT. Concerning time domain systems, the use of **special pulse sequences** has been adopted to cope in particular with severe ground conditions, e.g. again by Minelab with a technique termed Multi-Period Sensing. More information is available from the manufacturers' Websites and sometimes from their patents as well (see for instance the Candy/Minelab patents in [SIG02]).

22. The response of deeper targets will change more slowly than the one of shallow targets, and thus be more difficult to separate from the soil response.

2.4. Advanced Developments

Although the integration of mine detection dogs and mechanical system into humanitarian demining activities has considerably progressed in the last years, metal detectors do still play a considerable role and are present in nearly every multi-sensor system being researched (§1.3).

There are however a number of improvements proposed and studied for the metal detector itself, whether used together with other sensors or standalone. Apart from a further amelioration of the **background rejection**, we have already seen that the measured signal is rich in information (Figure 2.2):

$$V_{sec} = V(\sigma,\mu,R,d,...) \tag{2.12}$$

The possibility of delivering **quantitative information** on the target under analysis is therefore actively studied, such as:

- **Depth**, using overlapping coils or signal profile study (scanning on a line over the object);
- "**Size**", possibly with a rough estimate (small (=debris?) vs. large);
- **Object Type** (could be useful in situations where there are only a few targets in a given area);
- **Object Shape** (not easy to reach sufficient resolution; useful for larger objects?).

The practical usefulness of this approach is however still debated in the end user community.

We are in fact attempting to solve one or more facets of the *inverse electromagnetic induction problem* (see A1.1), whose aim is to determine the position (in particular the depth), shape, size and material parameters (conductivity σ, permeability μ) of a hidden object. In the general case this turns out to be a very difficult problem, and we are not aware of any general solution which does not rely on some a priori information or assumption. In addition it is in general much easier to detect an anomaly than to classify it (i.e. saying that "there is something" rather than saying "there is an object of a given type"), and classification results get usually worse with decreasing signal to noise ratio. Background effects and implementation constraints do also complicate the problem's solution.

We will therefore now review some different aspects of inverse electromagnetic induction problems, having in mind as far as possible practical limitations and applications. Indeed, a number of parameters will also strongly determine if the system will ever be fielded, e.g. *importance of the target application* (i.e. humanitarian demining problem specificity and real equipment price/performance enhancement)*, equipment cost, size, complexity, penetration depth, simple and/or user friendly man machine interface (MMI), etc*. [BRO98]. The risk of R&D is, as Colin King once put it, to devise systems which "work best where they are least useful" [BRU99a, KIN96]. Emphasis will be put in this section on qualitative aspects, quantitative ones will be the subject of the next chapter.

2.4.1. Object Characterisation (Object Type/Size)

Information on the target's nature and/or position is contained in the frequency or time response when above it, in the spatial dependency of the response when scanning along a line across it or on a horizontal surface for example, or obviously by combinations thereof.

In the general case an object's response depends on many parameters (Figure 2.2), and the scenario is complicated by additional factors: i) some parameters are lumped together into a single *response parameter* (§3.3), ii) the response can be orientation dependent, iii) the soil response has to be added as well, iv) the response is strongly dependent on the target's permeability, v) objects can be composite, etc.

It is therefore usually necessary to *make some assumptions to simplify the problem* and try to "disentangle" the dependencies on the target's parameters, at least for those assumed to be of interest for the given scenario(s). If the objects are known to be "small" it makes sense to use a dipole model, if they are known to be mostly ferromagnetic one can assume that their magnetic permeability is high, if one is looking for UXO most targets are likely to be elongated, etc.

As briefly discussed in A1.1, there are two general techniques that may be used to estimate the target parameters from measurements, namely "model fitting" and "pattern recognition".

- In the first approach – **model fitting** – one has to devise a mathematical model to describe the secondary (induced) fields as a function of the source parameters, which are then recovered by an inversion procedure. When using for example an induced dipole model (§3.6.1) one recovers the target's magnetic polarizability tensor. This quantity fully characterizes in principle the target's EM properties, but has usually to be further evaluated. A partial evaluation might already provide information on the target's symmetry [MER00], which represents in a number of situations a good indicator.

  Other models can be directly expressed as a function of the target's physical and electromagnetic parameters (σ,μ), or indirectly via derived quantities such as L/R in a simple circuit model (§3.1), the position of the object's pole(s) in the frequency domain (or equivalently its time decay constant(s) in the time domain) when thinking in terms of natural modes (§3.6.3), or its response parameter discussed above in the general case.

  A combination of different successive approaches to recover the parameters which are lumped together (σ,μ and sphere radius for example) is also possible in principle. The target's permeability can for instance be recovered using a magnetometer or a quite low frequency, followed by an estimate of the depth (from a fit of the spatial field dependency for example) which allows to estimate the object's volume knowing the signal amplitude (in an induced dipole model), and therefore its radius. At this point one can calculate the conductivity from the measured response parameter at a given frequency.

  Variations of simple models to cope with background signals have also been devised ([PAT99] and other similar patents [SIG02]).

  Model fitting is obviously limited by there being an applicable model, or conversely by how applicable/realistic the chosen model is. At the end of the day the information having been recovered might or might not be sufficient for the given task – in general some knowledge of the targets being sought is necessary as well.

- In the second approach – **pattern recognition** – characteristics of a set of EM data from an unknown object are compared with that from a known one, to determine if the two objects are the same. Pattern recognition is in a certain sense used by the deminers themselves, when they interpret the detector's audio signal and try to assess an object's depth and size by comparing it with what they are familiar.

  Some form of data reduction or compression ("feature extraction") might be necessary to make pattern recognition feasible. Ideal features have a high resolution capability, that is are capable of well separating objects belonging to different classes. It will however be sometimes necessary to trade resolution power for applicability and rely on less discriminating features. In some cases large libraries of feature vectors can be required. Also, the problem becomes usually less tractable as the number of possible object shapes and sizes increases.

  An example of a pattern recognition approach is EM induction spectroscopy (§3.6.2), which consists in measuring a target's induction response a several frequencies and comparing it to a set of known responses.

  Possible problems with the pattern recognition approach are represented by the stability of the chosen features, and the presence of unknown targets.

We will mostly take this second approach in order to estimate the target parameters from measurements. This has arisen in a natural way from the analysis of the response curves in the complex plane (Chapter 5), their simplification by extracting a corresponding set of features such as phase angles and signal ratios, and the addition of supplementary features (Chapter 6). It is also motivated by the large number of possible clutter shapes and by the number of clutter items usually overwhelming the number of mines.

Finally, let us note that although in an ideal case one might provide object classification (mine or debris) or identification (mine type), possibly starting from a database of templates, even without going that far it might still be possible to extract valuable additional information for the deminer, such as ferromagnetic or non-ferromagnetic target, or small object *vs.* large object.

Problems with this approach are represented by weak target signals and irregular background signals, nearby objects distorting the response, and obviously by the presence of unforeseen or unaccounted objects.

Object Size

In principle the object's size should represent an interesting piece of information, although opinions diverge. One way of estimating it could consist in measuring the induced magnetic field over an area in order to calculate the object's induced magnetic dipole moment, using the dipole model described in §3.6.1, which gives an indication of its "magnetic" volume. The object's depth has to be known beforehand or estimated at the same time from the model. Again, technical feasibility as well as applicability in the field and sources of errors have to be very carefully studied.

Weaker statements are possible using the target's response parameter (induction number), which depends on an average linear dimension of the body (§3.3). This is actually the route we will follow in Chapter 6.

2.4.2. Depth Determination

In the case of humanitarian demining it seems at first sight that several methods could be used. They rely on the fact that the objects's depth influences the spatial distribution of the induced magnetic field.

- In a first method at least **two measurements over the object should be taken**, employing for instance two coaxial receive coils of radius R_1 and R_2, at a distance d_1 and d_2 respectively from the target object. If the object is small with respect to the coils or far enough from them so that a dipole approximation is valid (this will be discussed in the next chapter), one can calculate the following ratio:

$$r_s = \frac{V_1}{V_2} = \frac{R_1^2(d_2^2 + R_2^2)^{3/2}}{R_2^2(d_1^2 + R_1^2)^{3/2}} = \frac{R_1^2(d_2^2 + R_2^2)^{3/2}}{R_2^2((d_2 + \Delta d)^2 + R_1^2)^{3/2}} \tag{2.13}$$

  Note that the two coils are coplanar (overlapping) when $\Delta d = d_1 - d_2 = 0$. Inversion of the previous equation allows to calculate the depth, which in this simple case does not depend on the object parameters [DAS85, McF89].

  The use of at least two measurements under different conditions to determine an object's depth is also well known in Non-Destructive Testing applications, in which it does however profit from a priori knowledge of the target scenario [BRU00a].

- In a second method it is possible to **exploit the detector's spatial response** when scanning it across the object. It is indeed also known to the deminers themselves that an object's response curve gets larger as the object gets deeper; examples are provided in Figure 7.4. Some of the curve's parameters which seem a priori interesting are its Full Width at Half Maximum (FWHM)

and the slope's behaviour, in particular the tails. It might also be possible to find a suitable analytic form for the curve's profile and use it to fit the experimental data, or match against a library of known responses [DAS90, THO98].

Two different objects at the same depth do however not necessarily produce identical spatial responses. In addition it is necessary to avoid excessive sensor height fluctuations.

- In a third method data is collected in a horizontal plane across the target and an **induced dipole model** is used to extract the values of the object's permeability tensor (see §3.6.1 for details). The target depth is one of the problem's parameters and can therefore be one of the results of the inversion as well.

2.4.3. Shape Determination

A complementary approach consists in providing information on the object's size and shape, which could be useful in discriminating in certain circumstances mines and/or UXO from clutter. "Conventional" metal detectors can indeed be used to generate images of buried metallic objects with varying levels of resolution. This will be the subject of Chapter 7.

2.4.4. Current Research Activities

Some improvements should be possible using or slightly modifying existing sensors, e.g. multifrequency or advanced pulse induction detectors. Others may require more *radical approaches*, such as:

- **New types of sensors**: It has been suggested to study sensors other than the ordinary coils currently used in metal detectors, e.g. giant magnetoresistive elements, or miniature fluxgate elements. They are expected to be broadband and provide better spatial accuracy; the construction of linear or bidimensional arrays should also be possible, delivering some kind of localised "image" of the soil metallic/magnetic contents (see §7.2 for details). On the other hand their overall sensitivity is likely to be smaller, which might very well discourage their use for certain applications (their use might be envisaged for the detection of UXO or mines with a relevant metal content, but not for minimum-metal mines).

  Research on an advanced Active/Passive Magnetic Gradiometer combining sensitive magnetic sensors with advanced techniques of applied field rejection has also been reported [CZI96].

- **New sensor geometries** (e.g. different coil arrangements): Another direction of research could consist in the study of "improved" magnetic field shapes, more compact than what is obtained with ordinary circular or rectangular coils, or featuring some other special structure (e.g. spatially periodic, see the description of the Meandering Winding Magnetometer in §7.2).

- **More complete field measurements**: Full measurement of the induced magnetic field vector for example, possibly using a rotating primary magnetic field which would allow to "illuminate" the object from different directions without actually having to move the detector (the soil response would probably change as well). A problem might be in the sensitivity to small pieces, if the distance from the coils to the ground has to be increased in order to accomodate a coil geometry capable of generating the required field geometry.

- Combine with some form of "**cavity detector**": The idea of using metal detectors to actually locate non-conducting targets, or more generally "cavities" in the soil, is not new, as a (large) non-conducting target does indeed alter locally the natural ground conductivity and/or permeability, and has led to the patent described in [MIL96]. A similar approach is detailed in [FOR00] using a three or four frequency system, as extension of the existing Minex detector.

  The possibility of detecting minimum-metal mines due to the void they create in some types of electrically lossy soils has also been clearly documented and discussed in [NEL01] using a time domain (pulse) detector; the void effects manifest themselves in the early time region, below about 10 μsec. Numerical frequency domain results of the effect of a void in a conducting background, represented as a lossless dielectric object situated in a lossy dielectric medium, are

reported in [YU00]; the expected enhancement of the void's signature with increasing soil water content (and therefore soil conductivity) is clearly demonstrated.

A *cavity detector* should work best for large objects in soils with high natural conductivity ("background" signal), looking for distinct localized changes in the ground signal. A quite interesting combination is represented by **a "cavity detector" coupled to a metal detector**, in which only cavities containing some metal, such as minimum-metal mines, would be detected. *In this case it would not be necessary to classify metallic targets, the fact that they are coincident or not with a cavity would be sufficient.*

- There is still some room for improvements of **arrays**; some of the corresponding research topics will be detailed in Chapter 7.

2.5. Conclusions

In this chapter we have defined and introduced metal detectors and their **basic principles**, from the **physics** as well as from the **technology** point of view. We have looked in particular at *Frequency Domain systems*, which are the subject of choice of this work, and have introduced the variables which characterise their response, and which will be analysed in more detail in Chapters 3 and 4 (theory) as well as in Chapters 5 and 6 (experiment). The **importance of soil effects** has also been stressed; they will be the subject of Chapter 4.

The *apparent lack of quantitative output* from sensors used for humanitarian demining on one hand, and the end user need for more information on the other, have prompted us to *identify needs and opportunities for improvements*, which are related to different aspects of the solution of the *inverse electromagnetic induction problem*. Some of them will be tackled in the following chapters, with the aim of providing target information which is nowadays mostly missing.

Concerning current research activities we have stressed research work on new types of sensors and the possibility of combining metal detectors with some form of *cavity detectors*, thereby combining two features which are quite characteristic of most mines: the presence of some metal in an area where the soil is absent. Research into this direction will deserve a closer look in the future.

Bibliography

[ALL92] J.C. Alldred, "The Pulse-Induction Principle", Protovale Oxford Ltd., Abingdon, England, Technical Note T-41, November 1992. http://www.protovale.co.uk/abtpi.html (reduced online form). Interesting short technical note on the pulse induction principle.

[ALL97] Alldred, J.C. Bar-Sizing of Reinforcement in Concrete – Comparison of Available Methods. Proceedings of the Fourth Int. Conference on Non-Destructive Testing in Civil Engineering, University of Liverpool, UK, 8-11 Apr. 1997, ISBN 0-903132-23-0.

[BRO98] Brooks, J.; Nicoud, J.D. *Applications of GPR Technology to Humanitarian Demining Operations in Cambodia: Some Lessons Learned*. Proceedings of the Third Annual Symposium on Technology and the Mine Problem, Naval Postgraduate School, Monterey, CA, USA, 6-9 Apr. 1998. Available online as ref. Brooks98a at http://diwww.epfl.ch/lami/detec/

[BRU99a] C. Bruschini, K. de Bruyn, H. Sahli, J. Cornelis, and J.-D. Nicoud, "EUDEM: The EU in Humanitarian DEMining – Final Report (Study on the State of the Art in the EU related to humanitarian demining technology, products and practice)", EPFL-LAMI and VUB-ETRO, Brussels, Belgium, July 1999. Available from http://www.eudem.vub.ac.be/ and http://diwww.epfl.ch/lami/detec/.

[BRU00a] C. Bruschini, "Metal detectors in civil engineering and humanitarian de-mining: overview and tests of a commercial visualising system", *INSIGHT – Non-Destructive Testing and Condition Monitoring*, vol. 42, no. 2, pp. 89-97, February 2000. Also available from http://diwww.epfl.ch/lami/detec/.

[BUN96] Bungey, H.; Millard, S.G. Testing of concrete in structures, 3rd ed. Blackie Academic & Professional, London, UK, 1996, ISBN 0-7514-0241-9.

[CHE84] R. H. Chesney, Y. Das, J. E. McFee, and M. R. Ito, "Identification of Metallic Spheroids by Classification of Their Electromagnetic Induction Response", *IEEE Trans. on Pattern Analysis and Machine Intelligence*, vol. PAMI-6, no. 6, pp. 809-820, Nov. 1984.

[CON96] C. Conger, "Fisher CZ6a, Garrett GMH CXIII and White's XLT" (comparative evaluation), 1996. Online at http://www.polbox.com/p/proscan/titans.htm

[CZI96] Czipott P.V., Iwanowski M.D., "Magnetic sensor technology for detecting mines, UXO, and other concealed security threats", in Terrorism and Counterterrorism Methods and Technologies, Proc. SPIE No. 2933, pp. 67-76, 20-21 Nov., 1996.

[DAS85] Y. Das, J. E. McFee, and R. H. Chesney, "Determination of Depth of Shallowly Buried Objects by Electromagnetic Induction", IEEE Trans. on Geoscience and Remote Sensing, vol. 23, no. 1, pp. 60-66, Jan. 1985.

[DAS90] Y. Das, J. E. McFee, J. Toews, and G. C. Stuart, "Analysis of an Electromagnetic Induction Detector For Real-Time Location of Buried Objects", IEEE Trans. on Geoscience and Remote Sensing, vol. 28, no. 3, pp. 278-288, May 1990.

[DAS98] Y. Das, and J. Toews, "Issues in Performance Evaluation of Metal Detectors", in Proc. UXO Forum 1998, 8 pp.

[FOR00] F. M. Förster, "Method and Device for Locating and Identifying Search Objects Concealed in the Ground, Particularly Plastic Mines", US Patent #6,097,190, 1 Aug. 2000. See also the German patent DE 196 48 833, 28 May 1998.

[GAR95] C. Garrett, "Totally Revised Modern Metal Detectors", Second Ed., Ram Publishing Company, Dallas, Texas, 1995. ISBN 0-915920-75-1.

[HUG1879] D. E. Hughes, "Induction-balance and Experimental Researches therewith", The London, Edinburgh and Dublin philosphical magazine and journal of science (*Phil. Mag.*), London Taylor & Francis 1876-1900, (Ser. 5) vol. 8, pp. 50-56, 1879.

[IPPTC01] Das, Y., Dean, J. T., Lewis, D., Roosenboom, J. H. J., and Zahaczewsky, G. (Eds.), International Pilot Project for Technology Co-operation – Final Report (A multi-national technical evaluation of performance of commercial off the shelf metal detectors in the context

of humanitarian demining), publication EUR 19719 EN, published by the European Commission, Joint Research Centre, Ispra, Italy, July 2001. Available from http://demining.jrc.it/ipptc/

[KAC98] P. J. Kaczkowski, "Pulsed Electromagnetic Induction (PEMI) for UXO Discrimination in JPG Phase IV – Preliminary Results", in Proc. UXO Forum 1998, 9 pp.

[KAU01] A. A. Kaufman, and P. A. Eaton, *The Theory of Inductive Prospecting.* Amsterdam, NL: Elsevier, 2001.

[KEI97] D. A. Keiswetter, E. Novikova, I. J. Won, T. M. Hall, and D. Hanson, "Development of a Monostatic, Multifrequency Mine Detector", in *Detection and Remediation Technologies for Mines and Minelike Targets II; SPIE Proceedings Vol. 3710* (Orlando, FLA, USA, April 21-24, 1997, pp. 831-839).

[KIN96] King C. *Mine Clearance…in the Real World*. Proceedings of the Technology and the Mine Problem Symposium, Naval Postgraduate School, Monterey, CA, USA, 18-21 Nov. 1996, pp. 3-3/3-9.

[JPL95] Peterson J.C. (Study Team Leader) Sensor Technology Assessment for Ordnance and Explosive Waste Detection and Location. Jet Propulsion Laboratory, Report JPL D-11367 Rev. B, Pasadena, CA, USA, Mar. 1995.

[LAG79] R. Lagal and C. Garrett, "The complete VLF-TR Metal Detector Handbook", Ram Publishing Company, Dallas, Texas, 1979. ISBN 0-915920-32-8 [NOTE: probably out of print].

[LeG69] E.S. LeGaye, "Electronic Metal Detector Handbook", Houston: Western Heritage Press, 1969 [NOTE: probably out of print].

[McF89] J.E. McFee, "Electromagnetic Remote Sensing; Low Frequency Electromagnetics", Defence Research Establishment Suffield, Ralston, Alberta, Canada, Suffield Special Publication No. 124 (report DRES-SP-124), January 1989.

[MER00] L. Merlat, and P. Druyts, "Progress Report on the Metal Detector: Signal Processing for Target Discrimination and Coil's Modelization", Progress Report of the HUDEM Project, Royal Military Academy, Brussels, Belgium, 29 Feb. 2000. Also ISL (Institut de Saint-Louis) Publication PU 322/2000, Saint-Louis, France.

[MIL96] Mills D., "Improvements to Mine Detectors", Australian patent application No. PO1408, 1996.

[NEL01] C. V. Nelson, *et al.*, "Wide Bandwidth Time-Domain Electromagnetic Sensor for Metal Target Classification", IEEE Trans. on Geoscience and Remote Sensing, vol. 39, no. 6, pp. 1129-1138, June 2001.

[PAT99] W. Patzwaldt, "Method for the operation and for the evaluation of signals from an eddy current probe and device for performing the method", US Patent #6,005,392, 21 Dec. 1999.

[POD82] M. Poddar, "A rectangular loop source of current on a two-layered Earth," *Geophys. Prospect.,* vol. 30, no. 1, pp. 101-114, 1982.

[RIG99] L. S. Riggs, T. Barnett, L. Lowe, J. E. Mooney, and R. Weaver, "Baseline performance of the U.S. Army's AN/PSS-12 metal detector", in *Detection and Remediation Technologies for Mines and Minelike Targets IV; SPIE Proceedings Vol. 3710* (Orlando, FLA, USA, April 1999, pp. 52-63).

[ROC99] G. Rocker, "Systeme zur Detektion und Ortung von Gegenständen und Personen" (Systems for Detecting and Locating Objects and Persons) (in German), Erfinderaktivitäten 1998, Deutsches Patent- und Markenamt (German Patent Office), 1999, 10 pp.

[ROS48] B. Roston, "Development of Locators of Small Metallic Bodies buried in the Ground", Journal of the Institution of Electrical Engineers (IEE Review), vol. 95, pp. 653-667, 1948.

[ROW] M. Rowan, and W. Lahr, "How Metal Detectors Work", White's Electronics. Available from http://www.treasurenet.com/whites/howmetaldetectorswork.html

[SIG02] Sigrist, C., and Bruschini, C., "Metal Detectors for Humanitarian Demining: a Patent Search and Analysis", EUDEM2 report, May 2002. Available from http://www.eudem.vub.ac.be/

[SZY99] P. Szyngiera, "A Method of Metal Object Identification by Electromagnetic Means", in *Proc.*

MINE'99 (Mine Identification Novelties Euroconference) (Florence, Italy, October 1-3, 1999, pp. 155-160). Available from http://demining.jrc.it/aris/events/mine99/index.htm.

[THO98] O. Thonnard, "Détecteur de Métaux – Analyse d'un Détecteur de Métaux et Conception d'un Système de Balayage afin de Produire des Images 2-D du Sol" (Metal Detector – Analysis of a Metal Detector and Design of a Scanning System for the Generation of 2-D Soil Images), Signal Image Centre, École Royale Militaire (Royal Military Academy), Brussels, Belgium, 1998 (M.Sc. Thesis, in French).

[YU00] T. Yu, and L. Carin, "Analysis of the Electromagnetic Inductive Response of a Void in a Conducting-Soil Background", IEEE Trans. on Geoscience and Remote Sensing, vol. 38, no. 3, pp. 1320-1327, May 2000.

[VUI94] P.-L. Vuillermoz, *Les courants de Foucault – Principes, mesure et contrôle*, AFNOR, Paris, 1994 (in French).

Appendix A2.

A2.1. Eddy Currents and the Skin Effect

Throughout this paragraph we will assume that the magnetic (***B***) and electric (***E***) fields propagate instantaneously, which is equivalent to neglecting displacement currents (§3.4.2). This assumption introduces a negligible error at low frequencies, or when the wavelength is larger than the typical dimensions under consideration (e.g. size of a measurement apparatus).

In this case we can give the following explanation for the setup of eddy currents (at least in extended conductors): an alternating magnetic field ***B***(t), such as the one generated by a radiofrequency driven coil, will induce by Faraday's law an oscillating electric field ***E***(t), where[23]:

$$\nabla \times \boldsymbol{E} = -\frac{\partial \boldsymbol{B}}{\partial t} \tag{A2.1}$$

A current of density ***J*** will therefore flow following Ohm's law (σ is the conductivity):

$$\boldsymbol{J} = \sigma \boldsymbol{E} \tag{A2.2}$$

and these currents, flowing in a conductor of (uniform) permeability μ, will in turn produce a (secondary) magnetic field according to Ampère's law:

$$\nabla \times \boldsymbol{B} = \mu \boldsymbol{J} \tag{A2.3}$$

This justifies the statement that eddy currents exist because of time-varying magnetic fields and are basically governed by the law of induction (Faraday's law). It also delivers a qualitative explanation for the fact that eddy currents are characterized by circulatory paths[24] and are often depicted as closed loops circulating in planes perpendicular to the magnetic flux, as shown in Figure 2.14. More generally speaking we can say that eddy currents travel parallel to a coil's winding and parallel to the surface.

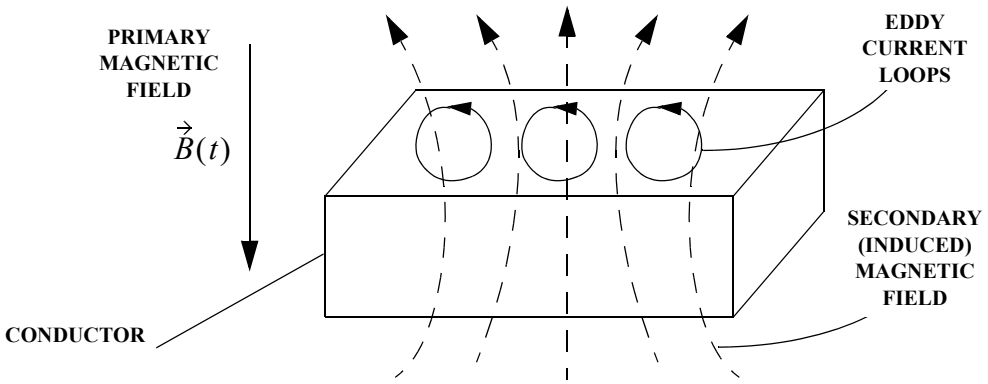

Figure 2.14: Pictorial view of eddy currents in a conductor placed in a time-varying (homogeneous) magnetic field

Note also that eddy currents flowing at any depth in the conductor will generate magnetic fields which, as a consequence of Lenz's law, will be opposed to the primary field. The total magnetic flux will therefore be reduced and the current flow will decrease for increasing depth. Alternatively one can think of the eddy currents on the surface as shielding the primary magnetic field and therefore weakening it with increasing depth. It can be shown that, for a sinusoidally varying induction of angular frequency ω, the eddy current density J_x behaves (in a thick conductor) as a function of the distance x from the surface in the following way:

23. The differential form of Maxwell's equations will be used here.
24. Here lies indeed the origin of the term "eddy".

$$J_x = J_0 e^{-x/\delta} \sin(\omega t - x/\delta) \tag{A2.4}$$

where δ is the skin depth in the given material at the frequency ω, and J_0 the value at the surface. This equation contains the well known exponential decrease modulated by an oscillating term, at the frequency ω of the primary field, its phase depending on the depth x. The last point is in fact instrumental in Non Destructive Testing to determine the depth of a defect in a sample (the defect, a crack for example, introduces a local change in the eddy current path).

A2.2. The magnetic field of a circular and a square coil

Even in a case as simple as that of a **circular loop** a general analytical expression for the magnetic field does not exist. Elliptical integrals have to be numerically evaluated [KAU01, §2.2.3]. As an alternative one can use the following series expressions for the scalar magnetic potential V_m in terms of either (r/a) for r<a, or (a/r) for r>a [KEI97]:

$$V_m(r,\theta) = \frac{\mu_0 I}{2}\left(1 - \left(\frac{r}{a}\right)P_1(\cos\theta) + \sum_{n=1}^{\infty}(-1)^{n+1}\frac{(2n-1)!!}{(2n)!!}\left(\frac{r}{a}\right)^{2n+1}P_{2n+1}(\cos\theta)\right) \quad \text{for } r \le a \tag{A2.5}$$

$$V_m(r,\theta) = \frac{\mu_0 I}{2}\left(\sum_{n=1}^{\infty}(-1)^{n+1}\frac{(2n-1)!!}{(2n)!!}\left(\frac{a}{r}\right)^{2n}P_{2n-1}(\cos\theta)\right) \quad \text{for } r \ge a \tag{A2.6}$$

The magnetic field itself can then be calculated using:

$$\boldsymbol{B}(r,\theta) = -\nabla V_m(r,\theta) \tag{A2.7}$$

with B_z, the field perpendicular to the plane of the loop, being:

$$B_z = -\cos\theta\frac{\partial V_m}{\partial r} + \frac{\sin\theta}{r}\frac{\partial V_m}{\partial \theta} \tag{A2.8}$$

In the case of a **rectangular loop** the components of the magnetic field intensity are on the other hand available analytically. The interested reader is referred for example to [DAS90], which follows [POD82].

3.

Electromagnetic Induction Modelling and Analytical Solutions to some basic Frequency Domain Problems

When first dealing with the subject of metal detectors (eddy current systems) for humanitarian demining applications one is often confronted with the lack of available scientific literature, in particular on the detector's response to typical scenarios of interest, e.g. the *response of basic objects* – spheres, cylinders, background (the soil itself). The understanding of this *direct (forward) problem* is of great importance for the solution of the *inverse problem* (§2.4, A1.1) which we will tackle in Chapters 5 and 6. We have therefore looked at other domains which make use of EM induction sensors, albeit often in modified form, in particular Geophysics and Non-Destructive Testing (NdT). Their specificities will be briefly detailed in §3.2.

A number of *analytical solutions* to some basic eddy current forward problems are thus reported in the following. While it is true that analytical solutions exist only for a few basic geometries and analytical models are thus less flexible than numerical techniques, they are an excellent tool when it comes to providing general insight into the physics of the scattering process and its dependence on the model's parameters.

We will look in detail at the response of a simple circuit model (§3.1) and at the general form of a target's EM induction response (§3.3), before specializing on representative basic targets such as the spheres (§3.4) or (transverse) cylinders (§3.5). They have been complemented in a semi-quantitative way for elongated ferromagnetic objects such as short cylinders (§3.5.2). Other target models will be the subject of §3.6; second order effects such as galvanic currents and the effects of induced currents in the host medium will be discussed in §3.7. Emphasis is put on the operating conditions prevailing in humanitarian demining and on frequency domain systems and their *phase response* in particular. The results can be extended to time domain systems by using Fourier transformation.

To ease understanding of this chapter's contents we already anticipate that, as it has also been stressed by others, this analysis and similar approaches indicate the possibility of *distinguishing* between different objects (e.g. ferromagnetic vs. non-ferromagnetic), and of *identifying* some metallic objects based on their characteristic phase response.

In addition, the phase shift of the received signal will turn out to be a continuous, monotonically decreasing function of the object size (all other parameters being kept constant). This will lead to the idea of a *coarse classification* based on target *size* (actually the response parameter, see §3.3.1 and §6.3), and/or of discriminating large objects by imposing a "phase threshold". We will comment on the effectiveness and feasibility of this *discrimination*-based approach at the end of Chapters 5 and 6.

In Chapters 5 and 6 we will exploit the experimental data from a particular Frequency Domain metal detector, the Förster Minex 2FD which generates two continuous wave frequencies at 2.4 and 19.2 kHz, and compare some experimental results with the corresponding theoretical expectations. We will therefore often consider in this chapter these two frequencies.

3.1. A Simple Circuit Model

Although not applicable "as is" to real situations, a very simple model can be used to get a feeling for what we should expect from a detector's inductive response. The method follows [McF89] (which in turn follows [GRA65]), and assumes fixed separation transmit and receive circuits operating at a frequency ω (see [TRA97, SZY99, WES91] for alternative derivations). The target object is modelled as an isolated conductive circuit with a lumped resistance *R* and inductance *L*. Labelling the transmitter circuit as "0" (driven by a current $I_0e^{i\omega t}$), the target circuit as "1", and the receiver circuit as "2", we denote the mutual inductances between any two of these circuits as M_{ij}, with $i, j = 0, 1, 2$ (see Figure 3.1). In fact, from the point of view of field theory, these are the difficult quantities to calculate.

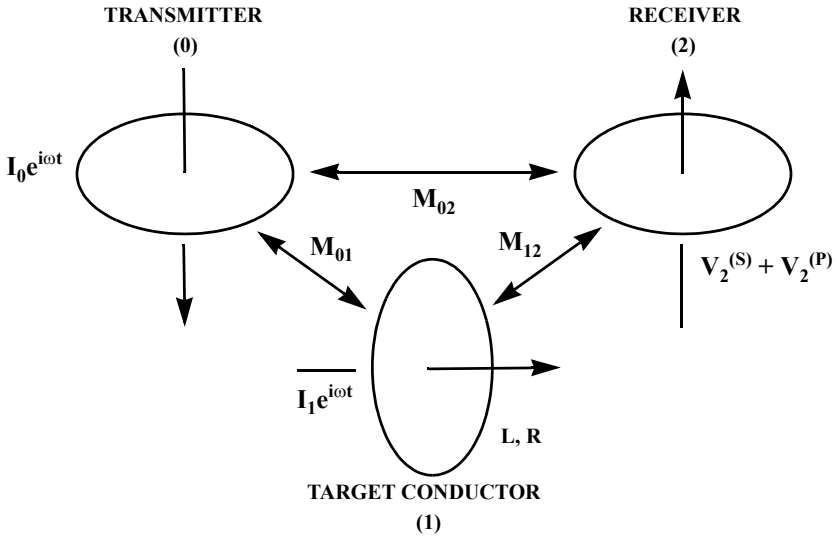

Figure 3.1: Simple Circuit Model of electromagnetic induction (from [McF89])

A "response", G(ω), can be defined as the ratio between the secondary and primary voltages in the receiver loop, $V_2^{(s)}(\omega)$ and $V_2^{(p)}(\omega)$ respectively. They can be shown to amount to:

$$V_2^{(p)}(\omega) = -i\omega M_{02} I_0 e^{i\omega t} \text{ and } V_2^{(s)}(\omega) = -i\omega M_{12} I_1 e^{i\omega t}, \text{ with } I_1 e^{i\omega t} = -\frac{M_{01}}{L}\left[\frac{i\omega L(R - i\omega L)}{R^2 + \omega^2 L^2}\right] I_0 e^{i\omega t} \quad (3.1)$$

Therefore:

$$G(\omega) = \frac{V_2^{(s)}(\omega)}{V_2^{(p)}(\omega)} = -\frac{M_{01}M_{12}}{M_{02}L}\left[\frac{i\omega L(R - i\omega L)}{R^2 + \omega^2 L^2}\right] = \beta\left[\frac{\alpha^2 + i\alpha}{1 + \alpha^2}\right] = \beta\left[\frac{i\alpha}{1 + i\alpha}\right] \quad (3.2)$$

$$\text{with } \alpha = \frac{\omega L}{R} \text{ and } \beta = -\frac{M_{01}M_{12}}{M_{02}L} \quad (3.3)$$

which does not contain any more the linear iω dependency of $V_2^{(s)}$ and $V_2^{(p)}$.

Studying G(ω) in more detail we can see that the coupling coefficient β depends only on the relative size and position of the circuits, whereas the term in square brackets depends on the frequency ω and the target's electromagnetic properties (*L*,*R*). We can write the latter, the "response function" *F*(α) (or quasi-magnetostatic transfer function [RIG98]), using its real and imaginary parts, X(α) (the in-phase component) and Y(α) (the quadrature-phase component) respectively, with α being the "response parameter":

$$F(\alpha) = \left[\frac{\alpha^2 + i\alpha}{1+\alpha^2}\right] = \frac{\alpha^2}{1+\alpha^2} + i\frac{\alpha}{1+\alpha^2} = X(\alpha) + iY(\alpha) \tag{3.4}$$

It is particularly interesting to investigate the limits of this function, which exhibits high-pass filtering characteristics:

- as $\alpha \to \infty, X(\alpha) \to 1$ and $Y(\alpha) \to 0$ i.e. $F(\alpha) \to 1$. This is denoted as the "**inductive limit**", and the response function gets purely real (i.e. in phase); the response is the largest and is given by $G_L = \beta$. This is the case when working at high frequency, or on a highly conductive (low *R*) or highly inductive target.
- As $\alpha \to 0, F(\alpha) \to i\alpha$. This is the "**resistive limit**", and the response function gets purely imaginary (i.e. in quadrature); the response is given by $G_R = i\beta\alpha$. This is the case when working at low frequency, or on a poorly conductive target (high *R*).

In summary, starting from low values of α (resistive limit) the response has initially a small amplitude and is in quadrature. For $\alpha = 1$, i.e. $\omega = R/L$, both components are equal ($F(\alpha) = 1/2(i+1)$), and for increasing values of α the inductive limit is approached. The phase goes from 90° at the resistive limit to 0° at the inductive limit. This behaviour is reproduced in Figure 3.2.

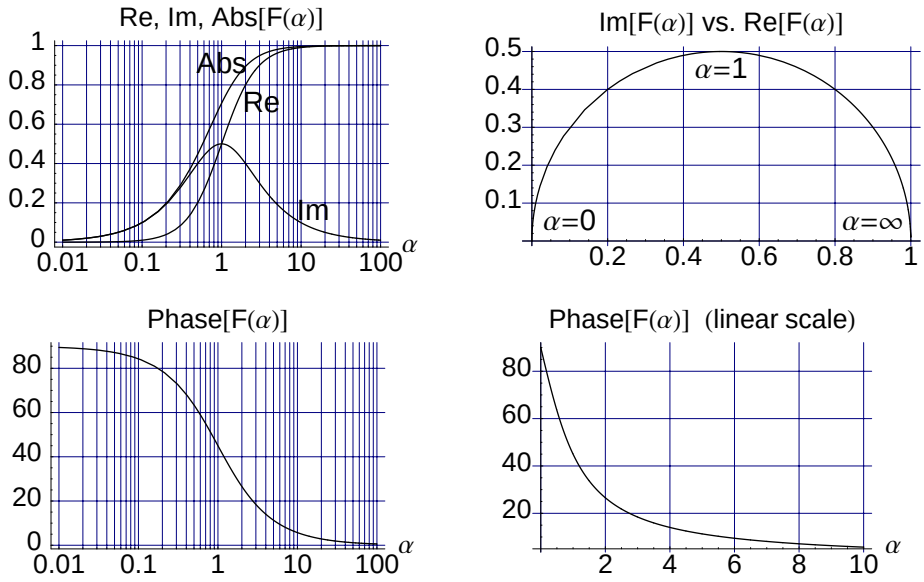

Figure 3.2: Response function for a simple circuit model of electromagnetic induction ($\alpha=\omega L/R$)

In a more general case the coupling coefficient turns out to be geometry dependent and must be examined separately for each particular model. *The response characteristics of this simple circuit model do however contain some general features that are inherent to a number of more realistic models.* Note in particular that the real part behaves as ω^2 at low frequencies, the imaginary part as ω. Overall the response is characterized by single pole at $\omega = R/L$ and a zero located at the origin.

3.2. Geophysical vs NdT Applications

As argued in the introduction to this chapter, other fields in which EM induction devices are used with profit have been analysed (*multidisciplinary approach*), in particular Geophysics and Non-Destructive Testing (NdT). Whenever possible we have also relied on *analytical solutions*, which can provide general insight into the scattering process and be useful as a check on numerical procedures [IDA95]. The scales involved in Geophysics and Non-Destructive Testing (NdT) are nevertheless usually quite different, which implies that some care has to be used when transposing the results to our problem (in which the coil size can be of the same order as the target object distance, and sometimes as the target object size as well). The excitation source is also not necessarily the same: a line source (current carrying cable) or a simple dipole source (loop at large distances) are often considered in Geophysics, instead of a circular coil.

It is interesting to note that up to the late 60's analytic solutions to some basic scenarios were still being sought, although they can be quite complex (when they exist) even for relatively simple shapes. As from the end of this period numerical methods (simulation) have gradually taken over, first in 2D and more recently also in 3D.

3.2.1. Geophysical Applications

Electromagnetic induction is in fact just one of the electromagnetic methods used in Geophysics, others are for example resistivity and magnetotellurics (see [WAR80] for an overview). A vast amount of literature is available, with one of the basic references being represented for example by [NAB87,NAB91] edited by SEG (Society of Exploration Geophysicists). [GRA65], [KEL66], [WAR67] and [WAI82] are probably out of print but still represent good textbooks on the subject, in particular the first. [KAU01] is a quite recent and interesting publication, although not necessarily the easiest to start with.

Amongst the basic differences to our application we have the following:

- The **scales** involved in geophysical EM induction systems and problems are obviously quite different from those of interest to us. The devices are usually much larger than those used in humanitarian demining (but not necessarily the receive coil), over larger distances as well, to probe deeper/seek larger objects (tens to hundreds of meters). The generated magnetic moments (product of current times coil surface) are also quite large.
- The **target conductivity** is on the other hand much lower (and therefore the conductivity contrast), and ground permeability has usually not been an issue.
- The **configuration** in which we are interested – overlapping transmit (TX) and receive (RX) coils moving together, or RX even arranged as a gradiometer, with the coils usually being horizontal (primary field corresponding to a vertical magnetic dipole) – does not seem to be amongst those of highest interest to geophysicists. The exception are perhaps Time Domain systems.
- Time Domain (step and pulse) methods have considerably grown in importance starting from about the 70's. In general there has been quite some technical progress, resulting for example in the development of **multifrequency/multicoil systems**. **Ground** as well as **airborne systems** have been studied and used, typically for the detection of ore bodies.
- The importance of the **background (soil response)** has been studied in depth. One of the major advances has been the understanding of the difference between **induction** (vortex) currents and **galvanic currents** (current channelling effects). The latter, which can heavily modify an object's response, should not play a role for metallic components isolated from the surrounding soil (as is mostly the case for a standard blast mine). Whether they are of any importance for large metallic objects such as UXO, or very conductive soils (sea water), remains to be seen.

  We will discuss them in more detail in §3.7.

- A **very conductive soil**, or a very conductive overburden (earth above the target, not necessarily in contact with it) can also influence the target's response, by rotating its phase and, depending on the conductivity, also attenuating its amplitude. This is likely not to represent a problem in our application, perhaps with the exception of deep objects and/or large background conductivity.

  We will discuss these aspects in §4.4.
- **Frequency differencing** methods have been used to reduce the so-called "geologic noise", in a manner similar to what implemented in the Förster Minex metal detector. They will be the subject of §4.3.

3.2.2. EM Non-Destructive Testing (NdT)

EM induction sensors have been in use for quite some time – with pioneering work carried out by Förster at the beginning of the fifties – for the analysis of metallic objects, typically rods, bars, sheets. Induction sensors have been used on one hand for the analysis of their electrical parameters (conductivity, permeability), and the other to check in a non-destructive way an object's integrity (cracks, defects). *Ferromagnetic* objects with high permeability are quite frequent, to the contrary of geophysical scenarios.

A trend similar to the one in Geophysics towards numerical solutions [IDA95] has taken place. Basic literature is represented for example by [LIB71], [McM86], [VUI94], [BLI97] and some articles in the [SHA] series.

3.3. General Form of an Object's EM Response

As briefly pointed out in §3.1, although the equations governing $F(\alpha)$ in the general case are more complicated than Eq. (3.4), the response characteristics of a simple circuit model are actually similar to those of more realistic models, some of which we will analyse in the following. A number of conclusions on the general form of an object's EM response can therefore already be drawn.

3.3.1. General Form of the Response Parameter

[GRA65] performs an interesting **dimensional analysis** to identify which are the parameters affecting a system's response (in general), and shows that the quantity replacing the adimensional response parameter α, also called **induction number**, will be of the form:

$$\alpha = \sigma\mu\omega l_j l_k \tag{3.5}$$

The linear dimensions l_j and l_k are those which effectively control the volume of the eddy current circulation. We will see later on that their product is a^2 in the case of a sphere (a= radius), whereas it is of the form t^2 for a sheet of thickness t, or ta for a disk of thickness t and radius a. Table 3.1 shows some typical examples [WAR67]. The loops mentioned in the 5th and 6th rows are horizontal coplanar, where ρ is the loop spacing and h is their height above ground, but the results are extensible to other configurations. Note in particular the difference between the loops *on* ($\sigma\mu\omega\rho^2$) and (well) *above* ($\sigma\mu\omega h^2$) the ground; there is evidently an intermediate regime where both factors must enter. The last row deals with the case of a single loop of radius r, to which we will come back in Chapter 4.

Object or System	*Response Parameter*
Sphere, uniform field	$\sigma\mu\omega a^2$
Cylinder, uniform field	$\sigma\mu\omega a^2$
Disk, uniform field	$\sigma\mu\omega ta$
Thin sheet	$\sigma\mu\omega t^2$
Horizontal loops **on** homogeneous earth	$\sigma\mu\omega\rho^2$
Horizontal loops **above** homogeneous earth (system raised well above the earth: h>ρ)	$\sigma\mu\omega h^2$
Horizontal loop **on** homogeneous earth	$\sigma\mu\omega r^2$

Table 3.1: Examples of response parameters for typical scenarios of interest [WAR67])

Eq. (3.5) is sometimes approximated by saying that EM systems respond to $\sigma\,\bar{l}^2$ ($\bar{l}$ is an *average linear dimension* of the body), when the average dimension is small in relation to the scale value of the system (overall or largest system dimension) [GRA65].

3.3.2. Spherical Conductor with Axial Symmetry

The special case of the primary magnetic field $\mathbf{H}_{prim}$ and a finite size conductive body characterised by axial symmetry with a common axis is treated in [KAU01, §3.4]. Examples include a spheroid in a uniform field (with $\mathbf{H}_{prim}$ along one of the symmetry axes), a vertical cylinder coaxial with a coil, or a horizontal disk in a uniform vertical field. Note that in these cases no surface electrical charges develop (and therefore no galvanic currents, see §3.7).

The resulting expression in cylindrical coordinates for the induced current density and the associated **H** and **E** fields exhibits discrete singularities, or poles, along the imaginary axis of the complex ω plane, the locations of which control the principal features of the frequency spectrum

(simple sum of fractions) or equivalently of the transient decay (simple sum of exponential):

$$H_z(\omega, a) = H_{0z} \sum_{n=1}^{\infty} d_{nz} \frac{i\omega}{(q_n/\sigma_0 \mu b^2) - i\omega}, \; H_r(\omega, a) = H_{0z} \sum_{n=1}^{\infty} d_{rz} \frac{i\omega}{(q_n/\sigma_0 \mu b^2) - i\omega} \tag{3.6}$$

$$E_\phi(\omega, a) = i\omega H_{0z} \mu b \sum_{n=1}^{\infty} f_n \frac{i\omega}{(q_n/\sigma_0 \mu b^2) - i\omega} \tag{3.7}$$

where the poles are given by

$$\omega = i\omega_n = -i \frac{q_n}{\sigma_0 \mu b^2} \text{ with } q_1 < q_2 < q_3 < \ldots . \tag{3.8}$$

a represents the observation point, *b* is an arbitrary geometrical parameter of the body (e.g. the radius, one of the semi-axes, etc.), σ_0 is the conductivity at a specific point. The adimensional coefficients (d_n, f_n) are basically coupling coefficients which determine the strength with which each mode is excited, and therefore the final response spectrum. As such they depend on the problem geometry as well as on the dimensions and shape of the conductive body[25].

3.3.3. General Confined Conductor Response Function

It can be shown that the previous results remain valid for the more general case of a *confined conductor*. Simplifying, the resulting representation of the induced currents consists of a set of current patterns, called *eigencurrents*[26] and in general infinite, each having a fixed geometry and representing a non-interacting (isolated) current which has the electrical properties of a simple loop with a pole at ω_n (or equivalently, with a time constant $\tau_n=1/\omega_n$). The eigencurrent set forms a basis into which any finite sized vortex of eddy currents can be decomposed.

Each eigencurrent depends only on the object's conductivity distribution, not on the primary field. The corresponding coupling coefficient c_n, which determines the excitation level of the *n*th eigencurrent and therefore the *overall response function* $F(\omega)$, does however depend on the source field [KAU78, NAB91 p.929, WES91]. Note that the poles are purely imaginary[27]: the denominator is equal to zero for $\omega=i\omega_n$ (ω_n real >0).

$$F(\omega) = a + \sum_{n=1}^{\infty} c_n \frac{\omega^2 + i\omega\omega_n}{\omega^2 + \omega_n^2} = a + \sum_{n=1}^{\infty} c_n \frac{\omega}{\omega - i\omega_n} \tag{3.9}$$

The corresponding time domain expression is again an infinite sum of damped exponentials. The constant offset *a* is necessary to take into account the response of ferromagnetic objects.

It is intuitively clear that the eigencurrents are similar to (resonating) modes. The principal mode is the eigencurrent with the lowest frequency (ω_1), or equivalently with the longest time constant ($\tau_1=1/\omega_1$), when the series is enumerated in order of increasing frequencies, and is usually the one which dominates. Indeed, the coupling coefficients c_n form a convergent series: their magnitude decreases systematically, but not necessarily uniformly, with *n*. The relationship between the late stage behaviour in the time domain and the low-frequency part in the frequency domain is discussed in detail in [KAU01, pp.222-225].

25. We will see in §3.4.5 that in some cases the geometry dependence uncouples, e.g. for a sphere.
26. Because they independently satisfy the homogenous (source-free) differential equations for the fields in a given conductivity distribution.
27. [KAU01] uses poles along the negative imaginary axis (p. 204).

The previously described behaviour of the response function does represent the essence of this chapter's contents, which will put the emphasis on an object's spectral response, rather than on its geometry and signal strength. A few important remarks have however to be made:

1) In the case of a **non-spherical object** each of the object's principal axes will usually support its own system of eigencurrents, and therefore have a different response function.

2) A **non-uniform primary field** can be expressed as a multipole expansion about the principal axes of the target object, whereby each term of the expansion creates its own system of eigencurrents similar to Eq. (3.9). The spectral response of each of the multipole terms of the induced (secondary) field is therefore the sum of many eigencurrents. However, when we are far from the object only a reduced number of multipole terms is necessary.

3) A target is usually analysed ("illuminated") from **different views**, for example by moving along a line over it. The configuration of the primary field at the target does therefore change, and from what just discussed at 1) and 2) the resulting eddy current patterns as well. Basically different modes can be excited, and their excitation strengths vary. This is particularly true for elongated **ferromagnetic** objects.

The overall response can also depend on the observation point (if far or close to the object for example) [WES91].

These issues and their actual importance will become clearer when looking at concrete examples, and later on at the experimental data.

3.3.4. Multiple Conductors (composite objects and coupling effects)

In a scenario featuring **multiple conductive objects** the total effect might not be, in general, a simple sum of the individual responses, depending on how well the objects are coupled (inductive interaction).

The case of coupled loops is described in [GRA65], which also studies the response of a disseminated conductor. The latter could serve as a basis, albeit probably with a number of restrictions[28], for the estimation of the response of an object mostly composed of a large number of small pieces such as a bounding fragmentation mine (e.g. the Valmara 69, which has a plastic envelope).

[NEG72] have considered the 2D problem of a cylindrical body surrounded by a coaxial shell, in the field of a line source. This covers for example the case of hollow cylinders. Complex phenomena can emerge for such a composite object, e.g. screening effects, especially at high frequency, due to the skin effect in the shell. *This constitutes one of the few examples of situations in which the phase does not necessarily decrease monotonically with frequency.*

After having discussed the general form of an object's EM response we will now analyse in detail two models for which exact solutions exist, namely the sphere and the infinite cylinder transverse to the primary magnetic field.

28. Each particle, such as a small sphere, can probably not be considered as being isolated from its neighbours.

3.4. The Response of a Homogeneous Sphere

The classical problem of a homogeneous sphere in the field of a dipole or a loop has been studied for quite some time, and its solution represents a good approximation to the response of small, regular objects. Exact solutions exist in a number of cases. We will first comment on the possible scenarios and introduce the quasi-static approximation, to then consider in detail the situation of a sphere in the field of a coaxial coil and the expansion in multipole terms of its response.

3.4.1. General Considerations

The response of a homogenous sphere has been studied in detail in a number of different scenarios. Broadly speaking we can categorize them as follows:

- Different *incident (primary) magnetic field patterns*, such as homogeneous, dipolar, or multipolar (e.g. with the sphere on a coil's axis).

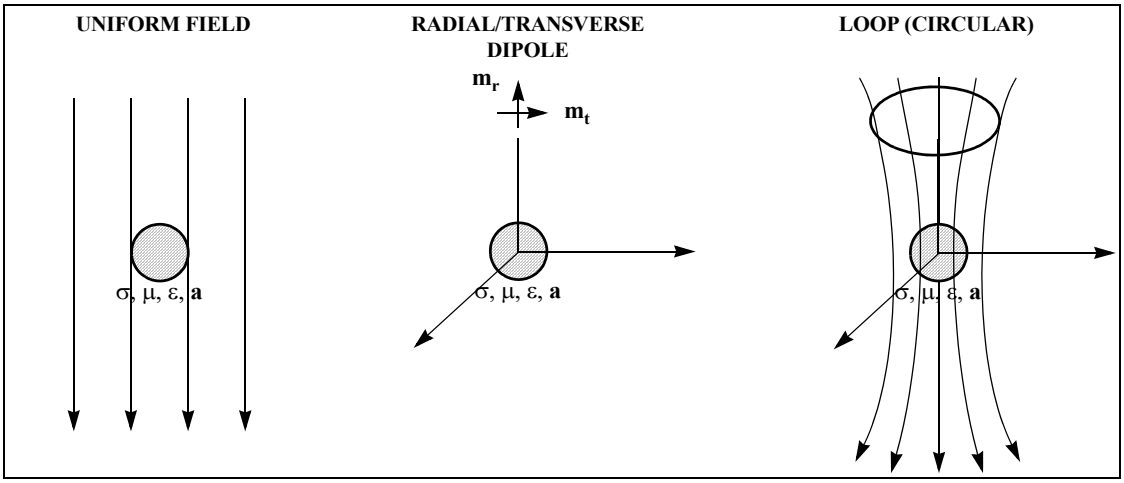

Figure 3.3: Different incident (primary) magnetic field patterns (valid for a general target).

- Different *surrounding medium*, such as (in increasing order of realism and complexity): **Empty space** (i.e. isolated target), embedded in a **full space** (infinite external medium, also called whole space), **approximations to the exact half space** solution (e.g. half space response + free space target, or first order interaction), emdedded in a **half space** (buried object, full interaction).

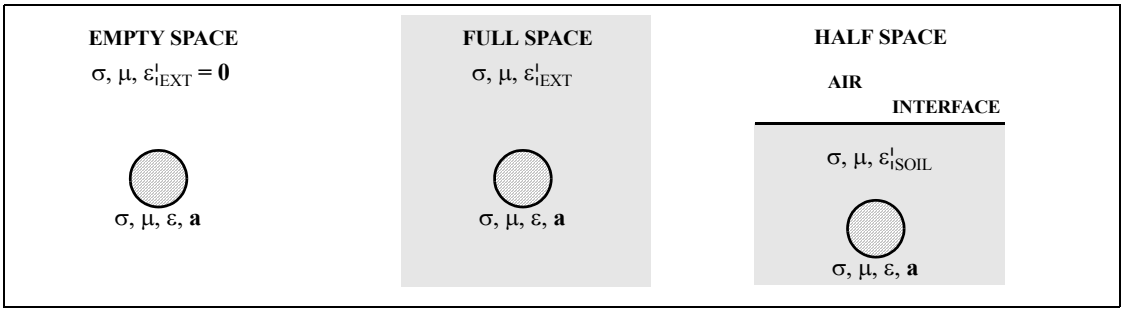

Figure 3.4: Different Surrounding Medium scenarios (valid for a general target).

We note in passing that different conventions are in use for the time factor (for alternating fields), which is usually omitted in intermediate calculations, and the propagation constant. For example, [WAR67] uses a time factor of $e^{-i\omega t}$ and his propagation constant is $k^2 = i\sigma_i\mu_i\omega + \varepsilon_i\mu_i\omega^2$; [WAI82] uses $e^{i\omega t}$ and $k^2 = i\sigma_i\mu_i\omega - \varepsilon_i\mu_i\omega^2$; [WAR87] uses $e^{i\omega t}$ and $k^2 = -(i\sigma_i\mu_i\omega - \varepsilon_i\mu_i\omega^2)$. The propagation constant is also called γ.

3.4.2. Homogeneous Sphere in a Homogeneous Full Space

We will start the analysis of the response of the homogenous sphere by considering the case of the target embedded in a homogenous full space, without however entering into the full details of the effect of the host medium on the secondary field. It is usually assumed that the host medium and the target response can be simply added as if they were non-interacting; this will be discussed in more detail in §3.7 (see Eq. (3.55)).

The main ideas behind the exact solution of the problem of a sphere embedded in a half space, more realistic but even more difficult to solve than the full space approximation used here, are available in A3.1.

Sphere in the Field of a Magnetic Dipole

Solutions to this configuration are available for instance in [WAR87] and [KAU01]. The first reference in particular deals with the problem in its Section 6, expressing the fields in terms of TM_r and TE_r modes (radial Transverse Magnetic and Transverse Electric modes, respectively). The magnetic dipole can be oriented in either the radial or the transversal direction (see also Figure 3.3); indeed, an arbitrarily oriented dipole can be resolved into a combination of a transverse and a radial dipole.

Quasi-Static Approximation

The solutions are then simplified, as is often the case when dealing with this type of electromagnetic problems, in the *quasi-static approximation* (low frequency approximation), i.e. assuming that the distances involved (in this case the dipole-sphere r_0 and observer-sphere distance r, as well as the sphere radius a) are much less than a wavelength[29], and assuming that *displacement currents* can be neglected. The quasi-static approximation can be expressed as:

$$|k_1 a|, |k_1 r|, |k_1 r_0| \ll 1 \tag{3.10}$$

with k_1 being the wave number in the external medium, whereas neglecting displacement currents is possible when

$$\mu\varepsilon\omega^2 \ll \mu\sigma\omega \Rightarrow \sigma \gg \varepsilon\omega \tag{3.11}$$

in which case the propagation constant also simplifies to (**the dependence on the dielectric constant ε disappears**):

$$k^2 = i\sigma\mu\omega \quad , \quad i = \sqrt{-1} \tag{3.12}$$

Eq. (3.10) is usually well satisfied, with the possible exception of high conductivity soils towards the higher frequency end (although only k is tabulated in Table 3.2, one can assume a maximum value of a, r and r_0 of the order of 1 m for our application, thus having an immediate idea of the approximation's validity).

Eq. (3.11) is very well satisfied in metals: indeed, even in the case of poor conductivity ($\sigma=10^5$ S/m say), $\varepsilon\omega/\sigma$ has a value of only $5.6\ 10^{-10}$ at 1 MHz. It usually also holds true in the case of soil, although this could not be the case for very low conductivity soils towards the high frequency end (see Table 3.2). Most soils are probably in the 10^{-3}-1 S/m range, with the possible exception of dry sand or where rocky conditions are prevalent [McF89].

29. Or equivalently, that the skin depth in the external medium is much larger than the distances involved and the sphere size. See also Eq. (3.15).

Soil conductivity	σ *(S/m)*	$\varepsilon\omega/\sigma$ *@ 1kHz*	$\varepsilon\omega/\sigma$ *@ 1MHz*	*k @ 1 kHz*	*k @ 1 MHz*	δ *@ 1 kHz*	δ *@ 1 MHz*
high	1	5.6×10^{-7}	5.6×10^{-4}	0.089	2.8	15.8	0.5
low	10^{-3}	5.6×10^{-4}	0.56	2.8×10^{-3}	0.089	500	15.8
very low	10^{-5}	5.6×10^{-2}	56	2.8×10^{-4}	8.9×10^{-3}	5×10^{3}	158

Table 3.2: Values of $\varepsilon\omega/\sigma$, k (in m^{-1}) and δ (in m) for some soil scenarios ($\varepsilon=10\varepsilon_0$, $\mu=\mu_0$ throughout)

The dielectric constant of geologic materials varies from 1 to about 81 (pure water), and is usually strongly related to water content. In Table 3.2 we have taken a typical value of $\varepsilon_r=10$, which might have to be increased for water saturated soils [McF89]. The relative permeability of soils is seldom greatly different from unity [WAR67], see also Table 3.3; in most cases it is determined by the magnetite content, with massive magnetite having $\mu_r=5$. Nevertheless, as discussed in Chapter 2, this can significantly impact the performance of metal detectors. The conductivity can reach a few S/m in salt water.

Mineral	*Relative Permeability* μ_r
Magnetite	5.0
Pyrrhotite	2.55
Ilmenite	1.55
Hematite	1.053
Pyrite	1.0015

Table 3.3: Relative Permeability values for some ferromag. minerals (in units of μ_0) (from [KEL66], Table 14)

Physically speaking these approximations mean that the magnetic field at any point in the medium is defined by the instantaneous values of current density throughout the conducting medium, and *can be calculated using only the Biot-Savart law*[30] (like in the case of a static magnetic field). Also, the propagation time for the electromagnetic energy can be neglected, i.e. it is assumed that the field travels instantaneously (propagation effects not considered). In this case the *wave equations* for the electric and magnetic fields reduce, when displacement currents can be neglected, to *diffusion equations* (they describe the penetration of energy, but do not take into account wave propagation) [KAU01,§2.5].

The quasi-static approximation is therefore valid when conduction currents dominate over displacement currents in a conducting medium, and when the arrival time for a signal in an insulator is much less than the duration of a measurement, or the period of the observed oscillations.

Sphere in the Field of a Loop

This is for example dealt with in [KAU01,§5.2], considering an external medium with $\mu_{ext}=\mu_0$. We will look at this geometry in the next paragraph, using however the quasi-static approximation, which is sufficient for our purposes, rather than the exact solution.

30. *The quadrature and in-phase components of the secondary magnetic field will therefore be generated by the corresponding components of the induced currents, and have similar frequency responses* [KAU01,§2.4.6.2].

3.4.3. Homogeneous Sphere in the Field of a Coaxial Coil

We will follow here the formulation of [McF89], with early solutions in Geophysics going back at least to the early fifties [WAI53] ([WON98] lists several classical papers by Wait on the subject). It is interesting to note that the problem has also been treated separately in NdT, e.g. in [VEI65], which presents the analytical details of a number of classical problems (coaxial circular coils in the presence of planar, cylindrical and spherical conductors, in free space), relying on the magnetic vector potential formulation and using appropriate boundary conditions. Extensions to a coil encircling two concentric, spherical shells (in free space) of finite (σ,μ), is provided in [LUQ70], with extensions to coil of finite sizes. No numerical results are reported in these two NdT references.

The response $V^{(s)}$ of a homogeneous sphere of radius *a,* conductivity σ and permeability μ ($\mu=\mu_0\mu_r$), placed in the field of a circular transmit coil of radius R_T, as measured by a circular receive coil of radius R_S, can be calculated exactly (in the quasi-static approximation described above and neglecting displacement currents). The coils are coaxial and placed on the sphere's axis at a distance d_T and d_S from the sphere's centre as shown in Figure 3.5.

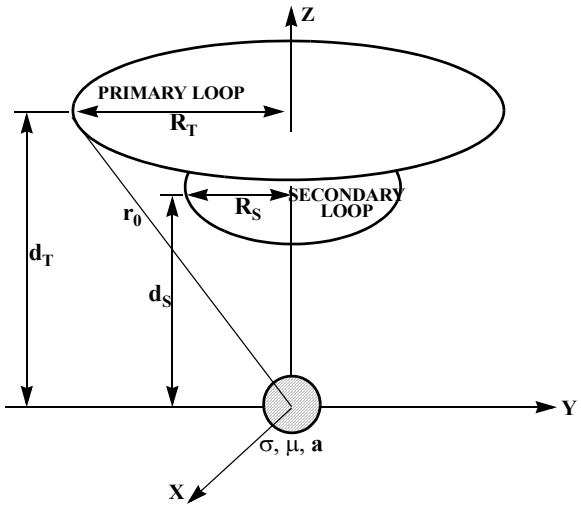

Figure 3.5: Geometry for the calculation of the response of a sphere in the field of a coil (adapted from **[McF89]**). Size and position of the primary and secondary loops are not representative.

The operating frequency is ω, and the transmit coil is traversed by a constant current *I*. Time dependence is implicitly assumed as $e^{i\omega t}$ and omitted in the following.

This analysis has the advantage of using a realistic geometry for small nearby objects; it also reduces in the limit to the commonly used uniform primary field or dipole approximation. Note that throughout this analysis we will assume a constant relative permeability μ_r. In fact this is far from obvious as μ_r can depend on the operating frequency and in particular on the strength of the applied field [SOW98b].

The primary field can be expanded in spherical harmonics, and each generates a spherical harmonic in the secondary field for the same index *n*. It can therefore be shown [McF89] that the induced voltage $V^{(s)}$ can be written as a sum of products of geometry and frequency dependent terms as follows (P_n^1 are associated Legendre polynomials and $I_{n+1/2}(ka)$, $I_{n-1/2}(ka)$ are modified Bessel functions of the first kind; see also A3.3):

$$V^{(s)} = 2\pi i\mu_0 I\omega \frac{R_S R_T}{(d_T^2+R_T^2)^{1/2}} \sum_{n=1}^{\infty} \frac{a^{2n+1}}{2n(n+1)} \frac{P_n^1(d_T/[d_T^2+R_T^2]^{1/2})P_n^1(d_S/[d_S^2+R_S^2]^{1/2})}{(d_T^2+R_T^2)^{n/2}(d_S^2+R_S^2)^{(n+1)/2}} \chi_n(ka) \quad (3.13)$$

$$\text{with } \chi_n(ka) = X_n(ka) + iY_n(ka) = \frac{[(n+1)\mu_r + n]I_{n+1/2}(ka) - kaI_{n-1/2}(ka)}{n(\mu_r - 1)I_{n+1/2}(ka) + kaI_{n-1/2}(ka)} \tag{3.14}$$

$$\text{and } k^2a^2 = i\sigma\mu\omega a^2 = i\alpha = 2i\frac{a^2}{\delta^2} \tag{3.15}$$

The adimensional expression $\chi_n(ka) = X_n(ka) + iY_n(ka)$, which plays a role similar to the *response function* F(α) previously encountered, contains all the frequency dependence (apart from the external ω factor) as well as the dependence on the object properties (apart from the a^{2n+1} term). The *response parameter* is now $k^2a^2=i\sigma\mu\omega a^2=i\alpha$ (adimensional and purely imaginary, with $\mu=\mu_0\mu_r$) rather than $\alpha=\omega L/R$; it is related to the skin depth δ as indicated in Eq. (3.15).

There are actually a number of different ways in which the response function can be expressed, using for example spherical modified Bessel functions instead of modified Bessel functions, and their derivatives. We will here only point out that the χ_n listed above are equivalent to the R_n (reflection) coefficients in Wait's original article [WAI53], which are in turn defined as S_n in [WAI60], r_{TEr} in [WAR87], etc.

Note that this response function is parametrized by the sphere's relative permeability μ_r. In fact we have implicitly assumed $\mu_{ext}=\mu_0$, otherwise one has to replace μ_r with the permeability contrast $K=\mu_{sph}/\mu_{ext}$. Note also that the external medium conductivity does not appear any more in the quantities of interest.

The rest of Eq. (3.13) contains the geometrical factors, i.e. the relative geometry of the sphere and the transmit and receive coils. We shall define in particular as "*geometry term*" $\boldsymbol{g_n}$ the adimensional expression to the right of the sum sign, which depends on *n*:

$$g_n(d_T, R_T, d_S, R_S; a) = \frac{a^{2n+1}}{2n(n+1)} \frac{P_n^1(d_T/[d_T^2 + R_T^2]^{1/2}) P_n^1(d_S/[d_S^2 + R_S^2]^{1/2})}{(d_T^2 + R_T^2)^{n/2} (d_S^2 + R_S^2)^{(n+1)/2}} . \tag{3.16}$$

Note also the presence of the ω factor, which means that the induced voltage grows linearly with frequency (apart from the $|\chi_n(ka)|$ behaviour). Concerning the transmit current *I*, from a practical point of view it might not be easy to keep it constant when driving the transmit coil at constant voltage, as its impedance ($R_{Transmit}+i\omega L_T$) grows when increasing ω.

Table 3.4 lists typical values of the response parameter $\alpha=\sigma\mu\omega a^2$ for spheres of radius 1 mm, 5 mm, 1 cm and 5 cm, at the two operating frequencies of the Förster Minex metal detector (f_1=2.4 kHz and f_2=19.2 kHz), which are typical of the frequency range of interest. Note that α increases quadratically with the object radius, and linearly with its conductivity and permeability, and with the frequency. This is why the highest values for a given sphere size and frequency are those of permeable steel, followed by copper. As a rule of thumb we can say that small values of *a* (small objects), low operating frequency and low conductivity tend to reduce α, the opposite when dealing with large objects, high operating frequency and good conductors or permeable objects.

Material	σ (10^7 S/m)	μ_r	α for a=1mm	α for a=5mm	α for a=1cm	α for a=5cm
Copper	5.8	1	1.10 (8.8)	27 (2.2×10^2)	1.10×10^2 (8.8×10^2)	2.7×10^3 (2.2×10^4)
Aluminium	3.54	1	0.67 (5.4)	17 (1.3×10^2)	0.67×10^2 (5.4×10^2)	1.7×10^3 (1.3×10^4)
Brass (yellow)	1.5	1	0.28 (2.2)	7.1 (57)	0.28×10^2 (2.2×10^2)	0.71×10^3 (5.7×10^3)
Steel (typical)	0.63	150	18 (1.4×10^2)	4.5×10^2 (3.6×10^3)	1.8×10^3 (1.4×10^4)	4.5×10^4 (3.6×10^5)

Table 3.4: Typical conductivity, relative permeability, and response parameter α for spheres of different sizes at f_1=2.4 kHz (and f_2=19.2 kHz) (using the conductors tabulated in Table 2.1)

Series Expansion of the Response Function

Each term χ_n of the response function can actually be expanded in a series, containing a sum of simple fractions [KAU01, §3.3], along the lines of what discussed in §3.3 (eigencurrents) and in particular in Eq. (3.9). The poles ω_{ns}:

$$\omega_{ns} = -\frac{iq_{ns}}{\sigma\mu a^2} \tag{3.17}$$

are again situated on the imaginary axis (negative values are due to the convention in [KAU01]), with the coefficients q_{ns} having the following properties:

$$q_{1s} = \pi^2 s^2 \; ; \; q_{n,s} < q_{n,s+1} \; ; \; q_{n,s} < q_{n+1,s} \; ; \; q_{n,1} \cong \frac{(2n+5)(2n+1)}{2} \tag{3.18}$$

A detailed expression will be given in Eq. (3.25) for the dipole approximation, to which in fact the q_{1s} coefficients correspond.

We will now analyse in more detail Eq. (3.13) for the most important cases.

3.4.4. Sphere in the Field of a Coaxial Coil – Multipole Terms (geometry, g_n)

Higher order terms decrease more rapidly with distance than lower order terms (this is easier to see for $d=d_T=d_S$, the coplanar case). Conversely, as the coils approach the sphere higher order terms become significant and the secondary field in the sphere receives contributions from higher order multipoles. The multipole terms do indeed scale as:

$$\frac{g_{n+1}}{g_n} = \frac{n}{n+2}\frac{a^2}{r_T r_S}\frac{P^1_{n+1}(r_T)P^1_{n+1}(r_S)}{P^1_n(r_T)P^1_n(r_S)} \quad \text{with} \quad r_T = \frac{d_T}{[d_T^2+R_T^2]^{1/2}}\,,\; r_S = \frac{d_S}{[d_S^2+R_S^2]^{1/2}} \tag{3.19}$$

which is similar but not equal to the well known behaviour of a sphere in the field of a magnetic dipole (see for example [GRA65]), whose multipole coefficients scale approximately as a^2/r^2 $[(n+2)/n]$ for a sphere of radius a at a distance r.

Coming back to our case, the contribution from higher order multipoles is illustrated in Figure 3.6, representing the geometry term g_n of Eq. (3.16) for n=1 to n=4 in the case of overlapping coils ($d=d_T=d_S$ and $R=R_T=R_S$) and a rather large sphere, of radius a equal to the coil radius R ($a=R$=0.1). The case of a small sphere will be analysed later. Units are in fact indifferent, but thinking in terms of meters for example provides realistic size and depth estimates. The plots are interesting for us for $d>a$ (top of the sphere below the coil); there the n=1 term clearly dominates, with an initially substantial contribution from the n=2 term (up to a distance of 2-3 times the sphere diameter) and a smaller contribution for n=3. Note that the g_n term scales – identical plots are obtained when multiplying a and R by a factor and modifying the distance plotting range limits by the same amount – as can be easily seen when rewriting g_n in terms of a/d and R/d.

3.4.4.1. Multipole Terms for a Non-Ferromagnetic Object (χ_n for μ_r=1)

Figure 3.7 illustrates the behaviour of the first four terms of the response function χ for a non-ferromagnetic object (μ_r=1). The phase has in fact been calculated over $i\chi$ (compare also with Eq. (3.13)) in order to reproduce the overall phase of the induced voltage, rather than the phase of the induced currents which generate the secondary field. The multiplication by i is due to time differentiation of the $e^{i\omega t}$ factor ($V^{(s)} = -\partial\Phi/\partial t$ with $\Phi = \int \boldsymbol{B}_{\text{sec}} \cdot d\boldsymbol{S}$ and $\boldsymbol{B}_{\text{sec}} \propto e^{i\omega t}$), and is equivalent to a counter-clockwise rotation of 90° in the complex plane (i.e. $\text{Re}(i\chi)=-\text{Im}(\chi)$ and $\text{Im}(i\chi)=\text{Re}(\chi)$).

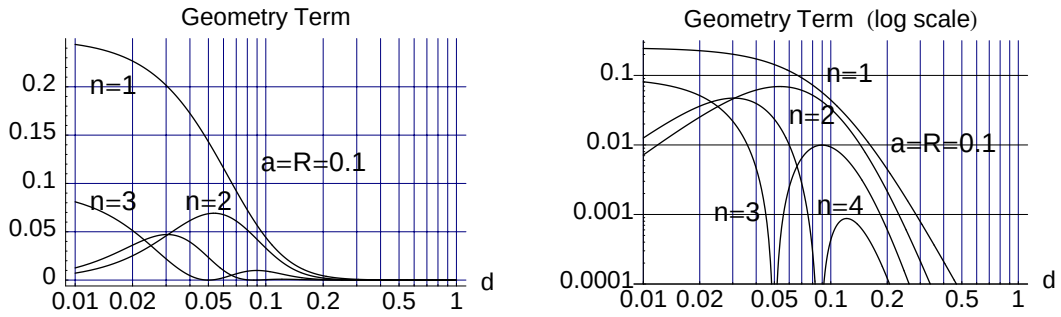

Figure 3.6: First 4 multipole expansions of the geometry term g_n for a "large" sphere (a=R=0.1, d=d_T=d_S and R=R_T=R_S)

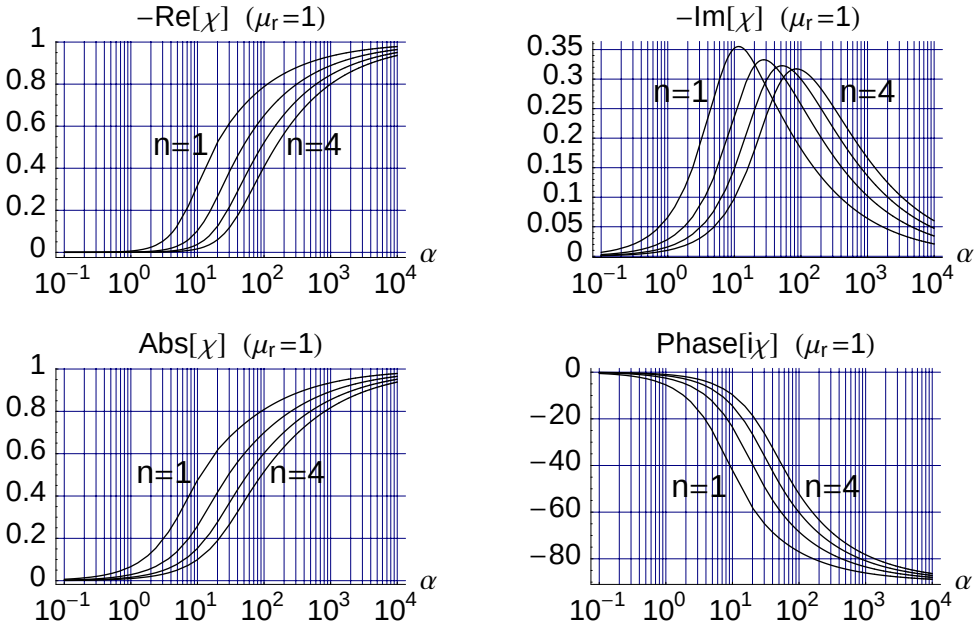

Figure 3.7: First 4 multipole expansions of the response function χ for a non-ferromagnetic object

The first term (n=1) has the largest absolute value and the strongest phase contribution. *The phase decreases steadily as* α *increases*, but *can increase at a given* α, with respect to the n=1 value, *if the higher order multipole terms are relevant* (see also the previous discussion of the geometry term g_n).

3.4.4.2. Multipole Terms for a Ferromagnetic Object (χ_n for μ_r=10)

Figure 3.8 illustrates the behaviour of three of the first four terms of the response function χ for a ferromagnetic object, having taken as example μ_r=10. Note that the absolute value is finite for $\alpha \to 0$ (for which the phase approaches +90°) due to an induced magnetization effect, and that there are values of α for which the dipole term (n=1) is not dominating (but it might very well do taking into account the contribution of the geometry term g_n). For $\alpha \to \infty$ the absolute value saturates and the phase approaches –90°, exactly as for the non-ferromagnetic case discussed above (inductive limit).

As in the case of the non-ferromagnetic object, *the phase decreases steadily as* α *increases*, but *can increase at a given* α, with respect to the n=1 value, *if the higher order multipole terms are relevant.* With the notable difference that the phase changes sign here.

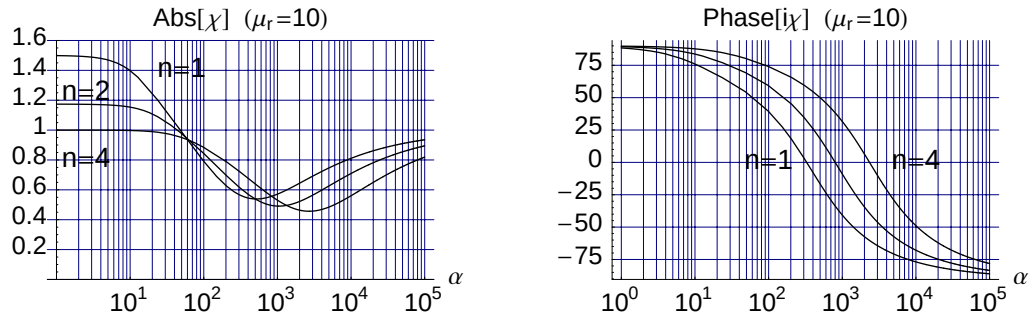

Figure 3.8: First multipole expansions (n=1, 2, 4) of the response function χ for a ferromagnetic object (μ_r=10)

3.4.5. Dipole Approximation (n=1) – General Considerations

If the sphere is far from the coils compared to its size ($d>>a$), or much smaller than the coil diameter ($a<<R$), it only "sees" a homogeneous (uniform) primary field and only the first term **(n=1)** is relevant (Dipole Approximation). This is illustrated in Figure 3.9, which shows the geometry dependent term for n=1 and n=2 in the case of overlapping coils ($d=d_T=d_S$ and $R=R_T=R_S$) and a small sphere (a=0.01=1/10 R).

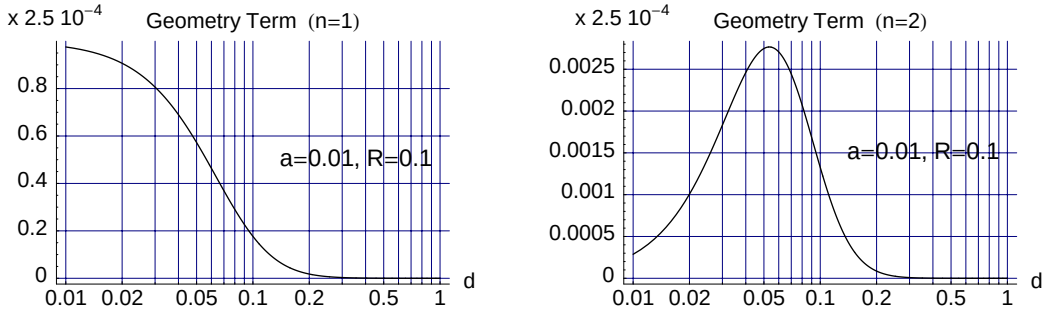

Figure 3.9: First 2 multipole expansions of the geometry term g_n for a "small" sphere (a=0.01=1/10 R, $d=d_T=d_S$ and $R=R_T=R_S$)

In this case the sphere behaves like a simple magnetic dipole with magnetic moment **m** ($\hat{z}$ is the unit vector in the z direction):

$$\boldsymbol{m} = -2\pi a^3 H_0 (X + iY)\hat{z} \tag{3.20}$$

$$\text{with } H_0 = \frac{I}{2}\frac{R_T^2}{r_0^3},\ r_0 = \sqrt{d_T^2 + R_T^2} \text{ and} \tag{3.21}$$

$$X + iY = \frac{[\mu_0(1+k^2a^2) + 2\mu]\sinh(ka) - (2\mu + \mu_0)ka\cosh(ka)}{[\mu_0(1+k^2a^2) - \mu]\sinh(ka) + (\mu - \mu_0)ka\cosh(ka)} = -\chi_1(ka)\ . \tag{3.22}$$

where $\chi_1(ka) = X_1(ka) + iY_1(ka)$ has been defined in Eq. (3.14) and H_0 is the transmit field at the sphere's centre. Here we have again implicitly assumed $\mu_{ext}=\mu_0$.

The induced magnetic moment **m** of a sphere in the dipole approximation is in fact always aligned along the transmit (or primary) field $\mathbf{H}_T$, i.e. we can simply replace $\hat{z}$ with $\mathbf{H}_T$ in Eq. (3.20). It is also worthwhile to note that the sphere's (dipole) *phase* response X+iY depends on its parameters (μ, σ, a) and on ω, but not on the problem's geometry (i.e. the sphere's position with respect to the coils), and is therefore constant for a given object (as long as μ_r does not change obviously) and working frequency ω [BAR96]. As we have seen this is not necessarily true when higher order multipole contributions are relevant.

Table 3.5 lists values (in degrees) of the phase of the induced voltage in the dipole approximation for the response parameter ($\alpha=\sigma\mu\omega a^2$) values of Table 3.4, again at f_1=2.4 kHz and f_2=19.2 kHz.

Material	*Phase for a=1mm*	*Phase for a=5mm*	*Phase for a=1cm*	*Phase for a=5cm*
Copper	−6.0 (−38.8)	−63.3 (−81.4)	−77.6 (−85.8)	−87.6 (−89.2)
Aluminium	−3.7 (−26.8)	−54.8 (−78.7)	−73.9 (−84.6)	−87.0 (−88.9)
Brass (yellow)	−1.5 (−11.8)	−33.3 (−72.4)	−63.8 (−81.4)	−85.3 (−88.4)
Steel (typical)*	+88.4 (+85.4)	+81.8 (+68.2)	+74.2 (+49.2)	+18.4 (−52.8)

Table 3.5: Phase of induced voltage in the dipole approximation at f_1=2.4 kHz (and f_2=19.2 kHz) for spheres of different sizes (*μ_r=150) (see also Table 3.4)

Induced Voltage in the Dipole Approximation

The overall expression of the induced voltage $V^{(s)}$ reduces in the dipole approximation to:

$$V^{(s)}\big|_{n=1} = 2\pi i\mu_0 I\omega\frac{a^3}{4}\frac{R_T^2}{(d_T^2+R_T^2)^{3/2}}\frac{R_S^2}{(d_S^2+R_S^2)^{3/2}}(X_1(ka)+iY_1(ka)) \tag{3.23}$$

Apart from the already stressed direct proportionality to the frequency ω, we also recognize the typical dependence of the magnetic field generated along a coil's axis, the term $R_T^2/(d_T^2+R_T^2)^{3/2}$ corresponding to the transmit (or primary) field and the term $R_S^2/(d_S^2+R_S^2)^{3/2}$ to the magnetic flux in the receive coil[31].

Induced Voltage for Overlapping Coils

In the case of overlapping coils ($d=d_T=d_S$ and $R=R_T=R_S$) the previous expression becomes:

$$V^{(s)}\big|_{n=1} = 2\pi i\mu_0 I\omega\frac{a^3}{4}\left[\frac{R^2}{(d^2+R^2)^{3/2}}\right]^2(X_1(ka)+iY_1(ka)) \tag{3.24}$$

In the case of a sphere in homogenous primary field the induced currents are circular and flow in planes perpendicular to the direction of the inducing field.

Series Expansion of the Response Function

The response function in the dipole approximation can be expressed as a series, containing a sum of simple fractions, along the lines of what discussed in §3.3 (eigencurrents) and in particular in Eq. (3.9). For a non-ferromagnetic object [KAU01, §3.1]:

$$X+iY\big|_{\mu_r=1} = \frac{6}{\pi^2}\sum_{n=1}^{\infty}\frac{1}{n^2}\frac{i\omega}{(\pi^2n^2/\sigma\mu a^2)-i\omega} \tag{3.25}$$

The poles on the imaginary axis[32] are here at:

$$\omega = i\omega_n = -i\frac{\pi^2n^2}{\sigma\mu a^2} \tag{3.26}$$

31. Or equivalently corresponding, using *reciprocity arguments*, to the field which would be produced by the receive coil at the object location.
32. The poles are, according to the convention of [KAU01] ($e^{-i\omega t}$ time dependence), on the negative imaginary axis. X is therefore negative rather than positive as in our case.

with the first pole (n=1) approximately situated at a value of the response parameter at which the real part of the response function is equal to the imaginary (crossover, see also Figure 3.10). Their magnitude is rapidly increasing, the corresponding coupling coefficients do however decrease with n^2.

Factorisation of the Response

This case, as well as that of a simple circuit previously discussed, are examples of situations in which the response separates explicitly into the product of a response function (physical property factor) and a coupling coefficient (geometric factor), or more precisely [WAR67]:

Response = (Inducing Field) x (Size Factor) x (Physical Property Factor) x (Geometric Factor)

In such simple cases the geometry effects can be studied separately from the effects of the physical properties (σ,μ,R) and of ω, i.e. the effect of the response parameter is independent of the system's position [GRA65]. This is in general not the case for broad conductors and/or ferromagnetic objects.

3.4.5.1. Dipole Approximation for a Non-Ferromagnetic Object (χ_1 for μ_r=1)

The dipole's approximation response function (Eq. (3.22)) further reduces, in the case of $\mu_r = 1$ (non-ferromagnetic object), to:

$$X + iY\big|_{\mu_r = 1} = 3\left[\frac{1}{k^2 a^2} + \frac{1}{3} - \frac{\cosh(ka)}{ka\sinh(ka)}\right] = -\chi_1(ka)\big|_{\mu_r = 1} . \qquad (3.27)$$

Its behaviour is reproduced in Figure 3.10, the term "Dipole" and $X + iY\big|_{\mu_r = 1}$ being equivalent; the phase has been calculated here over (–i Dipole**)** in order to again reproduce the overall phase of the induced voltage.

As expected the plots correspond to those of the first term in Figure 3.7, with the addition of the equivalent complex plane representation; *they are indeed qualitatively similar to what expected for a simple circuit model*.

Examples of working points at the Förster Minex operating frequencies are shown as circles and squares for copper spheres of radius 1 mm (very small object) and 1 cm respectively (see also Table 3.4 and Table 3.5).

For the smaller object there is a very large difference in the absolute value of the response function at the two frequencies, whereas for the larger one the ratio of the two absolute values approaches unity[33], as we are already close to the inductive limit (see Eq. (3.13)).

Considering the absolute value of the response function for non-ferromagnetic objects higher operating frequencies are therefore favoured, which is not necessarily true when phase-based identification is attempted, as the phase response curve flattens when approaching –90° [TRA97] (i.e. different objects tend to show similar phase behaviour when increasing the frequency). From the point of view of discriminating smaller debris from larger pieces a value of the phase threshold in the range –60° to –80° could represent a good starting point for further investigations (for non-ferromagnetic objects).

33. The overall induced voltage features in fact an additional factor ω, as we have already seen in Eq. (3.13).

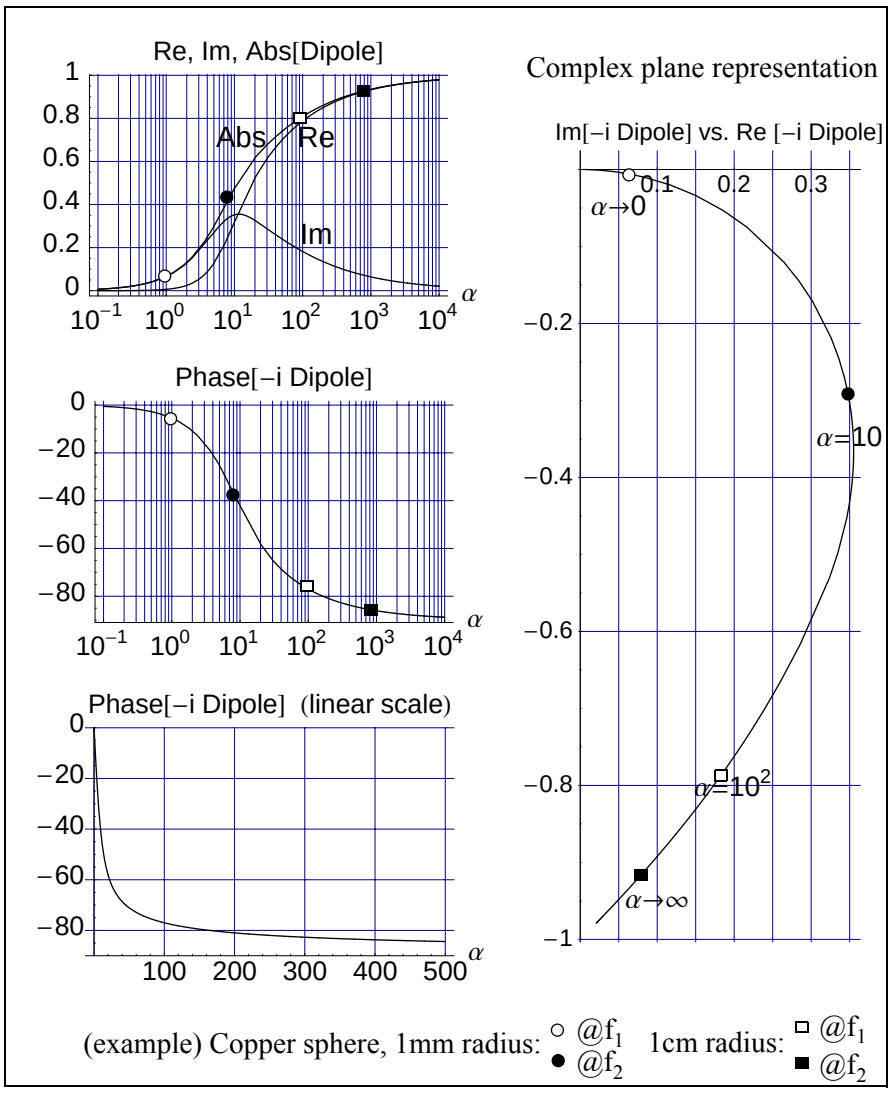

Figure 3.10: First multipole term (n=1: dipole approximation) of the response function χ for a non-ferromagnetic object (μ_r=1).

3.4.5.2. Dipole Approximation for Ferromagnetic Objects (χ_1 for μ_r>1)

The dipole's approximation response function (Eq. (3.22) or equivalently Eq. (3.14) with n=1) is reproduced in Figure 3.11 for two different ferromagnetic objects (μ_r=10 and μ_r=100) as well as for μ_r=1 (non-ferromagnetic) for comparison. The plots for μ_r=10 correspond to those of the first term (n=1) in Figure 3.8. The complex plane representation is here shown for μ_r=100 only. The behaviour of the phase includes again the factor *i* in order to reproduce the overall phase of the induced voltage. As we already pointed out, the response function for ferromagnetic objects is parametrized by μ_r (i.e. there is one curve for each value of μ_r).

Similarly to what already noted for Figure 3.10, for $\alpha \to \infty$ the absolute value saturates and the phase approaches –90°, as for the non-ferromagnetic case (inductive limit), whereas the phase approaches +90° and the absolute value is finite for $\alpha \to 0$ due to an induced magnetization effect (and $Abs[\chi] \to 2$ for $\mu_r \to \infty$) [McF89, TRA97]. This well-known fact could be used to determine if an object with negative phase response is ferromagnetic or not, using a magnetometer or multiple frequency measurements (with at least one frequency rather low). Indeed, from what said it is clear that a single phase measure resulting in a negative value is by itself not sufficient to state that the object is non-ferromagnetic. Still concerning the low frequency limit, note that:

$$\lim_{\alpha \to 0} |\chi| = \frac{2(\mu_r - 1)}{2 + \mu_r} \tag{3.28}$$

as can be verified in Figure 3.11 for μ_r=10 (limit: 1.5) and μ_r=100 (limit: about 2).

It can also be noted that the peak in the quadrature component at high permeability values is:

$$\alpha_{Peak(IM)} = \sigma\mu\omega_{Peak(IM)}a^2 \cong \mu_r^2 \Rightarrow \omega_{Peak(IM)} \cong \frac{\mu_r^2}{\sigma\mu a^2} \tag{3.29}$$

For a given μ_r *the phase decreases steadily as* α *increases*, again with the notable *difference* with respect to non-ferromagnetic objects that its sign changes. On the other hand *the phase increases when increasing* μ_r whilst keeping the other object parameters (σ,*a*) and the operating frequency ω constant. This can be seen by moving from example from the phase response at μ_r=10 for a given α_1 to the corresponding phase response at μ_r=100 (i.e. for α_2=10α_1 as shown by the arrow labelled "1" in Figure 3.11).

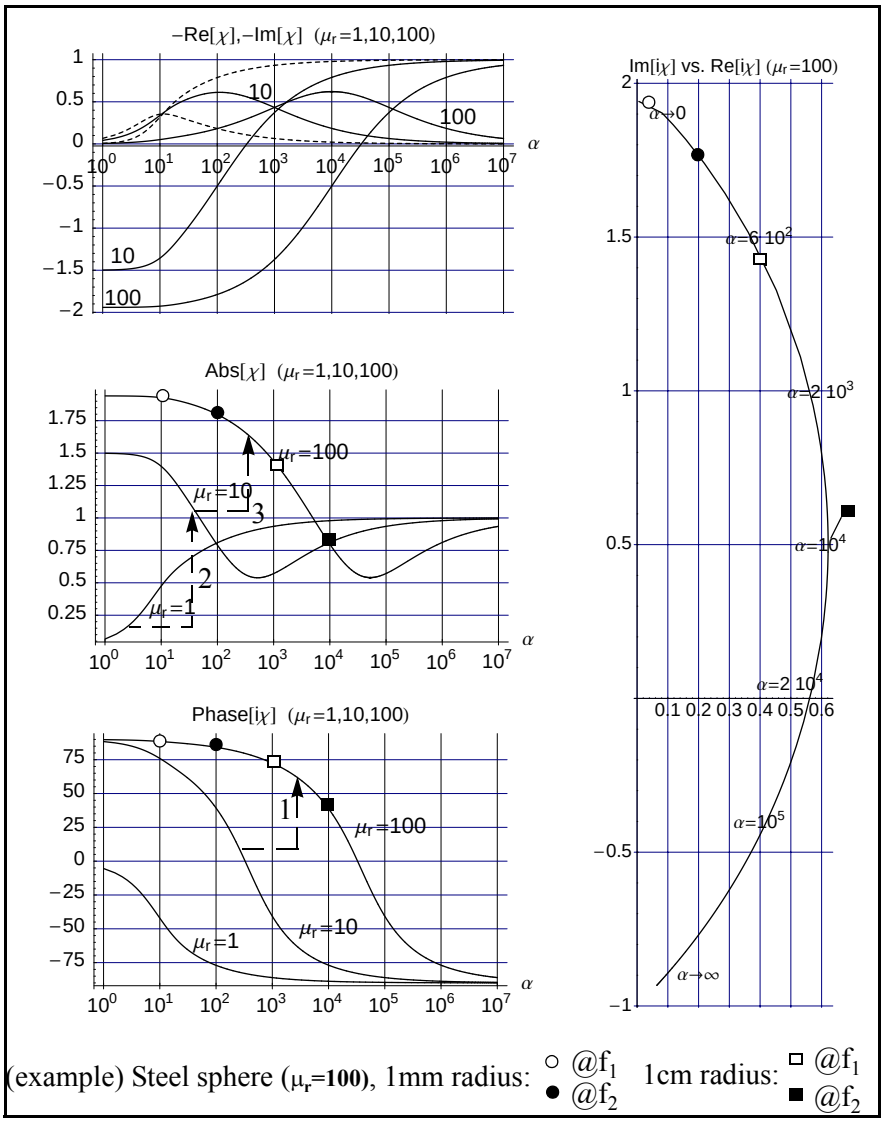

Figure 3.11: First multipole term (n=1: dipole approximation) of the response function χ for different ferromagnetic objects as well as for μ_r=1 for comparison (dashed in top plot; arrows: see text).

For a given μ_r the absolute value of the response function *decreases* as α increases and then slowly rises again; this seems to favour lower operating frequencies[34].

If instead we *increase* μ_r whilst keeping the other object parameters (σ, a) and ω constant, at low values of α the absolute value of the response function *increases* (follow the arrows labelled "2" and "3" in Figure 3.11). In this regime the difference between non-ferromagnetic and ferromagnetic objects can be significative. Moving to higher values of α this trend is reversed.

Examples of working points at the Förster Minex operating frequencies are again shown as circles and squares for mild steel spheres, with μ_r=100, of radius 1 mm (very small object) and 1 cm respectively (see also Table 3.4 and Table 3.5, where the values are in fact calculated for μ_r=150). From the point of view of discriminating smaller debris from larger pieces a value of the phase threshold around +75° could represent a good starting point for further investigations (but in particular the case of objects with high μ_r values has to be studied more attentively).

3.4.6. Summary of Theoretical Analysis (Sphere)

We will briefly summarize the basic findings of the previous theoretical analysis (response of a homogenous sphere in the field of coaxial circular coils, placed on the sphere's axis):

- The induced voltage can be expressed as the sum of an infinite number of multipole terms, which can be represented as the product of a geometry dependent term g_n (real) and a response function χ_n (complex). The latter is a function of the response parameter $\alpha=\sigma\mu\omega a^2$, which depends on the object's properties (σ, μ, *a*) and on the operating frequency ω (see Eq. (3.13) to Eq. (3.15)).
- Higher order multipole components are not important if the sphere is far from the coils compared to its size (d>>a), or much smaller than the coil diameter (a<<R) (dipole approximation, homogeneous primary field).
- Non-ferromagnetic objects behave similarly to what predicted by a simple circuit model. The behaviour of ferromagnetic objects is parametrized by μ_r; they exhibit a finite response for $\alpha \to 0$, and their phase ranges from +90° to –90°. In both cases the phase decreases monotonically with α, but it can increase when higher order multipole terms are important or for increasing μ_r.
- In the dipole approximation the sphere's response does not depend on its position, only on the object's parameters.
- Higher operating frequencies are particularly important for the detection of small non-ferromagnetic objects; the opposite tendency is true for ferromagnetic ones (thinking of the absolute value of the response function).
- In principle one can differentiate between ferromagnetic and non-ferromagnetic objects (only ferromagnetic objects exhibit a positive phase response). Note that a single phase measure resulting in a negative value is by itself not sufficient to state that the object is non-ferromagnetic.

These general trends should still hold also for non-spherical objects, especially for smaller ones for which the dipole approximation is more likely to be satisfactory.

34. Again, keeping in mind that the overall induced voltage features an additional factor ω (Eq. (3.13)).

3.5. Homogenous Cylinders

Cylinders represent another shape common to several objects of interest in humanitarian demining applications, e.g. some mine strikers when considering small objects, and some metallic mines and UXO when considering large objects. Analytical solutions can again provide insight into the scattering process, and be useful as a check on numerical procedures [IDA95]. We will deal first with horizontal infinite cylinders (§3.5.1), then with objects of finite length (§3.5.2 and §3.5.3).

3.5.1. Horizontal Infinite Cylinders

Analytical solutions for the cylinder case have been first available in Geophysics in an idealized situation featuring a homogeneous infinitely long circular object ($\sigma_2,\varepsilon_2,\mu_2$) immersed in a homogenous external medium (whole space ($\sigma_1,\varepsilon_1,\mu_1$)) with an exact solution being available when the source is represented by an infinite line source of electric current running parallel to the cylinder (e.g. a cable) (2D problem) [WAI52, WAR87, KAU01, §6.4.2] as shown in Figure 3.12. They constitute a geophysical extension of the classical problem of diffraction by a circular cylinder.

It will be shown that the inductive behaviour is similar to the one of a sphere when the magnetic field is perpendicular to the cylinder's axis.

3.5.1.1. Parallel Line Source (2D problem, exact solution)

The secondary magnetic field components in the region outside the cylinder can be written as follows, omitting the $e^{i\omega t}$ factors ($I_n(\gamma_i a)$, $K_n(\gamma_i a)$ are modified Bessel functions of the first and second kind respectively. The cylinder is defined as $\rho<a$ for $-\infty<z<\infty$ in cylindrical coordinates; the line source is located at (ρ_0,ϕ_0) and P is an observation point [WAI52].

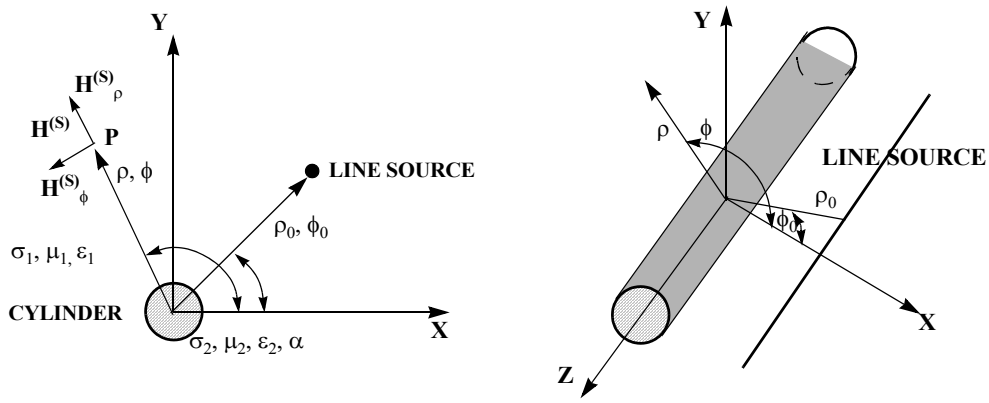

Figure 3.12: Geometry for the calculation of the response of an infinite cylinder in the field of a parallel infinite line source; section view, z axis towards reader and parallel to the cylinder (adapted from [KER60]).

The prime on a Bessel's function denotes a derivative with respect to its argument, and $K=\mu_2/\mu_1=\mu_{cyl}/\mu_{ext}$ is the magnetic permeability contrast [WAI73b]:

$$H_\phi^{(s)} = -\frac{I}{2\pi\rho}\sum_{n=-\infty}^{\infty} q_n \frac{K_n(\gamma_1\rho_0)}{K_n(\gamma_1 a)} I_n(\gamma_1 a) K_n'(\gamma_1\rho)\gamma_1\rho e^{-im(\phi-\phi_0)} \tag{3.30}$$

$$H_\rho^{(s)} = -\frac{I}{2\pi\rho}\sum_{n=-\infty}^{\infty} q_n \frac{K_n(\gamma_1\rho_0)}{K_n(\gamma_1 a)} I_n(\gamma_1 a) K_n(\gamma_1\rho) ime^{-im(\phi-\phi_0)} \tag{3.31}$$

with

$$q_n = \frac{\frac{1}{\eta_1}\frac{I_n'(\gamma_1 a)}{I_n(\gamma_1 a)} - \frac{1}{\eta_2}\frac{I_n'(\gamma_2 a)}{I_n(\gamma_2 a)}}{-\frac{1}{\eta_1}\frac{K_n'(\gamma_1 a)}{K_n(\gamma_1 a)} + \frac{1}{\eta_2}\frac{I_n'(\gamma_2 a)}{I_n(\gamma_2 a)}} \cong \frac{nK - \gamma_2 a\frac{I_n'(\gamma_2 a)}{I_n(\gamma_2 a)}}{nK + \gamma_2 a\frac{I_n'(\gamma_2 a)}{I_n(\gamma_2 a)}} = \frac{n(K+1)I_n(\gamma_2 a) - (\gamma_2 a)I_{n-1}(\gamma_2 a)}{n(K-1)I_n(\gamma_2 a) + (\gamma_2 a)I_{n-1}(\gamma_2 a)} \tag{3.32}$$

$$\eta_m = \left(\frac{i\mu_m\omega}{\sigma_m + i\omega\varepsilon_m}\right)^{1/2} = \frac{i\mu_m\omega}{\gamma_m} \tag{3.33}$$

where γ_m (m=1,2), are the usual propagation constants: $\gamma_m^2 = i\sigma_m\mu_m\omega - \varepsilon_m\mu_m\omega^2$ and q_n can be interpreted as a reflection coefficient which determines the amplitude and phase of the secondary cylindrical waves of order n, as they are reflected from the surface of the cylinder. The secondary field is expressed as the sum of a field of linear multipoles.

The first expression for q_n is quite rigorous and depends indeed on all electromagnetic parameters (σ_m,ε_m,μ_m), whereas the second is an approximation valid when the external medium conductivity (σ_1) is small (actually – quasi-static approximation already discussed [SIN73] – when $|\gamma_1 a|$, $|\gamma_1\rho|$, $|\gamma_1\rho_0| \ll 1$). The only dependence on the external medium parameters is now via K. Under such an approximation the secondary magnetic field can be expressed as:

$$H_\rho^{(s)} = \frac{I}{2\pi}\sum_{n=1}^{\infty} q_n \frac{a^{2n}}{\rho_0^n \rho^{n+1}} \sin[n(\phi-\phi_0)]\ ,\ H_\phi^{(s)} = \frac{I}{2\pi}\sum_{n=1}^{\infty} q_n \frac{a^{2n}}{\rho_0^n \rho^{n+1}} \cos[n(\phi-\phi_0)] + H_{\phi 0}^{(s)} \tag{3.34}$$

Note that the frequency spectrum for the secondary field will in general change depending on the observation point position (different contributions from each multipole term).

For K=1 the reflection coefficients can be further simplified to:

$$q_n\big|_{K=1} = -I_{n+1}(\gamma_2 a)/I_{n-1}(\gamma_2 a) \tag{3.35}$$

If displacement currents within the cylinder can be neglected, we have: $\gamma_2 a \cong (i\sigma_2\mu_2\omega)^{1/2} a$, and considerations similar to those made in the case of a sphere apply. The first four multipole terms of q_n are shown in Figure 3.13 in the upper half for a non-ferromagnetic object and in the lower half for a ferromagnetic object with μ_r=10; they are actually similar to the previously described solution for the sphere, i.e. a sum of similar multipole terms (linear in this case). [MIL01] also notes that the two solutions "converge" for high values of μ_r.

The case n=1 corresponds to a cylinder immersed in a homogeneous field, see [WAR67] (again cylinder embedded in a homogeneous whole space), or [WAR87]. The corresponding plots are shown in Figure 3.14.

Needless to say that the measured (experimental) quantity, i.e. the voltage at the output of the receiver coil, is not directly the magnetic field, rather the (time derivative of the) integral of the magnetic field over the receiver's coil surface.

The n=0 (Monopole) Term

The $H_{\phi 0}^{(s)}$ term in Eq. (3.34) – n=0 or monopole term – was actually missing in [WAI52] (see also [WAR87]), although the general solution was correct, and in some subsequent publications. It does not appear in $H_\rho^{(s)}$. This term corresponds to a unidirectional and azimuthally symmetric

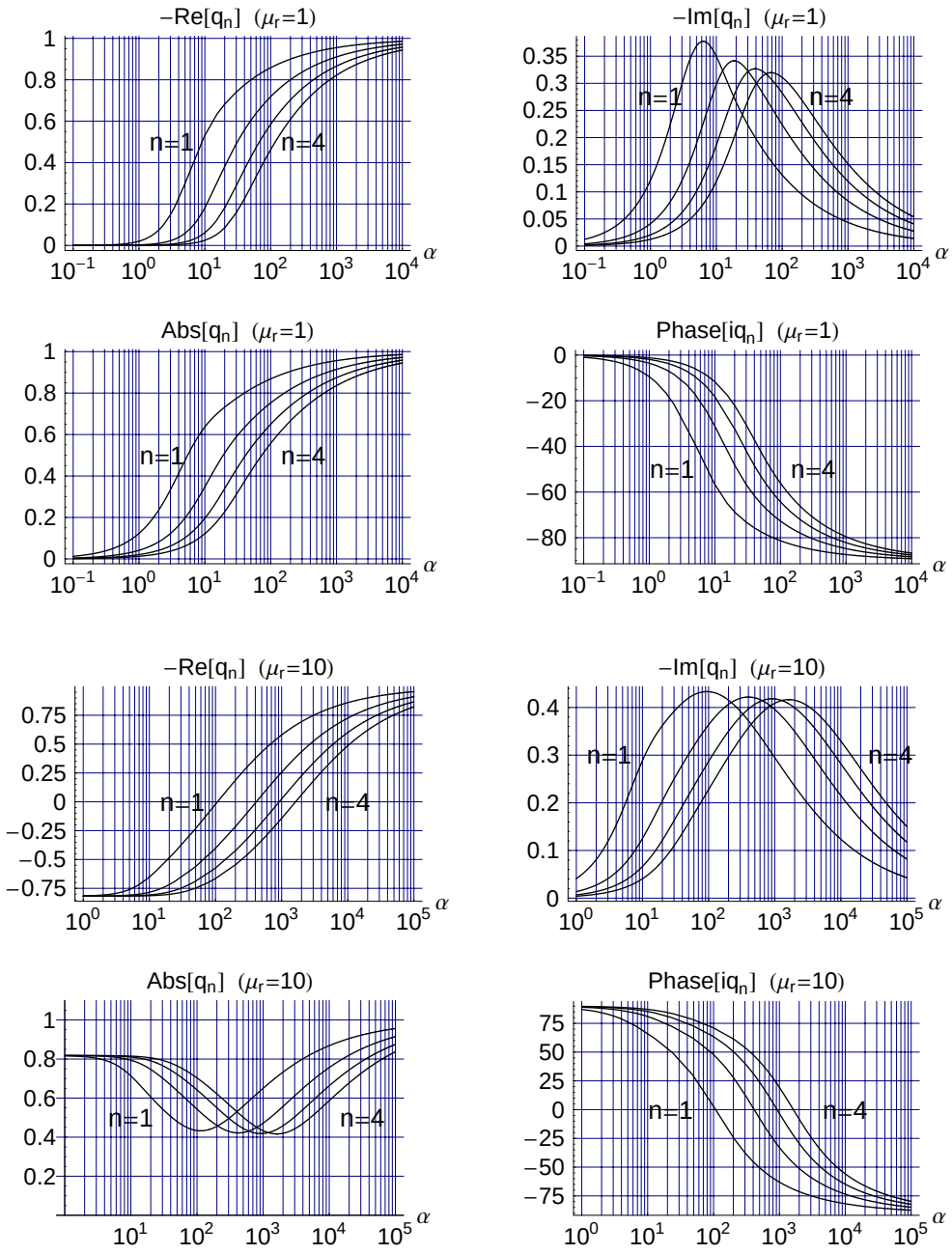

Figure 3.13: First 4 multipole expansions of the response function q_n for a non-ferromagnetic (μ_r=1, top) and a ferromagnetic cylinder (μ_r=10, bottom)

induced current, with the return current flowing from the ends of the cylinder through the external medium, which usually represents a higher impedance path with respect to the terms with n>0 (the n=1 term corresponds for example to a current loop flowing within the cylinder itself, see below[35]). Its importance has been discussed and debated in a number of references.

This term is actually not negligible for the 2D case considered (infinite cylinder and line source) [SIN73]. It is also present for finite-length cylinders and line sources [SIN74], [SIN77], although it has been proven [WAI73a], [HIL72] that its importance is reduced by the truncation of the cylinder (this last comment also applied to a point dipole source as discussed in [WAI60]; see also below). Note that it does however not arise when considering a (purely magnetic) homogenous transversal primary field (see [WAR67] or [WAR87]).

35. The higher order harmonics can also be interpreted as being fields generated by currents closed within the cylinder.

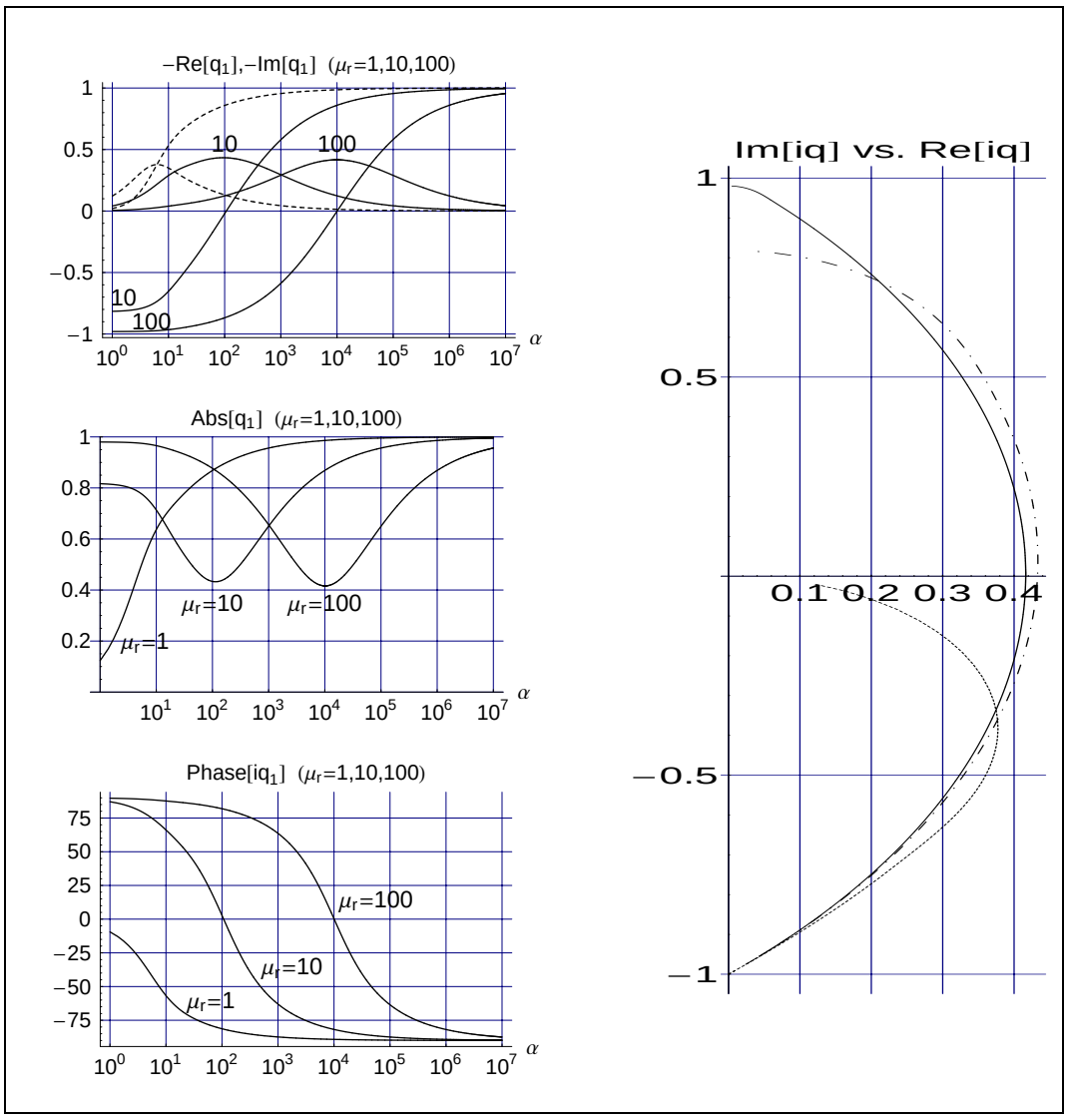

Figure 3.14: First multipole term (n=1: dipole approximation) of the response function q_n for different ferromag. cylinders as well as for μ_r=1 for comparison (dashed in top left and right plot; μ_r=10 is dot-dashed on the right).

[HIL72] analyzed its importance in the case of a perfectly conducting cylinder of finite length, looking in addition at the excitation from a long slender (rectangular) loop, approximated by two oppositely directed line sources. In the latter case they also found a reduced importance of the n=0 term (with respect to the line source only configuration), in particular when the loop approaches the object's normal (d=0).

Plots are also available in [KER60].

3.5.1.2. 2D Transversal Field

The problem of a conducting, non permeable infinite cylinder in a *general* (not necessarily homogeneous) *2D transversal magnetic field* (i.e. orthogonal to the cylinder axis) has been analyzed in [KER60], assuming a non-conductive external medium (σ_{ext}=0) and $\varepsilon=\varepsilon_0$, $\mu=\mu_0$ everywhere. The geometry is the same as in Figure 3.12 (left), without the line source obviously. The total magnetic field is represented outside the cylinder as:

$$H_\rho^{TOT} = H_\rho^{(P)} + H_\rho^{(S)} = \sum_{m=1}^{\infty} m(E_m \rho^{m-1} + I_m / \rho^{m+1}) \cos(m\varphi + \varphi_m) \tag{3.36}$$

$$H_{\varphi}^{TOT} = H_{\varphi}^{(P)} + H_{\varphi}^{(S)} = -\sum_{m=1}^{\infty} m(E_m \rho^{m-1} - I_m / \rho^{m+1}) \sin(m\varphi + \varphi_m) \tag{3.37}$$

The magnetic field corresponding to E_m (m=1,2,...) is the primary (or "external") magnetic field, developed here – in the cylinder's proximity – in power series (the ρ^{m-1} terms, with coefficients E_m). The magnetic field corresponding to I_m is the secondary (or induced, or "internal") magnetic field, which is a 2^m-pole field (see the $1/\rho^{m+1}$ terms). The relationship between E_m and I_m (for each E_m an associated I_m is given) is obtained by imposing the appropriate boundary conditions on the cylinder's surface (μ_r=1 everywhere[36]), leading to:

$$I_m\big|_{\mu_r=1} = a^{2m} \frac{J_{m+1}(\sqrt{-i\sigma\mu\omega}\,a)}{J_{m-1}(\sqrt{-i\sigma\mu\omega}\,a)} E_m \tag{3.38}$$

Eq. (3.38) has to be compared with the previous result for a line source (Eq. (3.35)), which is indeed a particular case of the 2D transversal field we are considering here. The E_m can in principle be calculated from the given primary field distribution. J_m are ordinary Bessel functions of order m.

The m=1 case corresponds again to a homogeneous primary field, the induced field being that of a 2D dipole ($1/\rho^2$ dependency). It is interesting to note that in this case the induced currents flow along the **z** direction (cylinder axis) in one half of the cylinder, and in opposite direction in the other as schematically shown in Figure 3.15, the current circuit closing at infinity. The exact internal current distribution is calculated in [KER60].

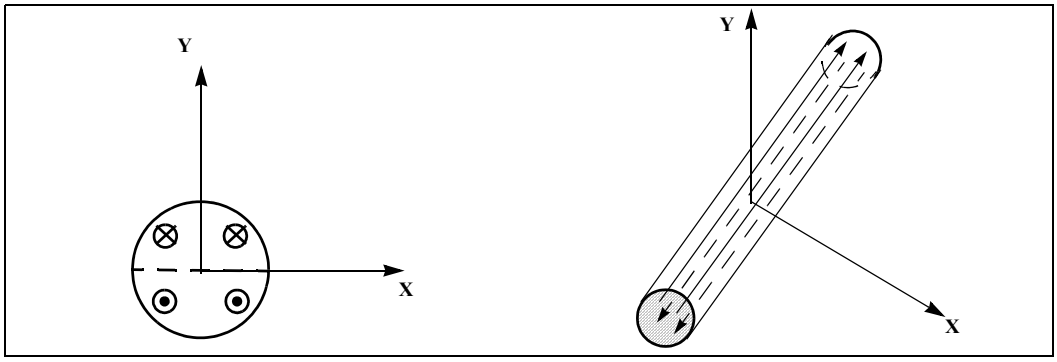

Figure 3.15: Schematic current flow in an infinite cylinder in a transversal magnetic field (for m=1).

An example is also provided for the case of a 2D dipole, which results in an infinite series of induced multipole terms (similarly to the case of a sphere in the field of a 3D dipole). It is pointed out that the induced quadrupole field is usually much smaller than the induced dipole field, given the attenuation of the corresponding primary field components at the cylinder, the reduced induction effect for m=2 with respect to m=1, and the attenuation of the induced quadrupole field at the point of observation with respect to the induced dipole field (again similarly to the case of a sphere in the field of a 3D dipole). The current and magnetic field distribution inside the cylinder are also calculated.

3.5.1.3. Dipole Source (approximate 3D problem)

[WAI60] has also analyzed the (3D) problem of an infinite circular horizontal cylinder excited by an arbitrarily located magnetic dipolar source, in particular when the source and the receiver are in the equatorial plane. In the latter case an approximate solution is available, at low frequency

36. Actually K=1, similarly to what seen before.

and for a small cylinder (small radius), consisting again of a multipole expansion whose response functions are identical to the q_n of the 2D case described above (see Eq. (3.32)). It can also be shown that under the previous assumptions the relative response decreases rapidly with increasing value of the "mode "number" n. This geometry is also treated in detail in [KAU01, §3.11].

3.5.1.4. Longitudinal Magnetic Field

When the uniform magnetic field is parallel to an infinite horizontal cylinder, ring currents are induced in it and there is an anomalous internal field distribution; however, if $k_{ext}^2 \cong 0$ the secondary fields are null everywhere outside the cylinder [WAR67], [WAR87]. This is obviously not the case for a cylinder of finite length.

NdT Applications

Concerning NdT applications, the theory of encircling coils and solenoids for tubes and bars (ideally of infinite length – end effects are neglected) is well established [McM86], [LIB71], [VUI94], [BLI97]. In the case of ideal solenoidal coils the primary field is homogeneous throughout the cross section and confined within the solenoid itself. This setup is not of direct practical application to the scenario we are considering, and is considered separately in A3.2 for the case of a cylindrical test bar (i.e. a full cylinder). What will be noted here is that the behaviour of the solution for a non-ferromagnetic bar is actually quite similar to the dipole term of a sphere [FOR86b]. The case of ferromagnetic bars is on the other hand quite different, as here the induced voltage is simply multiplied by the relative permeability μ_r (for large μ_r).

Solutions, expressed in terms of the vector potential, are also available in the case of *circular* coaxial (delta-function) *coils* (single coils, not a solenoid) encircling a coaxial infinite (full) cylinder. These are again reported in A3.2.

3.5.2. (Permeable) Finite Length Cylinders – a Semi-Quantitative Approach

The previous analytical models have been complemented in a semi-quantitative way in the case of elongated ferromagnetic objects such as short cylinders, for which demagnetization effects can be and are relevant.

"Short Parts" in NdT

Results for spherical bodies, of practical importance in NdT of short production test parts, have already been discussed. These exact results can actually be related in a semi-quantitative way [FOR86b] to those for other short production parts, such as cylinders, for which (demagnetization) end effects can become important (see also [STA86]).

Indeed, whereas the case of a non-ferromagnetic sphere approximates the situation of short non-ferromagnetic test objects, important differences do usually arise for ferromagnetic targets. In the latter case the magnetization is usually not uniform over the object length, decreasing towards the ends (in the case of an elongated object whose axis is aligned with the field axis) as a result of demagnetization effects[37]. The latter can be described by a **demagnetization factor** N_d, which depends mainly on the object shape (N_d is not highly dependent on the material's magnetic properties). In practice the object behaves as if it had an *apparent permeability* μ_{app} rather than its true permeability μ_r.

37. Certain elliptical shapes, for which the demagnetization field can be made homogenous, represent an exception.

The Apparent Permeability

The complex plane response curves of ferromagnetic objects of different shapes can be described in semi-quantitative terms by assuming that they behave essentially the same way at the inductive limit (e.g. for increasing frequency), whereas they strongly depend on the apparent permeability at the resistive limit, where magnetization effects dominate. In other words, the response curves in the complex plane are supposed to maintain a similar shape, starting however from a point $(0,\mu_{app}-1)$[38] at the resistive limit which changes according to the object's shape, size and relative permeability μ_r. At the inductive limit they all converge to (0,–1) (compare for example with the complex plane plots in Figure 3.11 and Figure 3.14).

In general, the apparent permeability μ_{app} shown by short parts of high permeability ($\mu_{rel} >> \mu_0$) can be written as[39]:

$$\frac{1}{\mu_{rel}} = \frac{1}{\mu_{app}} - N_d \Rightarrow \mu_{app} = \frac{\mu_{rel}}{N_d \mu_{rel} + 1} = \lim_{\omega \to 0} |\chi| + 1 \tag{3.39}$$

In the case of an elongated object whose **axis is aligned with the field axis** the demagnetization factor N_d tends to 0 for increasing axial ratios (long axis/short axis), i.e. increasing elongation, in which case μ_{app} approaches μ_{rel}:

$$N_d \to 0 \Rightarrow \mu_{app} \to \mu_r \text{ (increasing elongation)} \tag{3.40}$$

In the opposite case of highly permeable (μ_{rel}>100 say) but "short" objects (N_d>0.05 say), corresponding to small axial ratios, demagnetization effects are important and the apparent permeability becomes smaller. Eq. (3.39) simplifies to:

$$\mu_{app} \cong \frac{1}{N_d} \text{ (short, highly permeable parts)} \tag{3.41}$$

In this case N_d dominates. Examples of situations in which this applies include the following:

- *Sphere*: $N_{d,sph}$=1/3 and therefore, for high permeability, μ_{app}=3 (as implicitly already obtained in §3.4.5.2), independent of the actual value of μ_r!
- For *short cylinders* with length L_{cyl} and diameter D_{cyl}, *whose axis is parallel to the coil axis*, we have [FOR86b] $N_{d,cyl}$=3.4/(4π) for L_{cyl}/D_{cyl}=1, which means μ_{app}=3.7, whereas:

$$\mu_{app}^{cyl} \cong 6\frac{L_{cyl}}{D_{cyl}} - 5 \text{ for } 2<L_{cyl}/D_{cyl}<10 \tag{3.42}$$

  again independent of the actual value of μ_r.
- For *prolate ellipsoids with fields applied parallel to the long axis* and ratios of major (L_e) to minor diameter (D_e) between 1 and 10, the apparent permeability can be approximated as $\mu_{app,ell}=3L_e/D_e$. This compares favourably with the curves for μ_1/μ=100 in [BRA01].

The increase in apparent permeability with increasing object length, actually approaching the relative permeability as described by Eq. (3.40) ($\mu_{app} \to \mu_r$), can be interpreted in terms of the demagnetizing influence of the cylinder ends being diminished [FOR86b]. Under this assumption the apparent impedance curves tend to approach the curves for an infinitely long, solid cylinder discussed in A3.2, and are quite different in the low frequency part from the curves of a sphere or of a cylinder in a transversal magnetic field, for which μ_{app} is basically limited.

38. The –1 term is necessary due to a slight difference in the position of the complex (impedance) plane curves at the inductive limit ((0,0) in NdT, (0,–1) in our case).
39. We have used here SI units following [STA86], rather than [FOR86b]. Eq. (3.39) is basically equivalent to Eq. (7) in [MIL01] apart from the factor –2/3.

It is also important to note that in the case of short cylinders with **axis perpendicular to the coil axis**, the apparent permeability decreases from 3.7 to 2.0 for L_{cyl}/D_{cyl}=1 (because $N_{d,cyl}$=1/2), which points to the sensitivity to the object's orientation in the case of ferromagnetic targets.

Some recent quantitative results are available in [BRA01], whereas [CAR01] provides an interpretation in terms of natural (resonating) modes, which we will briefly discuss in §3.6.3, and associates them to dipole and higher order magnetic moments. When reasoning in terms of modes the variation of the response of a ferromagnetic cylinder with orientation can be interpreted as either being due to the excitation of a different set of modes, or to changes in the coupling coefficients, or both.

3.5.3. Finite Length Cylinder in the Field of a Parallel Finite Line Source

As an example of a configuration which has been solved analytically, and to illustrate the resulting complexity, we will have a look at the problem of a cylinder of electrical properties (σ,μ) and finite length *2s*, excited by a symmetrically located axial current filament (also of finite length, equal to *2l*, and traversed by a current *I*) and embedded in a homogenous medium of electrical properties (σ_0,μ_0). This has been treated in [WAI73b] (see Figure 3.16).

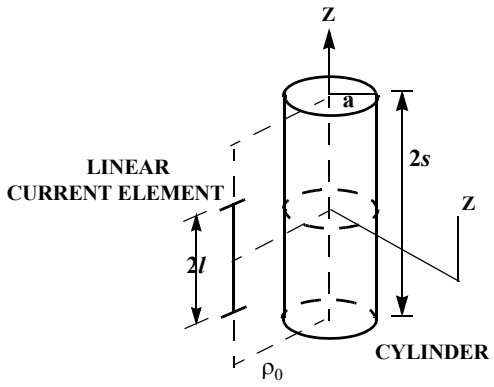

Figure 3.16: Geometry for the calculation of the response of a finite length cylinder in the field of a parallel linear current element (adapted from [WAI73b]).

The end conditions are that the total normal current density is zero, which should tend to be satisfied by a thin and highly conducting body. The secondary fields in the plane z=0 are, for ρ>a (a time factor $e^{i\omega t}$ is used, and omitted as usual):

$$H_\phi^{(s)} = \frac{I}{\pi}\sum_{m=-\infty}^{\infty}\sum_{n=0}^{\infty}\Lambda_{m,n}\frac{K_m(u_n\rho_0)}{K_m(u_n a)}I_m(u_n a)K_m'(u_n\rho)u_n e^{-im(\phi-\phi_0)}\frac{\sin(\lambda_n l)}{\lambda_n s}, \tag{3.43}$$

$$H_\rho^{(s)} = \frac{I}{\pi\rho}\sum_{m=-\infty}^{\infty}\sum_{n=0}^{\infty}\Lambda_{m,n}\frac{K_m(u_n\rho_0)}{K_m(u_n a)}I_m(u_n a)K_m(u_n\rho)ime^{-im(\phi-\phi_0)}\frac{\sin(\lambda_n l)}{\lambda_n s} \tag{3.44}$$

where the coefficients $\Lambda_{m,n}$ (n=0,1,2,...) replace the q_n reflection coefficients (response functions) previously introduced in the case of an infinite cylinder (Eq. (3.32)). In the inductive limit, for example in the case of a perfectly conducting cylinder, Λ_m=1. In detail:

$$\Lambda_{m,\,n} = \frac{\left[\frac{\gamma}{v_n\eta}\frac{I_m'(v_n a)}{I_m(v_n a)} - \frac{\gamma_0}{u_n\eta_0}\frac{I_m'(u_n a)}{I_m(u_n a)}\right]\left[\frac{\gamma\eta}{v_n}\frac{I_m'(v_n a)}{I_m(v_n a)} - \frac{\gamma_0\eta_0}{u_n}\frac{K_m'(u_n a)}{K_m(u_n a)}\right] + \left(\frac{1}{v_n^2} - \frac{1}{u_n^2}\right)^2\left(\frac{m\lambda_n}{a}\right)^2}{\left[\frac{\gamma}{v_n\eta}\frac{I_m'(v_n a)}{I_m(v_n a)} - \frac{\gamma_0}{u_n\eta_0}\frac{K_m'(u_n a)}{K_m(u_n a)}\right]\left[\frac{\gamma\eta}{v_n}\frac{I_m'(v_n a)}{I_m(v_n a)} - \frac{\gamma_0\eta_0}{u_n}\frac{K_m'(u_n a)}{K_m(u_n a)}\right] + \left(\frac{1}{v_n^2} - \frac{1}{u_n^2}\right)^2\left(\frac{m\lambda_n}{a}\right)^2} \tag{3.45}$$

The variables just used are as follows (γ, γ_0 are the usual propagation constants, written here neglecting displacement currents, for the cylinder and the surrounding medium respectively):

$$u_n = (\lambda_n^2 + \gamma_0^2)^{1/2}\ ,\ v_n = (\lambda_n^2 + \gamma^2)^{1/2}\ ,\ \lambda_n = (2n+1)\frac{\pi}{2s} \tag{3.46}$$

$$\gamma = (i\sigma\mu\omega)^{1/2}\ ,\ \gamma_0 = (i\sigma_0\mu_0\omega)^{1/2}\ ;\ \eta = \frac{i\mu\omega}{\gamma}\ ,\ \eta_0 = \frac{i\mu_0\omega}{\gamma_0} \tag{3.47}$$

Note that in the quasi-static approximation ($|\gamma_0 a|$, $|\gamma_0\rho|$, $|\gamma_0\rho_0| \ll 1$) u_n can be replaced by λ_n everywhere. However, unless $|\gamma a|$ is also small, the form for v_n must be retained. Also, the previous equations for the magnetic field components reduce to the ones for an infinite cylinder in the field of a line source (Eq. (3.30), Eq. (3.31)) when *l* and *s* tend to infinity. An interpretation in terms of natural (resonating) modes is again possible (§3.6.3), but we will not enter here into further details.

Numerical results of the resultant magnetic field are shown in [WAI73b], in the quasi-static limit, for a perfectly conducting cylinder. In this case the results (i.e. the spatial behaviour of the induced magnetic field in the proximity of the cylinder) depend significantly on the cylinder length, although the overall curve shapes (finite vs. infinite) are similar.

[HIL72] also considered the case of a perfectly conducting cylinder of finite length, looking in addition at the excitation from a long slender (rectangular) loop, approximated by two oppositely directed line sources.

3.6. Other Target Models

A number of other models, more specific to UXO/demining applications, have also been devised. They bear partial similarities with what discussed so far, which has been mostly derived in the context of geophysical applications. These models will be discussed in the following.

3.6.1. The Induced Dipole Model

For compact objects sufficiently far from the sensor, the response can be represented in terms of an *induced dipole moment* at the target location [BAU98, BEL01a, BEL01b, SOW98a] (the target is effectively concentrated at a point), which is related in a linear way to the primary field by a frequency-dependent 3×3 *magnetic polarizability tensor* $A(\omega)$. The latter fully characterizes the target's EMI (electromagnetic induction) dipole response, apart from possible nondipole effects; V is the object's volume. The model assumes a uniform primary field and higher order effects are neglected.

The induced dipole moment $\mathbf{m}(\omega)$ can therefore be expressed, at a frequency ω, as function of the primary field $\mathbf{H_T}$ as (omitting the usual factor $\exp(i\omega t)$):

$$\boldsymbol{m} = V\boldsymbol{A}\boldsymbol{H}_T \tag{3.48}$$

The tensor's elements α_{jk} (j,k=1,2,3) are dimensionless and depend on the target's electrical properties, shape and orientation in the primary field, but not on its volume. They are actually complex numbers, reflecting the well known frequency-dependent phase shift between primary and induced magnetic field. A similar model is also discussed in [WES87] in the context of geophysical applications.

For a pulsed sensor (time domain operation) the induced dipole moment $\mathbf{m}(t)$ can be expressed as a convolution of the Fourier transform of $V\alpha_{jk}(\omega)$ with the primary field waveform $\mathbf{H}(t)$. In terms of components:

$$m_j(t) = V\int \hat{\alpha}_{jk}(t-u)H_k(u)du \quad \text{where} \quad \hat{\alpha}(t) = \int \alpha(\omega)\exp(-i\omega t)d\omega \tag{3.49}$$

The quantity $\mathbf{A}(t)$ is in this case an effective polarizability obtained from the convolution of the magnetic polarizability tensor $\mathbf{A}(\omega)$ with the transmit waveform.

$\mathbf{A}$ is symmetric and can therefore be diagonalized by an appropriate rotation of the coordinate system:

$$\boldsymbol{A} = U\Lambda U^T \tag{3.50}$$

where U is a transformation matrix between the coordinate system of the sensor and the primary axes of the object. The polarizability tensor's **eigenvalues** $\alpha_i(\omega)$ correspond to *the responses that are induced when the primary field is aligned in turn along each of the principal axes of the object.*

In the limit $\omega \to 0$ demagnetization effects prevail and the induced dipole moment, and therefore the product $V\mathbf{A}\mathbf{H}_T$, must reproduce the static magnetic moment of the object. It can indeed be shown that $\mathbf{A}(0)$ can be expressed in terms of the object's permeability and of its demagnetization tensor (for details see [BEL01b]).

Note that the dipole model is not synonymous with "simple" spatial behaviour. Indeed, the response at any orientation is a linear combination of responses associated with each principal axis, and the total induced magnetic moment $\mathbf{m}$ is therefore not necessarily aligned with $\mathbf{H}_T$. This can be clearly seen in the following simplified expression of the induced dipole moment, which is often used for cylindrical objects:

$$\boldsymbol{m} = \boldsymbol{m}_L + \boldsymbol{m}_T = \alpha_L \boldsymbol{H}_L + \alpha_T \boldsymbol{H}_T \tag{3.51}$$

where *L* stands for Longitudinal (along the symmetry axis) and *T* for Transversal (perpendicular to the symmetry axis). This is equivalent to use the following polarizability tensor (diagonalized form):

$$\boldsymbol{A} = \begin{bmatrix} \alpha_L & 0 & 0 \\ 0 & \alpha_T & 0 \\ 0 & 0 & \alpha_T \end{bmatrix} \tag{3.52}$$

This applies also to ordnance items (UXO), which are mostly axisymmetric; two of the eigenvalues are therefore degenerate (in other words, only two eigenvalues are unique). Irregular objects tend on the other hand to have different responses in three orthogonal directions.

Induced Voltage

The induced dipole moment **m** can be used to calculate the induced flux $\Phi^{(s)}$ through the receive coil, whose time derivative gives then the induced voltage; the latter is therefore proportional to $-\partial \boldsymbol{m} / \partial t$ [BEL01a].

The voltage induced in the receive coil can also be calculated using reciprocity arguments (see [DAS90, DAS91] for details), leading to the following expression:

$$V^{(s)} \propto \boldsymbol{H}_T \cdot \boldsymbol{A} \cdot \boldsymbol{H}_R \tag{3.53}$$

where $\mathbf{H}_T$ is the primary field at the location of the target, and $\mathbf{H}_R$ is the (hypothetical) incident field which would be generated by the receiving coil IF it were used as a transmitter. This type of approach is often used to calculate a target's spatial signature.

Non-dipole Effects

Non-dipole effects can arise due to the fact that real objects have a finite size and that the primary fields are not uniform (existence of primary field gradients, for example for an elongated object placed along the detector's axis), or because the target response contains higher order multipole contributions. Examples are provided in [BEL01a].

In typical humanitarian demining scenarios most of the targets are small and probably well approximated by the dipole model; non-dipole behaviour is more likely to be due to **composite objects**, made up either of different parts or of separate pieces altogether.

A practical application is likely to have to be coupled to a precise positioning system, and will obviously have to cope with the soil response when this becomes important.

Where all conditions are met the dipole model should however be capable of producing interesting results, due in particular to the possibility of recovering the target's response along each of its principal axes.

3.6.2. Simple Parametric Response Models

A number of simple parametric models, more sophisticated than the circuit model presented in §3.1, have been proposed to describe the response of certain targets or target classes. They are usually valid when the primary field is aligned with a principal axis.

A simple generalization of the basic response for spheres and infinite cylinders, which according to the authors [BEL01a] does a fairly good job of fitting the EMI spectra of many compact object, especially **highly permeable** ones, is reported in Eq. (3.54). The model has been synthesized

from empirical studies of the EMI response of ordnance and clutter.

$$S(\omega) = A\left\{ s + \frac{(i\omega\tau)^c - 2}{(i\omega\tau)^c + 1} \right\} \tag{3.54}$$

The model's four parameters are an amplitude A, a response time constant τ, a factor c that determines the width of the spectrum, and a factor s that determines the relative magnitude of the asymptotic responses at high and low frequencies. This model is constructed so that it can reproduce the analytical solutions for a wire loop, and for a highly permeable sphere and an infinite cylinder[40]. Problems are on the other hand encountered for composite objects, i.e. objects made up of two or more distinct parts with different properties (the 20 mm projectile whose data we will discuss in Chapter 5 represents such a target).

Multiaxis Response

As the sensor moves over the target, the latter is in fact illuminated from different directions (different primary field patterns); different combinations of eigenvalues determine therefore the measured signal, as will be extensively detailed in Chapter 5.

If the measurement positions are accurately known it is however possible to recover the polarizability tensor (and the target's position, which is obviously unknown as well), either in the time or in the frequency domain, by fitting the measured response with the dipole model described in §3.6.1.

The polarizability tensor can then be diagonalized to obtain its eigenvalues $\alpha_i(\omega)$ (if working in the frequency domain), i.e. the response along each of the target's principal axes[41]. The eigenvalue spectra can then be fitted using for example Eq. (3.54) with a different parameter set for each of the principal axes [BEL01b]. This type of approach – exploiting an object's EMI spectral signature – has also been termed "*EMI Spectroscopy*". It is detailed in [WON01] for mines in air at a fixed orientation, and in [NOR01] for UXO using a set of "library spectra" and a linear and non iterative procedure. EMI mine spectra obtained in the laboratory have also been previously discussed by [TRA97], who obtained interesting results for objects with some metallic content such as a PMN.

Alternative approach to the exploitation of the eigenvalue distribution are obviously possible, the target discrimination capability depending in general on the extent to which the eigenvalue distributions of target and clutter do not overlap [BEL01a].

3.6.3. Natural (Resonating) Modes

The theoretical justification for the use of simple parametric models similar to Eq. (3.54) is in the prevalence of a few dominant *modes* [BEL01a] in the target's response. [BAU98] provides indeed a theoretical basis for modelling EMI responses in terms of *poles*[42] which are characteristic of the target, each having a constant (resonant) frequency and an amplitude (excitation strength) which depends on target orientation in the primary field. This is also referred to as the Singularity Expansion Method (SEM) representation, and *is not dissimilar to what discussed in §3.3.3, when we looked at the general form of an object's EM response for large objects.*

40. A simpler three-parameter model with c=1/2 is actually sufficient in most cases [BEL01b, MIL01].
41. In this way we have effectively removed the orientation dependence, if any.
42. These poles are situated along the imaginary axis of the complex frequency plane. Such purely imaginary resonant frequencies do therefore correspond to exponential decays in the time domain systems, having assumed an exp(iωt) time dependency [CAR01].

[GEN99] discusses in detail these *natural modes*, or *natural resonances*, which result in the time domain in a late-time response characterized by the sum of nearly purely damped exponentials, with the damping constants strongly dependent on target shape, conductivity and permeability. The general concept is specialized to body of revolution (BOR) type objects, comparing measurements with data calculated using the theory of cavities or dielectric resonators. [CAR01] extends these results to the response of finite-length cylinders and rings, possibly ferromagnetic; the resulting modes are interpreted in terms of dipole and higher order magnetic moments and a simple and accurate model is provided to compute their resonant frequencies.

It is possible to extract the poles from experimental data, usually a few being sufficient (two or three maximum), when not just one, to obtain good fitting results, and to attempt target classification by matching them against a library of responses. This procedure has also been called Magnetic Singularity Identification (MSI). Such an approach has been pursued by a number of researchers, amongst them [MER99, MER00, RIG01, SOW95, SOW99], and is critically analysed in [TAN01]. Detailed time-decay data is also shown for a variety of mines in [NEL01], which does not address the classification issue; it does however take into account soil effects, in particular on the response of minimum-metal mines. [MER00] stresses also the pole's sensitivity to environmental and historical factors, and suggest to put more emphasis on structural information contained in the polarizability tensor, such as symmetries and/or typical ratios of elements.

Finally, let us point out that the fact of being able to calculate resonant frequencies does obviously not mean that the overall target response can be calculated as well (the excitation strengths have to be known).

3.7. A Note on Induction vs. Galvanic Currents

Induction currents correspond to the usual eddy currents (largely confined to the target), which are generated in direct response to a time-varying magnetic flux cutting across the conductor.

There is however another class of effects which have in principle to be considered in electromagnetic induction, namely *galvanic* effects, which are associated with the accumulation of electric charges on the surface[43] of conductors (i.e. at their interface). They are included in the solutions discussed so far, even if we have not mentioned them explicitly.

Galvanic effects do not play a role in some scenarios of common interest, such as in the case of objects embedded in an *insulating medium* ($\sigma_{ext}=0$):

- *Sphere* in a *uniform magnetic field*: the radial component of the primary electric field is zero; therefore no electrical charge is formed [KAU01, §3.1].
- *Cylinder* in a *uniform magnetic field* perpendicular to the cylinder axis (cylinder elongated in the direction of the primary electrical field): electrical charges build up on the edges and on the surfaces near the edges. The influence of edge effects will however decrease progressively with increasing cylinder length and/or increasing distance of the observation point [KAU01, §3.6].
- *Sphere* in the field of an *arbitrarily oriented magnetic dipole*: the primary (vortex) electric field $\mathbf{E}_{prim}$ (accompanying $\mathbf{H}_{prim}$) does in general intersect the surface of the conductor, and therefore surface electrical charges will appear. The basic characteristics of the FD and TD responses (induced magnetic field) are however the same as obtained for the situation with axial symmetry [KAU01, §3.10].

The situation is somewhat more complicated in the case of objects embedded in a *conducting full-space* ($\sigma_{ext}>0$), for example:

- *Cylinder in the field of a parallel line source*: as we have seen (§3.5.1.1) the secondary field can be expressed as a sum of cylindrical harmonics. Those of higher order ($n\geq1$) correspond to the vortex part of the field, and are generated by currents closed within the cylinder. The fundamental, or $n=0$ component (monopole), corresponds to the galvanic part of the field, and is due to linear current closed within the host medium.
- *Sphere* in the field of an *arbitrarily oriented magnetic dipole*: $\mathbf{E}_{prim}$ flowlines cross the sphere, and therefore electrical charges do arise on its surface. Mathematically speaking this translates into secondary fields expressed in terms of potentials of the electric and magnetic type, corresponding respectively to TM_r and TE_r modes (radial Transverse Magnetic and Transverse Electric modes). The source of the second are the "usual" vortex-type induced currents in the target, the source of the first is the presence of charges and currents in both the target and host [KAU01, Chapter 6].

  Under certain conditions a secondary field is produced, which is equivalent to that produced by the combination of a magnetic *and* an electric dipole located at the origin of the model.

Conducting Full-Space: Axial Symmetry Geometry

The case of a *spheroidal object in the field of a horizontal loop, whose centre is on an object's axis of symmetry* (conductivity σ_i, radius a) represents a scenario of particular interest for the geometries we might be confronted with (Axial Symmetry). In this case the normal electrical field (i.e. the sum of the primary field and of the field generated by currents induced in the host medium) does not intersect the surface of the conductor. Therefore no surface electrical charges appear [KAU01, §5.2], and the only source for the secondary field will be vortex currents.

43. Within each piece of a piece wise uniform medium the volume density of charge is zero [KAU01,§2.5].

Axial Symmetry and the Effects of Induced Currents in the Host Medium

We will briefly point out here that for the geometry just discussed (axial symmetry, spheroidal object), if

$$\frac{\sigma_i}{\sigma_e} \gg 1 \quad \text{and} \quad |k_e a| \ll 1 \tag{3.55}$$

the current density in the spheroid will not depend strongly on the conductivity of the external medium [KAU01, §5.3], and *the secondary fields will therefore be similar to the free space ones*. In this case *the total scattered fields can be calculated adding the contribution due only to the currents in the host medium (no conductor present) to the contribution due only to the currents in the conductor situated in free space.*

This is a priori not guaranteed, i.e. in general the total response is not necessarily equal to the sum of the response of the host medium and of the anomalous conductor taken separately. They respond jointly [NAB91,p.32], similarly to what happens for two closely coupled conductors; for example, secondary currents can arise in the host medium due to the (induced) currents in the target.

The first condition in Eq. (3.55) is practically always satisfied in the scenarios of interest to us (high conductivity contrast), the second, which implies that there is no phase shift in the normal field (i.e. primary plus host!) within the area occupied by the spheroid, is discussed in more detail in §3.4.2.

Conducting Full-Space: General Geometry

For a general geometry one has in principle to take into account the galvanic part of the secondary field as well (also referred to as "*channelling*", or "current gathering" – see [SPI84] for a precise definition), which is due to the presence of charges and currents that flow in both the target and host.

The galvanic part is related to the properties of conductors in a different way than the vortex part, and *can very well represent the dominant contribution in scenarios of geophysical interest*, depending on the type of excitation, the frequency (or time), geometric factors, etc.

[WAL92] reports criteria to estimate the importance of inductive vs. galvanic contributions, for a thin vertical plate model, using a vertical magnetic dipole over a half-space. Applied to objects of interest to us and at the usual soil conditions and operating frequencies, induction effects should dominate for small objects as well as for UXO, with the possible exception of very large objects in high-conductivity soils. For a standard "blast" mine this should anyhow not be a problem, as its metallic parts are mostly isolated from the host medium. Also, the coincident loop configuration does apparently minimize galvanic effects [EAT87]. We will therefore not consider galvanic contributions in the following.

3.8. Conclusions

A number of analytical solutions to some basic eddy current forward problems of interest to us have been detailed in this chapter, with emphasis on the analysis of the **response function** and the operating conditions prevailing in humanitarian demining. The results for the case of the sphere are for example summarised in §3.4.6 and will not be repeated here.

While analytical solutions can not cover with precision a large number of scenarios, they have represented an excellent tool to gain general insight into the physics of the scattering process and its dependence on the model's parameters. They have been complemented in a semi-quantitative way for elongated ferromagnetic objects such as short cylinders, for which demagnetization effects are important (§3.5.2).

In addition the study of the **general form of an object's EM induction response** (§3.3) has allowed to confirm that these solutions are more general in nature, and to understand how they depend on the target's response parameter, and its magnetic permeability in particular. The **general form of the response parameter**, which can be obtained via dimensional analysis, is also noteworthy (§3.3.1).

As has also been stressed by others, e.g. in [SOW95,TRA97,KEI98,WON98,SOW98a, CAR99,SZY99], and in [BRU98a,BRU99b], this theoretical analysis and other similar approaches indicate the possibility of **distinguishing** between different objects (e.g. ferromagnetic vs. non-ferromagnetic), and point to the possibility of *identifying* some metallic objects based on their characteristic phase response, as already implemented up to a certain level for other applications.

In addition, the phase shift of the received signal turns out to be a continuous, monotonically decreasing function of the object size[44] (all other parameters being kept constant). This leads to the idea of a **coarse classification** based on target *size* (actually the response parameter, see §3.3.1 and §6.3), and/or of discriminating large objects by imposing a "phase threshold", in order to reduce the amount of detected clutter when operating in certain scenarios.

This **discrimination**-based approach is less ambitious than object identification, but should be more robust, which is of fundamental importance in humanitarian demining tasks, at least for general applications. In fact some think that even a reduction of the false alarm rate of a metal detector by a factor of 2 or 3 would be highly beneficial, obviously without compromising the detection efficiency. This approach is likely to work when looking for metallic objects of a certain size, such as those contained in non minimum-metal mines (e.g. the PMN or PMN2) or UXO, and when the clutter is mostly represented by small and/or poorly conductive metallic objects.

The theoretical analysis has also allowed us to identify a few likely problems (§3.3.3), such as the presence of *composite object* (§3.3.4) with a potentially complex response function, of *elongated ferromagnetic object* (§3.5.2), and the fact that the target's response can well be orientation dependent. Higher order multipole terms (§3.4.4) are on the other hand less likely to represent a problem in humanitarian demining scenario (they might when larger UXO are present).

Attention has also been drawn to certain second order effects, such as *galvanic contributions* well known in geophysical applications (§3.7); they should in general not be relevant for the applications of interest to us, with the possible exception of very large objects in high-conductivity soils. For a standard "blast" mine this should anyhow not be a problem, as its metallic parts are mostly isolated from the host medium.

44. Concerning applications similar to the one of interest to us, the use of a large phase difference between large metallic targets such as mines and low-conductivity magnetic nuisance items has already been detailed in [ROS48]. More recently it has been suggested in [BEL94, BAR96] to exploit the phase dependence for the characterisation of UXO, to obtain a very rough indication of the object size.

We have then briefly investigated the *interaction between the target and the host medium* in the form of a full space (the response of the host medium by itself will be the subject of Chapter 4). It is indeed often implicitly assumed that the two decouple (are additive) and this is probably an excellent approximation in most situations, with the possible exception of high conductivity soils towards the higher frequency end (see Eq. (3.55)), but strictly speaking it is not guaranteed a priori.

This chapter and the next set the **theoretical framework**. Experimental results will be then detailed in Chapter 5 and quantitatively analysed in Chapter 6; they will also be compared with some of the models' expectations. Initially unforeseen features will in fact result from the study of the experimental data, and we will come back when necessary to the models to study their behaviour. We will comment on the effectiveness and feasibility of the *discrimination*-based approach at the end of these chapters.

Some of these results have obviously already been known for a certain time, but to the best of our knowledge not necessarily in this form by those involved with metal detection systems applied to humanitarian demining needs. We therefore see added value in having put together this information in a coherent way, with emphasis on humanitarian demining specificities, and in having moved beyond the simple circuit (§3.1) and sphere approach.

Bibliography

[BAR96] B. Barrow, N. Khadr, R. DiMarco, and H. H. Nelson, "The Combined Use of Magnetic and Electromagnetic Sensors for Detection and Characterization of UXO", *Proc. Symposium on the Application of Geophysics to Engineering and Environmental Problems SAGEEP'96*, Keystone, CO, 1996.

[BAU98] C. E. Baum (Ed.), *Detection and Identification of Visually Obscured Targets*: Taylor & Francis, New York, 1998.

[BEL94] T. Bell, R. DiMarco, and B. Barrow, "UXO Signature Classification and Discrimination", in *Proc. Unexploded Ordnance Detection and Range Remediation Conference* (May 17-19, 1994, pp. 321-331).

[BEL01a] T. H. Bell, B. J. Barrow, and J. T. Miller, "Subsurface Discrimination Using Electromagnetic Induction Sensors", IEEE Trans. on Geoscience and Remote Sensing, vol. 39, no. 6, pp. 1286-1293, June 2001.

[BEL01b] T. Bell, B. Barrow, J. Miller, and D. Keiswetter, "Time and Frequency Domain Electromagnetic Induction Signatures of Unexploded Ordnance", Subsurface Sensing Technologies and Applications, vol. 2, no. 3, pp. 153-175, July 2001.

[BLI97] Blitz, J., 1997, Electrical and Magnetic Methods of Non-destructive Testing: Chapman & Hall, London, UK.

[BRA01] H. Braunisch, C. O. Ao, K. O'Neill, and J. A. Kong, "Magnetoquasistatic Response of Conducting and Permeable Prolate Spheroid Under Axial Excitation", IEEE Transactions on Geoscience and Remote Sensing, v. 39, no.12, pp. 2689-2701, Dec. 2001

[BRU98a] C. Bruschini, B. Gros, F. Guerne, P.-Y. Pièce, and O. Carmona, "Ground penetrating radar and imaging metal detector for antipersonnel mine detection", *J. of Applied Geophysics* **40**, pp. 59-71, 1998.

[BRU99b] C. Bruschini, "Metal Detectors for Humanitarian Demining: from Basic Principles to Modern Tools and Advanced Developments", in *Proc. MINE'99 (Mine Identification Novelties Euroconference)*, pp. 24-30, Florence, Italy, October 1-3, 1999. Available from http:// diwww.epfl.ch/lami/detec/.

[CAR99] L. Carin, I. J. Won, and D. Keiswetter, "Wideband frequency- and time-domain EMI for mine detection", in *SPIE Proceedings Vol. 3710*, pp. 14-25, Orlando, FLA, April 1999.

[CAR01] L. Carin, *et al.*, "On the Wideband EMI Response of a Rotationally Symmetric Permeable and Conducting Target", IEEE Trans. on Geoscience and Remote Sensing, vol. 39, no. 6, pp. 1206-1213, June 2001.

[DAS90] Y. Das, J. E. McFee, J. Toews, and G. C. Stuart, "Analysis of an Electromagnetic Induction Detector For Real-Time Location of Buried Objects", IEEE Trans. on Geoscience and Remote Sensing, vol. 28, no. 3, pp. 278-288, May 1990.

[DAS91] Y. Das, and J. E. McFee, "A Simple Analysis of the Electromagnetic Response of Buried Conducting Objects", IEEE Trans. on Geoscience and Remote Sensing, vol. 29, no. 2, pp. 342-344, March 1991.

[DOD68] Dodd, C. V., and Deeds, W. E., 1968, Analytical Solutions to Eddy-Current Probe-Coil Problems: Journal of Applied Physics, v. 39, no. 6, May, p. 2829-2838.

[DOD69] Dodd, C. V., Deeds, W. E., and Luquire, J. W., 1969, Integral Solutions to some Eddy Current Problems: International Journal of Nondestructive Testing, v. 1, p. 29-90.

[DYA59a] D'Yakonov, B. P., 1959, The diffraction of electromagnetic waves by a circular cylinder in a homogeneous half-space: (Izv.) Bull. Acad. Sci. U.S.S.R., Geophysics Series, no. 9, 950-955.

[DYA59b] D'Yakonov, B. P., 1959, The diffraction of electromagnetic waves by a sphere located in a half-space: (Izv.) Bull. Acad. Sci. U.S.S.R., Geophysics Series, no. 11, 1120-1125.

[EAT87] Eaton, P. A., and Hohmann, G. W., 1987, An evaluation of EM methods in the presence of geologic noise: Geophysics, v. 52, p. 1106-1126.

[FOR86a]Förster, F., 1986, Theory of encircling coil and internal axial coil tests of tubes: Section 4 in [McM86], p. 89-110; Analysis of encircling coil tests of wire, rods and bars: Section 5 in [McM86], p. 111-145.

[FOR86b]Förster, F., and Wilcox, L.C., 1986, Eddy current tests of spheres and short parts: Section 7 in [McM86], p. 189-204.

[GEN99] N. Geng, C. E. Baum, and L. Carin, "On the Low-Frequency Natural Response of Conducting and Permeable Targets", IEEE Trans. on Geoscience and Remote Sensing, vol. 37, no. 1, pp. 347-359, Jan. 1999.

[GRA65] F. S. Grant and G. F. West, *Interpretation Theory in Applied Geophysics*. New York: McGraw-Hill, 1965.

[HIL72] Hill, D. A., and Wait, J. R., 1972, Electromagnetic response of a conducting cylinder of finite length: Geofisica Internacional (Mexico), v. 12, no. 4, October, p. 245-266.

[IDA95] Ida, N., 1995, Numerical Modeling for Electromagnetic Non-Destructive Evaluation: Chapman & Hall, London, UK.

[KAU78]Kaufman, A. A., 1978, Frequency and Transient responses of EM fields created by currents in confined conductors: Geophysics, v. 43, p. 1002-1010.

[KAU01]A. A. Kaufman, and P. A. Eaton, *The Theory of Inductive Prospecting.* Amsterdam, NL: Elsevier, 2001.

[KEI98] D. Keiswetter, I. J. Won, T. Bell, B. Barrow, and N. Khadr, "Electromagnetic Induction Spectroscopy", in *Proc. Forum 1998*, Anaheim, CA, 5-7 May 1998.

[KEL66] G. V. Keller, and F. C. Frischknecht, *Electrical Methods in Geophysical Prospecting.* Oxford, UK: Pergamon Press, 1966.

[KER60] Kertz, W., 1960, Leitungsfähiger Zylinder im transversalen magnetischen Wechselfeld (Conducting cylinder in a transversal alternating magnetic field) (in German): Gerlands Beiträge zur Geophysik, v. 69, p. 4-28.

[LIB71] Libby, H. L., 1971, Introduction to Electromagnetic Nondestructive Test Methods: Wiley-Interscience, New York, USA.

[LUQ70] Luquire, J. W., Deeds, W. E., and Dodd, C. V., 1970, Axially Symmetric Eddy Currents in a Spherical Conductor: Journal of Applied Physics, v. 41, no. 10, September, p. 3976-3982.

[McF89] J.E. McFee, "Electromagnetic Remote Sensing; Low Frequency Electromagnetics", Defence Research Establishment Suffield, Ralston, Alberta, Canada, Suffield Special Publication No. 124 (report DRES-SP-124), January 1989.

[McM86]McMaster, R. C., McIntire, P., and Mester, M. L. (Eds.), 1986, Nondestructive Testing Handbook, 2nd Edition: Volume 4: Electromagnetic Testing: American Society for Nondestructive Testing (ASNT), USA.

[MER99]L. Merlat, M. Acheroy, "Improving quality of information from metal detectors", in Proc. 1999 ARIS Technical Workshop on Ground Survey for Humanitarian Demining, Brest, France, 26-27 Oct. 1999.

[MER00]L. Merlat, and P. Druyts, "Progress Report on the Metal Detector: Signal Processing for Target Discrimination and Coil's Modelization", Progress Report of the HUDEM Project, Royal Military Academy, Brussels, Belgium, 29 Feb. 2000. Also ISL (Institut de Saint-Louis) Publication PU 322/2000, Saint-Louis, France.

[MIL01] J. T. Miller, T. H. Bell, J. Soukup, and D. Keiswetter, "Simple Phenomenological Models for Wideband Frequency-Domain Electromagnetic Induction", IEEE Trans. on Geoscience and Remote Sensing, vol. 39, no. 6, pp. 1294-1298, June 2001.

[NAB87] Nabighian, M. N. (Ed.), 1987, Electromagnetic Methods in Applied Geophysics, Volume 1, Theory: Investigations in Geophysics No. 3, Society of Exploration Geophysicists (SEG), Tulsa, OK, USA.

[NAB91] Nabighian, M. N. (Ed.), 1991, Electromagnetic Methods in Applied Geophysics, Volume 2, Application: Investigations in Geophysics No. 3, Society of Exploration Geophysicists (SEG),

Tulsa, OK, USA.

[NEG62] Negi, J. G., 1962, Diffraction of EM waves by an inhomogeneous sphere: Geophysics, v. 27, Aug., p. 480-492.

[NEG63] Negi, J. G., 1963, Discussion on "Diffraction of EM waves by an inhomogeneous sphere", and Reply by author: Geophysics, v. 28, p. 665-667.

[NEG72] Negi, J. G., Gupta, C. P., and Raval, U., 1972, Induction anomaly due to an elongated covered ore-zone excited by a long current carrying cable: Geophysical Prospecting, v. 20, p. 193-211.

[NEL01] C. V. Nelson, *et al.*, "Wide Bandwidth Time-Domain Electromagnetic Sensor for Metal Target Classification", IEEE Trans. on Geoscience and Remote Sensing, vol. 39, no. 6, pp. 1129-1138, June 2001.

[NOR01] S. J. Norton, and I. J. Won, "Identification of Buried Unexploded Ordnance From Broadband Electromagnetic Induction Data", IEEE Trans. on Geoscience and Remote Sensing, vol. 39, no. 10, pp. 2253-2261, October 2001.

[OGU74] Ogunade, S. O, Ramaswamy, V. and Dosso, H. W., 1974, Electromagnetic Response of a Conducting Sphere Buried in a Conducting Earth: Journal of Geomagnetism and Geoelectricity, v. 26, no. 4, p. 417-427.

[OGU80] Ogunade, S. O., and Dosso, H. W., 1980, The Inductive Response of a Horizontal Conducting Cylinder Buried in a Uniform Earth for a Uniform Inducing Field: Geophysical Prospecting, v. 28, p. 601-609.

[OGU81] Ogunade, S. O., 1981, EM response of an embedded cylinder for line current excitation: Geophysics, v. 46, p. 45-52.

[RIG98] L. S. Riggs, J. E. Mooney, D. E. Lawrence, J. T. Broach, and A. H. Trang, "Identification of Metallic Mines using Low Frequency Magnetic Fields", in *Detection and Remediation Technologies for Mines and Minelike Targets III; SPIE Proceedings Vol. 3392* (Orlando, FLA, USA, April 13-17, 1998, pp. 146-157).

[RIG01] L. S. Riggs, J. E. Mooney, and D. E. Lawrence, "Identification of Metallic Mine-Like Objects Using Low Frequency Magnetic Fields", IEEE Trans. on Geoscience and Remote Sensing, vol. 39, no. 1, pp. 56-66, Jan. 2001.

[ROS48] B. Roston, "Development of Locators of Small Metallic Bodies buried in the Ground", Journal of the Institution of Electrical Engineers (IEE Review), vol. 95, pp. 653-667, 1948.

[SHA] R. S. Sharpe, Ed., "Research techniques in nondestructive testing", Academic Press, London, 1970-1985 (8 vol.).

[SIN73] Singh, S. K., 1973, On Axially Symmetric Electric Current Induced in a Cylinder Under a Line Source: Geophysics, v. 38, no. 5, October, p. 971-974.

[SIN74] Singh, S. K., 1974, Discussion on "Time Dependent Electromagnetic Fields of an Infinite, Conducting Cylinder Excited by a Long Current-Carrying Cable, with reply by author: Geophysics, v. 39, p. 355-356.

[SIN77] Singh, S. K., 1977, Discussion on "Time Dependent Electromagnetic Fields of an Infinite, Conducting Cylinder Excited by a Long Current-Carrying Cable: Geophysics, v. 42, p. 661-662.

[SOW95] Sower G.D., Cave S.P., "Detection and Identification of Mines from Natural Magnetic and Electromagnetic Resonances", in *SPIE Proceedings Vol.* 2496, pp. 1015-1024, Orlando, FLA, 17-21 Apr. 95.

[SOW98a] G. D. Sower and J. D. Endsley, "The Electrodynamics of Metal Mine Detection", in *Proc. Third Intnl. Symposium on Technology and the Mine Problem*, Monterey, CA, April 6-9, 1998. Proceedings on CD-ROM.

[SOW98b] G. D. Sower, "Eddy Current Responses of Canonical Metallic Targets", in *Detection and Identification of Visually Obscured Targets*, C. E. Baum Ed., pp. 243-282, Taylor & Francis, New York, 1998.

[SOW99] G. Sower, J. Endsley, and E. Christy, "Discrimination of Metal Land Mines from Metal Clutter: Results of Field Tests", in *SPIE Proceedings Vol. 3710*, pp. 78-88, Orlando, FLA, April 1999.

[SPI84] Spies, B. R., and Parker, P. D., 1984, Limitations of large-loop transient electromagnetic surveys in conductive terrain: Geophysics, v. 49, no.7, July, p. 902-912.

[STA86] Stanley, K. R., 1986, Diverted Flux Theory: Section 21 in [McM86], p. 607-630.

[SZY99] P. Szyngiera, "A Method of Metal Object Identification by Electromagnetic Means", in *Proc. MINE'99 (Mine Identification Novelties Euroconference)* (Florence, Italy, October 1-3, 1999, pp. 155-160). Available from http://demining.jrc.it/aris/events/mine99/index.htm.

[TAN01] S. L. Tantum, and L. M. Collins, "A Comparison of Algorithms for Subsurface Target Detection and Identification Using Time-Domain Electromagnetic Induction Data", IEEE Trans. on Geoscience and Remote Sensing, vol. 39, no. 6, pp. 1299-1306, June 2001.

[TRA97] A. H. Trang, P. V. Czipott, and D. H. Waldon, "Characterization of small metallic objects and non-metallic anti-personnel mines", in *SPIE Proceedings Vol. 3079,* pp. 372-383, Orlando, FLA, April 21-24, 1997.

[VEI62] Vein, P. R., 1962, Inductance between Two Loops in the Presence of Solid Conducting Bodies: Journal of Electronics and Control, v. 13, no. 5, p. 471-494. [Probable error in the coefficient for the sphere, Eq. (62)]

[VUI94] P.-L. Vuillermoz, *Les courants de Foucault – Principes, mesure et contrôle*, AFNOR, Paris, 1994 (in French). ISBN 2-12-260912-5.

[WAI52] Wait, J.R., 1952, The Cylindrical Ore Body in the Presence of a Cable Carrying an Oscillating Current: Geophysics, v. 17, April, p. 378-386. [In Eq. (13) replace μ_2/μ_1 by $n\mu_2/\mu_1$, and in Eq. (14) replace (k+n) by n(k+1) and (k–n) by n(k–1)]

[WAI60] Wait, J.R., 1960, Some Solutions for Electromagnetic Problems Involving Spheroidal, Spherical and Cylindrical Bodies: Journal of Research of the National Bureau of Standards–B. Mathematics and Mathematical Physics, v. 64B, no. 1, January-March, p. 15-32. [In equation (74) replace *ha* by $|ha|$; in equation (80) replace $hK'_m(\ )$ by $|h|K'_m(\ )$.]

[WAI73a] Wait, J.R., 1973, On electromagnetic induction in elongated ore bodies (Letters to the Editor): Geophysics, v. 38, no. 5, April, p. 984-985. [Replace "wipe out" by "de-emphasize"]

[WAI73b] Wait, J. R., and Hill, D. A., 1973, Excitation of a homogeneous conductive cylinder of finite length by a prescribed axial current distribution: Radio Science, v. 8, no. 12, December, p. 1169-1173.

[WAI82] Wait, J. R., 1982, Geo-electromagnetism: Academic Press, New York.

[WAI97] Wait, J.R., 1997, Belated comments on the electromagnetic cylinder scattering and the ubiquitous galvanic current distribution (Short Note): Geophysics, v. 62, no. 2, March-April, p. 449-450.

[WAL92] Walker, P. W., and West, G. F., 1992, Parametric estimators for current excitation on a thin plate: Geophysics, v. 57, no. 6, June, p. 766-773.

[WAR67] Ward, S. H., 1967, Electromagnetic Theory for Geophysical Applications, in Mining Geophysics, Vol. II, Theory: Society of Exploration Geophysicists (SEG), Tulsa, OK, USA, p. 12-196.

[WAR80] Ward, S. H., 1980, Electrical, electromagnetic and magnetotelluric methods: Geophysics, v. 45, no. 11, Nov., p. 1659-1666.

[WAR87] Ward, S. H., and Hohmann, G.W., 1987, Electromagnetic Theory for Geophysical Applications, in [NAB87], p. 130-311.

[WES91] West, G. F., and Macnae, J. C., 1991, Physics of the Electromagnetic Induction Exploration Method, in [NAB91], p. 5-45.

[WON98] I. J. Won and D. Keiswetter, "Electromagnetic Induction Spectroscopy", in *SPIE Proceedings Vol. 3392*, pp. 14-22, Orlando, FLA, April 13-17, 1998.

[WON01] I. J. Won, D. A. Keiswetter, and T. H. Bell, "Electromagnetic Induction Spectroscopy for Clearing Landmines", IEEE *Trans. Geosci. Remote Sensing*, vol. 39, no. 4, pp. 703-709, April 2001.

Appendix A3.

A3.1. Objects Embedded in a Homogenous Half-Space – Exact Solution

There are a few geophysical references dealing with the exact analytic solution of the problem of a conductive and permeable target embedded in a conductive half-space (complications arise due to the presence of the air-earth interface). We will describe in the following a few of them, without entering in details. Approximate solutions will be sufficient for our aims.

Sphere

[NEG62] describes and [NEG63] discusses the diffraction of waves from an inhomogeneous sphere embedded in a half-space, thereby studying the effects of the air-earth boundary, similarly to the original analysis of [DYA59b]. Primary fields with cylindrical symmetry are considered (e.g. a uniform magnetic field, or a vertical magnetic dipole). The expressions obtained are quite involved. We note in particular the interpretation of part of the response as due to multiple reflections from each of the boundaries. [OGU74] also presents results having mainly geophysical interest.

Cylinder

[DYA59b] obtained an exact analytical solution to the problem of a conducting cylinder buried in a uniform earth as a limiting case of the boundary value problem involving two non-concentric cylinders. [OGU81] treats an extension to this solution for an infinite horizontal cylinder in the field of a line source. The actual numerical results are not of particular interest for us.

A3.2. Infinite Cylinder in a Longitudinal Magnetic Field – NdT

Solenoidal Coils

Considering the case of a cylindrical test bar (i.e. a full cylinder) of diameter d_{bar}, the **total** voltage V^{sec}/V_0 induced in a *secondary* (receiving) *solenoidal* coil of diameter D_{coil}, normalized by the empty coil voltage V_0, or equivalently the impedance $Z=((R-R_0)/\omega L_0, \omega L/\omega L_0)$ in case a single coil is used, normalized by ωL_0, is [FOR86a]:

$$\frac{V^{sec}_{imag}}{V_0} = \frac{\omega L}{\omega L_0} = 1-\eta+\eta\mu_{rel}\mu_{eff(real)}\,,\ \frac{V^{sec}_{real}}{V_0} = \frac{R-R_0}{\omega L_0} = \eta\mu_{rel}\mu_{eff(imag)} \tag{A3.1}$$

$$\mu_{eff} = -\sqrt{\frac{2}{f/f_g}}\frac{J_1(\sqrt{if/f_g})}{J_0(\sqrt{if/f_g})}(1-i) \tag{A3.2}$$

where L_0 and R_0 are the self-inductance and the resistance of the empty encircling coil, $\eta=(d_{bar}/D_{coil})^2$ is the coil fill factor and J_0 and J_1 are Bessel functions of the zero and first order respectively. The effective permeability μ_{eff} plays here the role of response function, with the frequency ratio f/f_g used in NdT being nothing else than the response parameter $(ka)^2=\sigma\mu\omega a^2$. Note that *sec* refers here to the coil, not the voltage.

It is quite interesting to note that the behaviour of the solution for a non-ferromagnetic bar is actually quite similar to the dipole term of a sphere [FOR86b], as shown in Figure 3.17 (small dashed curve). The case of ferromagnetic bars is on the other hand quite different, as here the induced voltage is simply multiplied by the relative permeability μ_r (for large μ_r) – see the dot-dashed (μ_r=2) and continuous curve (μ_r=5) again in Figure 3.17.

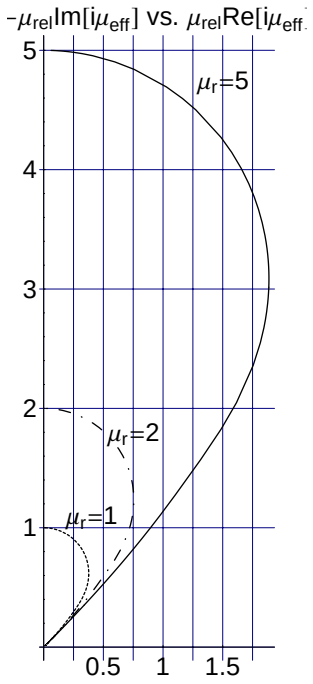

Figure 3.17: Response of a full infinite cylinder in a longitudinal field (generated by a solenoid) for η=1. Dashed: μ_r=1, dot-dashed: μ_r=2, continuous: μ_r=5.

Circular (delta-function) Coils

Solutions, expressed in terms of the vector potential, are also available in the case of *circular* coaxial (delta-function) *coils* (single coils, not a solenoid) encircling a coaxial infinite (full) cylinder of radius b (see Figure 3.18).

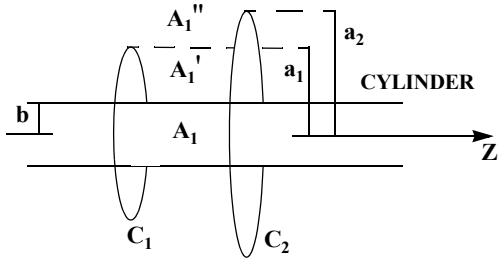

Figure 3.18: Circular coaxial coils encircling an infinite cylinder

If coil "1", of radius a_1 and placed at z=0, is the exciting coil, the general expression for the magnetic vector potential $A(\rho,z)$ outside the cylinder is (A_1' is valid for $b \le \rho \le a_1$, A_1" for $\rho \ge a_1$; A_1 will not be considered here) [VEI62]:

$$A_1' = \frac{\mu_0 a_1 I_1}{\pi}\int_0^\infty K_1(\lambda a_1)[I_1(\lambda\rho) + D_\lambda K_1(\lambda\rho)]\cos\lambda z d\lambda \qquad \text{(A3.3)}$$

$$A_1'' = \frac{\mu_0 a_1 I_1}{\pi}\int_0^\infty K_1(\lambda\rho)[I_1(\lambda a_1) + D_\lambda K_1(\lambda a_1)]\cos\lambda z d\lambda \qquad \text{(A3.4)}$$

The first term is due to the exciting coil itself (primary field), the second one corresponds to the disturbance introduced by the cylinder. The D_λ coefficient is ($W^2=\lambda^2-k^2$, where k is the usual propagation constant):

$$D_\lambda = \frac{\lambda\mu_r I_1(Wb)I_0(\lambda b) - WI_0(Wb)I_1(\lambda b)}{\lambda\mu_r I_1(Wb)K_0(\lambda b) + WI_0(Wb)K_1(\lambda b)} \tag{A3.5}$$

When a single coil is used, or two coincident coils, we can replace $\rho=a_1=a$ and $z=0$ in Eq. (A3.3) or Eq. (A3.4) and obtain for the total induced voltage:

$$V = j\omega\oint \boldsymbol{A}\cdot d\boldsymbol{l} = j\omega 2\pi a A\Big|_{z=0}^{\rho=a} = \ldots \tag{A3.6}$$

$$\ldots = j\omega 2\mu_0 a^2 I_1 \int_0^\infty K_1(\lambda a)[I_1(\lambda a) + D_\lambda K_1(\lambda a)]d\lambda = j\omega L I_1 + 2\mu_0 a^2 I_1 \int_0^\infty D_\lambda [K_1(\lambda a)]^2 d\lambda \tag{A3.7}$$

where the first term in the integral corresponds to the coil self-inductance L and contains a *logarithmic singularity* (as we are considering delta-function coils, i.e. of infinitesimal cross section). [DOD68], [DOD69] extend these results to coils of finite cross section encircling two concentric cylinders (which contains the special case of hollow cylinders).

A3.3. Special Functions

The associated Legendre polynomials are defined as (n, m integer):

$$P_n^m(x) = (-1)^m (1-x^2)^{m/2} \frac{d^m}{dx^m} P_n(x) \tag{A3.8}$$

where $P_n(x)$ is an ordinary Legendre polynomial of order n. We have in particular:

$$P_1^1(x) = -\sqrt{1-x^2}\ ,\ P_2^1(x) = -3x\sqrt{1-x^2}\ ,\ P_3^1(x) = -\frac{3}{2}\sqrt{1-x^2}(-1+5x^2) \tag{A3.9}$$

Note that some authors prefer to omit the $(-1)^m$ factor.

Concerning the modified Bessel functions of the first kind, we have in particular that:

$$I_{-1/2}(z) = \sqrt{\frac{2}{\pi z}}\cosh(z)\ ,\ I_{1/2}(z) = \sqrt{\frac{2}{\pi z}}\sinh(z)\ ,\ I_{3/2}(z) = \frac{2\cosh(z) - 2\sinh(z)/z}{\sqrt{2\pi z}} \tag{A3.10}$$

4.

Electromagnetic Induction Ground Response

The presence and importance of the soil signal for Frequency Domain systems have already been stressed in Chapters 1 and 2 (§2.2.4, §2.3.1 and §2.3.3.2 in particular). It is therefore important to gain a quantitative understanding of the role of the different parameters – the soil's EM properties, the metal detector's loop size and height – and of some techniques, such as frequency differencing methods, which are used to reduce soil effects. This will also help in understanding the behaviour of the experimental data in Chapter 5 and in the analysis of features more robust to background fluctuations (Chapter 6).

The response of the earth itself can be calculated using known results for the response of a (homogenous) half-space in Geophysics, or equivalently from a semi-infinite medium in NdT, although this might at first glance look astounding given the usually very different target scenarios involved (the range of conductivity values is very different in general – say of maximum 1 S/m in Geophysics vs. the conductivity of metals in the case of NdT). What is certainly different is the relative magnetic permeability of the half-space, which is usually very close to 1 for the soil, whereas it can assume very large values for a permeable metallic substrate.

In the following we will consider the response to a loop of finite size, leaving aside the large body of literature dealing with the dipole ("small loop") approximation. We will also be interested in the induced voltage rather than in the magnetic field; the latter can actually be expressed analytically for example at the centre of the loop, whereas all other quantities are available only in integral form in the general case.

Note that in geophysical articles the z-axis points often downwards, i.e. positive z is in the direction of the half-space, in NdT usually upwards; also, the origin is sometimes taken at the coil rather than at the surface.

4.1. Loop Response in Geophysics

Concerning geophysical applications, one of the earliest papers dealing with the problem of a (delta-function) horizontal circular loop above a horizontally layered half-space was [MOR69], specializing the solution to the total electric and magnetic fields in integral form at the surface. The harmonic fields are then used, as is often the case, to calculate transient quantities (a half sine wave current pulse in this case). This work is further developed in [RYU70], which overcomes the impracticality of numerical evaluation of the previously found solution when the loop is on or close to the surface (h~0) (severe oscillation of the integrand when the total fields are calculated, rather than the secondary only, in which we are interested). Solutions are obtained in particular for the fields outside and in the centre of the loop. The voltage induced in the loop, rather than the fields, was calculated in [LEE74], making use of the expression for the induced electric field at the loop itself. The result is then again used to calculate transient quantities.

The permeability of the ground is often assumed to be equal to unity in a number of geophysical papers. An exception is for example [IGN85], which starts by calculating the electric field in the frequency domain in terms of an appropriate Green's function. The total electric field is expressed as a sum of a "radiative" and evanescent and a "diffusive" and dissipative partial field; although the form is different, the expressions thus obtained are equivalent to Eq. (4.7) and Eq. (4.8). The solution is then inverted to the time domain (step current excitation) and the effects of changes in the permeability contrast and in the loop height are analyzed.

Finally, a number of results for rectangular and circular loops are also reviewed in [WAR87].

Superparamagnetic Ground (Magnetic Viscosity Effects)

The effect of a magnetic or superparamagnetic ground is also considered in detail, again for a circular loop (of finite cross section) and in the time domain, in [LEE84]. In a superparamagnetic material the permeability is allowed to vary with the frequency ω (*magnetic viscosity* effect), contrary to what we have assumed so far (constant permeability):

$$\mu = \mu_0\left\{1 + \chi_0\left[1 - \frac{\ln[(i\omega\tau_2 + 1)/(i\omega\tau_1 + 1)]}{\ln(\tau_2/\tau_1)}\right]\right\} \tag{4.1}$$

where χ_0 is the direct current value of the magnetic susceptibility, and τ_1 and τ_2 are the lower and upper time constant for the superparamagnetic ground, respectively[45]. Note that the permeability is now complex valued. It reduces to the usual expression:

$$\mu = \mu_0\{1 + \chi_0\} \tag{4.2}$$

when ω=0 or when $\tau_1 \to 0$, and can be simplified to the following expression in the range of frequencies for which $|\omega\tau_1|<<1$ and $|\omega\tau_2|>>1$ [LEE84]:

$$\mu \cong \mu_0\left\{1 + \chi_0\left(1 - \frac{\ln(i\omega\tau_2)}{\ln(\tau_2/\tau_1)}\right)\right\} \tag{4.3}$$

In this case the permeability difference at two frequencies ω_1 and ω_2 becomes purely real:

$$\Delta\mu = \mu(\omega_2) - \mu(\omega_1) = \mu_0\frac{\chi_0}{\ln(\tau_2/\tau_1)}\ln\frac{\omega_1}{\omega_2} \tag{4.4}$$

When working in the time domain the logarithmic frequency dependence translates into a $1/t$ behaviour of the induced voltage at late times. What happens from the physics point of view is that when the applied field is switched off, the induced magnetism does not collapse instantaneously, but with a logarithmic time relationship whose time derivative has been taken to calculate the induced voltage.

Magnetic viscosity has been well known in archaeology for quite some time. It has also been reported as a source of geological noise in exploration for gold nuggets in Western Australia, and is often observed in weathered environments, especially areas with lateritic soil cover [SPI91, pp. 338-342].

Approximated Responses

[KAU01] shows that the magnetic field due to currents in the host medium (non-permeable) can be approximated, at low frequency and at late times, as follows:

$$H(\omega) \cong \sum a_{1n}\omega^n + \sum a_{2n}\omega^{n+1/2} \tag{4.5}$$

$$H(t) \cong \sum \frac{b_{1n}}{t^{n+1/2}} + \sum \frac{b_{2n}}{t^n} \tag{4.6}$$

Eq. (4.5) pertains to the frequency domain, and has to be compared with the low frequency response of a confined conductor (§3.3.3), whose imaginary part behaves in first approximation as ω, the real part as ω^2 (the lowest order terms in Eq. (4.5) are in ω and $\omega^{3/2}$). The induced voltage can be calculated by multiplying with an additional factor iω as usual.

45. There is a probable typographical error in Eq. (3) of [LEE84].

Eq. (4.6) is relative to the time domain; the induced voltage is the time derivative thereof, and features therefore an additional factor $1/t$. The currents induced in the host medium decrease during the late stage much more slowly (as $t^{-3/2}$) than those of a confined conductor, whose late time response decays exponentially. It can therefore be problematic to measure small signals accurately. On the other hand one can in principle choose an optimum measurement range where the target signal is strongest relatively to the host medium response. The same argument is actually valid in the frequency domain (existence of an "optimum frequency range").

4.2. Loop Response in NdT

We will use as reference the result quoted in [CHE65], which is quite general. Considering a vanishingly thin (delta-function), circular coil of radius a in air, with axis oriented along the **z** axis (pointing upwards) and placed at $z=h$ of the cylindrical coordinate system (ρ,ϕ,z), in the proximity of a semi-infinite medium (half-space) of electrical parameters $(\varepsilon_1,\sigma,\mu_1)$ occupying the region $z<0$ (see Figure 4.1), the **total magnetic vector potential** $\boldsymbol{A}_\phi$ can be expressed in integral form as follows in air ($z>0$) and in the medium ($z<0$) respectively:

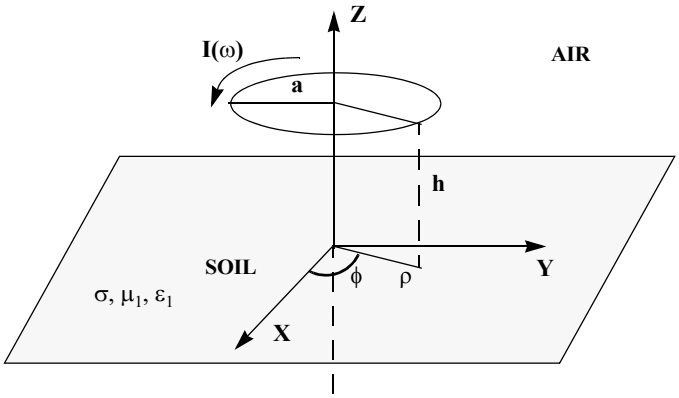

Figure 4.1: Circular loop above a homogenous medium (soil)

$$A_\phi\big|_{z>0} = \frac{\mu_0 Ia}{2}\int_0^\infty J_1(\xi\rho)J_1(\xi a)e^{-\lambda_0|z-h|}\frac{\xi d\xi}{\lambda_0} + \frac{\mu_0 Ia}{2}\int_0^\infty J_1(\xi\rho)J_1(\xi a)e^{-\lambda_0(z+h)}\left\{\frac{\mu_1\lambda_0-\mu_0\lambda_1}{\mu_1\lambda_0+\mu_0\lambda_1}\right\}\frac{\xi d\xi}{\lambda_0} \quad (4.7)$$

$$A_\phi\big|_{z<0} = \frac{\mu_0 Ia}{2}\int_0^\infty J_1(\xi\rho)J_1(\xi a)e^{\lambda_1 z-\lambda_0 h}\frac{2\mu_1\xi d\xi}{\mu_1\lambda_0+\mu_0\lambda_1} \quad (4.8)$$

where J_1 is the Bessel function (of the first kind) of the first order, and k_0 and k_1 are respectively the propagation constants in air and in the medium:

$$\lambda_0 = \sqrt{\xi^2-k_0^2}\ ,\ \lambda_1 = \sqrt{\xi^2-k_1^2} \text{ with } k_0^2 = \varepsilon_0\mu_0\omega^2\ ,\ k_1^2 = \varepsilon_1\mu_1\omega^2 - i\sigma\mu_1\omega \quad (4.9)$$

The previous expression for A_ϕ are complete (not quasi-static).

The factor in braces in Eq. (4.7) can be interpreted as a reflection coefficient, and [CHE65] shows that it corresponds indeed to the reflection coefficient r_{TE} in air of horizontally polarized plane waves (TE or Transverse Electric mode), into which the spherical waves involved in this problem can be expanded. Additional elements can be found in [WAR87].

Starting from the vector potential a number of physical quantities characteristic of induction phenomena can again be calculated, in particular the voltage induced in a second coil coincident with the one just considered, or in the coil itself [DOD68, DOD69]. Indeed, letting $z=h$ and $\rho=a$ in Eq. (4.7) we obtain for the **total induced voltage** V^{TOT}:

$$V^{TOT} = i\omega a \int_{-\pi}^{\pi} A_\phi\big|_{z=h}^{\rho=a} d\phi = i\omega 2\pi a A_\phi\big|_{z=h}^{\rho=a} = \dots \tag{4.10}$$

$$\dots = i\omega\mu_0\pi I a^2 \left\{ \int_0^\infty [J_1(\xi a)]^2 \frac{\xi d\xi}{\lambda_0} + \int_0^\infty [J_1(\xi a)]^2 e^{-2h\lambda_0} \left\{ \frac{\mu_1\lambda_0 - \mu_0\lambda_1}{\mu_1\lambda_0 + \mu_0\lambda_1} \right\} \frac{\xi d\xi}{\lambda_0} \right\} = V^{PRIM} + V^{SEC} \tag{4.11}$$

The first term within brackets corresponds to the coil voltage induced by the primary field in the absence of the infinite medium, and is actually logarithmically singular corresponding to an infinite coil self-impedance L due to the assumption of delta-function coil, as already seen in A3.2. This would not happen for a coil of finite cross section. The second term is regular and corresponds to the secondary voltage, for which there are some numerical convergence problems for h~0 and $\mu_1>\mu_0$ due to strong oscillations of the Bessel function; they are however damped by the exponential when the coil is lifted from the ground (h>0). There is also a singularity due to λ_0, with which we will in fact not be confronted (see the approximations below).

[CHE65] shows a number of plots for conductivity values of interest in NdT ("metallic" values), which are, as we said, much higher than those of typical interest in Geophysics.

It is actually of interest to introduce (adimensional) quantities **normalized** in terms of the coil radius a. This is achieved by dividing the height by a and multiplying λ_0, λ_1 and ξ by a, resulting in (the quantity within braces is now adimensional as well):

$$V^{TOT} = i\omega\mu_0\pi I a \left\{ \int_0^\infty [J_1(x)]^2 \frac{x dx}{\lambda_{1N}} + \int_0^\infty [J_1(x)]^2 e^{-2h_N\lambda_{0N}} \left\{ \frac{\mu_1\lambda_{0N} - \mu_0\lambda_{1N}}{\mu_1\lambda_{0N} + \mu_0\lambda_{1N}} \right\} \frac{x dx}{\lambda_{0N}} \right\} = \dots \tag{4.12}$$

$$\dots = V^{PRIM} + (i\omega\mu_0\pi I a)\chi_{HS} \tag{4.13}$$

with

$$h_N = h/a \;,\; \lambda_{0N} = a\lambda_0 \cong a\xi = x \;,\; \lambda_{1N} = a\lambda_1 \cong \sqrt{a^2\xi^2 + i\sigma\mu_1\omega a^2} = \sqrt{x^2 + i\alpha} \tag{4.14}$$

$$x = a\xi \;,\; \alpha = \sigma\mu_1\omega a^2 \tag{4.15}$$

Whereas Eq. (4.12) is again exact, in Eq. (4.14) approximated expressions for λ_{0N} and λ_{1N} have been obtained neglecting displacement currents in both the air and the ground (quasi-static approximation). χ_{HS} is the **half-space response function** which will be plotted in the following, using α, the usual adimensional response parameter (induction number) which depends here on the coil radius a, as plotting variable. Note that the height h_N is normalized by the coil radius. The induced voltage can be obtained by multiplying the response function values with the normalization factor $i\omega\mu_0\pi Ia$; the latter depends in particular on ω.

Note that we are interested in *quite low values* of α, with maximum of about 10^{-3}-10^{-2} say for a typical metal detector of radius 10-15 cm in a high conductivity soil at a frequency of 100 kHz (see also Table 3.2). In the case of large loops – radius of order 1 m – α_{max} could be of the order of 1-10.

More complex scenarios than the uniform half-space have been studied as well, although results are often specialized to non-permeable media, such as multiple (metallic) layers. [DOD68, DOD69] detail the solutions for a two-layer planar conductor and also extend the results to coils of finite cross section and to a number of physical quantities of interest. It can be shown that the previously quoted results are a special case of the more general ones. The geophysical analogue is a stratified ground (layered earth models), which has been discussed in some of the previously mentioned references as well as in [WAI82]. Concerning more recent NdT literature, analytical

and numerical results are also discussed in [OAT92, BLI97][46]. Linear, isotropic and homogeneous media are usually assumed throughout.

Further comments can be found in the interesting overview of EM methods in NdT of wire ropes by Wait [WAI79], which includes a summary of papers dealing with the basic concepts and techniques for testing of cylindrical conductors by both electric and magnetic methods, and recalls the extensive related work on electromagnetic probing of geophysical targets.

In the following we will analyse the half-space response function for a number of scenarios of interest.

4.2.1. Non-Magnetic Ground (μ_r=1)

The response function for a non-magnetic ground with the loop *on the ground* (h_N=0) is plotted in Figure 4.2, and resembles the one for a non-ferromagnetic sphere. Our interest is here however towards *much lower values of the response parameter.*

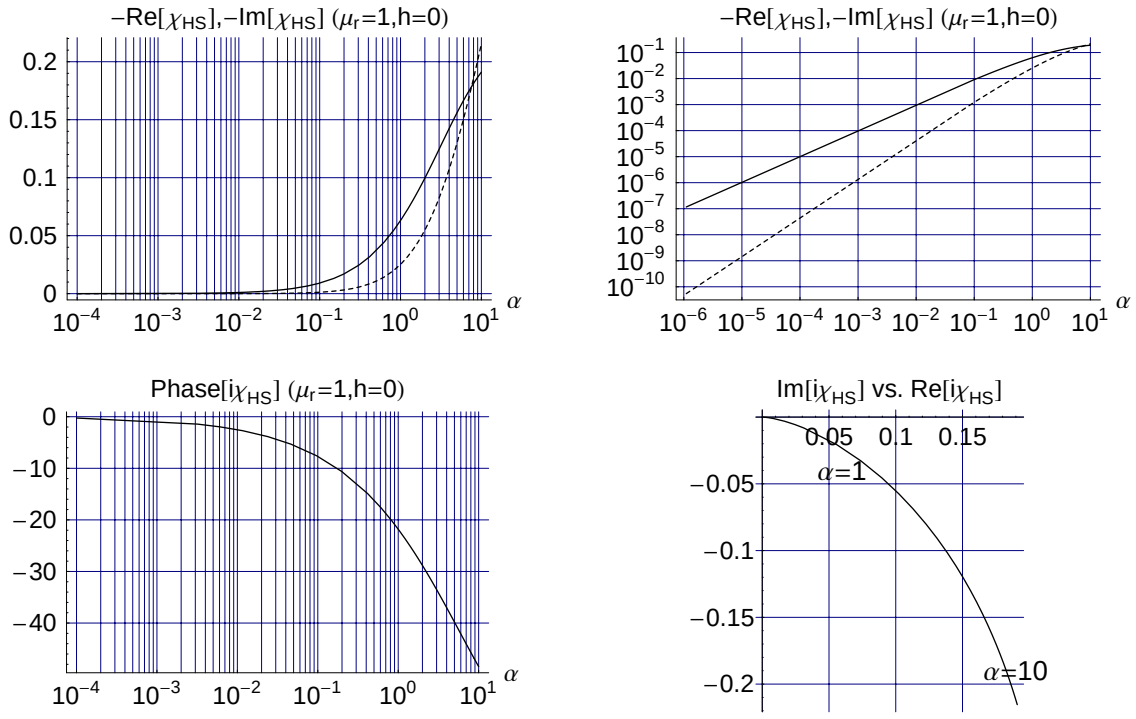

Figure 4.2: Half-space response function for a **non-magnetic** soil (μ_r=1) and h_N=0 (loop **on the ground**). Top: –Re is dashed, –Im continuous. Bottom left: phase, bottom right: complex plane.

The imaginary component (continuous line) is a straight line with slope equal to one, which means linear dependence on α and therefore on ω in particular; the real component (dashed line) has slope 3/2, implying dependence on $\alpha^{3/2}$ and therefore on $\omega^{3/2}$. The phase does not exceed a few degrees for a typical metal detector, as in this case the real part is several orders of magnitude smaller than the imaginary one[47].

From the numerical point of view there is practically no difference in this case between using h_N=0 or h_N=0.01 (see below). Also, an upper integration limit of 10 was sufficient for the second integral in Eq. (4.12) when μ_r=1. The results coincide with those obtained from Eq. 5.50 in [KAU01], apart from a factor π.

46. Both publications refer to an error in the original differential equation for the vector potential by Dodd and Deeds [DOD68], which we have however not been able to identify (the corresp. equation seems dimensionally correct).
47. Note that the phase of $i\chi_{HS}$ is plotted, to obtain directly the phase of the induced voltage.

The results for a loop on and *above the ground* are shown in Figure 4.3 (–Phase is plotted here). For a 10 cm radius loop, for example, the case h_N=0.1 corresponds to an absolute height of 1 cm, h_N=1 to 10 cm. Note the decrease in amplitude with height, more marked for the imaginary component.

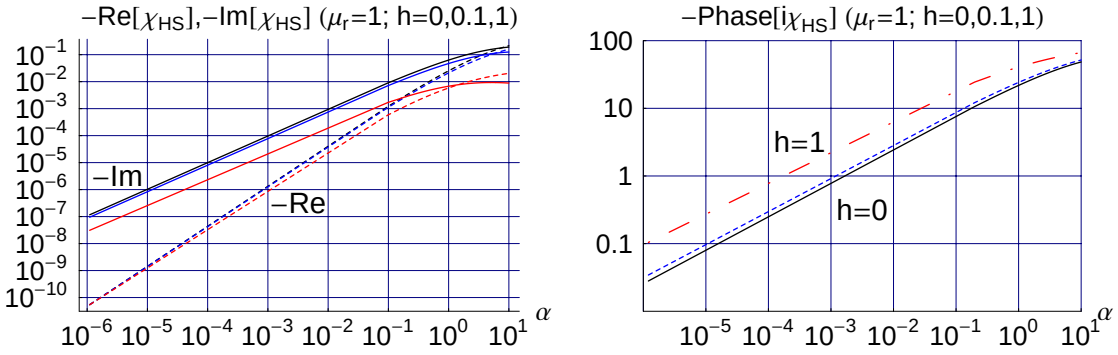

Figure 4.3: Half-space response function for a **non-magnetic** soil (μ_r=1) as a **function of loop height**: h_N=0 (black), h_N=0.1 (blue) and h_N=1 (red, dot-dashed on the right). Left: –Re is dashed, –Im continuous.

4.2.2. Magnetic Ground (μ_r>1)

The response function for a para- or weakly ferromagnetic ground with the loop *very close to the ground* (h_N=0.01) is plotted in Figure 4.4, and resembles the one for a ferromagnetic sphere. Our interest goes however again to much lower values of the response parameter.

The real part of the response function, whose absolute value is plotted, decreases at decreasing α, becomes negative (values to the left of the dip in the logarithmic scale) and reaches a plateau due to induced magnetization effects. When working in this region the real part of the response is basically frequency- and conductivity independent and represents therefore a constant shift with respect to the value for μ_r=1. Under these conditions the real part can be much larger than the imaginary one, which translates into values of the phase response very close to +90°. The imaginary part of the response function is basically unaffected by permeability changes.

It can also be shown that the constant plateau value thus reached is proportional to the permeability for small values of μ_r, up to about 1.5. Indeed, in the case of a loop on a half-space the vertical component of the magnetic field at the centre of a loop varies at low frequencies with the ground's magnetic susceptibility κ as [THO77]:

$$\frac{\Delta H_z}{H_z} = \frac{\Delta\kappa}{(1+\kappa)(2+\kappa)} \quad \text{where} \quad \mu = (1+\kappa)\mu_0 \tag{4.16}$$

which is in first approximation proportional to $\Delta\kappa$ for small susceptibility values.

From the numerical point of view the integration at h_N=0 is somewhat impractical; we have therefore chosen to use h_N=0.01. Also, the upper integration limit was extended to 100 in the second integral in Eq. (4.12).

The results for a loop *very close to and above the ground* are shown in Figure 4.5. Note the decrease in amplitude with height, more marked here for the real component (the uppermost curves correspond to h_N=0.01, the lowermost ones to h_N=1), whose zero crossing position (dip in the Log scale) moves towards lower values of α. As the imaginary part is not much affected by the permeability, the resulting phase is quite influenced by height changes, in particular for lower values of μ_r. The bottom right plot covers the low α region, where the phase is very close to +90°.

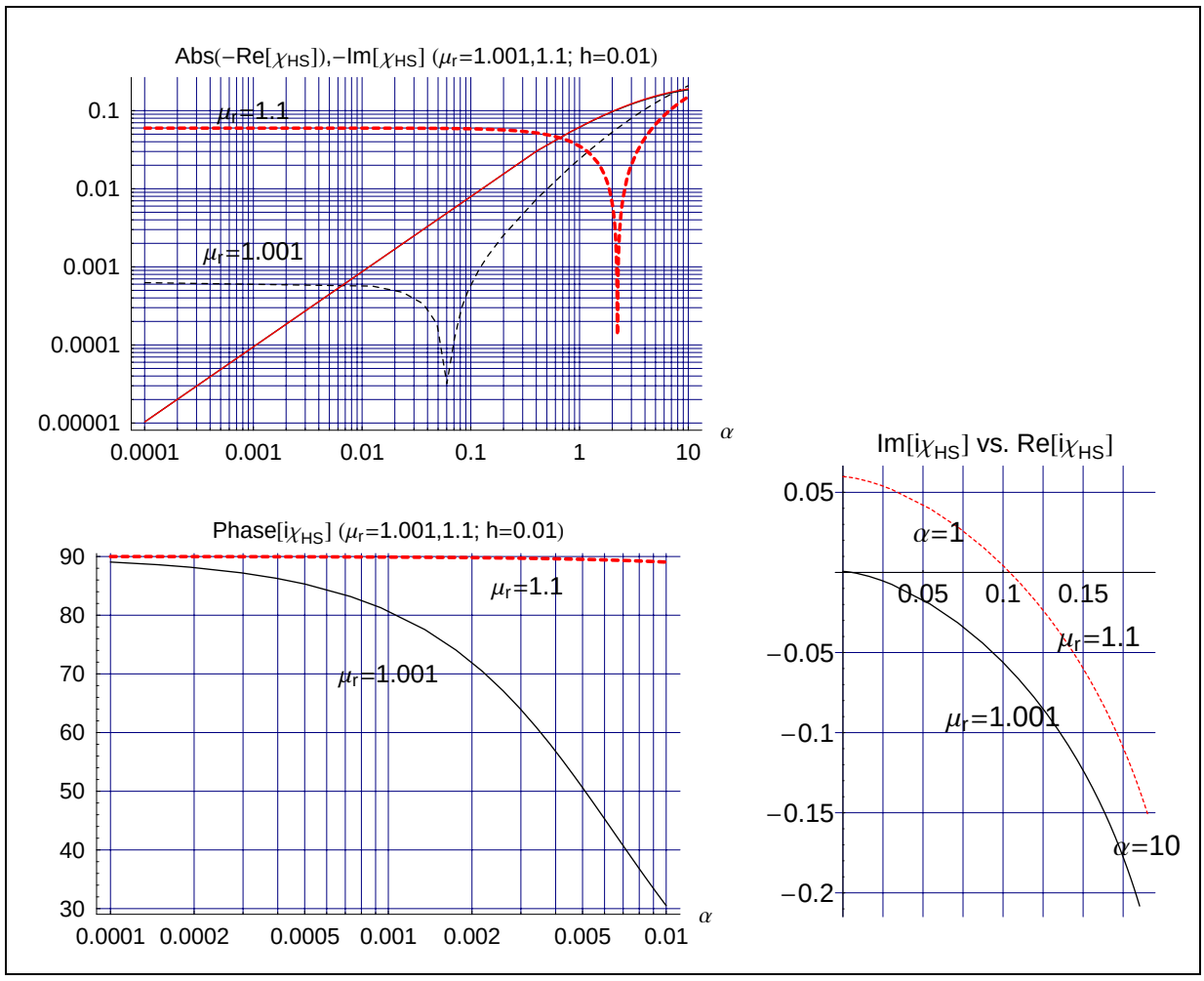

Figure 4.4: Half-space response function for a **magnetic** soil (μ_r=1.001-black, μ_r=1.1-red) and h_N=0.01 (loop **very close to the ground**). Top left: –Re is dashed (values to left of dip are negative!), –Im continuous.

Results for time domain systems are available in [IGN85], as already pointed out in §4.1. The decrease in signal amplitude with height at late times, corresponding to low frequencies, seems to be much less marked than what the previous results indicate; the reason for this behaviour is not immediately clear.

From the numerical point of view the upper integration limit of 10 in the second integral in Eq. (4.12) was again sufficient.

The effect of a magnetic permeability μ_r slightly larger than 1, as is the case for most magnetic soils, has in fact long been known in Geophysics but is usually small and has therefore often been neglected in the interpretation (inversion) of electromagnetic data. Results similar to those just illustrated have been detailed in [BEA98] for a Horizontal Coplanar (HCP) coil configuration (instead of a coincident coil system).

An extension of this work to take into account also the effect due to the electrical permittivity ε_r is presented in [HUA01], whose authors introduce a complex induction number $\theta=(\omega^2\varepsilon\mu h^2-i\omega\sigma\mu h^2)^{1/2}$ (which is nothing but $k_1 h$, h being their sensor height, and k_1 is defined in Eq. (4.9)), valid for the setup they are considering (airborne system), and map the system's response in a 3D parameter space. They also show that the effect of dielectric permittivity is similar to that of magnetic permeability, in that both tend to decrease the in-phase (real) and increase the quadrature (imaginary) part of the response.

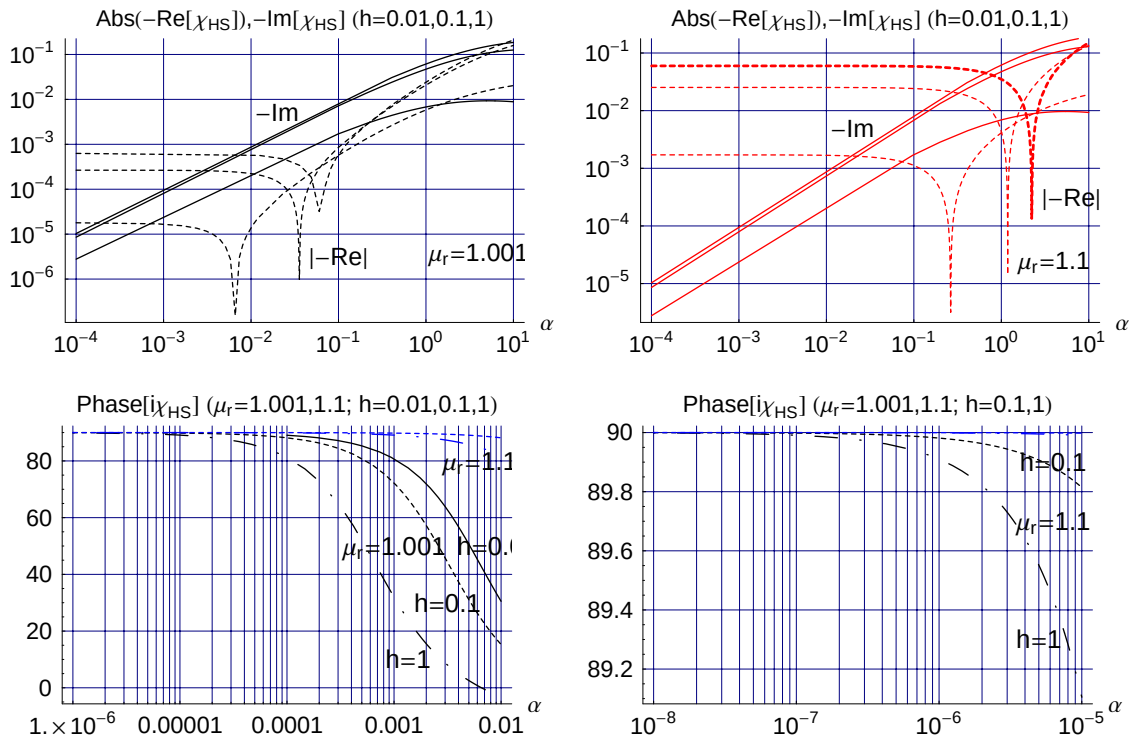

Figure 4.5: Half-space response function for a **magnetic** soil as a function of **loop height**. *Top row*: left: μ_r=1.001, right: μ_r=1.1, and h_N=0.01 (uppermost curves), h_N=0.1 and h_N=1 (lowermost curves); –Re is dashed (values to left of dip are negative!), –Im continuous. *Bottom row*: h_N=0.01 (continuous), h_N=0.1 (dashed) and h_N=1 (dot-dashed).

We have on the other hand chosen to ignore displacement currents, as already discussed, which leads to a simpler response parameter of the well known $i\omega\sigma\mu a^2$ form where a is here the coil radius, see Eq. (4.14) and Eq. (4.15). This is a good approximation, in our scenario, when not working at high frequencies, say less than 100 kHz, and in not excessively resistive ground, i.e. when displacement currents can be prevalent, as already discussed in §3.4.2.

4.3. Frequency Differencing Methods

The possibility of reducing the background signal due to the soil, in order to enhance the signal to noise ratio, has been recognized quite a long time ago. One of the possible techniques when working with frequency domain systems foresees the use of two or more different frequencies. [WAR67] does already mention the use of multiple frequency operations to reduce terrain noise, whereas [KEL66] describes the use of difference signals for background rejection. Frequency differencing methods are also well known in Non-Destructive Testing, e.g. to reduce the background response due to interfering (fixed) objects.

The basic idea is that the difference signal(s) is/are null when no target object is present, whereas in presence of a conductive zone the mutual coupling between the transmitter and the receiver coil changes (more at the higher than at the lower frequency) and an anomaly is recorded in the difference channel(s). Multigeometry systems have also been described as well in the geophysical literature.

There are actually several different ways of combining a detector's output at different frequencies to generate difference signals, and their degree of effectiveness depends in general on the nature of the background, on the type of the target and on the operating conditions (system frequency and geometry, which influence the background and target response parameters). [KAU89] discusses a few of them for several geophysical scenarios, and compares the results to those achievable with time domain methods.

Note that one might well recover the target signal and be able to detect it, but the same is not necessarily true for target discrimination; in other words, an increase in target detection capability is not necessarily accompanied by an increase in target discrimination capability.

In NdT a standard way consists in scaling the response at a second (higher) frequency and shifting its phase, so that it nulls the response at a first (lower) frequency.

In Geophysics it has been observed that the response function at low induction numbers, e.g. at low frequencies, is proportional to ω. It has therefore been suggested [KAU78, KAU01] to use the quantity:

$$\Delta Im \;=\; Im(\omega_2) - \frac{\omega_1}{\omega_2} Im(\omega_1) \tag{4.17}$$

where *Im* is the imaginary (quadrature) component of the magnetic field[48], or equivalently of the response function, to reduce the influence of "geological noise" from poorly conductive structures relative to the response from more conductive targets, for example at $\omega_2=2\omega_1$.

An alternative, used in the "Genie" system[49] and described in [JOH86], consists in measuring the ratio *R* of the magnetic field amplitudes at two widely separated frequencies:

$$R \;=\; \left\{ \frac{A(\omega_2)}{NA(\omega_1)} - 1 \right\} \times 100 \text{ percent } \cong Re(\omega_2) - Re(\omega_1) \text{ percent} \tag{4.18}$$

where $A(\omega)$ is the amplitude of the (vertical) magnetic field at the frequency ω, *N* is a normalizing factor taking into account the difference in transmitter moments at the two frequencies, and $Re(\omega)$ is the real (in-phase) response component. The approximated result in Eq. (4.18) is actually valid for small values of $Re(\omega)$ and $Im(\omega)$. The measurement of *R* allowed to obtain clean in-phase data, eliminating coil separation/orientation errors.

What is of interest to us here is in particular the idea of calculating the difference of the real part of the response function, although it will be done primarily to eliminate the influence of magnetic ground. The reader is also referred to [SIG02] for references to patents dealing with frequency differencing techniques and with other ways to reduce the ground effect.

Finally, note that we will reason in the next paragraphs in terms of the response function, which is equivalent to measured induced voltages divided by iω as usual.

4.3.1. Ground Response

The **relative difference of the half-space response function** χ_{HS} (see Eq. (4.12)) of a magnetic ground, calculated using both frequency differencing methods previously explained, is plotted in Figure 4.6 for two representative permeability values, μ_r=1.001 and 1.1, and for two frequency ratios[50], f_2/f_1=2 and 8, the latter being typical of the Förster Minex metal detector, §5.1, whose data we will analyse in the following. The left plot corresponds to an implementation of Eq. (4.18), the right to Eq. (4.17). The ground permeability has been here assumed as frequency independent.

The difference of the *real part* of the response function χ_{HS} is plotted to the left in relative terms, i.e. normalized to $Re(\omega_1)$. It is apparent that the effect of the plateau in the response function in Figure 4.4 has been removed. The absolute difference is actually very similar at the two permeabilities, and increases with increasing frequency ratio. The plot for a non-magnetic ground

48. The equivalent quantity for the measured voltage has therefore to take into account the usual factor iω.
49. Which consisted of Horizontal Coplanar (HCP) coils and measured the vertical magnetic field.
50. Actually at two different ratios of the response parameter $\alpha=\sigma\mu_1\omega_1 a^2$ (*a*= *coil* radius, see Eq. (4.15)).

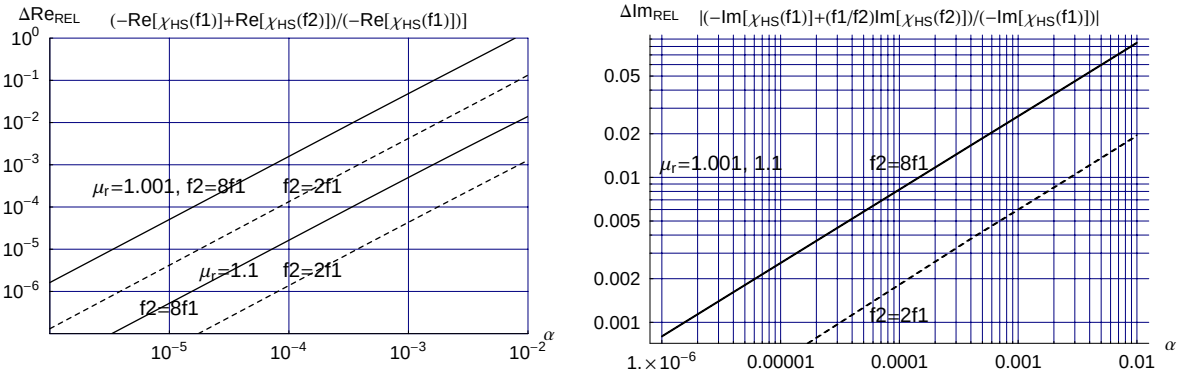

Figure 4.6: **Frequency differencing** techniques applied to a **magnetic** half-space's (ground) response functions, for $f_2=8f_1$ (continuous) and $f_2=2f_1$ (dashed). Right: the curves for $\mu_r=1.001$ and 1.1 are basically coincident.

($\mu_r=1$) would not have shown a significant gain with respect to measuring the real part at the highest of the two frequencies, as can be deduced from Figure 4.2. Finally, note that in the case of a superparamagnetic ground this simple difference might have to be replaced with one including a logarithmic frequency factor (see Eq. (4.4)).

The difference of the *imaginary part* of the response function χ_{HS} is plotted to the right, again in relative terms, i.e. normalized to $Im(\omega_1)$. The curves for the different permeability values are practically coincident. The differencing effectiveness gets again worse for increasing frequency ratios.

In practice the differencing scheme corresponding to the plot on the left is usually employed to suppress the effect of magnetic soil (for example by the Förster Minex), the one corresponding to the right plot to suppress the effect of conductive soils.

Frequency differencing methods will obviously affect the target response as well. We will therefore look in the next paragraph at the overall response of a sphere, a representative target whose response function we already discussed in detail in Chapter 3.

4.3.2. Sphere Response

The **difference of a sphere's response function** χ_{SPH}, ferromagnetic and non ($\mu_r=10$ and $\mu_r=1$ respectively), calculated again using both frequency differencing methods previously explained, is plotted in Figure 4.7 for the same frequency ratios[51] as above starting from Eq. (3.14). The continuous curves correspond to the standard response at f_1. The left plot corresponds again to an implementation of Eq. (4.18), the right to Eq. (4.17).

Notice in particular how the response is reduced:

- for targets with low response parameter (e.g. low conductivity and/or small size) in the case of ΔIm, and ΔRe for a ferromagnetic object in particular.
- for target with high response parameter (e.g. high conductivity and/or large size) as well in the case of ΔRe.

resulting in a bell-shaped response curve peaking at some intermediate value of the response parameter. In addition the magnitude of the difference curves decreases with decreasing frequency ratio. Some care has therefore to be applied when using these types of differences, depending on the type of target sought.

51. Actually at two different ratios of the response parameter $\alpha=\sigma\mu_1\omega_1 a^2$ (a= *sphere* radius, see Eq. (3.15)).

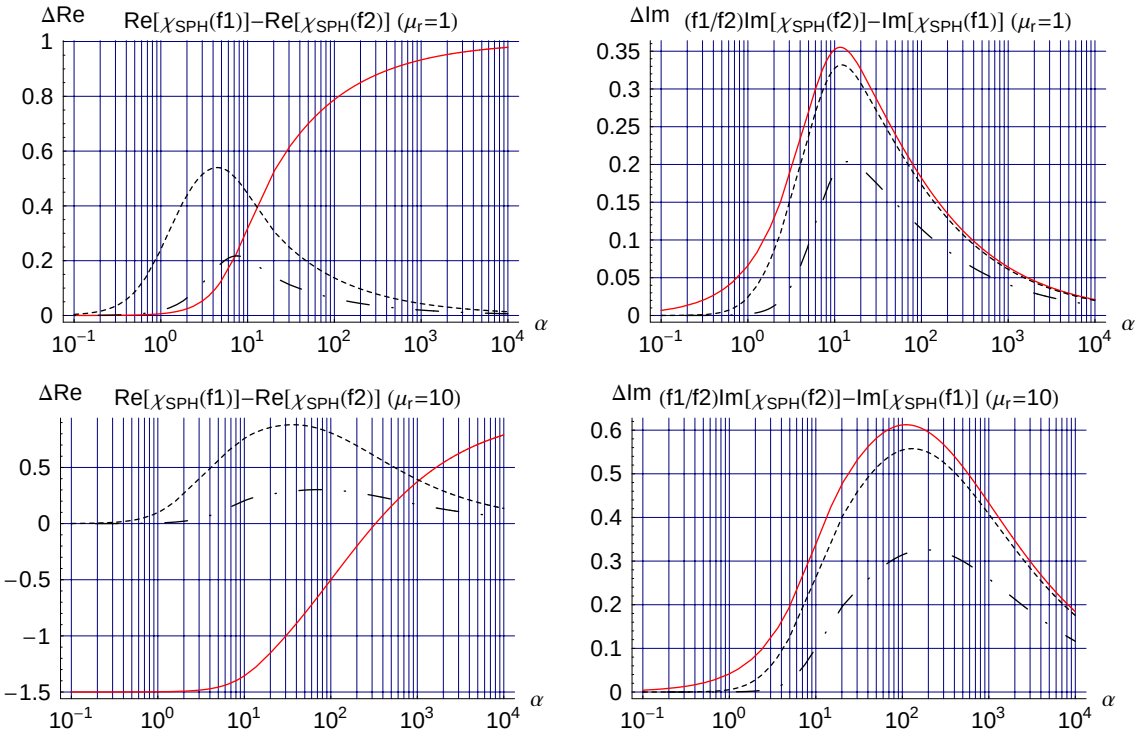

Figure 4.7: **Frequency differencing** techniques applied to a **sphere's** response function, non-magnetic (top) and magnetic (bottom, μ_r=10), for f_2=8f_1 (dashed) and f_2=2f_1 (dot-dashed). In red (continuous): –Re[χ],–Im[χ] at f_1.

4.4. On the Ground's Influence on the Primary and Scattered Fields

We have already discussed in some detail in the previous chapter the response of a conductor embedded in a conductive medium, in a number of scenarios of interest. What we want to point out here is that even in the case where the total secondary fields cannot be separated in a contribution due to the host medium alone plus a contribution due to the conductor situated in free space (see the discussion in §3.7 and Eq. (3.55)), a simplified response might still available, valid in particular for "small targets".

We might indeed consider the ground effect on the primary and secondary fields as being in first approximation equivalent to a *phase shift*, i.e. a rotation in the complex plane, proportional to frequency, and an *attenuation* of the primary field on its way to the target, with a similar effect on the secondary field on its way back to the receiver (§3.2.1). When the host medium is conductive but still relatively ease penetrated by the EM fields, and the transmit and receive locations are close to the target, such a low-pass filtering behaviour is just a phase shift, and has been approximated in [NAB91,pp.36-38] with the following response function:

$$T \cong \exp[-2i\sigma\mu_1\omega l d] \;=\; \exp\left[-4il\frac{d}{\delta^2}\right] \tag{4.19}$$

where d is the target depth, σ and μ_1 are the ground conductivity and permeability, l is a horizontal scale parameter (of the order of the coil radius in our case), and $\delta=(2/\sigma\mu_1\omega)^{1/2}$ is the skin depth in the soil (see also Table 3.2).

The previous response function applies directly to both the target vortex (eddy) and galvanic response (§3.7), if any. The total secondary fields are then obtained by adding the contribution from the ground itself (host response). This effect is likely not to represent a problem in our application, perhaps with the exception of high conductivity ground and/or for deep objects, and when operating at higher frequencies. In these cases it would however introduce a change in target signature, which could not simply be compensated by subtracting the ground response measured in the absence of the target.

4.5. Conclusions

Soil effects, whose presence we have recognized early on during this work and which are often not sufficiently considered in the existing scientific literature related to humanitarian demining applications, have been calculated in this chapter by studying the response of a circular loop in a homogenous half-space model, for different soil permeabilities and (normalized) detector heights. This has allowed to confirm in quantitative way their **importance** (for FD systems in particular). We have also drawn attention to **superparamagnetic** effects, which can play a role under certain conditions.

The role of the soil's *permeability*, which heavily affects the *real* part of the response function, has been clearly shown (plateau effect at low frequencies). The *imaginary* part is on the other hand linear in the response parameter (induction number). The latter is of the $i\omega\sigma\mu a^2$ form, confirming the dimensional analysis of A3.3.1. The effects of *changes in the detector's height* are also apparent, in particular on the real part of the response function for magnetic soils.

These dependencies can also be extrapolated to give an idea of the importance of **fluctuations in the ground's parameters** (inhomogeneities, height profile fluctuations), which will inevitably be present in real conditions, and which are also clearly documented in the experimental data of Chapter 5. For example, a 10% fluctuation in soil permeability will be roughly equivalent to a similar fluctuation in the imaginary component of the induced voltage, and therefore be more important in absolute terms when working in difficult ground conditions (high permeability).

Frequency differencing methods to reduce soil effects have also been described, and two of them studied in more detail. The half-space model has allowed us to understand why they work and to assess in a quantitative way how well they work; at the same time we have shown what is the price to pay in terms of reduction of the target's response in the case of a sphere. This will also help in understanding the behaviour of the experimental data in Chapter 5 and in the analysis of features more robust to background fluctuations (Chapter 6).

Some of these results have obviously already been known to the metal detector community from the experimental point of view for a certain time, and partly to the geophysical community as well, although the latter does usually put less emphasis on the ground's permeability. We therefore see added value in having joined the two ends, putting together this information in a coherent way with emphasis on humanitarian demining specificities, and with the necessary scientific rigour.

We have hereby finished setting the theoretical framework, and can now move to the analysis of the experimental data.

Bibliography

[BEA98] Beard, L., and Nyquist, J. E., 1998, Simultaneous inversion of airborne electromagnetic data for resistivity and magnetic permeability: Geophysics, v. 63, no. 5, September-October, p. 1556-1564.

[BLI97] Blitz, J., 1997, Electrical and Magnetic Methods of Non-destructive Testing: Chapman & Hall, London, UK.

[CHE65] Cheng, D. H. S., 1965, The Reflected Impedance of a Circular Coil in the Proximity of a Semi-Infinite Medium, IEEE Transactions on Instrumentation and Measurement, v. IM-14, no. 3, p. 107-116.

[DOD68] Dodd, C. V., and Deeds, W. E., 1968, Analytical Solutions to Eddy-Current Probe-Coil Problems: Journal of Applied Physics, v. 39, no. 6, May, p. 2829-2838.

[DOD69] Dodd, C. V., Deeds, W. E., and Luquire, J. W., 1969, Integral Solutions to some Eddy Current Problems: International Journal of Nondestructive Testing, v. 1, p. 29-90.

[HUA01] Huang, H., and Fraser, D. C., 2001, Mapping of the resistivity, susceptibility, and permittivity of the earth using a helicopter-borne electromagnetic system: Geophysics, v. 66, no. 1, January-February, p. 148-157.

[IGN85] Ignetik, R., Thio, Y.-C., and Westfold, K. C., 1985, Transient electromagnetic field above a permeable and conducting half-space: Geophysical Journal of the Royal Astronomical Society, v. 81, p. 623-639.

[JOH86] Johnson, I. M., and Doborzynski, Z. B., 1986, A novel ground electromagnetic system: Geophysics, v. 51, no. 2, February, p. 396-409.

[KAU78] Kaufman, A. A., 1978, Resolving capabilities of the inductive methods of electro-prospecting: Geophysics, v. 43, p. 1392-1398.

[KAU89] Kaufman, A. A., 1989, A Paradox in Geoelectromagnetism, and its Resolution, Demonstrating the Equivalence of Frequency and Transient Domain Methods: Geoexploration, v. 25, p. 287-317.

[KAU01] A. A. Kaufman, and P. A. Eaton, *The Theory of Inductive Prospecting.* Amsterdam, NL: Elsevier, 2001.

[KEL66] G. V. Keller, and F. C. Frischknecht, *Electrical Methods in Geophysical Prospecting.* Oxford, UK: Pergamon Press, 1966.

[LEE74] Lee, T., and Lewis, R., 1974, Transient EM response of a large loop on a layered ground: Geophysical Prospecting, v. 22, p. 430-444.

[LEE84] Lee, T., 1984, The transient electromagnetic response of a magnetic or superparamagnetic ground: Geophysics, v. 49, no. 7, July, p. 854-860.

[MOR69] Morrison, H. F., Phillips, R. J., and O'Brien, D. P., 1969, Quantitative interpretation of transient electromagnetic fields over a layered half-space: Geophysical Prospecting, v. 21, p. 1-20.

[NAB87] Nabighian, M. N. (Ed.), 1987, Electromagnetic Methods in Applied Geophysics, Volume 1, Theory: Investigations in Geophysics No. 3, Society of Exploration Geophysicists (SEG), Tulsa, OK, USA.

[NAB91] Nabighian, M. N. (Ed.), 1991, Electromagnetic Methods in Applied Geophysics, Volume 2, Application: Investigations in Geophysics No. 3, Society of Exploration Geophysicists (SEG), Tulsa, OK, USA.

[OAT92] Oaten, S. R., and Blitz, J., 1992, Impedance analysis for air-cored cylindrical eddy current coils scanning the surfaces of defect-free conductors: Nondestructive Testing and Evaluation, v. 6, p. 323-335.

[RYU70] Ryu, J., Morrison, H. F., and Ward, S. H., 1970, Electromagnetic fields about a loop source of current: Geophysics, v. 35, no. 5, October, p. 862-896.

[SIG02] Sigrist, C., and Bruschini, C., "Metal Detectors for Humanitarian Demining: a Patent Search

and Analysis", EUDEM2 report, May 2002. Available from http://www.eudem.vub.ac.be/

[SPI91] Spies, B. R., and Frischknecht, F. C., 1991, Electromagnetic Sounding, in [NAB91], p. 285-425.

[THO77] Thomas, L., 1977, Electromagnetic Sounding with Susceptibility among the Model Parameters: Geophysics, v. 42, no. 1, February, p. 92-96.

[WAI79] Wait, J. R., 1979, Review of Electromagnetic Methods in Nondestructive Testing of Wire Ropes: Proc. of the IEEE, v. 67, no. 6, June, p. 892-903.

[WAI82] Wait, J. R., 1982, Geo-electromagnetism: Academic Press, New York.

[WAR87] Ward, S. H., and Hohmann, G.W., 1987, Electromagnetic Theory for Geophysical Applications, in [NAB87], p. 130-311.

5.

Metal Detector Raw Data Analysis

In order to i) compare the experimental data with theoretical expectations, ii) get qualitative indications of a CW (Continuous Wave) metal detector response to objects of interest in humanitarian demining (mines and clutter), and iii) analyse the possibility of identifying targets of interest, or at least discriminating some metallic objects based on their characteristic response (in particular the phase), we have acquired and analysed an extensive amount of metal detector raw data using a commercially available differential CW system, the Förster Minex 2FD.

We have recorded the detector's internal signals, i.e. the in-phase and quadrature-phase component at each frequency, as well as the difference of the two quadrature-phase components and the audio signal available to the operator. Experimental data has been acquired by varying different object parameters, in a laboratory setup with the objects either flush or buried. Linear scans, and in some cases series of parallel scans as well, have been carried out with a high density of points in the scan direction, placing the detector on a Cartesian gantry.

Scans of general interest will be detailed first (§5.2), followed by an analysis of the response of *reference objects* (spheres, cylinders, etc.; §5.3), of the response variation with *distance* (§5.4), with *axial offsets* (2D parallel scans; §5.5) and with the object's *orientation in the horizontal plane* (§5.6). Detailed responses will then be shown for a *minimum-metal mine* and its components (§5.7), a **`PMN`** *mine* (medium metal content mine; §5.8), *metallic mines* (**`PROM`**, **`PMR-2A`**) and a *composite UXO* example (§5.9). Finally, several tens *metallic clutter pieces* will be looked at (§5.11). Overall results will be extensively summarized at the end of the chapter (§5.12). No particular attempt at background subtraction has been done other than the subtraction of the mean values (to remove offsets).

The collection of data as a function of movement enables the possibility of analysing the data in the complex, or impedance, plane (in-phase vs. quadrature-phase component). This method resembles measurements carried out in Non-Destructive Testing (NdT), from where it was inspired, and makes it possible to exploit global object properties rather than only local ones.

5.1. The Förster Minex Metal Detector

This Förster Minex 2FD is a CW system which generates **two continuous wave frequencies**, at 2.4 kHz and 19.2 kHz. The first frequency is aimed in particular at the detection of ferromagnetic objects, the second at the detection of stainless steel and alloys, in agreement with the modelling results of Chapter 3 and the corresponding frequency dependence.

The transmitter of the Förster Minex 2FD consists of a conventional copper coil (diameter 230 mm), whereas its receiver is composed of an eight-layer printed circuit board (diameter 200 mm), coaxial and coplanar with the transmitter, arranged as a gradiometer (see Figure 5.1).

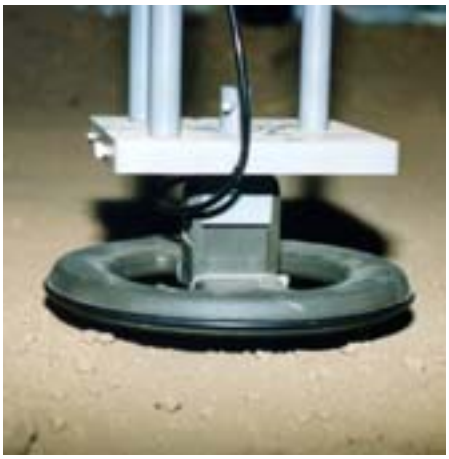

Figure 5.1: Förster Minex 2FD detector head on gantry support frame [BRU00b].

This results in a differential left-right system, its output audio signal vanishing (no tone) when the detector's mid axis crosses the object's centre, thus allowing a very precise spatial localisation along one dimension as schematically represented in Figure 5.2, with the standard response shown for comparison. The differential setup also helps in background suppression and enhances the separation power (localizing nearby objects). On the other hand mechanical tolerances are stricter, and sensitivity is probably somewhat reduced, given that the receiving coil has been split into two, effectively halving the sensitive area.

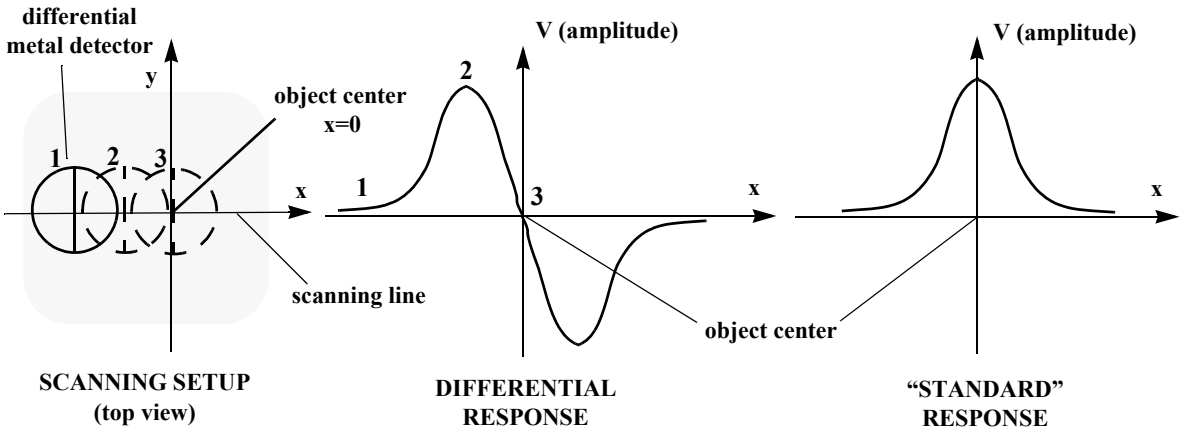

Figure 5.2: Differential response, and standard response for comparison (both qualitatively), for a linear scan along x

The physical quantity which the detector measures is therefore an approximation of the gradient of the induced magnetic field (actually its vertical component) along a direction perpendicular to the detector's axis, i.e. $\partial B_z^{\text{sec}} / \partial x$ when working as shown in Figure 5.2.

To fully exploit the detector's capabilities we intercept, at the output of the receiver-transmitter module, five signals ($f_1 0°$, $f_1 90°$, $f_2 0°$, $f_2 90°$, Delta) corresponding respectively to the real ($f_1 0°$, $f_2 0°$, or equivalently f_1 REAL and f_2 REAL) and imaginary parts ($f_1 90°$, $f_2 90°$, or equivalently f_1 IMAG and f_2 IMAG) (in the complex plane) of the analog signals $V_1^{(s)}$ and $V_2^{(s)}$ induced at f_1 and f_2 in the receiver, and the difference of the imaginary parts multiplied by a constant (Delta=c($f_1 90° - f_2 90°$)), which turns out to be quite insensitive to changes in (back)ground conditions.

These internal signals are normally not available to the standard user and do not depend on the sensitivity setting. They are continuously analysed by a microprocessor which delivers an output (Audio), the standard audio signal (i.e. what the operator would hear), relying mostly on the Delta signal. The Audio signal depends heavily on the sensitivity chosen[52].

The induced voltages $V_1^{(s)}$ and $V_2^{(s)}$ are amplified by a factor F_1 and F_2 respectively, which are chosen to satisfy the following relationship (I_1 and I_2 are the currents in the primary coil at f_1 and f_2 respectively):

$$F_1 \cdot \omega_1 \cdot I_1 = F_2 \cdot \omega_2 \cdot I_2 \tag{5.1}$$

This scaling effectively removes the linear dependency on ω of the induced voltage (see for example Eq. (3.13)) and makes it possible to use the Delta signal defined before to suppress the soil influence. It also allows us to compare the ratios and trends of the induced voltages with those of the response function χ.

The real part is again often referred to as "in-phase", the imaginary part as "quadrature-phase" component, whereby the phase is measured with respect to the transmitted signal shifted by a constant amount (a few degrees), representing a reference angle which corresponds to a typical magnetic soil. This phase shift stays constant unless a "ground cancellation (balancing) procedure", one of the detector's options, is explicitly performed. A slow "ground following" adaptation function is also implemented.

Note that a magnetic object, e.g. ferrite, would deliver a purely quadrature phase signal (90° phase shift).

Typical signals are shown in Figure 5.3 and Figure 5.5 taking as example the object represented in Figure 5.4, bottom left (striker pin of a minimum-metal mine). Data collection has been carried out in a straight line across the object's centre, recording the signals with a dedicated 16 bit conversion card over +/–5 Volt every 0.56 mm (about 2 points per mm); the data acquisition card and gantry which make this possible have been realised by Frédéric Guerne at the EPFL.

Typical scan lengths were between 60 and 100 cm with the detector at 2-3 cm above the ground unless otherwise specified. The data was then lowpass filtered with a simple sliding window 30 to 90 data points wide[53], and centred (subtraction of mean value to remove offsets). The Audio signal was median filtered over 5 data points to eliminate outliers.

The detector's differential response is clearly visible in Figure 5.3, where "Left" has been assigned to lower value coordinates. When moving in the direction of increasing coordinates – from "Left" to "Right" – a first peak is traversed to the left of the object ("LeftPeak"); the object centre then comes at about x=600 mm, followed by a second peak to the right of the object ("RightPeak"). Note that the signal for such a small and shallow object is about as wide as the detector head itself.

52. Three different levels of sensitivity (1, 2 and 3) are user-selectable. Default is 1 (lowest), 3 is equivalent to extremely sensitive.
53. Actually the MATLAB® "filtfilt" function was used (zero-phase forward and reverse digital filtering); the effective filter order is therefore twice the figure quoted.

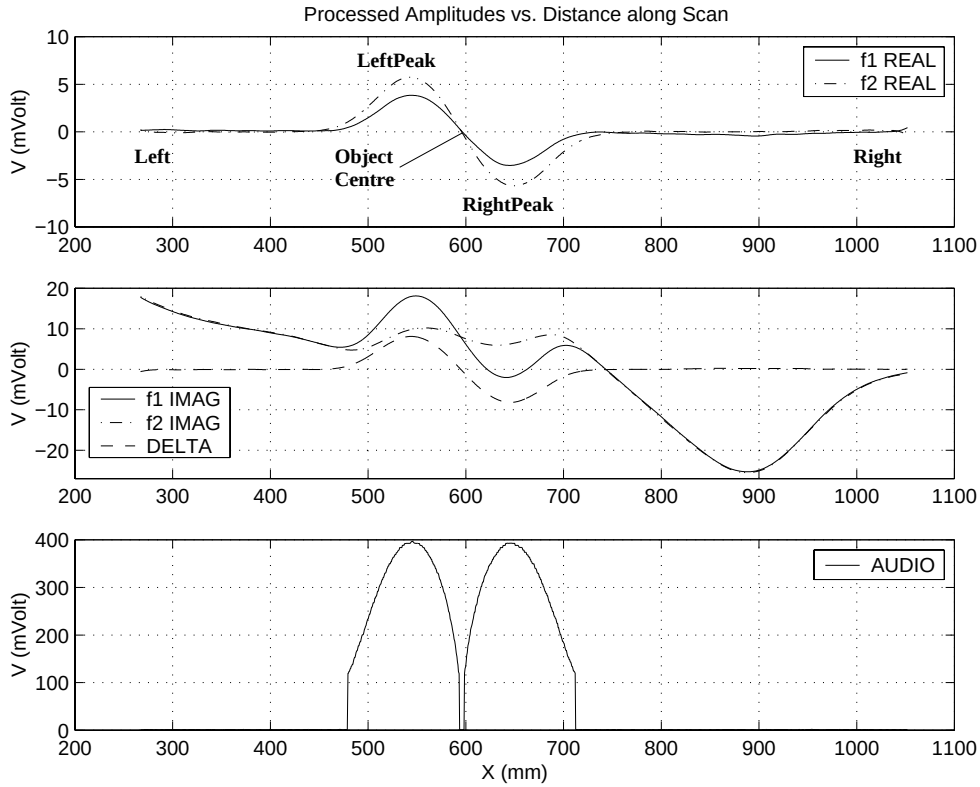

Figure 5.3: Typical processed (i.e. filtered and entered) internal and Audio signals from the Förster Minex 2FD metal detector [BRU00b].

The imaginary components show large fluctuations outside the zone of interest, probably due to soil inhomogeneities and/or surface height variations; these fluctuations are in fact strongly correlated and the imaginary signals practically overlapping. The resulting difference (Delta) is therefore non zero only in correspondence of the target. The real components are on the other hand clean and unambiguous in the given experimental conditions. Note that the Audio signal results from a thresholding, towards positive and negative values, of the sole Delta signal; the former is measured by our data acquisition system as unipolar, but is in fact bipolar – a different tone is emitted for each polarity, which greatly eases pinpointing. The object's centre is in a position corresponding to the dip in between the peaks of the audio signal at x=600 mm, in correspondence of the zero crossing of Delta.

Standard Scanning Setup

After having checked that the soil is free of metallic objects, scans were carried out using the standard parameters detailed in A5.1 (unless otherwise indicated).

Summarising, linear scans, and in some cases series of parallel scans as well, have been carried out with a high density of points in the scan direction, placing the detector on a Cartesian gantry [BRU98a]. The latter has been transferred in 1998 from the EPFL in Lausanne, where initial data collections have taken place [BRU98a, BRU98b], to the VUB in Brussels. Preliminary results have been detailed in [BRU00b].

A number of mines to which we will often refer in the following are grouped in Figure 5.4, which details in particular their metallic content.

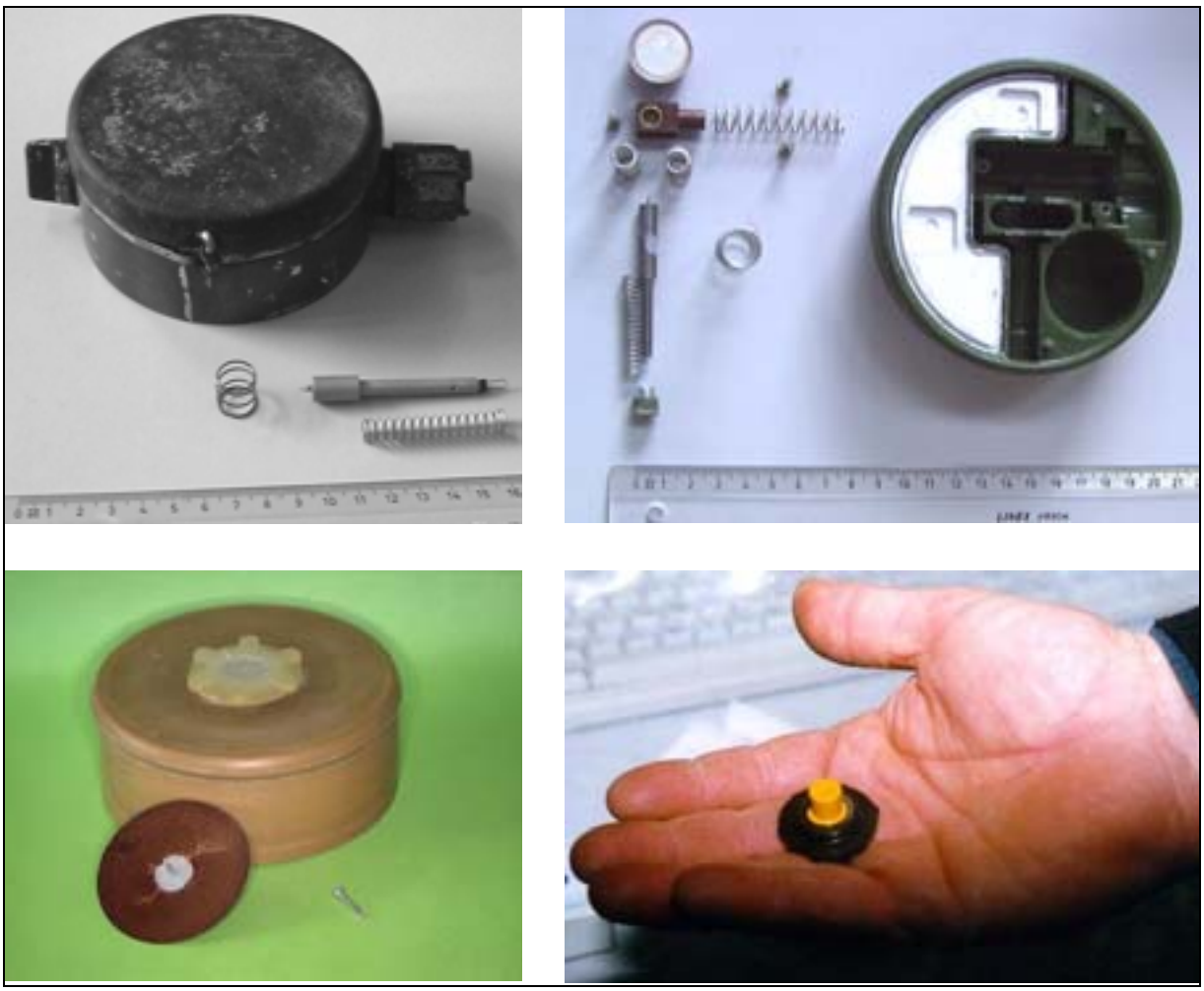

Figure 5.4: Metallic content of a Russian PMN (**`pmnCambodia`**; top left), a Russian PMN2 (top right), and an LI11 min.-metal mine (**`mich`**; bottom left), with detail of striker pin (**`mist`**) and original detonator (**`midereal`**, bottom right). (Source: EPFL/DeTeC)

Amplitude Ratio

Apart from the phase response behaviour there is an additional parameter of interest on which we will comment in this chapter in a qualitative way, the ratio of the amplitudes of the received signal at the two frequencies (*Amplitude Ratio*, or *AR*). It will be defined in §6.2.2 and its distribution analysed in more detail in §6.2.6.

5.2. Data Collection Results: Scans of General Interest

We will detail in this paragraph the detector's response for scans of general interest, i.e. mostly aimed at sensor and environment understanding and characterization. No particular attempt at background subtraction has been done other than the subtraction of the mean values already described (to remove offsets).

For each data point in the complex plane we can obviously calculate a magnitude and a phase along the lines discussed in §2.2.4. When the phase response of the received signal changes little over the whole scan we get diagonal lines and the phase is nothing else but their slope. When this is not the case, either because the object has a characteristic phase response or because the background signal is prevailing, or both, there might still exist a general trend which can be used to calculate an "average phase". Another possible choice is for example to take the phase where the signal is strongest [SZY99], at the positions we previously labelled "LeftPeak" and "RightPeak". We will concentrate here on the qualitative aspects of the received signal (the curves' slopes and shapes). A quantitative analysis of the phase response will be undertaken in Chapter 6.

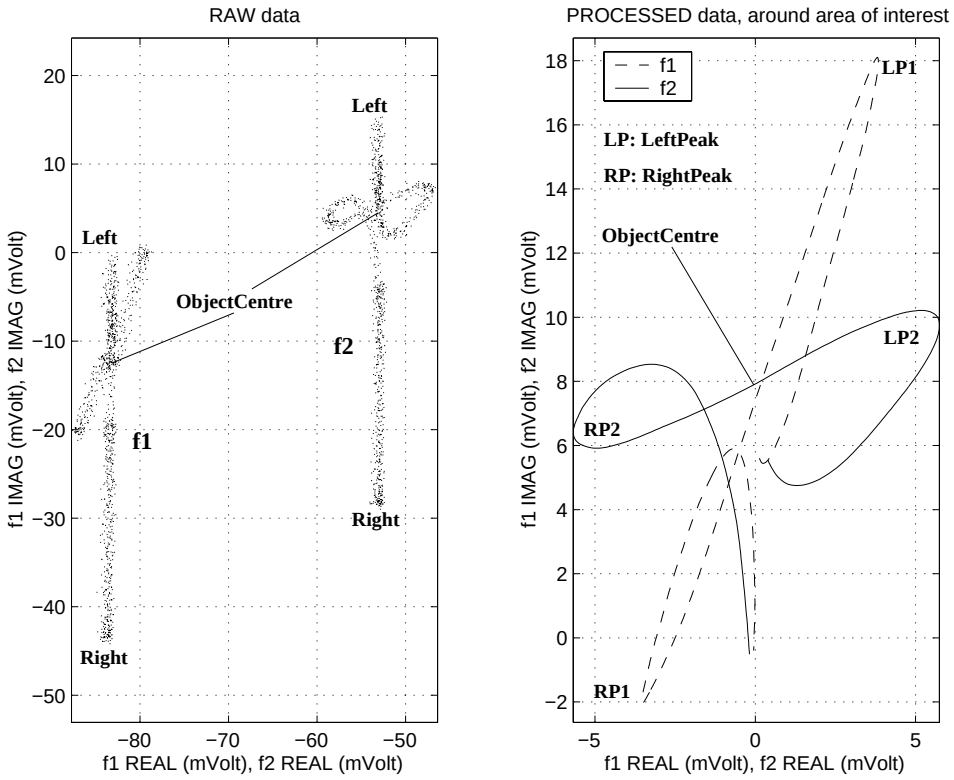

Figure 5.5: **Raw** and **processed** internal signals (see also Figure 5.3) plotted in the complex plane [BRU00b]

Raw vs. processed data in the complex plane and background fluctuation effects

The right half of Figure 5.5 shows the processed data from Figure 5.3, plotted this time directly in the complex (impedance) plane and taken around the area of interest only (from x=450 mm to x=750 mm). The left half of Figure 5.5 shows the raw data from the same acquisition, that is all data unprocessed; the sets of data points at the two frequencies are well separated, due to the signals having different offsets. These offsets seem to be rather constant.

In this particular case the background fluctuations, probably due to soil inhomogeneities as discussed before, are not negligible and the corresponding curves in the complex plane are distorted, in particular at f_2. The target signals, corresponding to the diagonally lying sets of points, are however still strong enough and we can rather clearly separate them in the left half of

the image from the background signals[54] (the fluctuating imaginary component which translates into vertically distributed data points). This is unfortunately not always the case.

Soil 2D Scans

Detailed soil scans (sand) were carried out at the EPFL and the VUB sandbox. Under these conditions *reproducible fluctuations are clearly visible in the imaginary components* ($f_1$90°, $f_2$90°), at the mV level (Figure 5.6) and basically identical for both components. They are most likely due to *fluctuations in soil homogeneity and/or ground profile*. Fluctuations in the real component ($f_1$0°,$f_2$0°) are at the noise floor level (of the order of 0.1 mV) and are not shown. This behaviour is consistent with the modelling results of Chapter 4 for a resistive paramagnetic ground.

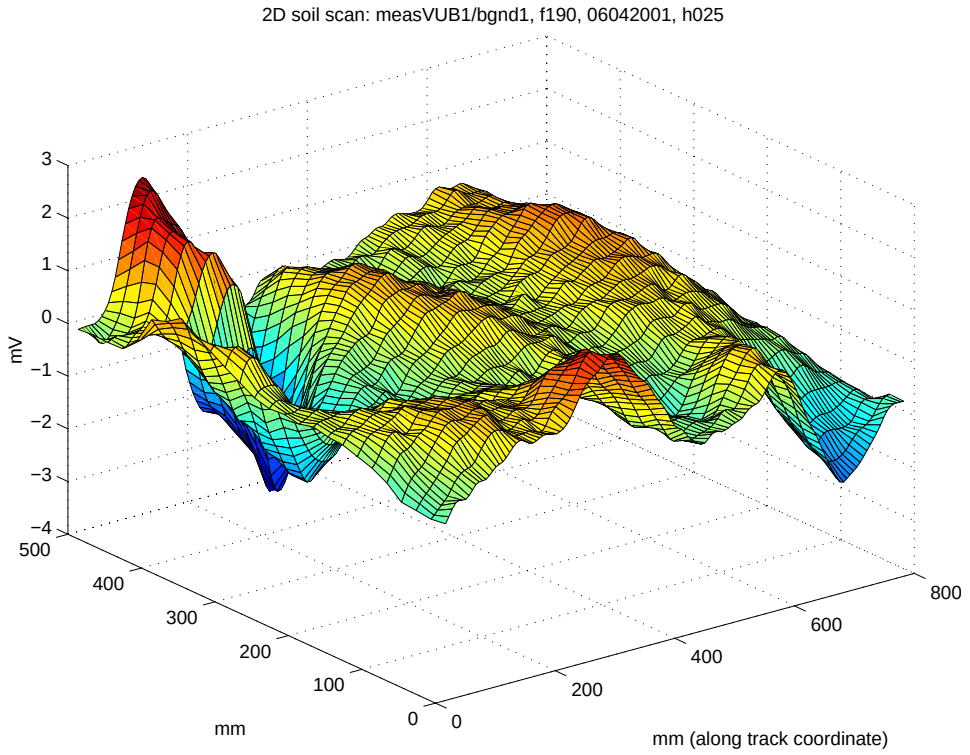

Figure 5.6: 2D **soil** scan (sand), $f_1$90°. *z*: Amplitude (in mV).

These 2D scans were taken, as most of the following ones, over a surface of 500×800 mm with 26 parallel scans, separated by 2 cm, along the y axis (y is the along track coordinate).

Additional scans were taken after having disturbed the sand surface, in particular (**`bgnd3v2`**) after having disturbed the surface in the upper right (455,655) and lower left corner (140,192), and (**`bgnd3v3`**) after having dug a conical hole (30 cm dia, 15 cm depth at lowest point) in the centre (210, 446), removing the sand from the test area. **`bgnd1v2`** represents undisturbed soil, see Figure 5.7.

Differences are clearly visible, although it is not straightforward to relate them to the action taken (e.g. the hole should be in the centre!). This could point to additional (electronics?) filtering effects, which are not apparent under normal operating conditions aimed at the detection of small high conductivity targets.

54. Which have been cut in the right half of the image as already said.

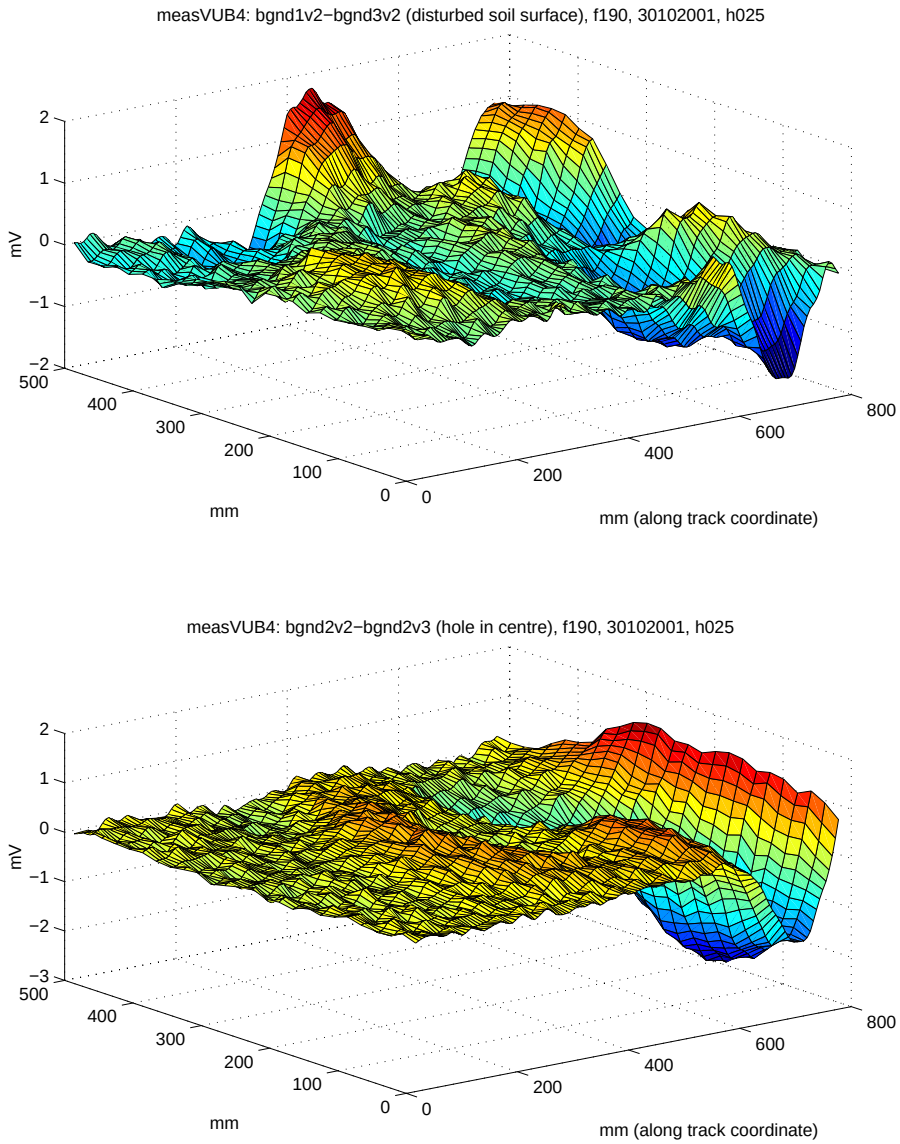

Figure 5.7: 2D **soil** scan (sand), $f_1$90°, after having disturbed the surface twice (see text).

Other Soil Scans

A one dimensional scan of a Cambodian soil sample (lateritic earth) is shown in Figure 5.8. A small quantity of sand has been taken out of the sandbox, in the centre of a 1D scan, and replaced by the test earth sample; a localized anomaly is therefore generated. A small but clear *"magnetic" response* is visible (imaginary components), equal at both frequencies, corresponding to a phase angle of about 2-3°. Another Cambodian sample was analysed in the same way; no appreciable difference with the surrounding sand was remarked.

Forward/Reverse Scans

Scans were carried out along the same line and over the same object once in "forward" (i.e. with increasing along track coordinate value) and once in "reverse" direction. No signal differences were recorded, apart from a shift of 5-7 pixels (2.5-3.5 mm) possibly due to the gantry itself or to the (electronics) filtering effects previously described.

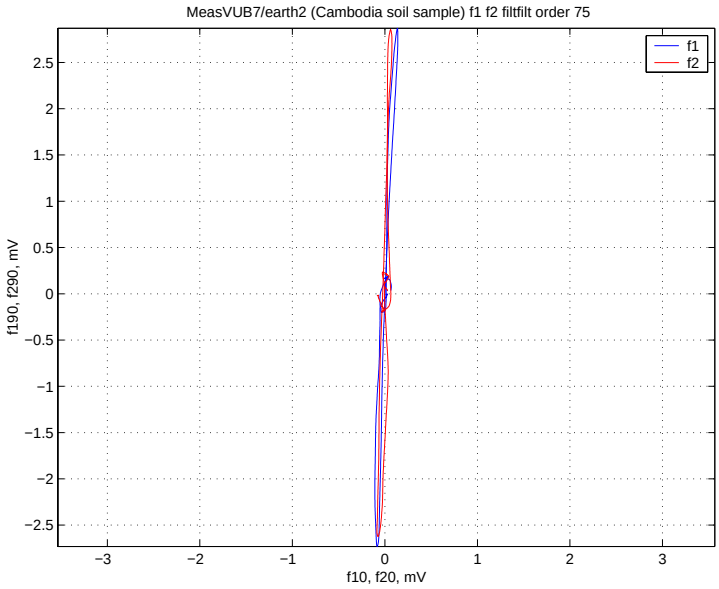

Figure 5.8: 1D scan over a **lateritic soil** sample (origin: Cambodia).

All 3 Sensitivity Levels

Identical scans were carried out varying the sensitivity level. The Audio signal does obviously change, all others are practically the same apart from a possible shift of +/–1 pixel, likely due to the gantry. Figure 5.9 presents an example of the Audio output for a small steel sphere (**`sts1`**) and a large one (**`sts4`**).This test does also constitute a measure of drift effects, which were not noticed on this time scale (several minutes).

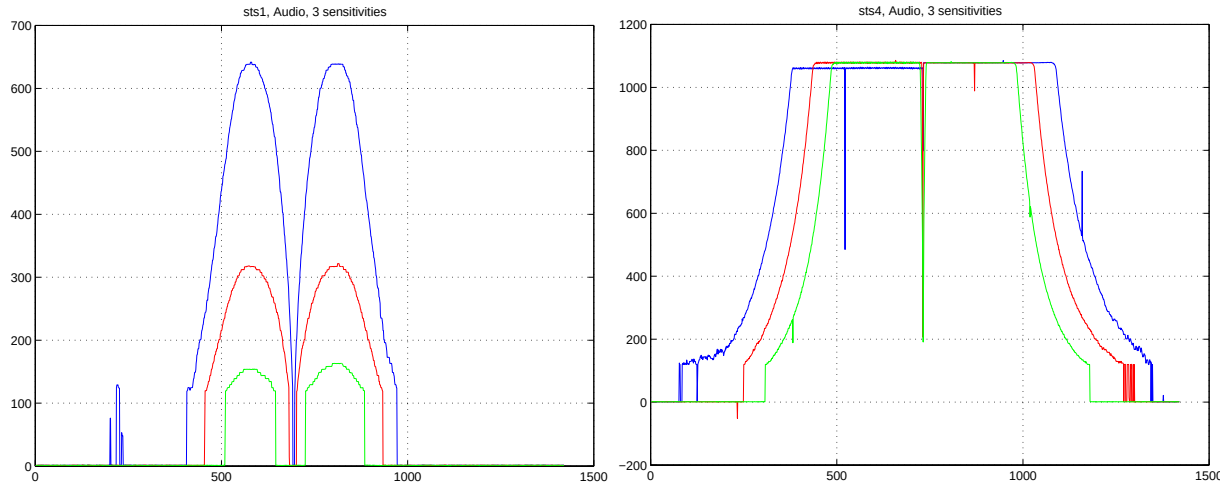

Figure 5.9: **Audio** output (3 sensitivity levels) over **`sts1`** (Left) and **`sts4`** (Right) (s=1: green, s=2: red, s=3: blue). x: samples, y: signal amplitudes (mV)

Second MD Head

All acquisition carried out at the EPFL sandbox used one and the same MD head, shown in Figure 5.1. As this was slightly damaged it was decided to employ a second head for most of the data acquisition carried out at the VUB, keeping the same electronics. No differences in response were noticed.

Background (Soil) Signal Subtraction

Most of the scans have been carried out on objects placed on the surface (usually for small objects) or just underneath it (*flush*), to ease data acquisition while at the same time taking into account the response from the soil itself, at least to first order. The latter is not negligible, even under these conditions, when looking at some of the smaller objects. Background (soil) scans, i.e. without target, should therefore ideally be taken for each object in 1D (along a line) or 2D (parallel lines).

As a compromise we decided to take background scans before and after each series of scans, for example when measuring different spheres one after the other under the same conditions. These background scans were then compared. In some cases there was a weak offset, which does not represent a serious drawback; a difference between the $f_1 90°$ and $f_2 90°$ channels was recorded in some cases as well in the centre of the scan (where the target objects were buried). Although this was generally not a problem, it implies that the background (soil) can change as a consequence of the measurement procedure (putting the object/s in place and removing it/them), and that *individual background scans* have to be performed when the highest measurement precision is required and/or the signals are very weak.

Normalized Plots

Metal detector data is quite often characterized by large amplitude differences from one scenario to the other. In order to be able to compare them we will often normalize the complex plane data by dividing each data point – its real and its imaginary part – by the maximum of the amplitude in the complex plane (each frequency separately). As the phase angle of each point does not change this transformation preserves the plot's aspect ratio. A normalized plot's scales are adimensional.

Typical Scan Configurations

Figure 5.10 reproduces the most typical data acquisition scenarios. The corresponding data will be described in the following paragraphs.

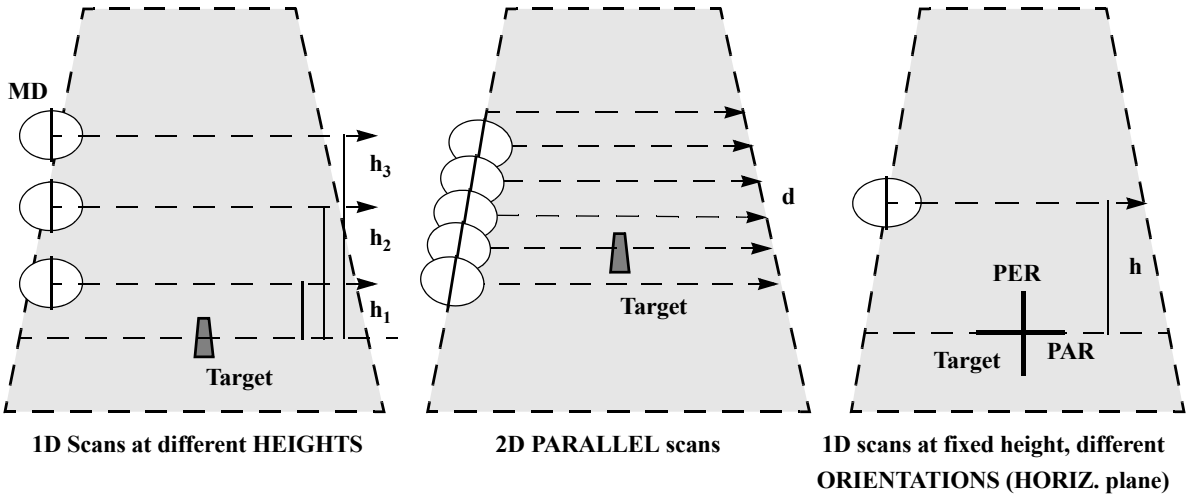

Figure 5.10: Typical data acquisition scenarios

See also A5.2 for a **Glossary** of the terms used in the following and A5.3, A5.4 for a list of **Filename and Object codes**.

5.3. Reference Objects

Before moving to more complex objects and scenarios it is useful to study the response of canonical targets such as spheres, cylinders, loops and magnets.

Spheres (sts1-sts4)

The non-normalized responses of the four reference steel spheres (**sts1** to **sts4**) are plotted in Figure 5.11 (offsets have not been subtracted): the phase angles are decreasing (the straight lines rotate in clockwise direction) when moving from f_1 to f_2 and from a smaller sphere to a larger one, in agreement with the modelling results of §3.4.5.2.

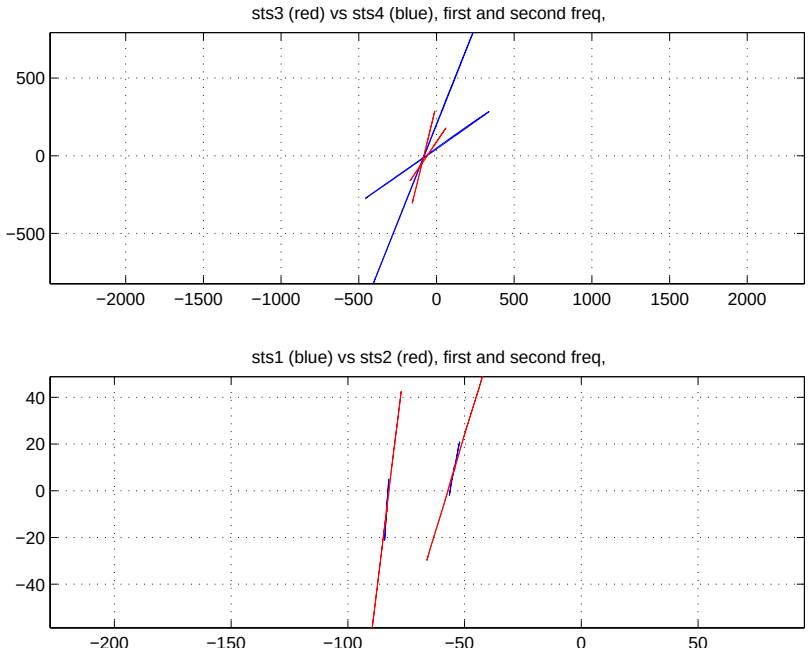

Figure 5.11: **Steel spheres**. Top: **sts3** (red, smallest amplitudes), **sts4** (blue). Bottom: **sts1** (blue, smallest amplitudes), **sts2** (red). Scales are in mV. x: f10,f20; y: f190,f290.

The *amplitude ratio AR* (see §6.2.2) is well above 1 for **sts1**, the smallest sphere, and decreases when moving towards **sts4**, in agreement with §6.2.6.

Cylinders

1D non-normalized responses for all cylinders except **msc2** (large: cyl2, small: cyl1), placed perpendicularly to the scanning direction (PER orientation), are shown in Figure 5.12, which confirms the expected phase and amplitude trends for increasing conductivity and is similar to the one for a sphere.

The amplitude ratio is >1 for **aac1**,**2** (ferromagnetic), <<1 for **alc1**,**coc1**, and <1 for **alc2**,**coc2** (aluminium and copper). This is again in agreement with §6.2.6, even if the cylinders are of finite length.

AR is quite small for the **inc1**,**2** *stainless steel cylinders* (about 1/3 and 1/7 respectively), and their response is *quite weak* as well, especially at f_1. Also, their phase is positive for **inc1** at both frequencies (practically invisible in the f_1 plot), and at f_1 for **inc2** as well (barely visible). This is in principle non possible for a non-ferromagnetic object, and might be explained with a small residual permeability of the stainless steel[55].

55. One could therefore discriminate between the stainless steel situation (phases>0) and that of a ferromagnetic object (§5.9) by looking at the amplitude ratio.

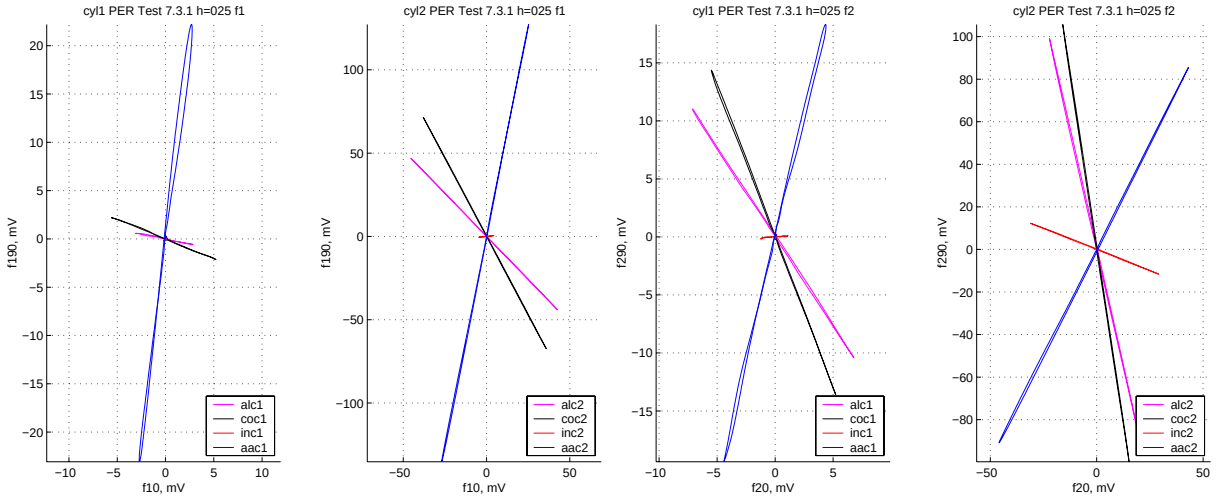

Figure 5.12: Response at f_1 (Left) and f_2 (Right) for all **ref. cylinders** (except **`msc2`**), placed perpendicularly to the scanning direction (PER orientation). Left: "small" cylinders, Right: "large" cylinders. Not normalized.

Comparison between Vertically/Horizontally placed objects (VER vs. PAR, PER configs.):

- *Ferromagnetic* (Figure 5.13): the shape of the VER curve is a straight line (like for PER), the phase is however closer to the one of PAR (especially the straight section), possibly because the contribution from the field along the cylinder axis is dominant. These effects are consistent with what seen in §3.5.2 (**orientation sensitivity of short ferromagnetic parts**).

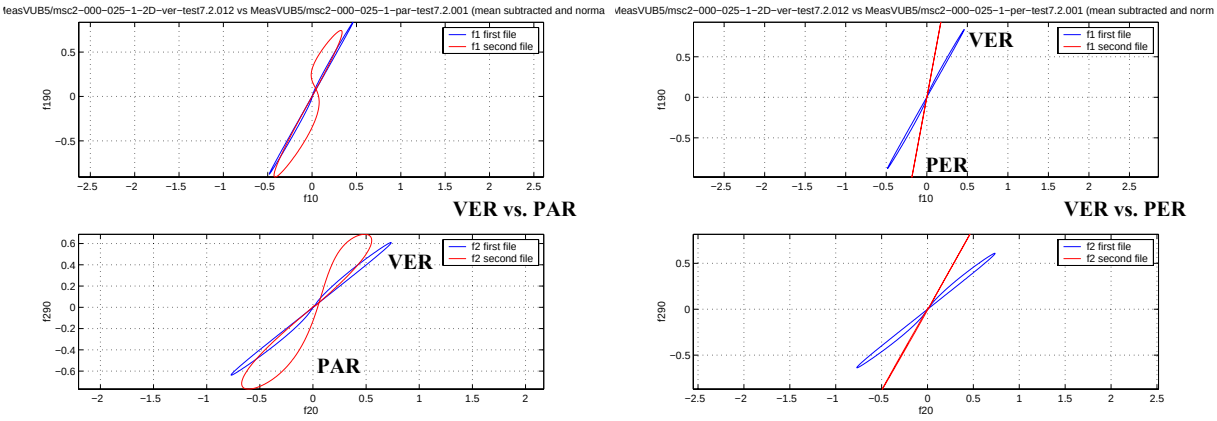

Figure 5.13: Response at f_1 and f_2 to a **mild steel cylinder** (**`msc2`**) for **different orientations**. Left: VER vs. PAR, Right: VER vs. PER. Normalized.

- *Non-ferromagnetic*: tests were carried out with the copper reference cylinders (**`coc2`** and **`coc1`**). In general **nearly identical phases are recorded for all orientations**[56], with small differences between the vertical setup and the other configurations. PAR, PER, QU1 and QU4 have comparable amplitudes, larger than VER (which is not astonishing, given that in the vertical setup the top of the object is flush; its bulk is therefore buried and farther from the sensor). Similar results should hold for other non-ferromagnetic objects.
- *Other studies dealing with orientation effects* (not only for cylinders): Results for *different orientations* in the vertical plane are reported in [KEI98, COL99b] for GEM-3 UXO data; [CHE84] also reports significant differences for prolate steel spheroids, using TD equipment. Horizontal vs. vertical orientation differences are reported in [TRA97] for several mines using laboratory FD equipment. Most data is acquired for the target in a fixed spatial position, [KEI99] representing an exception.

56. Horizontal orientations are described in A5.2.

Small Loop and Magnet

A small loop and a permanent magnet are quite useful to understand the general response trends: very good conductor on one hand, ferromagnetic (high μ_r) non-conductive object on the other.

The very strong response[57] from a closed loop (**loo2**, copper wire) is shown in Figure 5.14, bottom left (scales are in mV and mV×10^4), and clearly approaches the inductive limit (–90°) at f_2, in agreement with §3.1. The response from a similar open loop (**loo1**, top left) is as expected very much lower, with the phase at f_1 close to 0°.

The magnet's response (**mag1**) in the complex plane is nearly vertical, with ϕ_1~89°, ϕ_2~90° (Figure 5.14, right). The response at f_1 does indeed feature a small real component with amplitude~1 mV, whose origin is not immediately apparent (possible due to μ_r changing with frequency?).

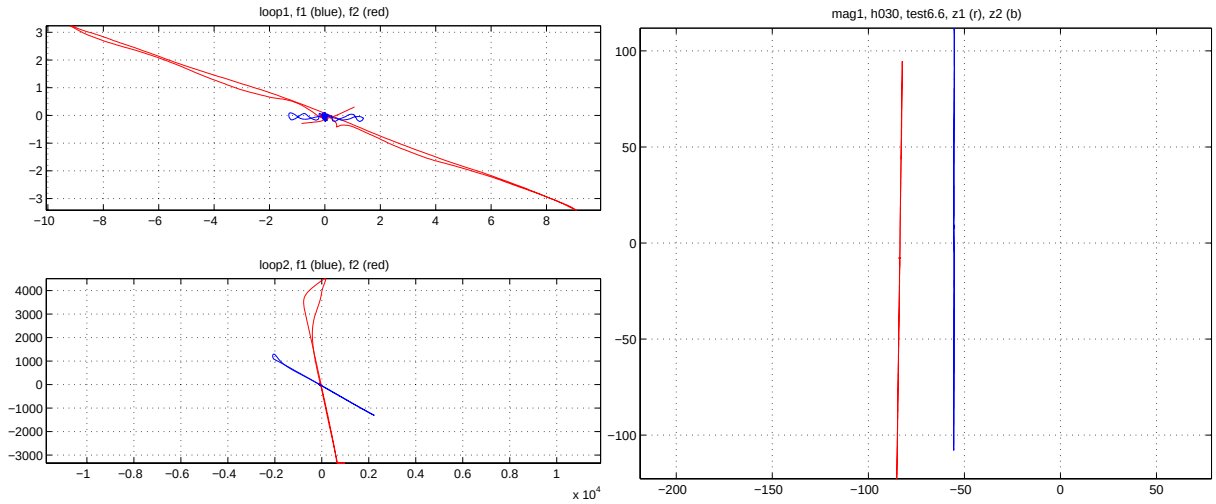

Figure 5.14: Left: Small **open loop** (top), **closed** (bottom). Right: Small **permanent magnet**. Scales are in mV.

Non-ferromagnetic vs. Ferromagnetic Object

Figure 5.15 represents well the *difference between non-ferromagnetic objects and (small) ferromagnetic* ones.

As an example of the first we have taken as an irregularly shaped, long and slender piece of copper, whose response is shown in the upper half; the real and imaginary components have opposite polarity, which translates into a negative slope in the complex plane (the phase angle of interest here is the one measured in the fourth quadrant (+,–)). Aluminium and stainless steel would, amongst others, behave in the same way.

As an example of the second we have taken a small mild steel cylinder (**msc2**), of diameter 7 mm and height 30 mm, placed flatly in the horizontal (xy) plane and transversally (PER orientation) to the scanning direction. Its response is shown in the lower half of the image; the real and imaginary components have the same polarity, which translates into a positive slope in the complex plane (the phase angle of interest here is the one measured in the first quadrant (+,+)).

Note how the phase angle decreases from f_1 to f_2 in both cases. Notice also that the absolute value of the response at f_1 is larger than at f_2 for the ferromagnetic object, the inverse for the copper piece. These trends are consistent with the previous theoretical analysis of the response function's behaviour (Chapter 3). Again, the signals themselves are unfortunately not always as strong and regular as in this case, in which it is easy to differentiate the objects.

57. The signal at f_2 is actually partially clipped.

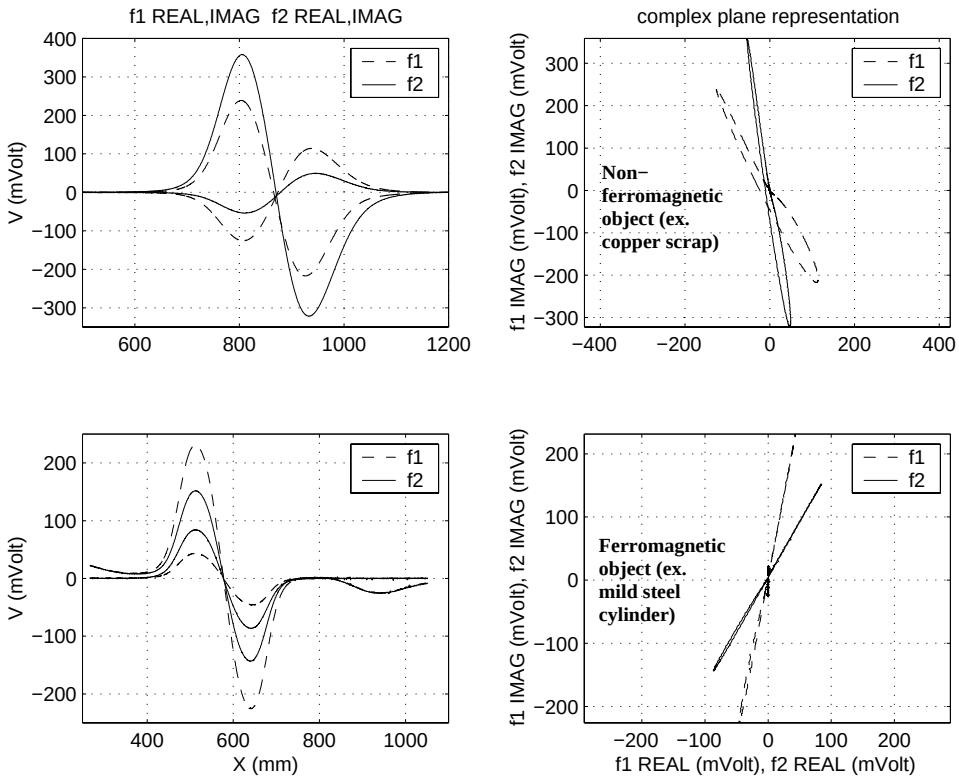

Figure 5.15: Typical response of **non-ferromagnetic** vs. **ferromagnetic** objects [BRU00b]

Two Different Objects of the same Type

Tests were carried out on pairs of visually identical reference steel spheres (**`sts1`** to **`sts4`**). The phase of the response was identical to about +/–1.5°, with the response for **`sts1`** too weak to make precise quantitative statement (there was however qualitative agreement).

Two Identical Spheres Placed in Contact

The average phase value of two identical spheres in contact are the same as those of a single sphere of the same type, but the individual curves are slightly "figure 8" shaped (like in the case of a parallel steel cylinder) as shown in Figure 5.16, left. The exact profile does probably depend on the position of the spheres with respect to the scanning direction.

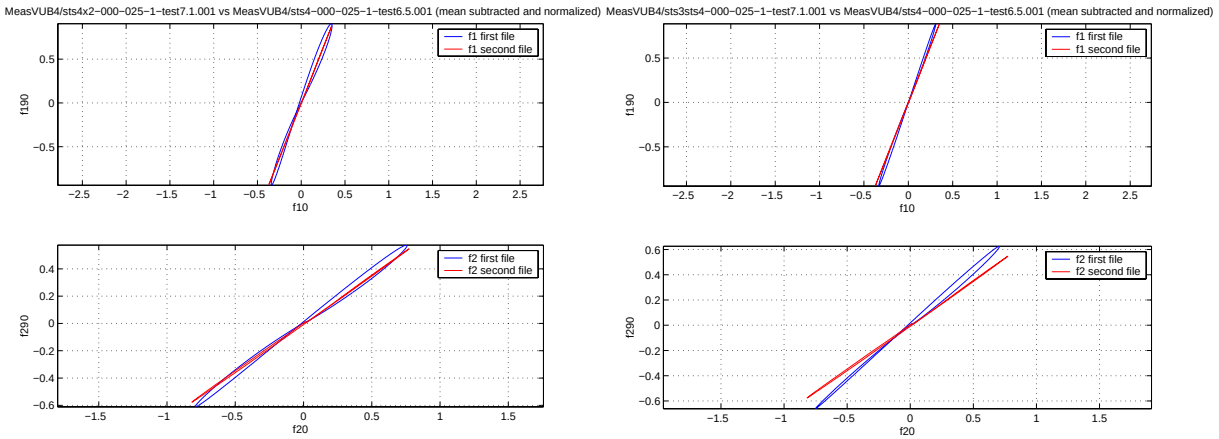

Figure 5.16: Left: **Two identical spheres** placed in contact, compared with a single sphere of the same type (**`sts4`**)**.** Right: **Two different spheres** placed in contact (**`sts3`**+**`sts4`**), compared with **`sts4`**.

Two Different Spheres Placed in Contact

The resulting phase values for this configuration are intermediate between those of the largest and the smallest object, like those resulting from a simple vector sum, which is rigorously true only for uncoupled objects (see §3.3.4). In the tested configuration they are however closer to the largest object (the largest amplitude dominates); an example is provided in Figure 5.16, right, for **`sts3`**+**`sts4`**. This also implies that the combined object can look "smaller", from the point of view of the phase angle, than the largest of the two objects, although the overall object mass and dimension have obviously increased, as well as the total signal amplitude.

5.4. Phase vs. Distance (depth)

Scans at increasing distance from the object were carried out raising the detector head in 1 or 2 cm increments, without displacing the object; this is definitely easier than changing burial depth, even if obviously less realistic, and has the advantage that the influence of the background is reduced too as the height increases, not only the target signal.

Spheres (sts2, sts4)

Up to about 10 cm in the case of **`sts2`** and 16-18 cm for **`sts4`** (both steel spheres) **the phases are basically identical**, then the signals get too weak for a simple quantitative comparison[58]. The responses from the individual channels do obviously change, becoming broader at increasing distance. *No multipole effects are apparent for the large sphere*, which is consistent with the analysis of §3.4.4 for a sphere of this size.

Ferromagnetic Cylinders in the Horizontal Plane

The response of a ferromagnetic cylinder (**`msc2`**) for each of the four orientations in the **HORizontal plane** (PAR, PER, QU1, QU4) is shown in Figure 5.17 at increasing detector heights. *The PER profiles do not change, whereas the PAR ones do* and become somewhat more irregular (larger variation in phase angles) with increasing height. An exception is the straight section in each plot, which stays unchanged; it corresponds to the approach phase – up to the first peak say – and when moving away from the object, after the last peak say.

Similar comments apply for a small ferromagnetic cylinder (**`msc1`**, see Figure 5.18). In addition: the amplitude ratio (PAR vs. PER) changes with the height, and is closer to 1 at f_2 than at f_1. The shapes are again quite complex in the PAR configurations, becoming more irregular with increasing height; this effect is more marked than for **`msc2`**. The difference between the PAR and PER configurations is important, and is also more marked than for **`msc2`**.

Target in Vertical Plane

Tests were carried out with a vertical reference copper cylinder (**`coc2`**). All scans at increasing heights featured nearly identical phases, and should hold for other non-ferromagnetic objects. Similar results have also been obtained for parallel scans at a fixed height (§5.5).

Scans at different heights were also analysed with a vertical **`msc2`** cylinder, i.e. an elongated ferromagnetic object. The phase stays constant from one to the other. This is not true any more for parallel scans at a fixed height (see again §5.5).

Similar effects for prolate steel spheroids at a fixed orientation have been reported using a time domain system in [CHE84].

58. Note that the detection limits are higher than the values just indicated.

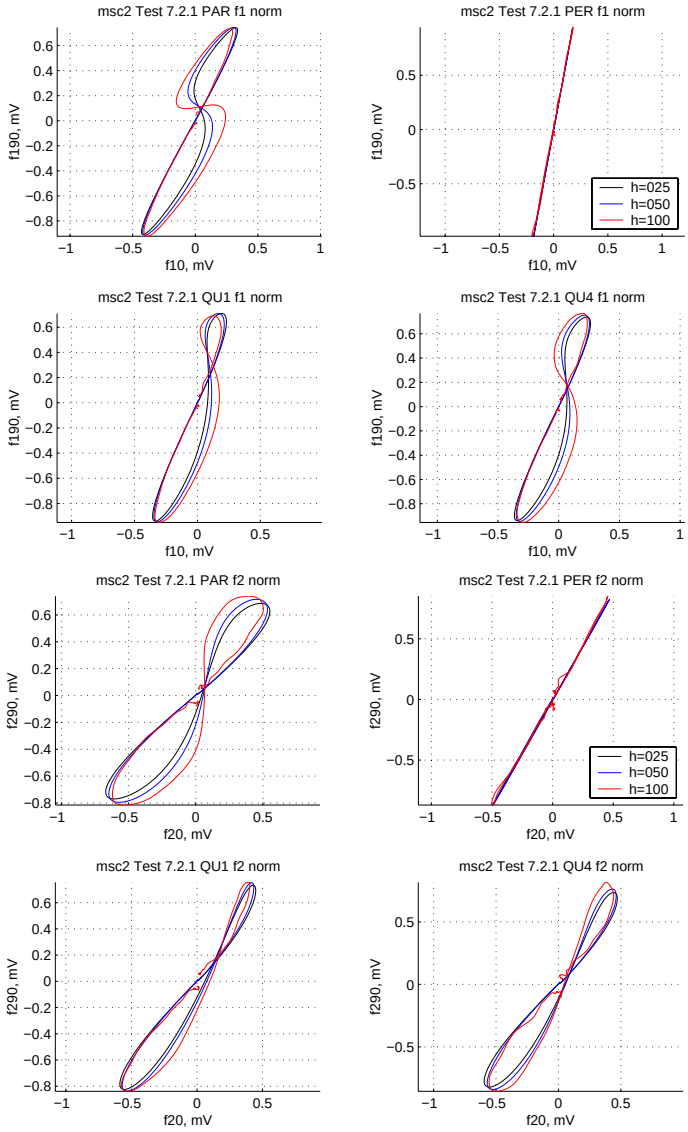

Figure 5.17: Response at f_1 (Top) and f_2 (Bottom) to a **mild steel cylinder** (**`msc2`**) placed flush with the surface, **at increasing detector heights** for each of the four orientations in the horizontal plane. Normalized.

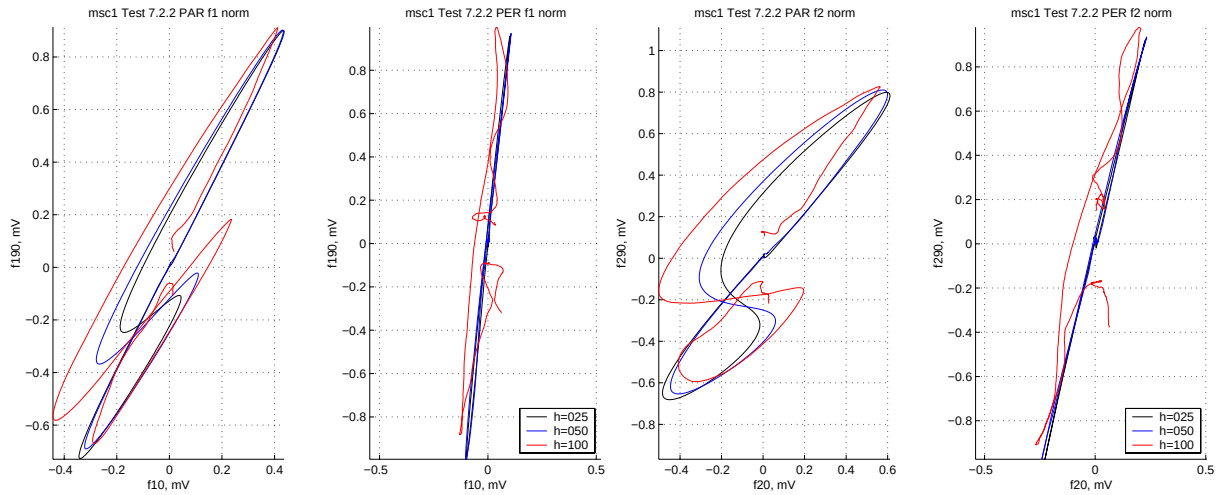

Figure 5.18: Response at f_1 (Left) and f_2 (Right) to a small **mild steel cylinder** (**`msc1`**) placed flush with the surface, **at increasing detector heights** for the PAR and PER orientations in the horizontal plane. Normalized.

5.5. Phase vs. Axial Offsets (Parallel Scans)

The behaviour of scans not carried out exactly over the target has been analysed by means of series of parallel scans at constant detector height and object position. Results will be shown in this paragraph for some reference objects and a representative large non-ferromagnetic target. Results for other objects (minimum-metal mine, **PMN**) are detailed in §5.7 and §5.8.

We will see that there can be substantial axial offset effects for ferromagnetic objects and/or composite objects such as the PMN, which are in general not easy to model in detail. For most non-ferromagnetic objects there are some changes for different axial offsets, but this does not seem to represent a major effect; the same is true for the minimum-metal mine in the configuration we studied.

Steel Sphere

Parallel plots have been carried out on the "large" steel reference sphere (**sts4**). The phase response is constant from one scan to the other. This does however not imply that the profile of each channel is invariant as well. There are indeed profile differences moving away from the central scan, the profile getting larger for increasing horizontal distance, similarly to what happens for increasing depth in the case of a buried object.

Ferromagnetic Object in the Vertical Plane

The response of a ferromagnetic cylinder (**msc2**) placed *vertically* is analysed in Figure 5.19, left (normalized), when approaching the object, and in Figure 5.19, right (non-normalized), for a few central scans. The latter behave in the same way, whereas the phase changes (*decreases*, i.e. moves towards 0°) when moving towards the target; there is a *clockwise curve rotation* when moving from scan 5 to 9. All curves are slightly open (not straight lines).

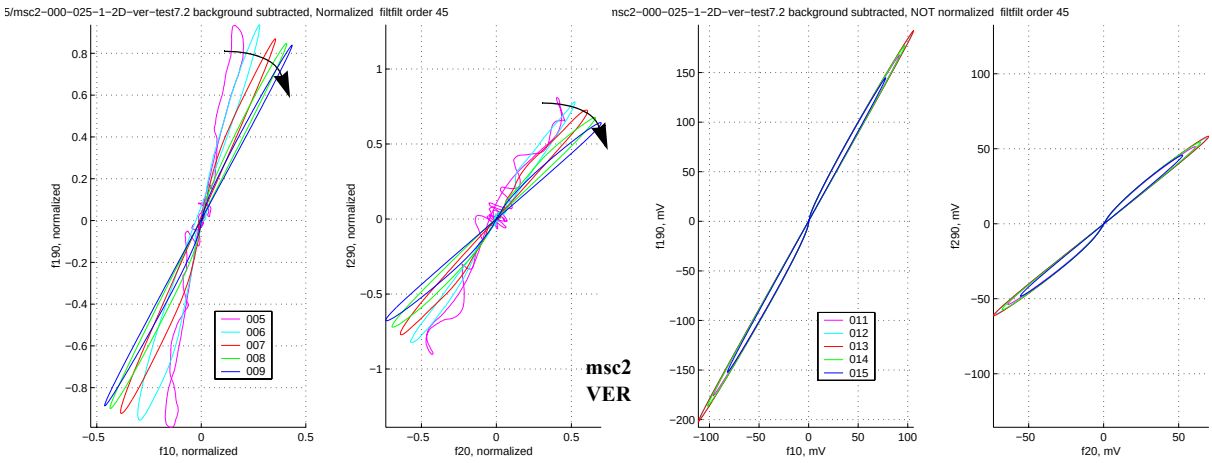

Figure 5.19: 2D response (**parallel scans**) at f_1 and f_2 to a **mild steel cylinder** (**msc2**) placed **vertically** (top at surface level). Left: normalized, scans 5-9 (approach phase), Right: scans 11-15 (passing over the target).

This situation bears similarity to what shown in Figure 5.13, Bottom (VER vs. PER orientations).

The amplitude ratio is of about 2.4, larger than for the PAR, PER orientations and not compatible with the model of a cylinder in a transverse magnetic field, as will be discussed in §6.2.7.

Ferromagnetic Object in the Horizontal Plane

Perpendicular orientation (PER): the response curves are nearly straight lines in the phase plane, but the phase changes from one scan to the other (see Figure 5.20)! The phase increases, i.e. moves towards +90°, when moving towards the target – *counter clockwise curve rotation* when moving from scan 5 to 9 – and is maximum over the object. Scan 12 features the maximum phase, and *the minimum amplitude* (in the object's proximity obviously): *lateral scans have a higher amplitude, contrary to standard scenarios*. This is probably again a consequence of end effects (magnetic depolarisation). The PER phase response does therefore also change with axial offset.

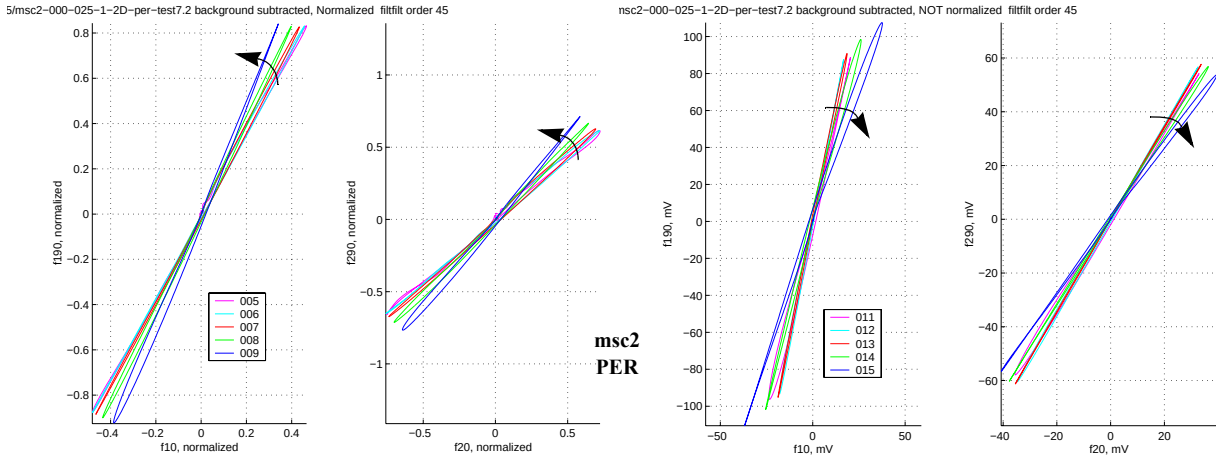

Figure 5.20: 2D response (**parallel scans**) at f_1 and f_2 to a **mild steel cylinder** (**`msc2`**) placed **PERpendicularly** (HOR plane). Left: normalized, scans 5-9 (approach phase), Right: scans 11-15 (passing over the target).

Note that this behaviour is the *opposite* of what just discussed for the *vertical* orientation.

Parallel orientation (PAR): the response curves are "figure 8" shaped as expected (see Figure 5.21), and the amplitude seems to have a "normal" behaviour (maximum for central scan). The curves are similar in close proximity to the object and change when moving away from it, but less than in the PER case. The non-symmetric behaviour is possibly due to some misalignment.

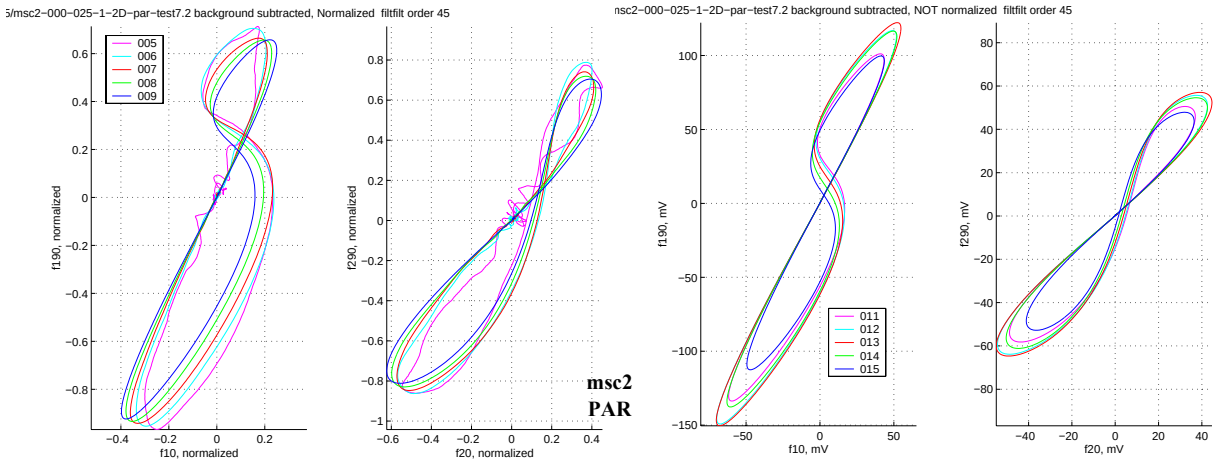

Figure 5.21: 2D response (**parallel scans**) at f_1 and f_2 to a **mild steel cylinder** (**`msc2`**) placed **PARallel** (HOR plane). Left: normalized, scans 5-9 (approach phase), Right: scans 11-15 (passing over the target).

Non-Ferromagnetic Object in the Vertical Plane

The response of a non-ferromagnetic cylinder (**`alc2`**) placed vertically is analysed in Figure 5.22 (left, normalized) for a few central scans. **The phase responses are practically unchanged**, although some slight variations are not excluded far from the object. There is a slight opening of the curve(s), which does not happen with the PAR and PER configurations; it might be due to a tilting of the cylinder's axis.

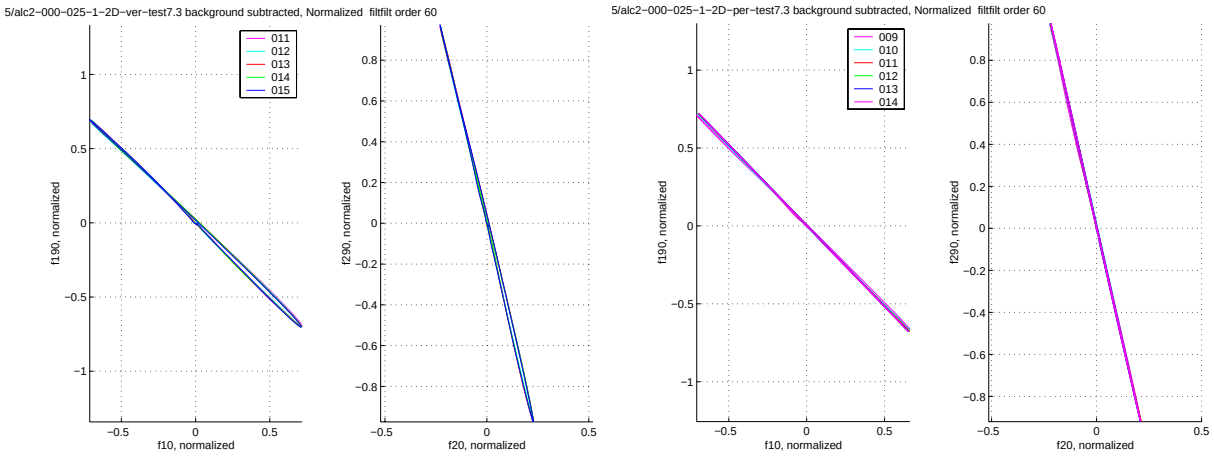

Figure 5.22: 2D response (**parallel scans**) at f_1 and f_2 to an **aluminium cylinder** (**`alc2`**). Left: placed **vertically** (top at surface level); normalized, scans 11-15 (passing over the target). Right: placed **PERpendicularly** (HOR plane); normalized, scans 9-14 (passing over the target).

Note again that same phase does not mean that the individual channels' response profiles are spatially identical.

Non-Ferromagnetic Object in the Horizontal Plane

Perpendicular and Parallel orientation (PER, PAR): **the phases are practically unchanged** (see for example Figure 5.22, right), although a slight increase is not excluded when moving from the centre towards the edges – the phase seems to increase, i.e. moves towards 0° (from negative values), very slightly (a few degrees maximum).

Large Non-ferromagnetic Object

In Figure 5.23 the target object is the large and irregularly shaped piece of copper already encountered. Within each scan there are some changes in the phase response, especially at f_1, which could be due to the object's irregular shape and/or higher order multipole terms; it would nevertheless still be easy to define an "average phase". From one scan to the other *there are no remarkable differences*, apart from the response at f_1 for D–12cm (scan 8, at the outer edges of the object) which features also a reduced absolute value.

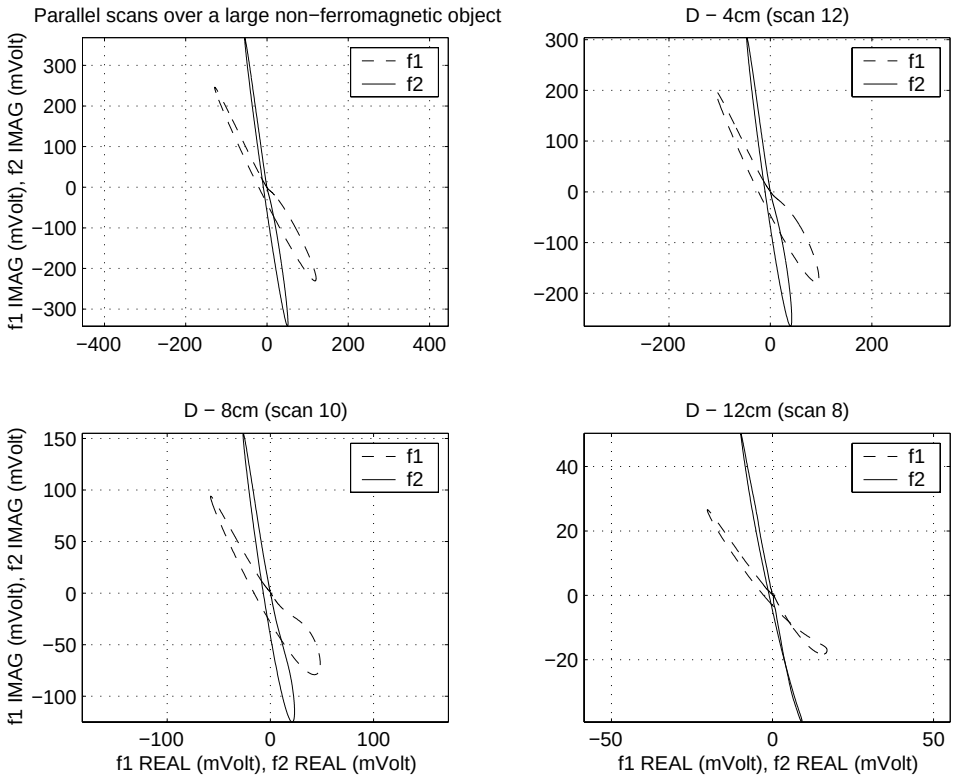

Figure 5.23: Response at f_1 and f_2 to a large **copper debris**, for **four parallel scans** at increasing axial offset from the object.

5.6. Phase vs. Orientation in the Horizontal Plane

We will analyse in this paragraph how the target's response depends on its orientation in the horizontal plane, the plane into which the metal detector moves.

Non-ferromagnetic Cylinders

Non-ferromagnetic cylinders, e.g. of aluminium or copper, **do not show any noticeable difference** (see also previous discussion for **`coc2`** in §5.3).

Ferromagnetic Cylinders

The non-normalized response of a ferromagnetic cylinder (**`msc2`**) is shown in Figure 5.24 at fixed heights for each of the four orientations in the HORizontal plane (PAR, PER, QU1, QU4). **The response is strongly orientation dependent**. At f_1 the PAR orientation features the largest amplitude, PER the smallest. The PAR profile is "figure 8" shaped, PER linear, QU1 and QU4 intermediate. The behaviour at f_2 is similar, but the "figure 8" curves are more regularly shaped (symmetric).

The curves for the smaller cylinder (**`msc1`**) show similar trends, with an even more marked difference between the PAR and PER configurations.

There is in fact is not a large difference *between the parallel configurations* for **`msc1`** and **`msc2`**, especially at f_1 (the straight section in particular is the same; compare Figure 5.17 and Figure 5.18). Probable explanation: the length, which is the same for **`msc1`** and **`msc2`** (only the cylinder diameter changes), is the dominant factor, and with it the magnetic depolarisation effects. This seems consistent with the data in [BRA01].

Ferromagnetic Cylinders: Individual Channel Profiles

Individual profiles are shown in Figure 5.25, with the figures not being always symmetric, possibly due to a non perfect positioning of the object[59].

The shape of the real and the imaginary part curves (f_1 and f_2 REAL and IMAG) is not necessarily the same any more, with the real part which seems to be the more irregular one; there are also parts of the curves in which the two have opposite polarity, corresponding to a negative phase. The peaks do also not necessarily occur at the same spatial position. A closer look at the curves shows that it is the central section between the first and last peak which exhibits the greatest variation; the phase is rather constant to the left and to the right of it, i.e. while approaching the object and while moving away from it (not when over it). Similar plots are in fact well known in Non-Destructive Testing applications.

This behaviour can be explained qualitatively as follows[60], thinking of the situation in which the cylinder is parallel (longitudinal) to the scanning direction: far away from the coil it sees basically a horizontal primary magnetic field aligned along its axis, which emphasizes induced magnetization effects (and possibly increases μ_r). The object's ferromagnetic nature prevails. Right over the coil the primary magnetic field is vertical and therefore transversal to the cylinder axis; eddy current effects can prevail and the object can appear to behave as non-ferromagnetic. The field orientation effect is well illustrated in [END98, SOW99].

59. This measurement set is different from the previously shown ones; the curves are therefore not identical.
60. K. Ausländer, Institut Dr. Förster, *Private Communication,* March 2000.

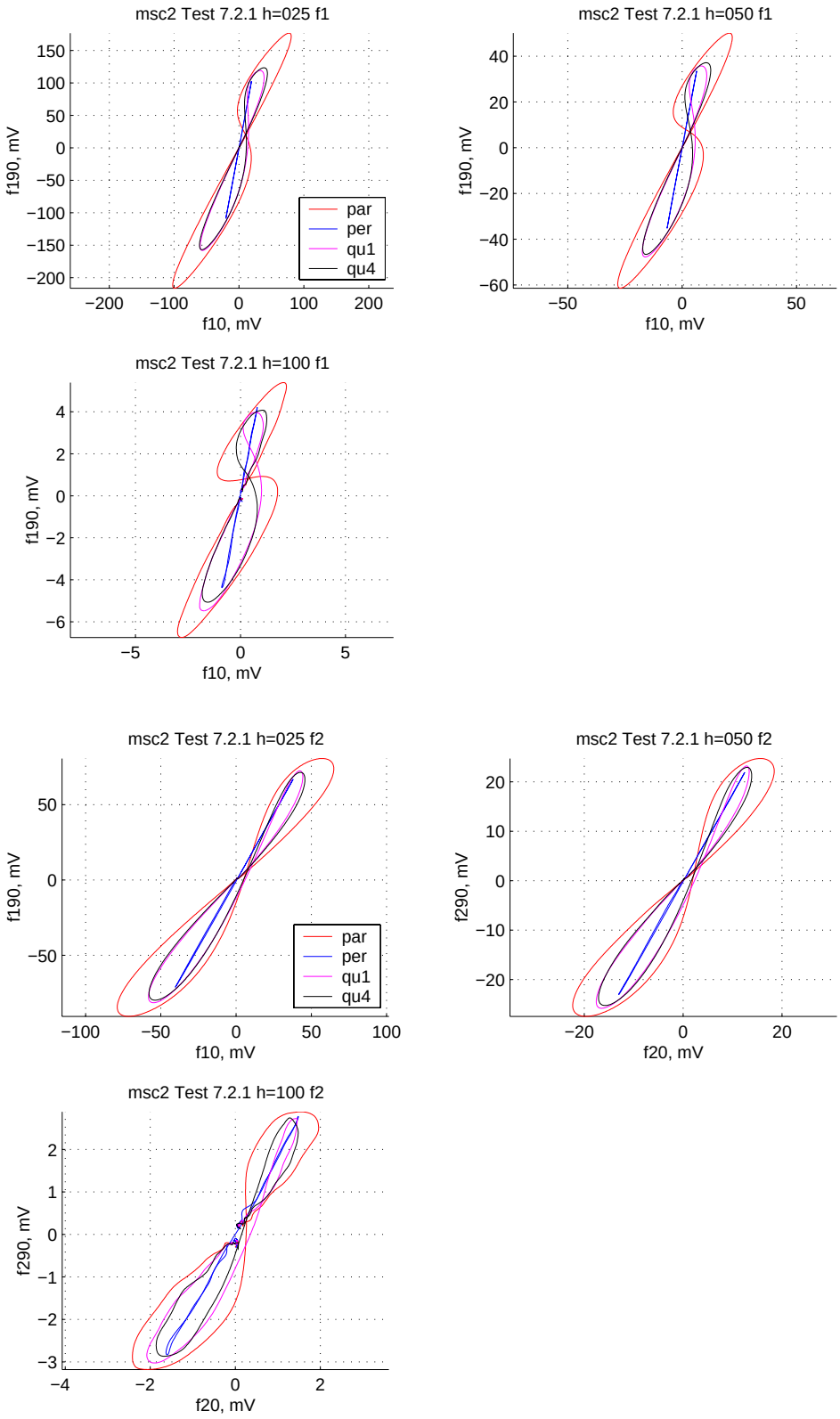

Figure 5.24: Response at f_1 and f_2 to a **mild steel cylinder** (**`msc2`**) placed flush with the surface, **at fixed heights** for each of the four orientations in the horizontal plane.

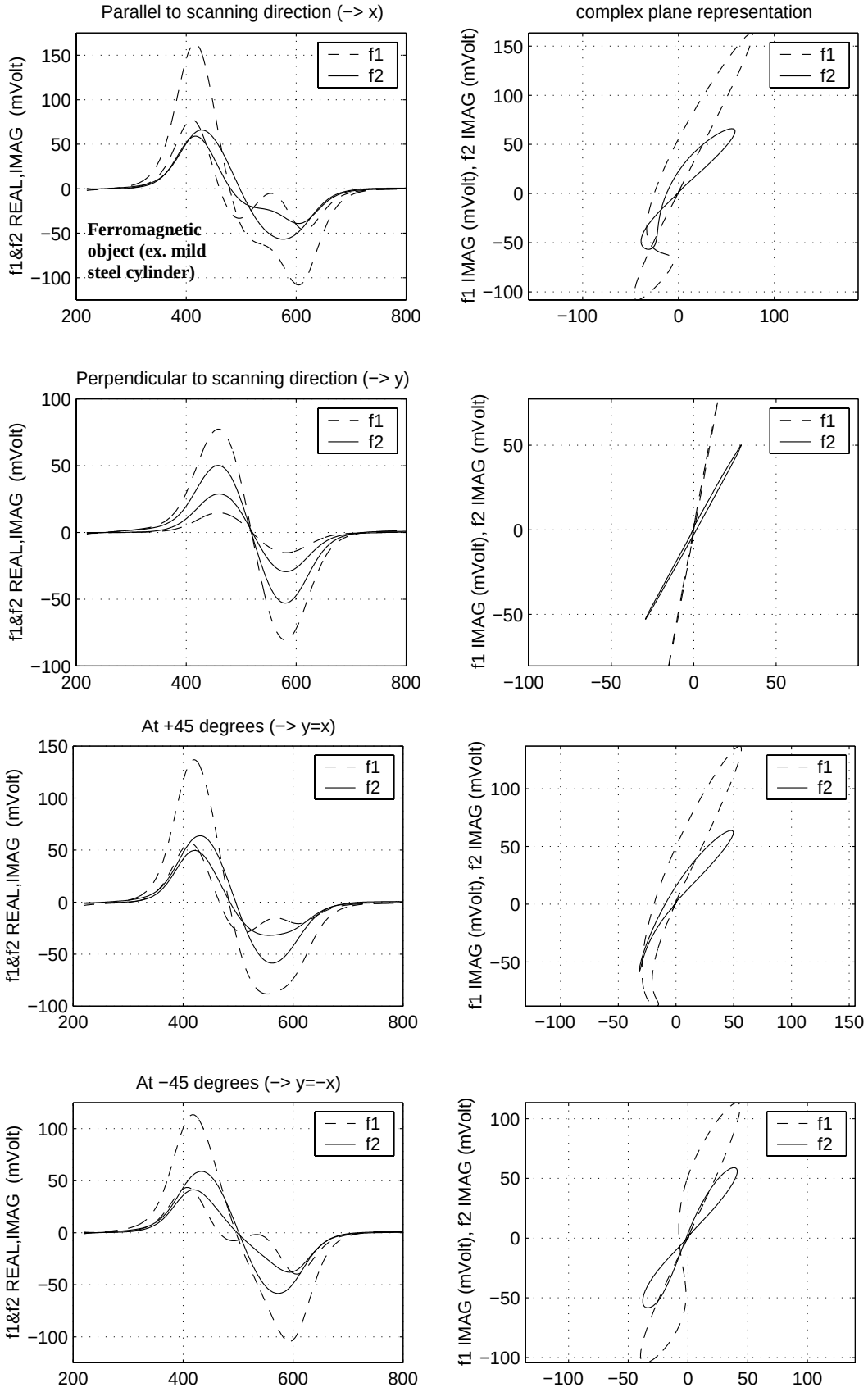

Figure 5.25: Response at f_1 and f_2 to a **mild steel cylinder** (**`msc2`**, flush), at four **different orientations** in the **horizontal plane** (parallel and orthogonal to the scanning direction, and at +45 and –45 degrees to it).

5.7. Response for a Minimum-metal Mine and its Components

We will analyse in the following the response of a minimum-metal mine and of its components. Although this particular type of mine is not widely diffused, it is still representative of the category, and will allow to draw a number of interesting conclusions.

Complete Live (i.e. real) Mine

Figure 5.26 features the response of the live (real) minimum-metal mine (**`mich`**) shown to the right of Figure 5.4 – i.e. of a **composite object** – and of its metallic components separately, the small steel striker pin, **`mist`**, and the real detonator, **`midereal`**.

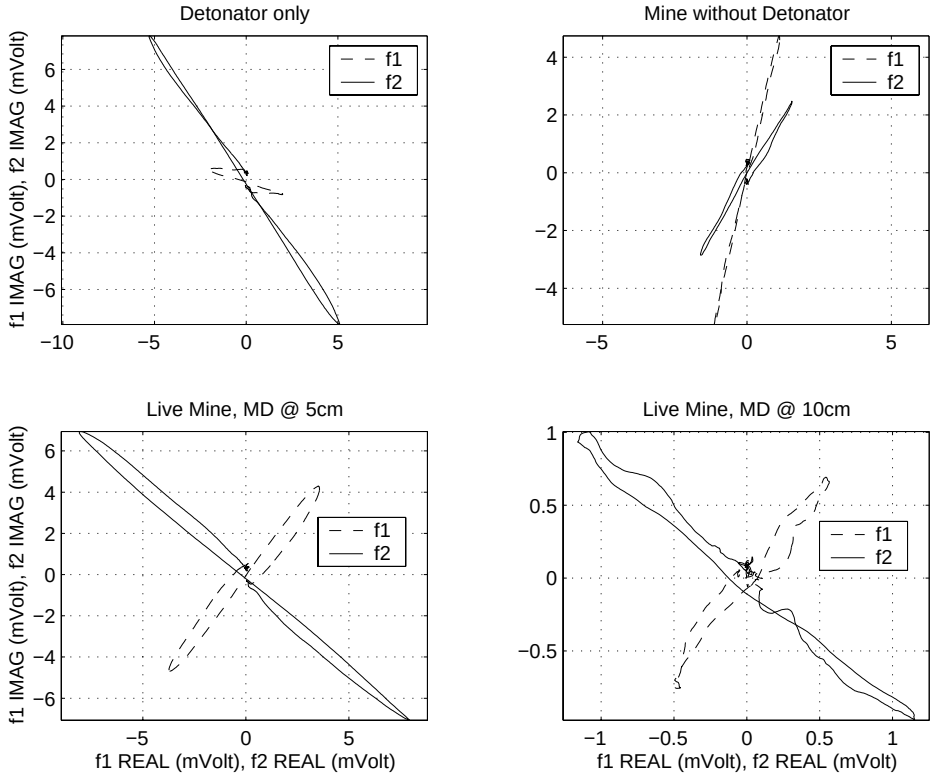

Figure 5.26: Minimum-metal mine: response to a detonator cap (**`midereal`**), to the mine without detonator, i.e. striker pin only (**`mist`**), and to the live (real) mine (**`mich`**) at two different detector heights (all objects flush) [BRU00b]. EPFL data, taken with the assistance of the Swiss Defence Procurement Agency.

It is very interesting to see that *the detonator*, which is actually just above the striker pin and therefore slightly closer to the detector, delivers a *significant and absolutely not negligible signal*, non-ferromagnetic in nature (perhaps due to the thin capsule containing the primary explosive) with an f_2 component much larger than the f_1 component. This would indeed be indicative, according to the models of Chapter 3, of a rather small object. It is in any case a reminder to include whenever possible the detonator, or equivalent metallic pieces, in the study of minimum-metal mines.

The signal of *the mine without detonator* is on the other hand of ferromagnetic nature, the mine containing in this case only the steel striker pin already analysed in a number of plots (actually a vertically placed steel nail, of diameter 1.5 mm, length 11 mm and weight 0.1-0.2 g).

The signal of the *real complete (live) mine* is an interesting combination of the two – actually simply the vector sum of the first two plots – looking like the response of a ferromagnetic object at f_1 and of a non-ferromagnetic one at f_2; this seems quite characteristic indeed. All scans were carried out on flush objects with a detector height of 5 cm. The live mine was also scanned at a detector height of 10 cm, and the corresponding responses look quite similar to those at 5 cm.

Mine Striker Pin at Increasing Distance

Figure 5.27 represents the response to the striker pin only (**`mist`**), placed vertically. The detector head was raised in 2 cm increments, without displacing the object. The plots at a distance of 3 cm correspond in fact to the signals shown in Figure 5.3 and Figure 5.5.

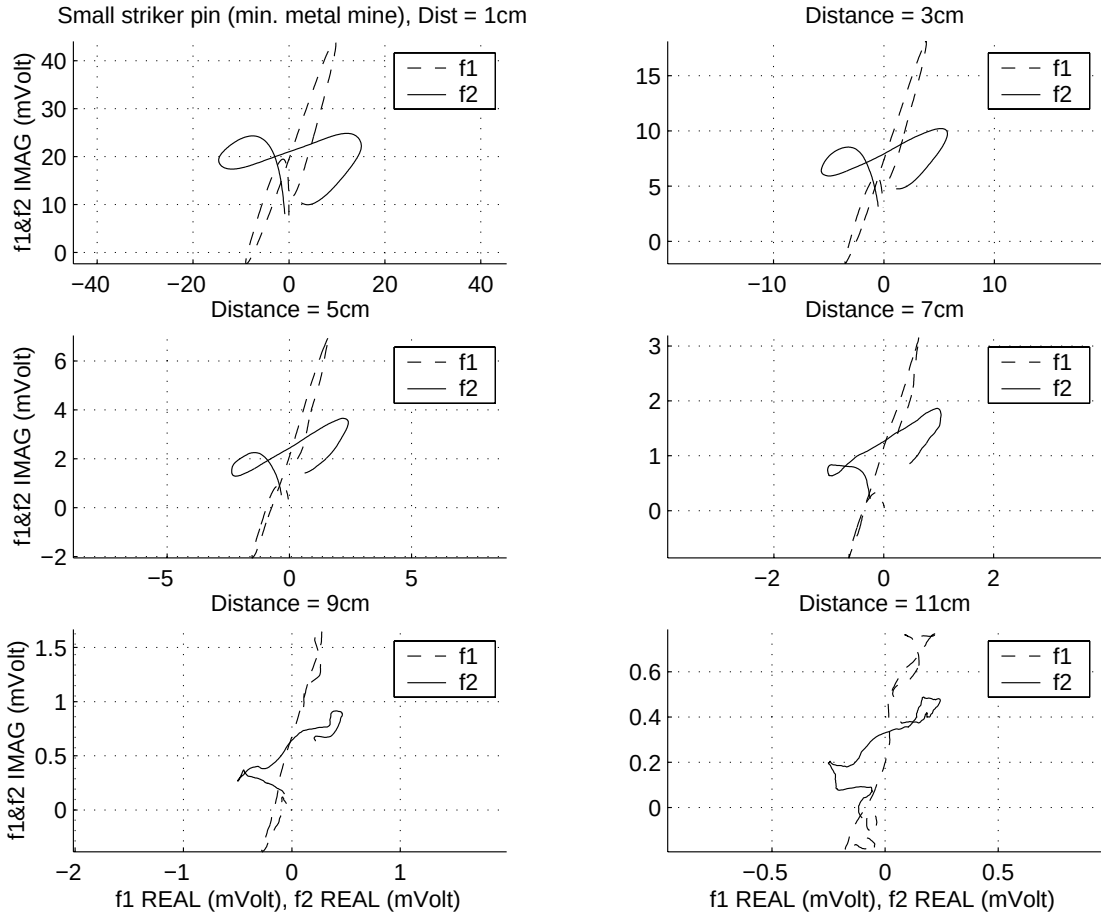

Figure 5.27: Response at f_1 and f_2 to a small striker pin (**`mist`**) contained in a minimum-metal mine placed **flush** with the surface, for **increasing detector heights**

The phase of the object seems to stay constant in this case too, but it is difficult to make precise statements because of the varying background signal (the f_2 component in particular is strongly perturbed). These, together with the actual form of the object, long and slender and therefore far from resembling a sphere, and/or its placement (vertical), might explain why the phase angle is much smaller than one would expect for such a small object. These plots do also represent a good example of unfavourable signal to noise ratio.

Comparison of Striker Pins

Different versions of the striker pin described above (**`mist1,2,3`** – inert mine components) have been compared among them and with the striker of the real mine tested at the EPFL; the pins were placed vertically (usual configuration). *No differences were detected.*

Measurements were also carried out with the striker pin in the horizontal plane, parallel (PAR) and perpendicular (PER) to the scanning direction. This corresponds to an *unusual placement of the mine*, which however can not be totally excluded a priori, either due to natural events or to a deliberate act. An instance of the latter was for example recorded in the Sarajevo area a few years ago, when a deminer hit the pressure plate of a vertically placed mine while prodding.

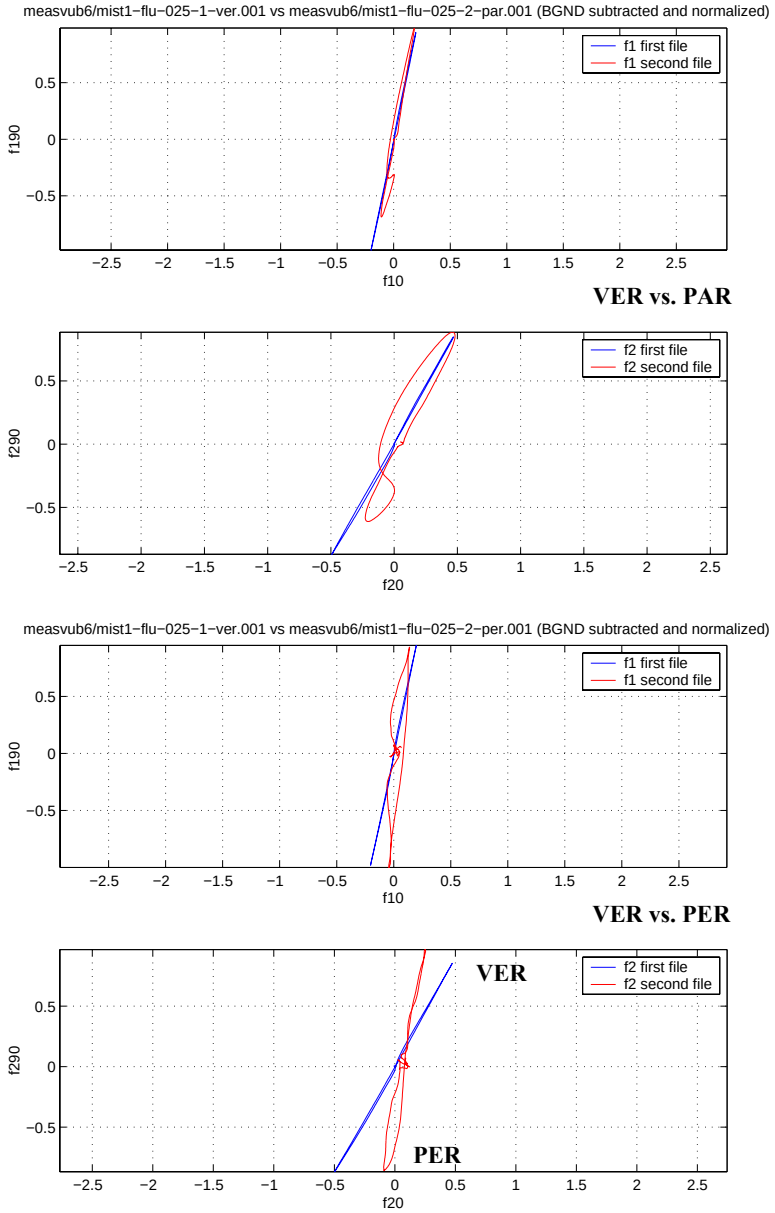

Figure 5.28: Minimum-metal mine striker pin (**`mist1`**): response to **different orientations**. Top: VER vs. PAR, Bottom: VER vs. PER. Normalized.

The resulting behaviour, shown in Figure 5.28, is quite similar to what previously described for the larger steel cylinder (**`msc2`**) in §5.3 (see Figure 5.13). *Note in particular the difference between the VER and PER orientations*. The signal amplitudes are in the following order: VER (Delta~5 mV), PAR (Delta~2 mV), PER (Delta<0.5 mV, barely detected at s=2). In the PAR orientation the individual channels exhibit multiple peaks.

The overall mine response would obviously include the contribution from the detonator as well.

Comparison of Mine Detonators

Comparison with real detonator: A replica detonator (**mide**) (essentially composed of a cylindrical foil), provided by the Swiss Defence Procurement Agency, was compared to the original detonator of the real mine tested at the EPFL[61] (**midereal**). *The behaviour is similar but the phases are not identical* (Figure 5.29, left); the replica detonator does therefore represent a good but not perfect reproduction. The actual angle at f_1, which is quite small, is in fact slightly lower than what shown due to important background effects.

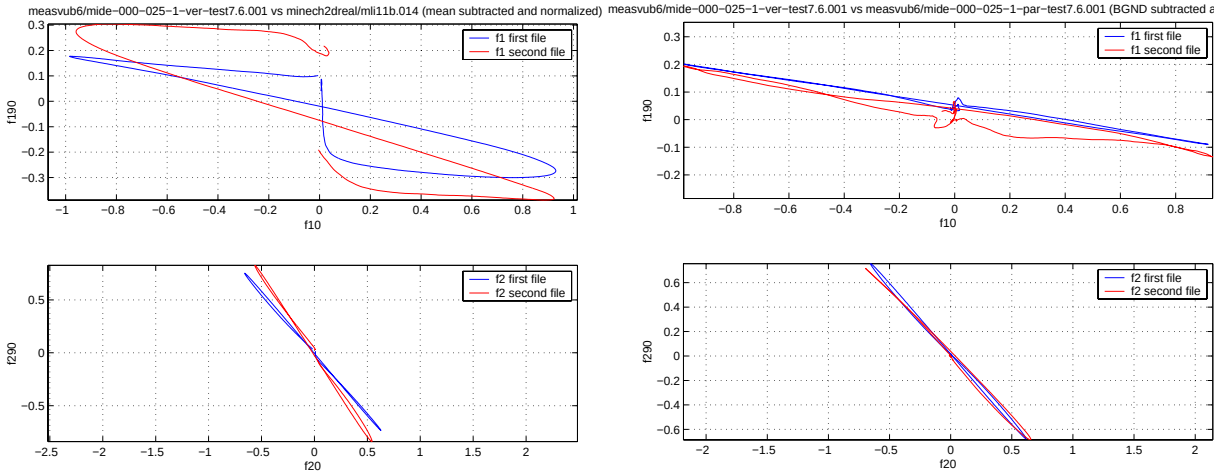

Figure 5.29: Minimum-metal mine detonators: Left: replica (**mide**) vs. original one (**midereal**, shown in Figure 5.4); normalized. Right: replica (**mide**) response to different orientations, VER vs. PAR; normalized, background subtracted.

The background subtracted profile is visible in Figure 5.29, right; this is also a reminder of the importance of soil effects, in particular for small objects/weak signals. As already noted elsewhere the response at f_1 is much weaker than at f_2. The amplitude ratio is about 1/6, characteristic of a quite small and/or poorly conductive non-ferromagnetic object.

Comparison at different heights: The response was checked at a height of 2.5, 5, 10 and 15 cm. *It does not change* at least up to 10 cm, although it is quite weak at f_1. At 15 cm the target is barely detectable at s=3.

Comparison of different orientations (VER vs PER, PAR): no changes in phase response are apparent, and in this case background subtraction works quite well as shown in Figure 5.29, right.

"Upside down" Mine

A complete mine was placed "upside down", i.e. with the striker above the detonator, as well as on its side. The response is quite different from the standard one, the striker pin prevailing in the first case (closer to the coil).

This is a good example of problems due to composite objects, which can probably not be described with one of the models discussed in Chapter 3.

Axial Offsets (Parallel Scans)

In Figure 5.30 the target is again the real (live) version (real detonator). The distance between the scans plotted is 4 cm, with the scan running directly over the object being in between the second and third (in fact between scan 13 and scan 14, which is 2 cm to the right of scan 13). There are some changes in the phase at f_2 and the ratio of the absolute values of the induced voltages at f_1 and f_2 is not constant, in particular for the last scan shown (C+7cm, scan 17).

61. Live detonators are not easily available for tests due to the presence of very sensitive primary explosives.

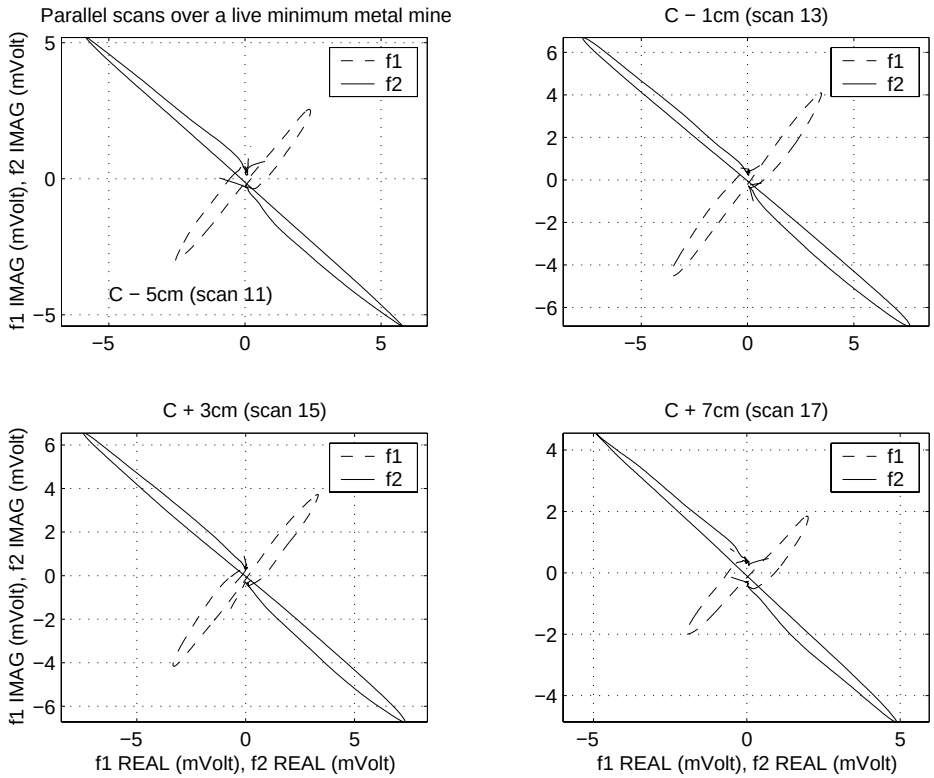

Figure 5.30: Response at f_1 and f_2 to a minimum-metal **live mine** (flush), for four **parallel scans** (the scan running directly over the object being in between the second and third) [BRU00b].

5.8. Response for a PMN mine

We will analyse in the following the response of the Russian PMN, a widely diffused non minimum-metal AP mine (see Figure 5.4).

5.8.1. Phase vs. Distance (depth)

PMN data was collected at the VUB sandbox with the mine at different depths (5, 10, 20, 26 cm to top of mine) using a PVC cylinder to ease data taking. Scans were first taken with the empty tube (*BGND),* then the empty tube with the mine placed as in Figure 5.31 ("*emptyhole"*), and finally the tube containing the mine and filled with sand ("*fillhole"*), corresponding to a realistic setup of a buried mine. This starting from the deepest position, moving upwards from one sequence to the next.

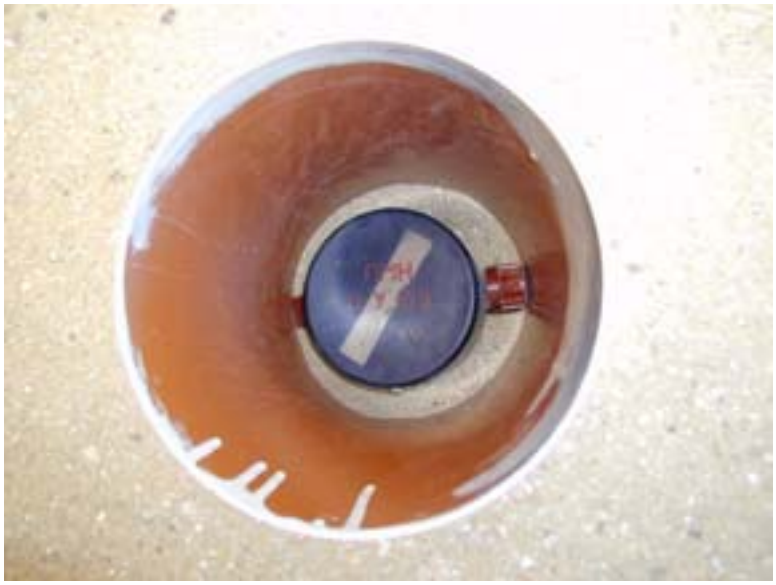

Figure 5.31: Setup for the measurement of a **PMN** mine at the VUB sandbox (see text).

The PMN used in these tests (**pmnVUB**, similar to the one in Figure 5.4) featured the ferromagnetic cover retaining ring; it was not yet armed (the arming pin was still in place, the ring usually attached to it had however been removed).

We will concentrate here on the data of the "*emptyhole"* scans, background subtracted to obtain the response from the mine alone. Results are shown in Figure 5.32, which compares the response at 5 cm with the one at 10 cm and 20 cm.

The phase seems clearly non-ferromagnetic at f_2 (eddy current effects prevail), a superposition at f_1. The straight section at f_1 (with negative slope) does probably correspond to the ring, and should correspond to the response right above the mine. As from 20 cm there are appreciable differences due to the soil (in the tube). Background subtraction seems however not to be efficient enough for a clear soil effect cancellation; the data at a depth of 26 cm is therefore quite irregular.

Some phase response differences with depth are clearly visible.

5.8.2. Phase vs. Axial Offsets (Parallel Scans) and Orientation in the HOR Plane

Four different orientations were analysed in the horizontal plane, namely PAR1 (as in Figure 5.31) followed by 3 successive counter clockwise rotations: PER1, PAR2 and PER2. Thirteen 2D scans were carried out at a pitch of 4 cm instead of the usual 26 scans at a pitch of 2 cm.

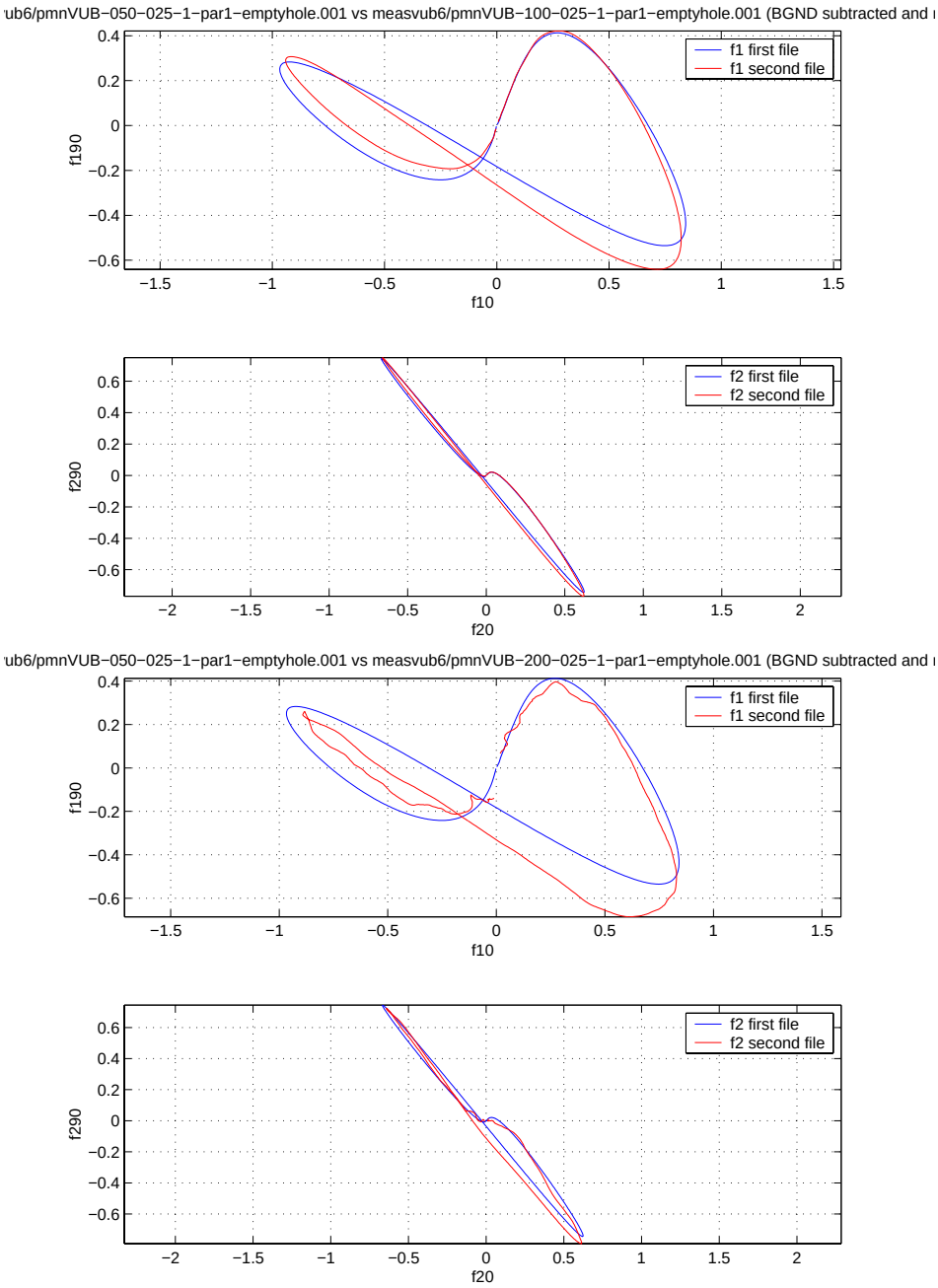

Figure 5.32: **`pmnVUB`** response, complete mine at different depths, 1D scan over the mine; depth=5 cm vs. 10 cm (Top) and 5 cm vs. 20 cm (Bottom). Normalized.

The data corresponding to the *PAR1* configuration is shown in Figure 5.33. The target looks typically ferromagnetic at large distances (scan 3 for example); the response "rotates" then towards the response above the target[62], scan 7, which is in fact the one already shown in Figure 5.32.

Very important phase response differences with axial offset are clearly visible.

Comparison of different orientations in the horizontal plane: PAR1 and PER1, PAR2 and PER2, look similar although they are not identical as clearly shown in Figure 5.34, in particular far from the object (approaching and moving away). Note that the PAR2 and PER2 responses go through the origin at f_1, whereas PAR1 and PER1 are vertically offset. The amplitude of the response at f_2 is much larger than at f_1.

62. The maximum is actually between scans 7 and 8.

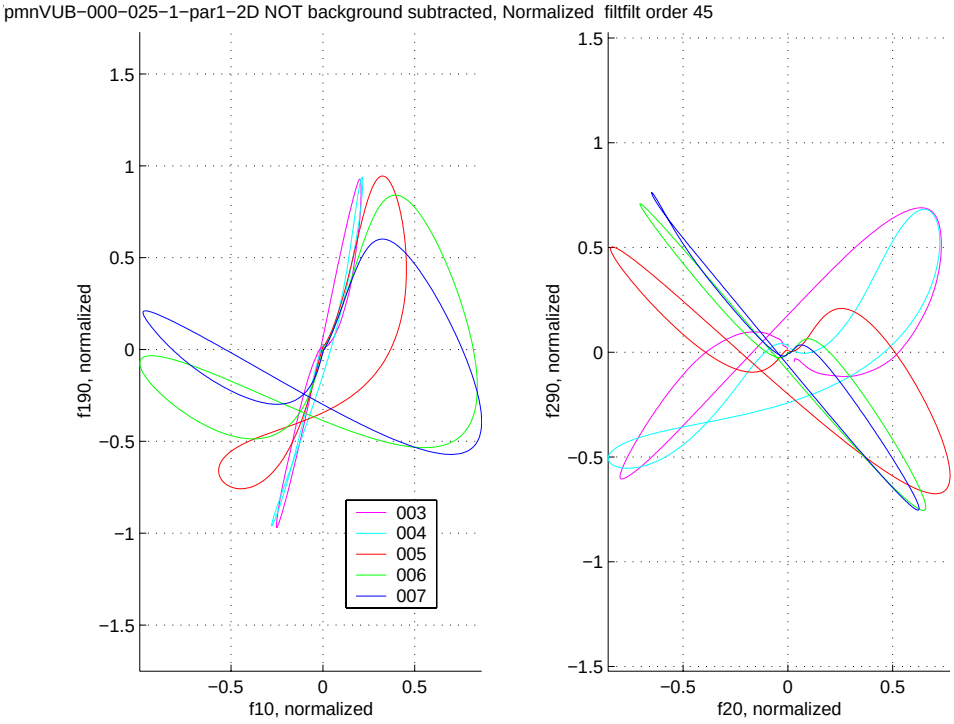

Figure 5.33: 2D response (**parallel scans**) at f_1 and f_2 for **pmnVUB**, placed at PAR1 (HOR plane). Normalized, scans 3-7 (approaching the target; centre of target between scans 7 and 8), 4 cm increments.

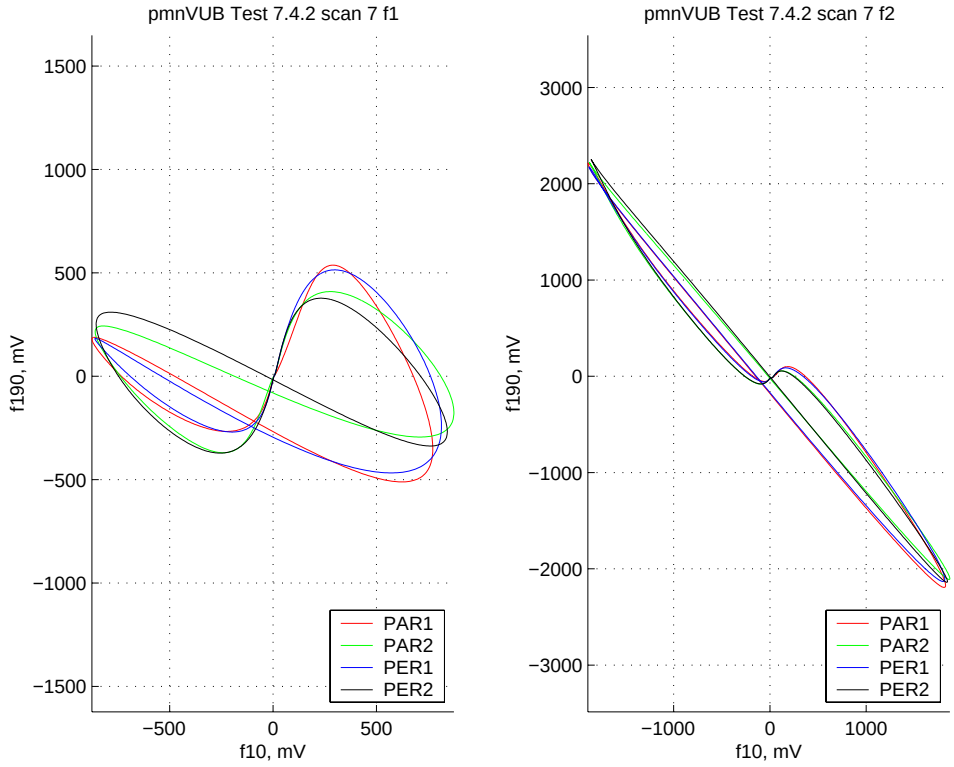

Figure 5.34: Comparison of the response at f_1 and f_2 over **pmnVUB**, for 4 **orientations in the HOR plane**; scan 7 (above the target).

5.8.3. Response for Different Versions of a PMN mine

Mine Striker

A PMN replica version was initially obtained from MILTRA Engineering in the UK. This replica mine contains a steel striker, believed to be an exact copy of the original, composed of two cylinders aligned along the same axis, with diameter 9 mm and 5 mm and length 19 mm and 39 mm respectively. This is the mine's largest metallic object apart from the ferromagnetic cover retaining ring, also visible in Figure 5.4.

The phase response to this steel striker is strongly orientation dependent, given that it is composed of two coaxial steel cylinders and that it is ferromagnetic.

Later on we also had access to a mine, coming from Cambodia (**`pmnCambodia`**), which looked very much like a PMN but which turned out to have a slightly smaller non-ferromagnetic (!) striker pin, possibly made of an alloy. This is in fact the mine actually shown in Figure 5.4 to the left. The response to its striker pin is displayed in Figure 5.35, and is obviously very different to the one of the replica version. The mine could be a Chinese copy of the PMN, but this episode was actually very useful in *reminding us of the limits of a target identification based approach.*

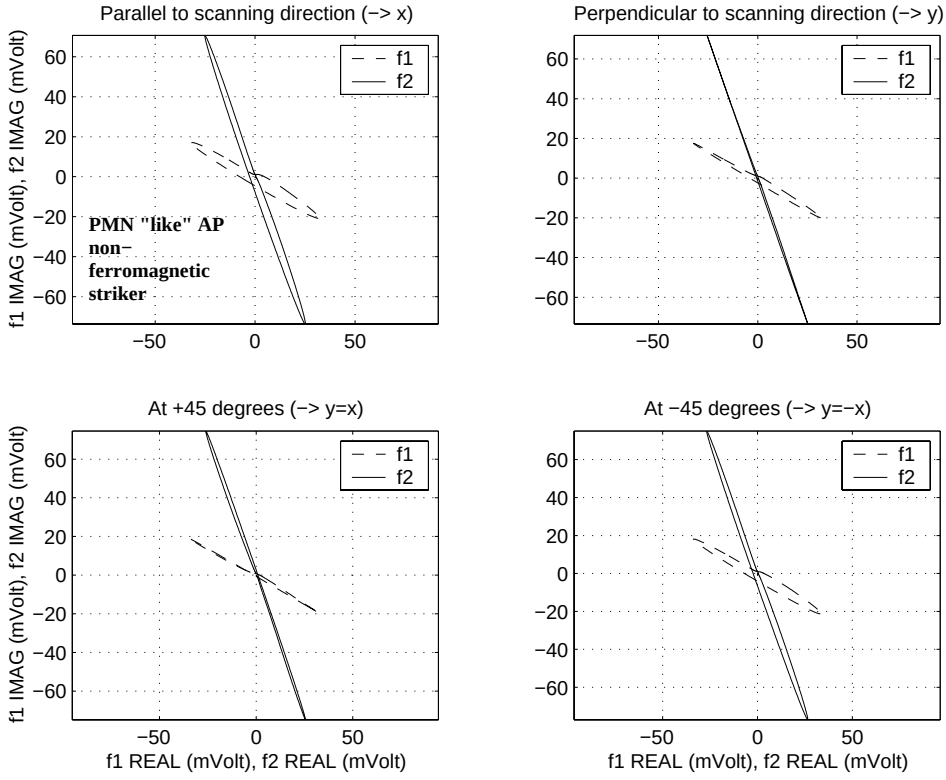

Figure 5.35: Response at f_1 and f_2 to a PMN "like" AP mine (**`pmnCambodia`**) **non-ferromagnetic striker** (flush), at **four different orientations** (parallel and orthogonal to the scanning direction, and at +45° and –45°).

Complete Mine

The complete **`pmnCambodia`** mine was analysed for the different orientations in the HOR plane. The results are *qualitatively similar* to those of **`pmnVUB`**, however *not identical* (the response at f_2 over the mine depends for instance on its orientation). This could be due to some *differences in the components* and/or in the *mine setup* (armed for **`pmnCambodia`**, unarmed for **`pmnVUB`**). This has again to be taken into account in a target identification based approach.

5.9. Response for Metallic Mines and (composite) UXO

Metallic AP mines are usually designed to kill via fragmentation, up to some tens of meters, and are composed of a relevant mass of metal as well as of explosive. Examples of a *bounding fragmentation mine* and a *stake fragmentation mine* are shown in Figure 5.36. The first is designed to be buried, the second to placed on a (wooden) stake just above the surface.

Figure 5.36: Metallic mines. Left: **PROM** (bounding fragmentation), Right: **PMR-2A** (stake fragmentation; stake not shown). Origin: Ex-Yugoslavia. Ruler length: 20+2.5 cm.

Metallic mines are in principle easier to detect, often even visually. There are however circumstances in which the stake mine is found lying on the surface[63] or even buried. In addition, *if we are relying on a discriminative metal detector we must be sure that the signal from such a type of mine is not going to be rejected by error*. We have therefore investigated the response of the previously mentioned mines, as reported below.

5.9.1. PROM – Bounding Fragmentation Mine

A cylindrically shaped **PROM** bounding fragmentation mine, whose steel body is about 20 cm long, was buried vertically, with only the top (a pronged striker about 4 cm long) sticking above the soil, and acquisitions taken in 2D. The results are shown in Figure 5.37.

Note the phase response at f_1, which is slightly negative above the mine and slightly positive far from it (scans 1-5, not shown). In order to avoid mistaking the mine for a (small) non-ferromagnetic object it could therefore be quite useful to:

- rely on a third lower frequency as well, or
- impose a threshold on the signal amplitude above which any target is declared as suspicious (which might anyhow be the case to cope with the problem of a small target close to a larger innocuous object), or

63. In case the wooden stake breaks or rots for example.

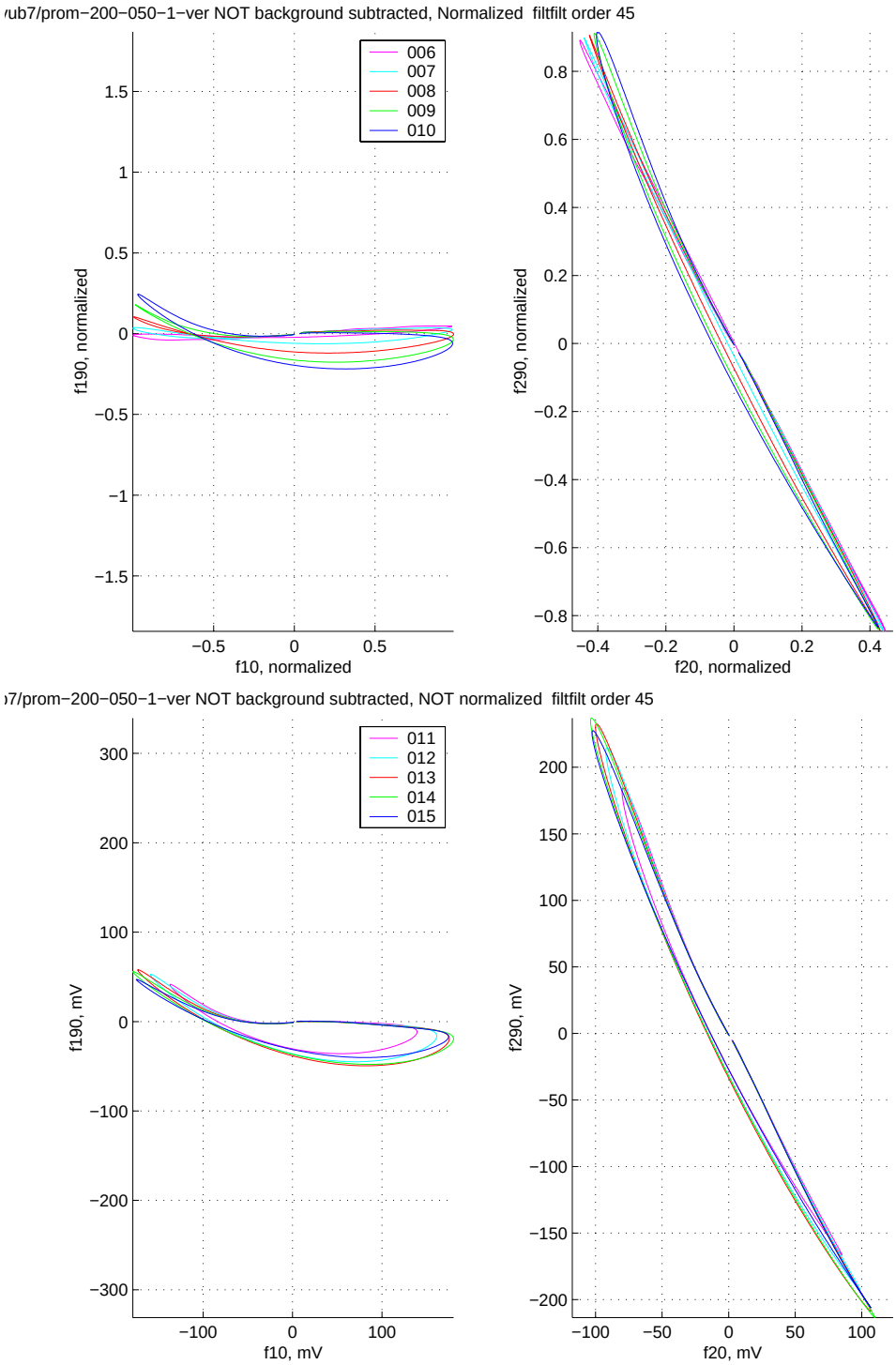

Figure 5.37: 2D response (parallel scans) at f_1 and f_2 to a **PROM** mine placed **vertically** (pronged striker above surface). Top: normalized, scans 6-10 (approach phase), Bottom: scans 11-15 (passing over the target).

- exploit the fact that the phase response curves are quite open, or
- exploit the amplitude ratio information: *AR* is slightly <1 here, and therefore quite unlikely to correspond to a small non-ferromagnetic object (see also §6.2.6).

Incidentally, the overall amplitudes are not very large in this case, given the mass of the mine, and they change only slightly over the mine.

5.9.2. PMR-2A – Stake Fragmentation Mine

Vertical orientation: A cylindrically shaped PMR-2A stake fragmentation mine, also made of steel and overall about 20 cm long, was placed vertically above the ground, and acquisitions taken in 2D.

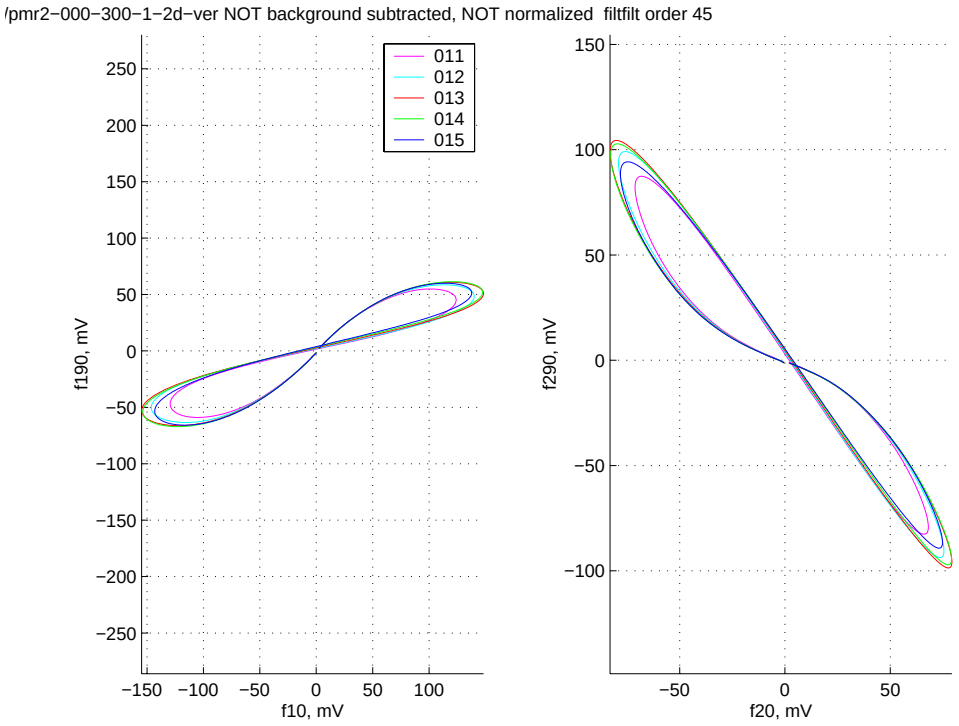

Figure 5.38: 2D response (parallel scans) at f_1 and f_2 to a **`PMR-2A`** mine placed **vertically** (mine above surface). Scans 11-15 (passing over the target).

The results, shown in Figure 5.38, represent a **nice example of the response of a large ferromagnetic object**, with a positive phase response at f_1 and a largely negative one at f_2, with open curves (typical of ferromagnetic objects) and *AR*~1.3, and *would allow an easy target identification*. Note that the straight section does here correspond to the central part of the scan, above the object, when the magnetic field is mostly aligned along the mine's axis of symmetry. Signal amplitudes are not very large in this example.

Perpendicular and Parallel orientation: Measurements were also carried out with a mine lying on the surface (as if it had fallen down, see introductory remarks). Four different orientations were analysed, namely PAR1 (parallel to the scanning direction and detector first scanning the pin, then the mine body) followed by 3 successive counter clockwise rotations: PER1, PAR2 and PER2. The detector output was unfortunately partially saturated due to the close proximity to the mine.

The responses to the PER1 and PER2 orientations are nearly identical, PAR1 and PER2 are similar but not exactly equal. What is perhaps more important is that *PAR and PER are more similar to each other than to the vertical orientation*. Their phase response is rotated at both frequencies towards the vertical compared to the VER configuration (see also Figure 5.39); it is however still positive at f_1 and negative at f_2, with quite a large phase difference between the two values, and *should therefore still be quite distinctive*. This situation bears some similarity to the results for the large reference cylinder (**`msc2`**), VER vs. PER configurations (see Figure 5.13).

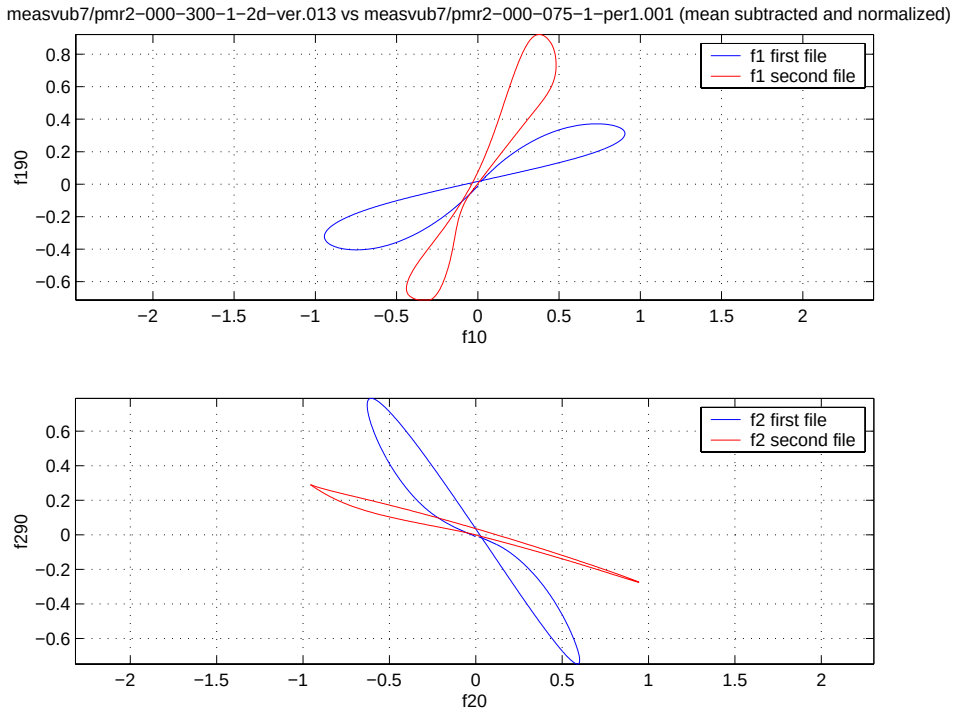

Figure 5.39: Response at f_1 and f_2 to a **PMR-2A** mine at **different orientations**: VER vs. PER. Normalized.

5.9.3. A Composite UXO Example

Tests were also carried out with a 20 mm projectile shown in Figure 7.12, an interesting **composite object** about 14 cm long, featuring a non-ferromagnetic tip (likely aluminium) on top of a cylindrical steel body. The overall response can therefore be **highly orientation-dependent**, according to the strength of the responses of the two parts (the overall behaviour can probably be approximated with the sum of two physically separated dipoles).

Vertical orientation: the target was placed vertically with the nose upwards ("up") and downwards ("down"), with the detector carrying out 1D scans at different heights (Figure 5.40, Top). The response is *radically different for the two orientations*, in particular at f_2, due to the fact that in one case the non-ferromagnetic tip is closest to the object, in the other it is farthest. The response is largest with the target pointing downwards; *it depends here also on the height*.

The response amplitude ratios are about 2.75 (down) and 2.1 (up) at a height of 2.5 cm, the first value being typical of an elongated ferromagnetic object when the primary magnetic field is mostly aligned with its symmetry axis.

Perpendicular and Parallel orientations: Measurements were also carried out with the target lying on the surface at four different orientations, PAR1 and PAR2, PER1 and PER2 (Figure 5.40, Bottom). The PAR1 and PAR2 responses are quite irregular and change somewhat with distance, whereas PER1 and PER2 are much more stable (straight lines), especially at f_1. In this case the parallel orientation seems to deliver a less strong signal than the perpendicular one, contrary to what we have seen for most other cylindrical ferromagnetic objects.

In spite of the response changes with orientation, the target can be clearly identified at all orientations as a large (mostly) ferromagnetic object.

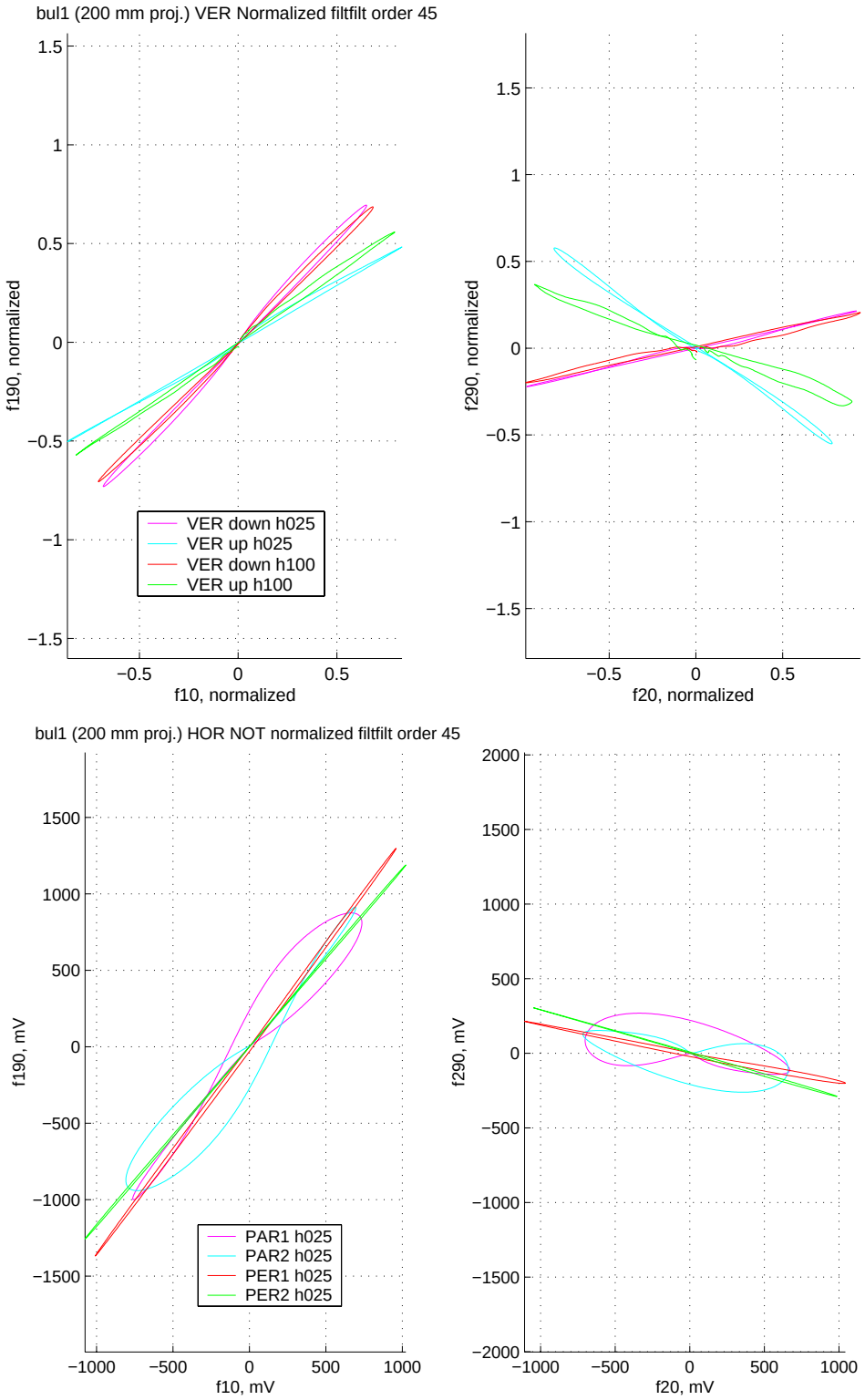

Figure 5.40: Response at f_1 and f_2 to a 20 mm projectile (**`bul1`**), flush. Top: **vertical** down and up, at two different detector heights (normalized); Bottom, **horizontal** at 4 different orientations (detector at 2.5 cm)

5.10. Response for Other Mine Types

Figure 5.41 shows the response of a Vietnamese MD-82B AP mine (**miviet**), also collected in Cambodia. This mine does visually look like a US M-14 AP; it does however contain different metal components – the fuzing system is completely different – and is "easily" detectable. In this sense it is not a minimum-metal mine. The response is clearly ferromagnetic and does not change with distance for the scans carried out.

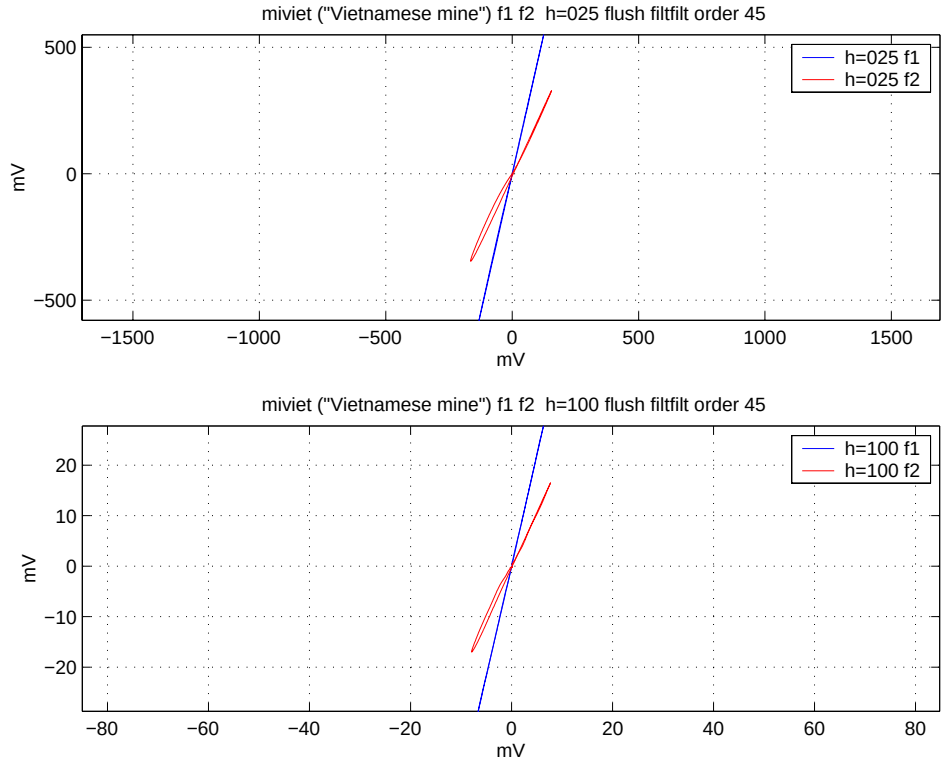

Figure 5.41: Response at f_1 and f_2 to a Vietnamese MD-82B AP mine (**miviet**), flush, at two different detector heights.

5.11. Clutter (Debris) Analysis

During the tests carried out by the EPFL DeTeC team in Cambodia with a GPR prototype [BRO98], numerous metallic debris samples were collected from a simulated minefield situated next to a village. Although inert mines had been emplaced, the Halo Trust team followed their standard operating procedures using an Ebinger Ebex 420 SI MD. Each metallic piece, or set of pieces, was then removed and collected. The land was otherwise untreated; the collected clutter should therefore be representative. Examples are provided in A5.5.

In the following we have tried to form groups of similar objects whenever possible. Note that all sizes in the following table are approximate.

Debris Group #1: deb01-16, 16 objects – Cylinders, Plates

The objects in this group are listed in the following table:

ID	*Description*	*Geometry*	*Size (cm)*	*Comments*	*MD Response Comments*
01	Rusted nail	CYL	L:6 Ø:0.5		
02	Rusted nail	CYL	L:5.5-6 Ø:0.5	Irregular Ø (strong)	
03	Rusted cyl	CYL	L:7.5 Ø:0.3-0.4		
04	Rusted nail	(bent) CYL	L:6 Ø:0.3-0.4	Bent in middle	No straight line
05	Rusted nail	CYL	L:4 Ø:0.3-0.4	Irregular Ø (weak)	
06	Rusted cyl	CYL	L:2.5 Ø:0.2-0.3		
07	Rusted nail, bent	linear	L:3 Ø:0.2	Bent at 1cm	Weak response
08	Plate	RECT	L,H: 2.5	"T" shaped, flat	Irregular at f_2
09	Plate	RECT	L,H: 2.5	"T" shaped, flat	Irregular at f_2
10	Plate	"L" shaped	L,H: 2	Outer dim.	
11	Bottle cap	ROUND	Ø: 3	Earth covered	Very odd!
12	Shrapnel	IRREG	L:3 H:2		Open curve, ferro
13	Shrapnel	IRREG	L:3 H:2		Ferro
14	Piece of hard plastic?	TRAPEZ	L:3 H:3	Flat	Non-ferro
15	Fragments	IRREG		Scattered, flat	Magnetic, no MD alarm (s=3)
16	Rivet head	ROUND	Ø:0.8 H:0.3	short	Weak response. Non-ferro

They can be indicatively subdivided as follows (all are *ferromagnetic* except 14, 16):

- *Cylindrical objects* (nails etc.; **`deb01-07`**). MD signals for the PAR orientation are usually quite stronger than for PER. The responses (see Figure 5.42) bear qualitative similarity to the ones from ferromagnetic cylinders.
- *Plates* (**`deb08-10`**): the phase angles are closer to +90° than the previous cylindrical objects (Figure 5.43, Top).

- Other: **deb11** has a quite irregular behaviour; **deb14** and **deb16** are typically non-ferromagnetic; **deb15** are magnetic fragments (Figure 5.43, Bottom).

deb15 represents a type of target, usually magnetic with a clear imaginary signal (a few mV), to which the Förster MD does not react with an alarm. This might be due to the fact that on the field a different MD has been used, which might be sensitive to (purely) magnetic objects, and/or that such objects were close to a normal (conductive) target.

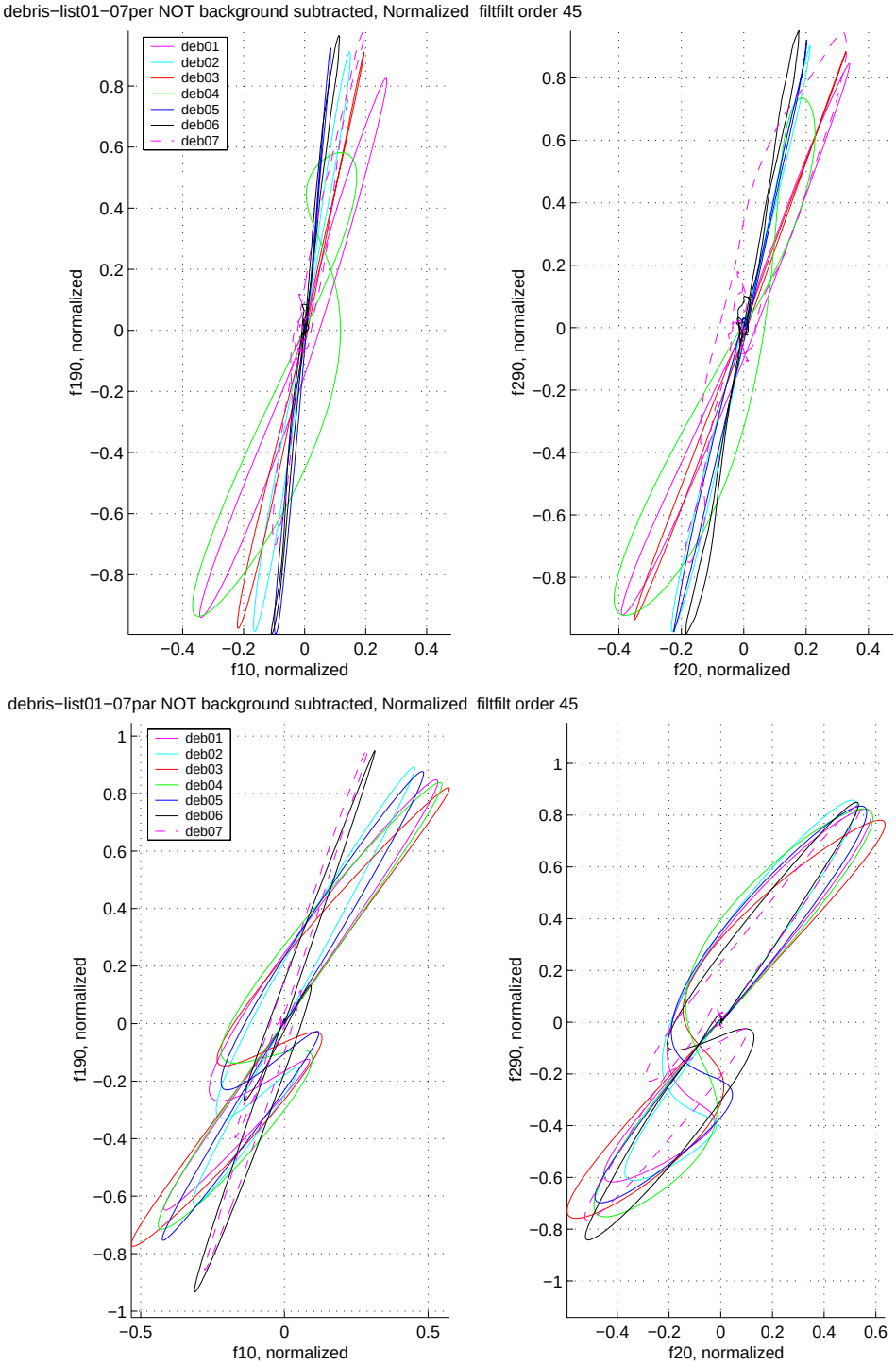

Figure 5.42: Response at f_1 and f_2 to **deb01-07** in the horizontal plane; normalized, objects on the surface. Top: PER, Bottom: PAR.

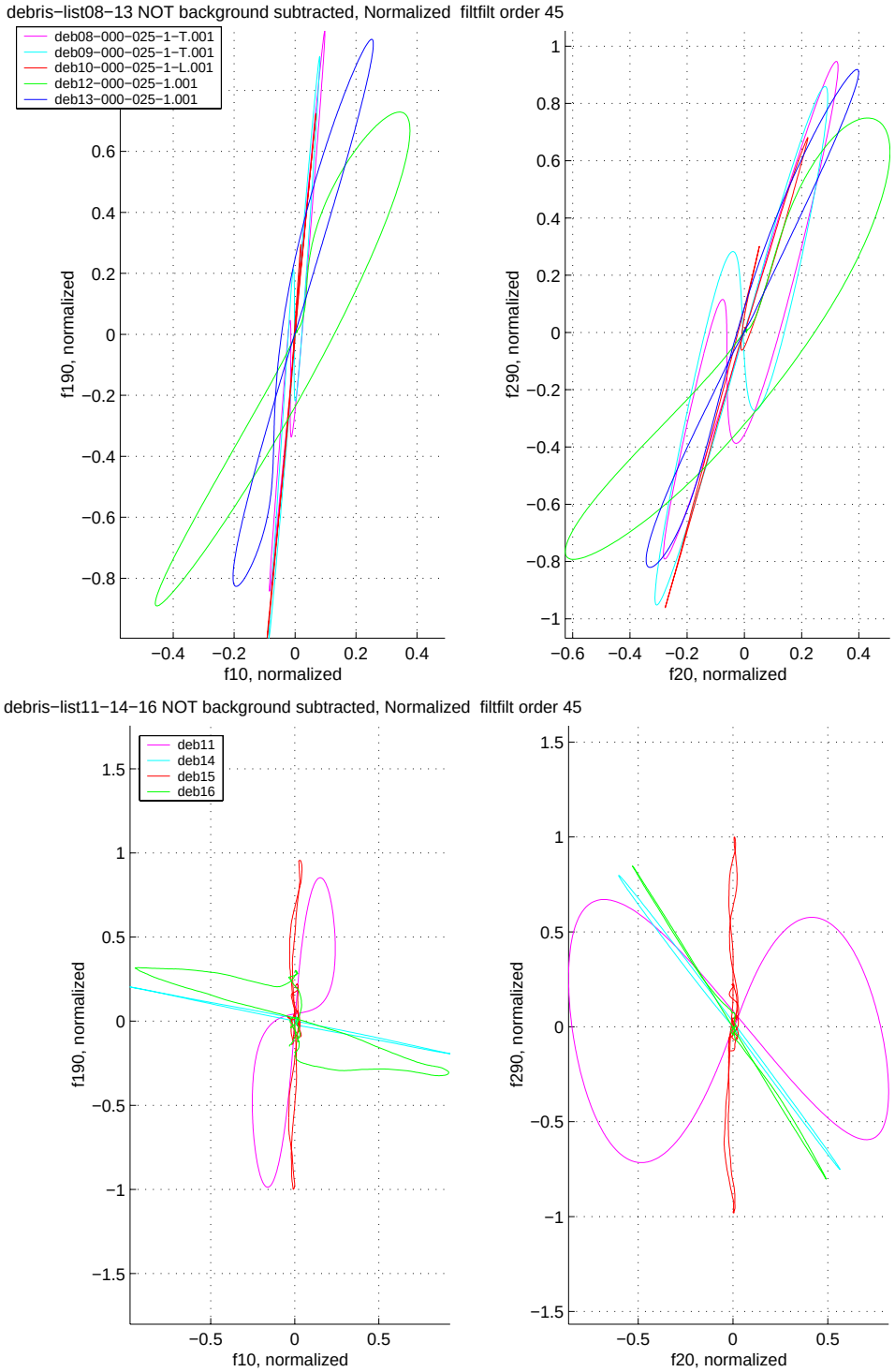

Figure 5.43: Response at f_1 and f_2 to **deb08-10&12-13** (Top) and **deb11&14-16** (Bottom) in the horizontal plane; normalized, objects on the surface.

Debris Group #2: deb20-26, 7 objects – Non-Ferromagnetic Foils

Objects in this group are **non-ferromagnetic foils**:

ID	*Description*	*Geometry*	*Size (cm)*	*Comments*	*MD Response Comments*
20	Large foil	RECT	L,H: 10	irregular	Strong response
21	Foil	RECT	L: 6 H: 2	irregular	
22	Foil	RECT	L: 3 H: 1.5		
23	Small foil	RECT	L: 1.5 H: 2		
24	Small foil	RECT	L: 3 H: 1		
25	Foil pieces	RECT	L,H: 1 (max)	7 pieces	
26	Foil pieces	RECT	L:2 H:1 (max)	8 pieces	

Their main characteristics are (see Figure 5.44):

- The responses are mostly quite weak, especially at f_1; actually: *AR*~1/7-1/8.
- All phase are close to 0°, excepted **`deb20`** (see Figure 5.44).

Note that plotting the phase difference would give a very low value for all objects (excepted **`deb20`**), resulting in good discrimination. In this case discriminating on the amplitude ratio should also work well.

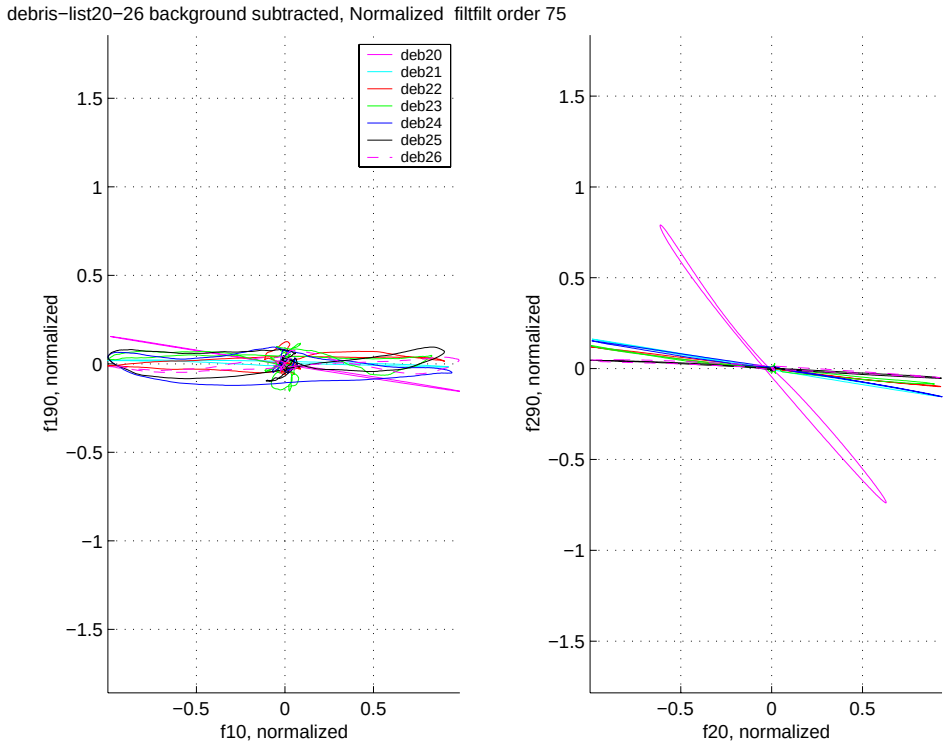

Figure 5.44: Response at f_1 and f_2 to **`deb20-26`** in the horizontal plane; normalized, objects on the surface.

Debris Group #3: deb30-39, 10 objects – Ferromag. Foils and Small Fragments

Objects in this group are **ferromagnetic foils** and collections of **small fragments** thereof:

ID	*Description*	*Geometry*	*Size (cm)*	*Comments*	*MD Response Comments*
30	Rusted	RECT	L,H: 4		ferro
31	Rusted	RECT	L,H: 6	Large irregular	Open curve
32	Rusted	RECT	L,H: 5	Large irregular	
33	Rusted	RECT	L: 3 H: 2		
34	Rusted	RECT	L: 2.5 H: 1.5	irregular	
35	Rusted	RECT	L: 4 H: 3	irregular	Open curve
36	Rusted	RECT	L: 2 H: 1	Small irregular	
37	(Rusted) Pieces	RECT	L: 2 H: 1 (max)	8 pieces	
38	(Rusted) Pieces	RECT	L1,H1: 1 (max)	2 pieces	Magnetic, no MD alarm (s=3)
39	(Rusted) Pieces	RECT	L,H: 1.5 (max)	7 pieces	

Their main characteristics are (Figure 5.45):

- Their phase responses are quite close to +90° (excepted **`deb31`**, a large object, and **`deb35`**).
- Some of them give small phase difference (and sometimes, when the amplitudes at f_1 and f_2 are quite close, small amplitude difference values as well). This could again be used as a discrimination criterion.

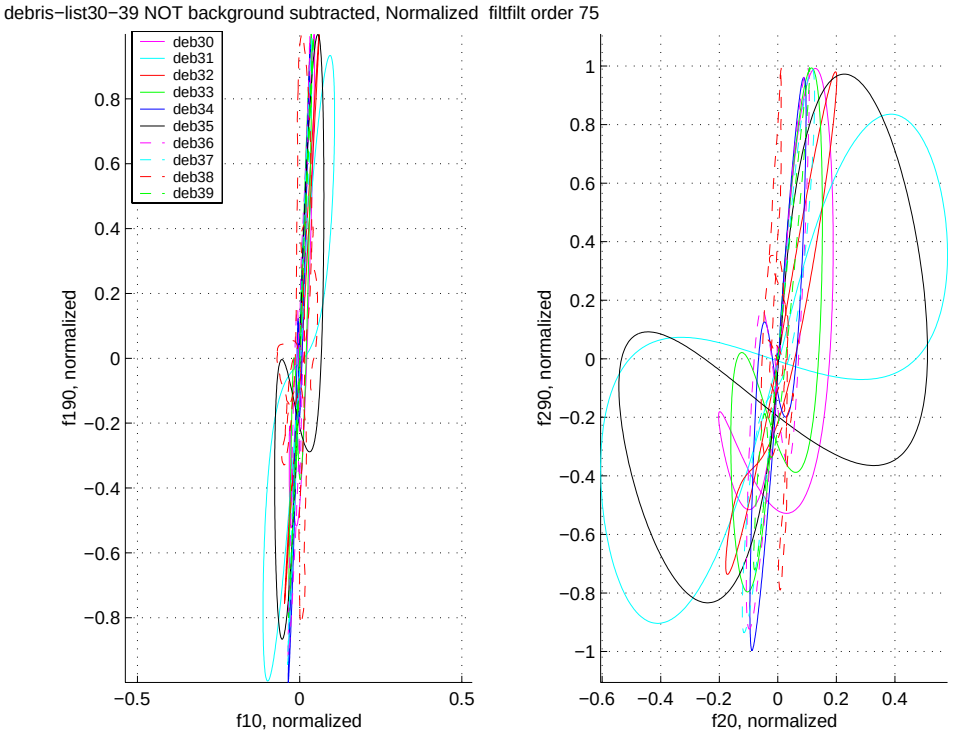

Figure 5.45: Response at f_1 and f_2 to **`deb30-39`** in the horizontal plane; normalized, objects on the surface.

Debris Group #4: deb40-41, 2 objects – Wires

Objects in this group are non-ferromagnetic wire pieces. Their main characteristics are:

- The responses are mostly quite weak, especially at f_1; actually: *AR*~1/7-1/8, the amplitude at f_2 being of 1-2 mV.
- The phase angles are also quite low, about –8° at f_1 and –20° at f_2.
- The phase differences are again quite small (lower for **deb40** than for **deb41**).

ID	*Description*	*Geometry*	*Size (cm)*	*Comments*	*MD Response Comments*
40	Wire strand Twisted	CYL	L:10 Ø:0.3-0.4	bent	
41	Wire strand	CYL"L" shaped	L:3+3 Ø:0.3-0.4	bent	

Debris Group #5: deb50-53, 4 objects – Misc

Objects in this group are miscellaneous. Their main characteristics are:

- The phase response of **deb50** and **deb51** is very close to +90°. Although the imaginary component is clear (about 5 mV) they are very weakly detected at s=3 in the PAR orientation. The amplitudes at f_1 and f_2 are quite close, and their difference is therefore quite small. This could perhaps again be used as a discrimination criterion.
- **deb52** gives a clear ferromagnetic signal, **deb53** practically no signal at all (could have been included by mistake).

ID	*Description*	*Geometry*	*Size (cm)*	*Comments*	*MD Response Comments*
50	Shrapnel	~CYL	L:2 Ø:0.3-0.4	Weakly magnetic	Very weakly detected (s=3,PAR)
51	Shrapnel	~CYL	L:1.5 Ø:0.3-0.4	Weakly magnetic	Very weakly detected (s=3,PAR)
52	Clip	CYL	L:3.5 Ø:0.1-0.2	Thin, bent. Strongly mag.	
53	Charcoal	IRREG	L:0.8 H:0.5	Small piece	No MD alarm (s=3)

Debris Group #6: deb60-66, 7 objects – Small Pieces (no MD alarms)

Objects in this group are small pieces, *none producing an MD alarm*, even at s=3. Their main characteristics are:

- All except **deb62** and **deb64** give practically no signal at all.
- **deb64** is clearly magnetic (Im~2.5 mV).
- **deb62** responds in a singular way: the signal at $f_2$0° is very weak (~0.2 mV) but clear, all other channels are practically zero. It could be an object with quite a low conductivity.

ID	*Description*	*Geometry*	*Size (cm)*	*Comments*	*MD Response Comments*
60	Small pieces	IRREG	L,H: 1 (max)	10 pieces	
61	Small pieces	RECT	L,H: 1.5 (max)	2 pieces	
62	Small piece	TRIANG	L1,L2: 1		f_2 REAL>0 but no alarm!
63	Small pieces	RECT/TRIANG	L,H: 1.5, L1,H1: 1	2 pieces	
64	Small piece	RECT	L: 2 H: 1		Magnetic
65	Small piece	RECT	L: 1 H: 1.5		
66	Small pieces	RECT	L1-4, H1-4: 0.5, L5: 2, H5: 0.5	4+1 pieces	

Debris Group #7: deb70-82 (deb74 missing), 12 objects – Misc (mostly ferromag.)

Objects in this group are miscellaneous (*ferromagnetic* excepted **`deb77-79)`**; they are listed in the following table:

ID	*Description*	*Geometry*	*Size (cm)*	*Comments*	*MD Response Comments*
70	Large foil	RECT	L: 11, H: 8-9	Irregular. Not flat	Non-ferro. Very strong response.
71	Rusted nail	CYL	L: 4, Ø: 0.5		Ferro. Weak response (PER)
72	Bullet	CYL	L: 4, Ø: 1		Ferro. PER~PAR!
73	Nail	CYL	L:5.5 Ø:0.3-0.4		Ferro
75	Shrapnel	IRREG (bent, flat surface)	L: 3, Ø: 0.5-1		Ferro, weak. Irregular at f_2
76	Nail	CYL	L: 4 Ø: 0.3		Ferro
77	Cylinder	CYL	L: 3, Ø: 0.5-1		Non-ferro
78	Plate	RECT	L: 2.5 H: 2		Non-ferro
79	Alum. cyl. (hollow and open)	CYL	L: 2, Ø: 1.5		Non-ferro
80	Shell fragment	RECT	L:3.5, H:2, d:0.8		Ferro
81	Shell fragment	RECT	L:3, H:1, d:0.9		Ferro
82	Shell fragments	RECT	L1: 2,H1: 1, L2,H2: 2	2 pieces, thickness~0.6	Ferro. Very irregular at f_2.

Their main characteristics are (see Figure 5.46, Figure 5.47):

- For some of these ferromagnetic objects the phases are quite close at f_1 and f_2.
- For all these *ferromagnetic* objects *AR* is about 1.5-2 for PAR, closer to 1 for PER. For all these *non-ferromagnetic* objects the amplitude ratio is usually less than 0.5.
- **`deb79`** features interesting *orientation effects*, in particular along VER, *quite atypical for a non-ferromagnetic object* (its signal amplitude is about 1/3 of the other orientations).

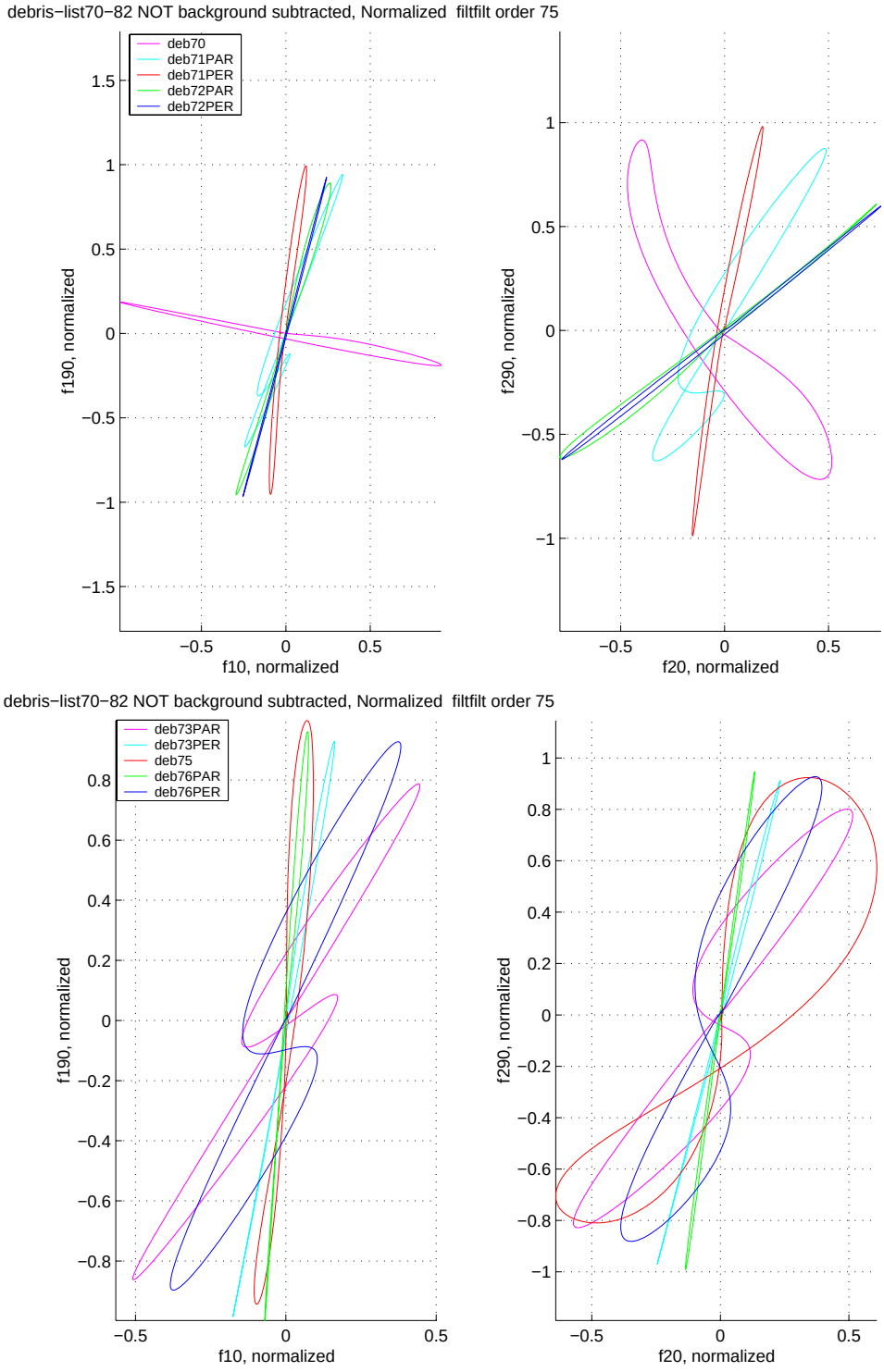

Figure 5.46: Response at f_1 and f_2 to **`deb70-72`** (Top) and **`deb73&75-76`** (Bottom) in the horizontal plane; normalized, objects on the surface.

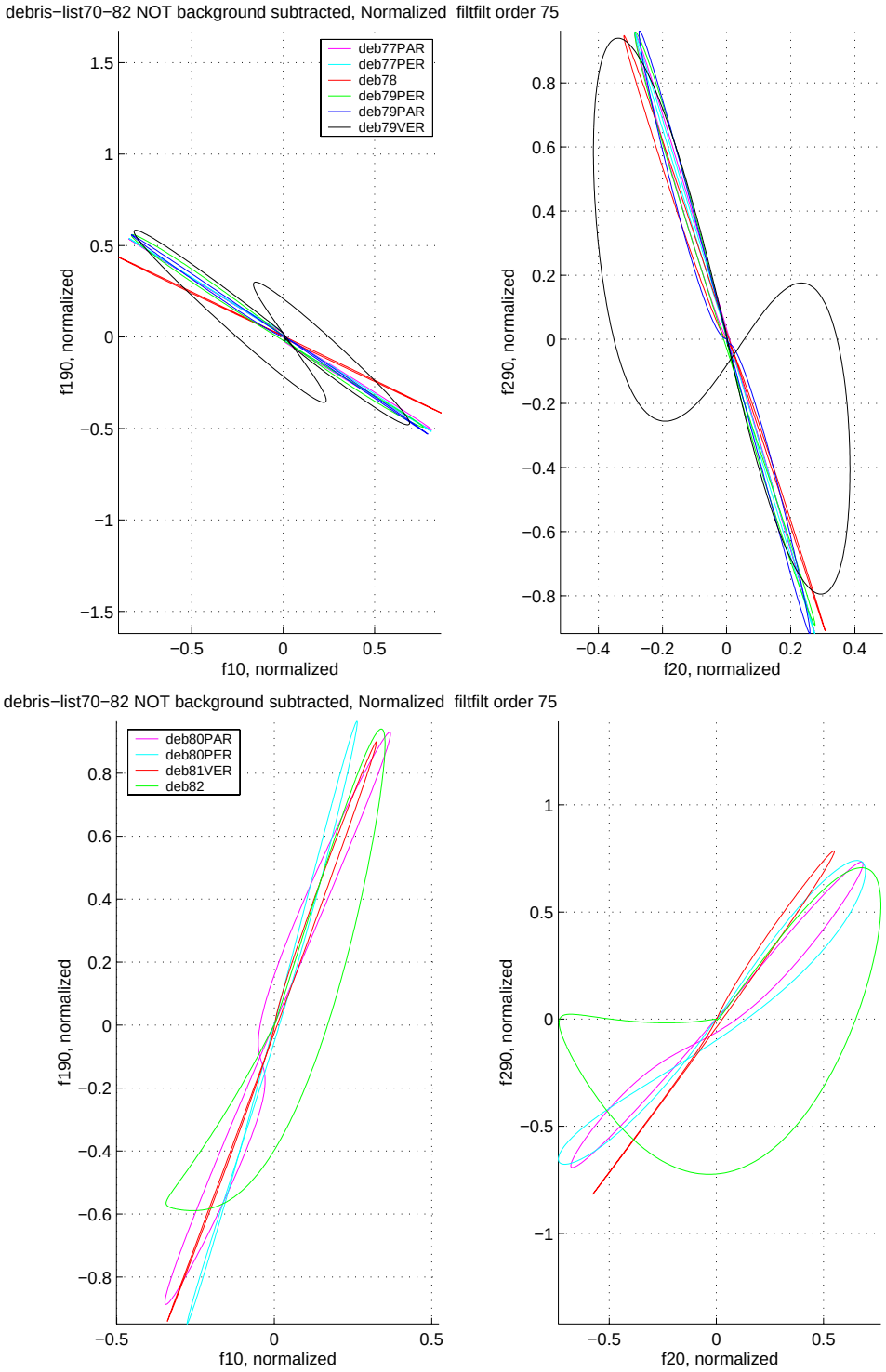

Figure 5.47: Response at f_1 and f_2 to **`deb77-79`** (Top) and **`deb80-82`** (Bottom) in the horizontal plane; normalized, objects on the surface.

Debris Group #8: deb90-96, 7 objects – Misc

Objects in this group are miscellaneous. Their main characteristics are:

- **deb90** and **deb96** are non-ferromagnetic. The amplitude ratio is about 1/5 for the first and 1/4.5 for the second.
- **deb91** gives practically no signal at all.
- The other objects are various small ferromagnetic pieces, whose responses are quite similar to one another. The amplitude ratios are in this case around 1.2.
- **deb92-93**, **deb95** and **deb96** are probably parts of different fragmentation mines.

ID	*Description*	*Geometry*	*Size (cm)*	*Comments*	*MD Response Comments*
90	Spent cartridge	CYL	L: 6 Ø: 1.5		Non-ferro
91	Stone	RECT	L: 1 H: 0.7		No MD alarm (s=1)
92	Steel ball	ROUND	Ø: 0.5		Ferro
93	Steel ball	ROUND	Ø: 0.5		Ferro
94	Shell fragment (molten)	RECT	L: 1.7, H: 1, d: 0.7		Ferro
95	Steel ball	RECT	L: 1	Slightly rounded	Ferro
96	Burst open fragment?	RECT	L: 1 H: 1.3		Non-ferro. Weak response.

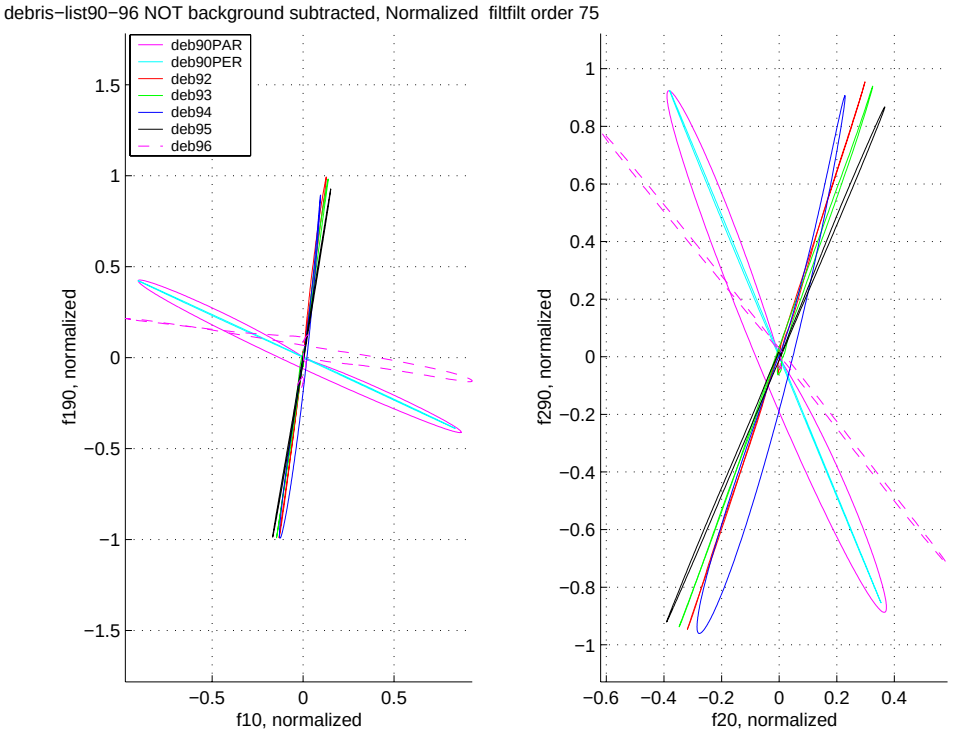

Figure 5.48: Response at f_1 and f_2 to **deb90&92-96** in the horizontal plane; normalized, objects on the surface.

Debris Group #9: deb100-107, 8 objects – Large Non-Ferromagnetic

Most of the objects in this group are *large non-ferromagnetic pieces*, actually large UXO fragments collected from a testing range (**deb101** was collected in Cambodia). Their main characteristics are (see Figure 5.49):

- **deb100** to **deb104** produce very strong signals close to inductive limit. The response from **deb101** is irregular and does actually contain some positive phase values (multipole effects?).
- The responses from these large non-ferromagnetic objects are mostly *orientation invariant* (PAR, PER).

ID	*Description*	*Geometry*	*Size (cm)*	*Comments*	*MD Response Comments*
100	Massive fragment	RECT	L:8, H:7, d:2		Non-ferro. Very strong response.
101	M16-like magazine (hollow)	RECT	L:12, H:7.5, d:1.5		Non-ferro. Very strong response.
102		RECT/IRREG	L,H:8.5, d:0.5	Probably copper	Non-ferro. Very strong response.
103	?		L:7, H:4.5, d:2.5		Non-ferro. Very strong response.
104		RECT	L:10, H:4	Not flat	Non-ferro. Very strong response.
105		RECT	L:11, H:4, d:0.1	Strip, bent at 3/4 of the length	Ferro.
106		RECT	L:12.5, H:1, d:0.1	Strip (see deb 105), straight.	Ferro.
107		RECT/IRREG	L:6, H:2		Non-ferro.

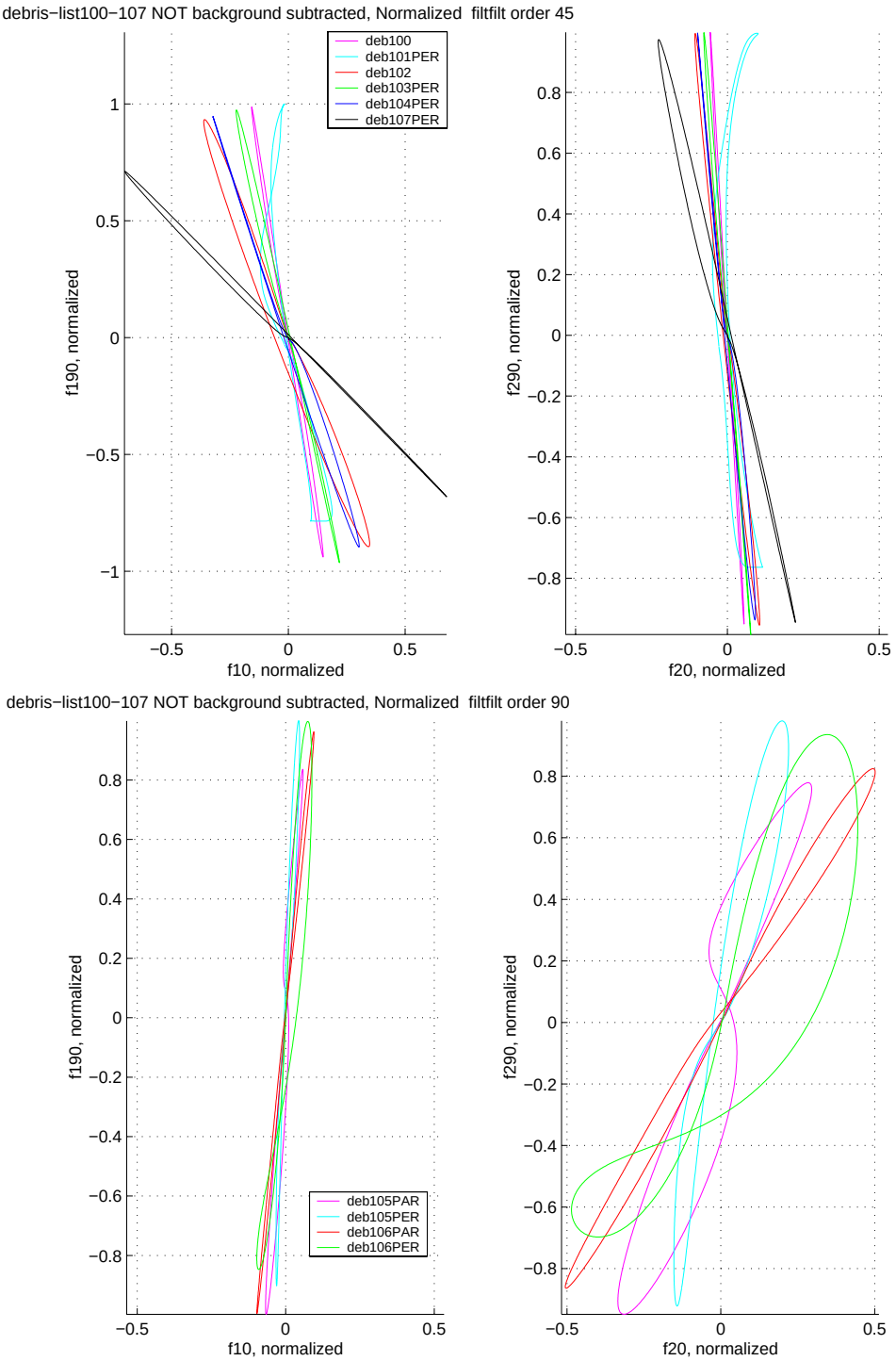

Figure 5.49: Response at f_1 and f_2 to **deb100-104&107** (Top) and **deb105-106** (Bottom) in the horizontal plane; normalized, objects on the surface.

5.12. Summary of Experimental Results

A number of elements of the theoretical models we looked at were confirmed (at least for the objects and experimental conditions described before) by the experimental results obtained with the CW two frequency system. In particular:

- The phase of (small) ferromagnetic and non-ferromagnetic objects shows a sign difference, but features similar trends: in both cases the *phase* decreases for increasing frequency and behaves in the same way at the inductive limit.
- Large ferromagnetic objects can have a positive phase at f_1 and a negative at f_2 (e.g. **`PMR-2A`**), or even both negative (e.g. **`PROM`**).
- The *absolute value* of the induced voltages increases for increasing frequency considering non-ferromagnetic objects or large ferromagnetic ones (e.g. **`PROM`**), the contrary for small ferromagnetic ones[64].

The experimental results also tell us that:

Soil Effects

- The importance of the **background (soil) effects,** due to soil inhomogeneities and/or surface height variations, has been confirmed, in particular on the imaginary component ($f_1$90°,$f_2$90°) of the received signal[65].
- The corresponding *signal fluctuations* do affect in particular the identification of small and/or deep objects; similar conclusions have been reached in [GAO99] using the GEM-3 sensor. From the detection point of view they can be effectively countered, at least under the experimental conditions tried out, by frequency differencing techniques.

Orientation/Distance Effects

- The response of **non-ferromagnetic objects** is usually not strongly orientation sensitive, nor influenced by height (distance) variations or axial offsets (exceptions are possible, see the case of **`deb79`**, or for large objects close to the detector).
- The response of (elongated) **ferromagnetic objects** is usually strongly *orientation* dependent, all the more so for those configurations in which the primary magnetic field moves from being predominantly aligned along the symmetry axis to being predominantly perpendicular to it (in which case the response tends to rotate counter clockwise, i.e. towards +90°), or vice versa (in which case the response tends to rotate clockwise, i.e. towards 0°). A VERtical placed object does therefore bear similarities to one place PARallel to the scanning direction, in the horizontal plane. This can probably be well explained with a sum of induced dipole moments (§3.6.1 and §3.6.3).
- The response of (elongated) **ferromagnetic objects** can therefore also change considerably with the detector *distance*, depending on their orientation.

Mines

- The response of a **minimum-metal mine**, composed of a detonator containing non-ferromagnetic metal and a ferromagnetic striker pin, can be well approximated with the sum of the two individual responses (like for two non-interacting objects). In the particular case we studied the mine's overall response is **highly characteristic** (two responses at nearly 90° difference).

  However, as the two components are separated by a distance of a few cm the overall response can be strongly dependent on the target orientation.

64. Strictly speaking we are considering as usual the response function behaviour, i.e. dividing the induced voltage by $i\omega$.
65. In our experimental conditions the real components were quite stable.

- An inert **detonator** has also been compared with a real one, and **inert strikers** have been compared among themselves; in the first case some differences have been encountered, in the second the responses were the same.

  If we take *the detonator alone*, a situation which is typical of a number of minimum-metal mines, it will definitely be *harder to discriminate it from clutter,* as its response will be similar to that of other small non-ferromagnetic objects[66].
- The *detonator* can produce a non-negligible response in a minimum-metal mine.
- The components of *similarly looking mines* can have completely *different* responses (e.g. the striker of the **`pmnCambodia`** mine and of the Miltra PMN replica).
- The response of a **`PMN`**, a typical medium metal content mine, represents a good example of a composite object whose phase response can vary considerably with axial offset and orientation (open curves at f_1, etc.) and is **quite typical**.
- The response of some **metallic mines** (**`PROM`** – bounding fragmentation, and **`PMR-2A`** – stake fragmentation mine) and UXO (Unexploded Ordnance) can in part be well approximated by the response of **large ferromagnetic cylinders**. The phase response of the **`PROM`** is particularly interesting, as it could be mistaken for a non-ferromagnetic object, discriminating on the phase response alone. The response of the **`PMR-2A`** is **quite characteristic** of a *large ferromagnetic object*, positive at f_1 and negative at f_2.

Clutter (Debris)

Several tens **metallic clutter pieces**, mostly collected in Cambodia on a simulated mine field, have been analysed as well. Most of the clutter seems to be *ferromagnetic*.

- **Small ferromagnetic pieces** (nails, plates, pieces) feature mostly a phase response between +90° and +45° (indicative values), foils even less, between +90° and about +75°.
- **Non-ferromagnetic foils** feature mostly a small phase response, between 0° and about –15°.

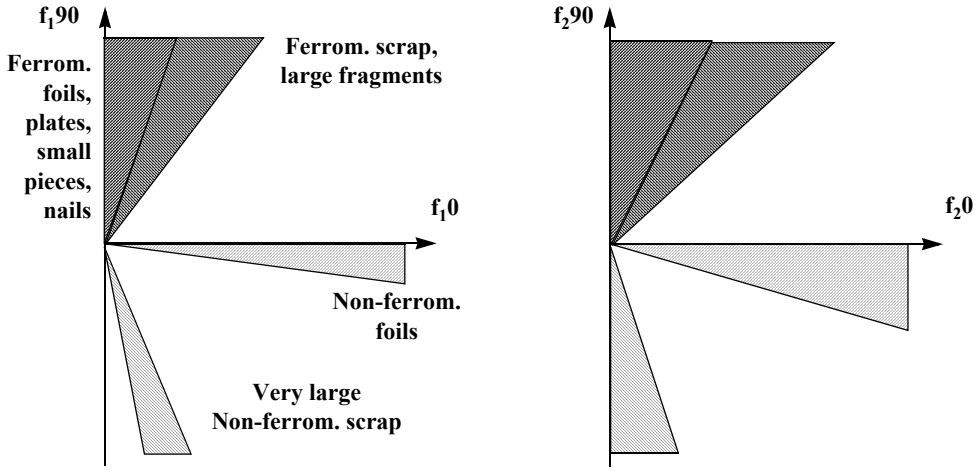

Figure 5.50: Schematic debris responses at f_1 (left) and f_2 (right, same categories as f_1).

- **These clutter items can be quite clearly distinguished from the response of larger objects** (at least under laboratory conditions; see Figure 5.50 for a schematic representation) and could constitute a basis for object discrimination. Larger clutter items are harder to discriminate, although this could still be possible when looking for mines with larger metallic components.
- Some ferromagnetic objects have quite an irregular response (e.g. a bottle cap, **`deb11`**) and are also harder to discriminate.

66. In principle we could still distinguish it from ferromagnetic clutter, though.

5.13. Conclusions

In a certain sense some deminers are already discriminating metallic objects themselves, or some of their parameters such as burial depth, using as input "only" their detector's audio signal and relying on their experience. Whether or not they take decisions based on their interpretation depends a lot on the operating context. The answer ranges from a policy of strictly investigating each alarm to some degree of freedom of decision (to reject weak signals for example, see also §1.3). What we are basically investigating is if we can provide similar reliable (and operator independent) information directly and reproducibly from the detector's internal signals.

Summarising this chapter's results, we have exploited spatial high-resolution scanning to analyse, in a laboratory setup with the objects either flush or buried, the response from reference objects and targets, ranging from a minimum-metal mine and its components to larger metallic mines and UXO. We have also carried out a detailed clutter (debris) analysis used representative objects.

The raw data has been collected using the **internal signals** of a commercially available differential CW system, the Förster Minex 2FD; the availability of this type of unprocessed information from existing systems was in no way granted at the time this work started. The use of "only" two frequencies is partially compensated by they being placed towards the limits of the frequency band of interest.

In this chapter we have dealt mostly with **qualitative** aspects of the **phase response**, looking at signal trajectories in the **complex plane**. This method, inspired from NdT, makes it possible to exploit global object properties rather than only local ones. Similar work has also been carried out independently by Szyngiera [SZY99]. Some multifrequency data collected at discrete spatial locations with the GEM-3 sensor has also been represented in the complex plane [KEI99].

A number of theoretical elements of the basic models we looked at have been confirmed (see §5.12 for details), in particular the trends in the phase response with increasing object size and/or conductivity (actually increasing induction number), the difference between ferromagnetic and non-ferromagnetic objects, and important demagnetization effects. **Fluctuations in the soil signal** are also clearly documented in the experimental data.

Where we see particular added value for the scientific community is in the **detailed response analysis**, which has allowed to highlight a number of effects such as orientation dependencies or changes due to axial offsets (elongated ferromagnetic targets). Subtle effects have also been documented, such as the response of composite objects and their variability, or of different versions of a same mine.

We have also shown that it is possible to distinguish smaller clutter items from larger objects, and that *some mines* have quite *characteristic responses* (e.g. **`PMN`**). A *"qualitative" (coarse) target classification is therefore possible*, at least for situations with a sufficient signal to noise (S/N) ratio.

Provided that such a discrimination approach, or a similar one, will prove to be feasible in the field, it is however likely that the actual discrimination rate will depend a lot on the target(s) being sought, as well as on the actual debris distribution of course. This will be discussed in more detail at the end of Chapter 6. Other possible application scenarios include the use of metal detectors after having employed mechanical devices and possibly dogs, as certain teams look at this point only for larger metallic pieces. Quality Control applications might also be considered.

Practical Problems

Needless to say, some problems might complicate a practical implementation and some of them might have to be carefully thought over. For example (*"D"* means applicable to the Discrimination approach, *"I"* to the Identification):

- Data analysis gets obviously more difficult with *decreasing signal to noise ratio*, e.g. for smaller and/or deeper objects.
- *(I/D)* The *object parameters* (σ, μ, perhaps even the shape) can vary. These variations can be small, for example within a single batch of metallic pieces, or larger, between different batches. Copies of mines might also use different pieces.
- *(I)* There might be a metallic piece close to a minimum-metal mine, faking its response. Unforeseen objects can also be found.
- *(D)* The variability in the type and distribution of clutter (debris) can be truly impressive.
- *(D)* The effect of co-located ferromagnetic and non-ferromagnetic objects needs to be studied more attentively.
- *(I/D) Background signals*, in particular due to the soil itself, could become THE problem in a number of ground conditions, in particular when weak signals (small and/or deeply buried objects) or ground inhomogeneities are present. How to overcome them whilst guaranteeing robust identification or discrimination is likely to be far from trivial. We recall that most objects were buried flush with the surface in the experimental data shown.

Apart from technical issues there are certainly practical problems to deal with, such as making sure that a sufficient number of application scenarios do actually exist, and insuring acceptance by the end users (who accepts the responsibility for certain choices for example?).

As a final comment we note that although some of these results were already known to the metal detector community, their diffusion has rarely happened, to the best of our knowledge, in a public document and in a coherent way, with the necessary scientific rigour.

Bibliography

[BRA01] H. Braunisch, C. O. Ao, K. O'Neill, and J. A. Kong, "Magnetoquasistatic Response of Conducting and Permeable Prolate Spheroid Under Axial Excitation", IEEE Transactions on Geoscience and Remote Sensing, v. 39, no.12, pp. 2689-2701, Dec. 2001

[BRO98] J. Brooks and J.-D. Nicoud, "Applications of GPR Technology to Humanitarian Demining Operations in Cambodia: Some Lessons Learned", in *Proc. Third Intnl. Symposium on Technology and the Mine Problem* (Naval Postgraduate School, Monterey, CA, USA, April 6-9, 1998). Proceedings published on CD-ROM. Also available from http://diwww.epfl.ch/lami/detec/.

[BRU98a] C. Bruschini, B. Gros, F. Guerne, P.-Y. Pièce, and O. Carmona, "Ground penetrating radar and imaging metal detector for antipersonnel mine detection", *J. of Applied Geophysics*, vol. 40, pp. 59-71, 1998.

[BRU98b] C. Bruschini, "Förster Documentation Overview: Part I: Matlab Algorithms; Signals and Data Acquisition Format (8 pp.); Part II: Metal Detector Test Data (58+6 pp); Part III: 2D Deconvolution Tests (12 pp.)", EPFL-LAMI and VUB-ETRO-IRIS, Lausanne, Switzerland, Internal Note, April 1998.

[BRU00b] Bruschini, C., and Sahli, H., Phase angle based EMI object discrimination and analysis of data from a commercial differential two frequency system, in *SPIE Proceedings Vol. 4038,* pp. 1404-1419, Orlando, FLA, April 24-28, 2000.

[CHE84] R. H. Chesney, Y. Das, J. E. McFee, and M. R. Ito, "Identification of Metallic Spheroids by Classification of Their Electromagnetic Induction Response", *IEEE Trans. on Pattern Analysis and Machine Intelligence*, vol. PAMI-6, no. 6, pp. 809-820, Nov. 1984.

[COL99b] L. Collins, P. Gao, N. Geng, L. Carin, D. Keiswetter, and I. J. Won, "Discrimination of UXO-like Metal Targets using Wideband Electromagnetic Induction", in *Proc. UXO Forum 1999* (Atlanta, GA, USA, May 25-27, 1999). Available online from http://www.uxocoe.brtrc.com/conferen.htm.

[END98] J. Endsley, G. D. Sower, and E. Christy, "Metal Mine Discrimination on the EG&G IGMMDT Vehicle", in *Proc. Third Intnl. Symposium on Technology and the Mine Problem* (Naval Postgraduate School, Monterey, CA, USA, April 6-9, 1998). Proceedings published on CD-ROM.

[GAO99] P. Gao, L. Collins, J. Moulton, L. Makowsky, R. Weaver, D. Keiswetter, and I. J. Won, "Enhanced Detection of Landmines using Broadband EMI", in *Detection and Remediation Technologies for Mines and Minelike Targets IV; SPIE Proceedings Vol. 3710* (Orlando, FLA, USA, April 1999, pp. 2-13).

[KEI98] D. Keiswetter, I. J. Won, T. Bell, B. Barrow, and N. Khadr, "Electromagnetic Induction Spectroscopy", in *Proc. Forum 1998* (Anaheim, CA, USA, 5-7 May 1998). Available online from http://www.uxocoe.brtrc.com/conferen.htm.

[KEI99] D. Keiswetter, I. J. Won, B. Barrow, and T. Bell, "Object Identification using Multifrequency EMI Data", in *Proc. UXO Forum 1999* (Atlanta, GA, USA, May 25-27, 1999). Available online from http://www.uxocoe.brtrc.com/conferen.htm.

[SOW99] G. Sower, J. Endsley, and E. Christy, "Discrimination of Metal Land Mines from Metal Clutter: Results of Field Tests", in *Detection and Remediation Technologies for Mines and Minelike Targets; SPIE Proceedings Vol. 3710* (Orlando, FLA, USA, April 1999, pp. 78-88).

[SZY99] P. Szyngiera, "A Method of Metal Object Identification by Electromagnetic Means", in *Proc. MINE'99 (Mine Identification Novelties Euroconference)* (Florence, Italy, October 1-3, 1999, pp. 155-160). Available from http://demining.jrc.it/aris/events/mine99/index.htm.

[TRA97] A. H. Trang, P. V. Czipott, and D. H. Waldon, "Characterization of small metallic objects and non-metallic anti-personnel mines", in *Detection and Remediation Technologies for Mines and Minelike Targets II; SPIE Proceedings Vol. 3079* (Orlando, FLA, USA, April 21-24, 1997, pp. 372-383).

Appendix A5.

A5.1. Standard Scanning Setup

After having checked that the soil is free of metallic objects, scans were carried out using the following standard parameters (unless otherwise indicated):

- **Scan length**: min 60, max 100 cm (-> **80 cm typical**).
- **Coil height** (i.e. distance from the bottom of the coil to the soil surface): typically 2-3 cm (say **2.5 cm**).
- Default Sensitivity Level: 1.
- Move to **Sensitivity 2** if very weak Audio signals are recorded, or none at all (this can be the case when scanning at increasing heights). The same but moving to Sensitivity 3 (maximum) if the audio signals at Sensitivity 2 are too weak.

And when carrying out **parallel scans** (2D acquisition):

- **Pitch** (distance between parallel scans): **2 cm**.
- **Number** of parallel scans: min 21, **typical 26** (corresponds to a total scanning width of 50 cm).
- **Direction**: **unidirectional** (one way) preferred (not bidirectional, i.e. two ways).

All single scans are on a straight line passing through the centre of the object (X: 25 cm, Y: 40 cm, when scanning over 50×80 cm), placed flush and perpendicularly to the scan direction, unless otherwise specified.

A5.2. Scanning Glossary

The following terms are often referenced:

- **STANDARD SETUP:** the metal detector is perfectly horizontal, and its axis (the line dividing it into left and right) is perfectly perpendicular to the scanning direction (see Figure 5.1 and Figure 5.2).
- **HORIZONTAL PLANE (XY):** the plane defined by the metal detector head (i.e. parallel to the ground surface) and into which the metal detector moves.
- **VERTICAL PLANE (YZ):** the plane defined by the metal detector support structure (Z: vertical axis). It passes through the MD axis (Y axis). An object placed **vertically** is labelled "**VER**".
- **FLUSH**: even with the surface (in case of a large object, e.g. a mine: the top is even with the surface). **For small objects** this is equivalent to saying that it is placed on the surface, slightly pushing it into the surface (in the case of sand) until it is effectively flush, with minimal disturbance of the soil.
- **ORIENTATIONS**: The four main orientations in the horizontal plane are described in Figure 5.51.

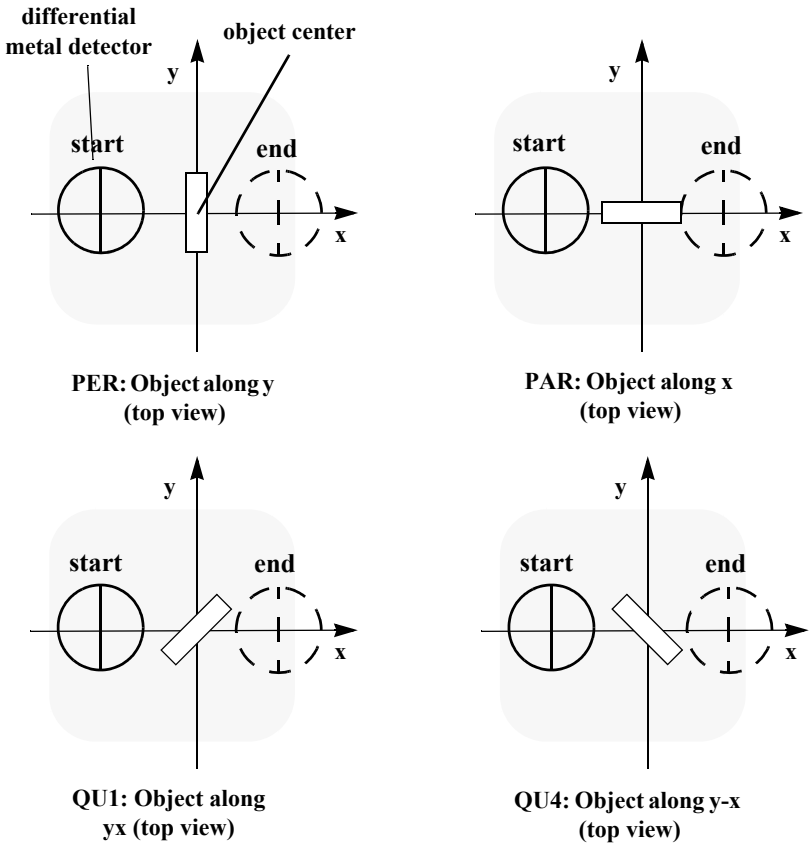

Figure 5.51: The four main orientations in the Horizontal (HOR) plane (object in origin, but could be anywhere along the scanning axis, preferably in the centre; not to scale, size of object exaggerated).

A5.3. Filename Code, v2

The following filecode has been used (the *Object Code* is described in Table 5.1):

ObjectCode_ObjectDepth(mm)_DetectorHeight(mm)_Sensitivity_Other.filenum (or orientat).

Examples:

1) msc2_000_025_1_rev.001:

ObjectCode: msc2, Depth: 0mm (flush), Height: 25mm, Sensitivity: 1, reverse scan, filenum: 1

2) alc2_050_150_2.y-x:

ObjectCode: alc2, Depth: 50mm, Height: 150mm, Sensitivity: 2, orientation: y-x

3) mide_000_025_1_2D.022:

ObjectCode: mide, Depth: 0mm (flush), Height: 25mm, Sensitivity: 1, 2D scan (standard head position), filenum: 22

4) sts4_BGND_025_1_2D.011:

Background measurement corresponding to the ObjectCode: sts4, Height: 25mm, Sensitivity: 1, 2D scan (standard head position), filenum: 11

5) BGND_AIR_xxx_2_2D_09012001.002:

Background measurement IN AIR, Height: xxxmm, Sensitivity: 2, 2D scan (standard head position), date: 9 Jan. 2001, filenum: 2

A5.4. Object Codes

Table 5.1 contains a list of the most common test objects, a short description and their *Object Code* (ex. "coc1"), which is used throughout the text as well as for the Filename itself.

Description	*Type, Material*	*Size (cm)*	*Object Code*
Test cylinder #1 ("small")	Aluminium / Copper / Steel type 3 (*stainless*)	L: 3, Ø: 0.3	alc1 / coc1 / inc1
" "	Steel type 1 (mild) / Steel type 2 ("Acier Argent")	" "	msc1 / aac1
Test cylinder #2 ("large")	Aluminium / Copper / Steel type 3 (*stainless*)	L: 3, Ø: 0.7	alc2 / coc2 / inc2
" "	Steel type 1 (mild) / Steel type 2 ("Acier Argent")	" "	msc2 / aac2
Steel spheres	"Very small" (#1)	Ø: 0.4	sts1
" "	"Small" (#2)	Ø: 0.635	sts2
" "	"Medium" (#3)	Ø: 1.2	sts3
" "	"Large" (#4)	Ø: 2.0	sts4
Background tests	–	–	bgndn
Background IN AIR	–	–	BGND_AIR
Small loop, open / closed	copper wire	Ø: 5	loo1 / loo2
Small permanent magnet	–	Ø: 2-3	mag1
CH mine (complete)	minimum-metal mine		mich
CH mine det. (replica)	– (mainly foil)		mide
CH mine detonator (real)	– (mainly foil)		midereal
CH mine striker pin(s)	steel (ferromagnetic)	Ø: 0.15, L: 1.1	mist1,2,3
PMN, VUB	VUB sample		pmnVUB (pmnc)
PMN, Cambodia	Cambodia sample		pmnCamb.

Table 5.1: Details of most common test objects

A5.5. Debris Examples

Figure 5.52: Example of debris (Source: Objects: EPFL/DeTeC, Images: VUB)

6.

Metal Detector Data Feature Extraction and Classification Opportunities

The previous chapter has been focused on the qualitative aspects of the phase response behaviour (signal trajectories in the complex plane), and showed that a "qualitative" target classification is possible, at least for situations with high Signal to Noise (S/N) ratios. In particular, the possibility of differentiating small objects from large ones (and therefore to eliminate some clutter) has been stressed, as well as the fact that some mines have quite characteristic responses.

In this chapter we extend the previous results providing a quantitative analysis, in order to:

- Provide complementary information to the "complex plane" user interface;
- Address situations in which an object by object analysis by a human operator is not possible (automated interpretation), having for example vehicle based systems in mind,
- Study classification opportunities.

After a preprocessing step we will define a number of features and propose ways to calculate them in practice from the experimental data sets available. The resulting feature distributions will then be analysed and object classification opportunities discussed. The following analysis will partly "phenomenology driven", being based on the actual experimental results of the test samples (debris, mines and their components in particular). We will obviously also exploit the results from the models studied in the previous chapters.

6.1. Metal Detector Data Preprocessing

Prefiltering

We recall – see §5.1 – that the five metal detector signals, or channels, we are looking at correspond to the real ($f_1 0°$, $f_2 0°$, or equivalently f_1 REAL and f_2 REAL) and imaginary parts ($f_1 90°$, $f_2 90°$, or equivalently f_1 IMAG and f_2 IMAG) (in the complex plane) of the analog signals $V_1^{(s)}$ and $V_2^{(s)}$ induced at f_1 and f_2 in the receiver, with the addition of the difference of the imaginary parts multiplied by a constant (Delta=c($f_1 90° – f_2 90°$)).

In this chapter we will refer to them as f_1REAL and f_2REAL, f_1IMAG and f_2IMAG, which make up the overall measured signals V_1 at f_1 and V_2 at f_2, as well as DeltaImag (for clarity).

The preprocessing of the metal detector raw data is preceded by the following steps, applied independently to each channel:

- Subtract the mean to eliminate offsets;
- Lowpass filtering as already described in §5.1, with a sliding window of width FiltWidth.

  We have used FiltWidth in the range 30-90 samples (one sample is taken every 0.56 mm).
- Remove the left and right edges, i.e. the first and last FiltWidth samples which are often affected by the filtering.

If a *background* file has been specified – usually a scan taken under the same conditions but without target object – it is subjected to the same processing steps just described before being subtracted from the preprocessed data, channel by channel. The resulting data is then again mean subtracted.

Region of Interest (RoI) Definition

Regions of Interest (RoI) are then defined to isolate the part of the data of interest, which is then analyzed in more detail[67]. A two element *RoIEdge* vector contains the RoI start (left) and end (right) coordinates, one vector for each frequency.

The **REAL** parts of the signals are analysed first, using the following steps (see Figure 6.2):

- **REAL S/N check**: check of the signal amplitude of the real channels: if max(f_1REAL) and max(f_2REAL) are both larger than $Th_{S/NRe}$, the target has a high Real *Signal to Noise* (S/N) ratio, otherwise a low one.

  We have set $Th_{S/NRe}$=0.2 mV.

- **High Real S/N case**: select the *N* highest amplitude peaks, independently for |f_1REAL| and |f_2REAL|, where at least *M* samples have to separate one peak from the next (as implemented in the Matlab **`pickpeak`** function). A "peak" is defined by having an amplitude at least as large as its neighbour(s); this guarantees that monotonically decreasing values are not selected as peaks.

  We have taken *N*=5 and *M*=100, corresponding to a distance of about 56 mm.

- **Low Real S/N case**: apply a polynomial FIR *smoothing filter* (Savitzky-Golay filter) of order *PolyOrder* and width *FrameSize* samples to the sum of the absolute values of f_1REAL, f_2REAL and DeltaImag (see Eq. (6.1)). Select the 2 peaks with highest amplitude. The sum has been taken in order to increase the S/N ratio.

$$LowRe(S/N) = |Re(f_1)| + |Re(f_2)| + \Delta Imag \tag{6.1}$$

  The best results were obtained with a filter with *PolyOrder*=2 and *FrameSize*=151; the use of this type of filter is however not critical. Examples of the gain in S/N are shown in Figure 6.1 for an object, **`deb51`**, with very weak responses in two different orientations: in the first it is barely detected at the maximum sensitivity, in the second it is not detected at all.

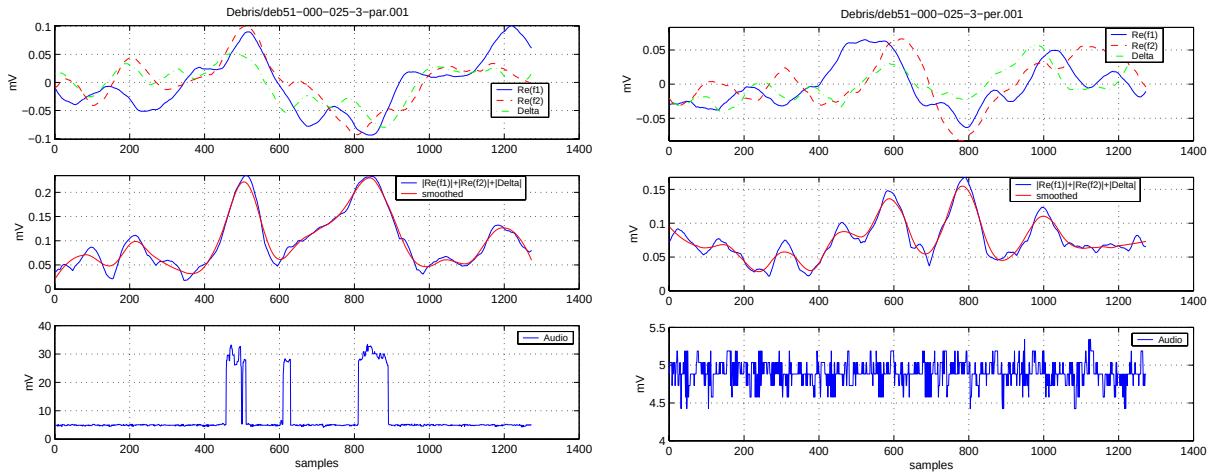

Figure 6.1: Low Real S/N case: peak finding using the sum of the absolute values of f_1REAL, f_2REAL and DeltaImag (**`deb51`**). The last row features the detector's standard Audio output.

- **Select peaks above threshold**: in both cases: select the peaks with amplitude above a threshold $Th_{PeakReHigh}$, defined as max(*maxPeakFractionRe*·*maxPeakAmplRe*, *peakThreshRe*) where *maxPeakFractionRe* is a fixed fraction of the highest peak amplitude and *peakThreshRe* is a fixed value:

$$Th_{PeakReHigh} = max(maxPeakFractionRe \cdot maxPeakAmplRe, peakThreshRe) \tag{6.2}$$

67. A similar operation is sometimes defined as "triggering" in treasure hunting applications, although it is usually carried out there in real time.

We used *maxPeakFraction*=0.1 (i.e. 10% of the highest peak amplitude) and *peakThreshRe*=0.1 mV.

- **Fit data and define RoI limits**: take the first and last peak along the scanning direction (the two outermost peaks), fit the data and follow the fit outwards on each side[68] until the amplitude falls below a threshold. The sample thus reached constitutes the left, viz the right, RoI limit. The threshold Th_{RoI} is defined as max(*PeakFraction*·*PeakAmpl*, *peakThresh*), where *Peak Fraction* is a fixed fraction of the first point (the amplitude of the left or right peak) and *peakThresh* is a fixed value:

$$Th_{RoI} = max(PeakFraction \cdot PeakAmpl, peakThresh) \tag{6.3}$$

We used *PeakFraction*=0.1 (i.e. 10% of the highest peak amplitude) and *peakThresh*=0.1 mV, and fitted with a cubic polynomial.

At the end of this section we have either two *RoIEdge* vectors, *RoIEdgeRealf1* and *RoIEdgeRealf2*, in the case of high S/N, or only one in the case of low S/N, *RoIEdgeReal.*

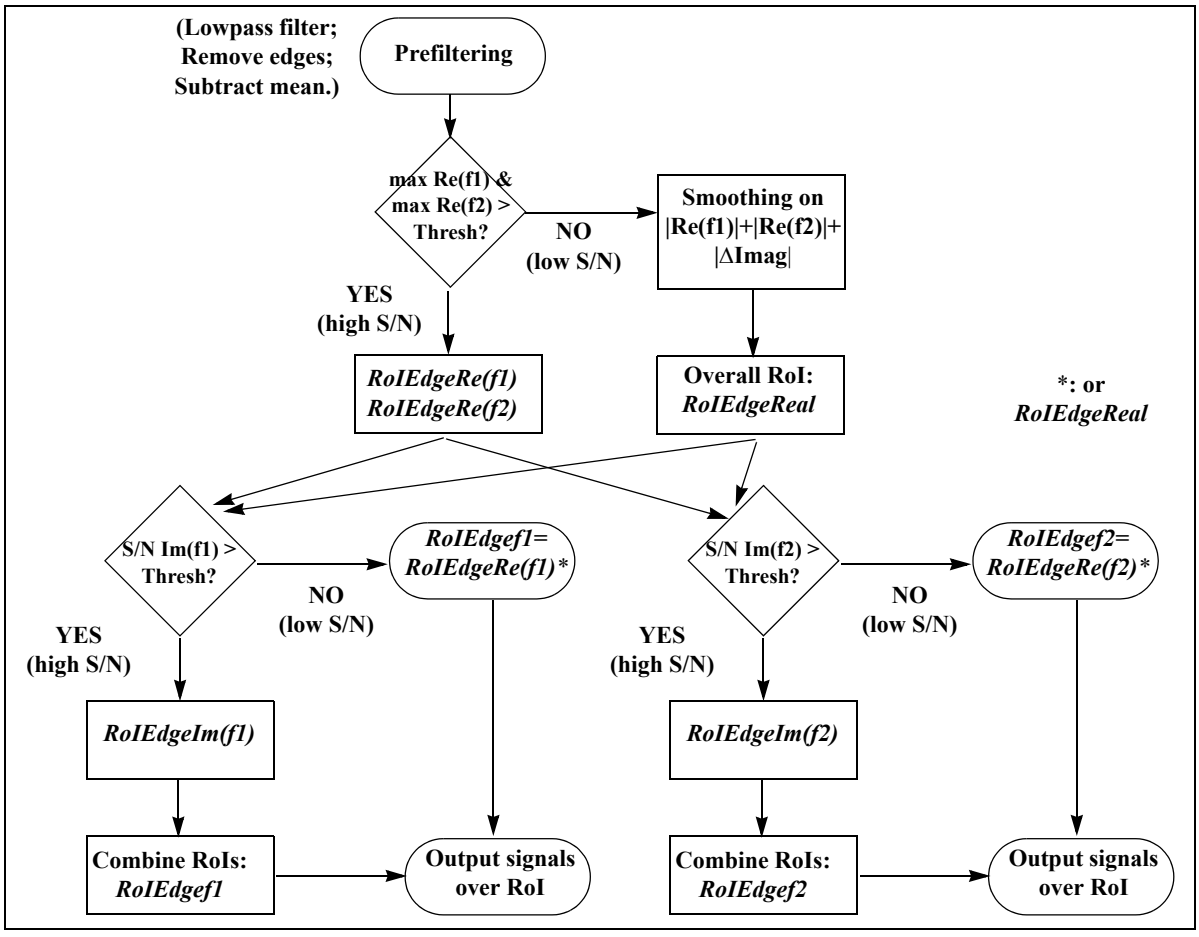

Figure 6.2: Preprocessing: Region of Interest (RoI) definition algorithm. The individual threshold are described in the text.

We note that it is possible that in some cases the Region of Interest is as large as the whole scan length. An incorrect behaviour is also possible in presence of multiple objects with very different response levels (the RoI definition might correspond only to the largest object), or with weak signals. Some fine tuning of the algorithm is therefore necessary.

Other RoI definitions are obviously possible, e.g. based on thresholding of the DeltaImag signal.

68. That is, leftwards from the first peak and then rightwards from the last peak.

Attention is then turned to the **IMAGINARY** parts of the signal, which is in principle more complicated as they are more affected by the background, and we try to estimate how much. The following steps have been used (see again Figure 6.2):

- **IMAGINARY S/N check:** the S/N ratio for each imaginary channel, S/N(f_1IMAG) and S/N(f_2 IMAG), is calculated as the ratio of the channel's RMS inside and outside the RoI of the corresponding real channel[69].

$$(S/N)Imag = \frac{RMS(Im(f_i))\big|_{InsideRoI}}{RMS(Im(f_i))\big|_{OutsideRoI}} \quad , \ i=1,2 \tag{6.4}$$

  If S/N(f_1IMAG) is larger than $Th_{S/NIm}$ the target has a high Imaginary S/N ratio at f_1, otherwise a low one; similarly for f_2.

  We have set $Th_{S/NIm}$=10.

- **High Imaginary S/N case**: the same algorithm is applied as for the High Real S/N case, with the same parameters. The output is one RoI for each imaginary channel, $RoIEdgeImagf_1$ and $RoIEdgeImagf_2$.

  The two RoI for the real and imaginary channel at f_1 are then combined into one, $\boldsymbol{RoIEdgef_1}$, by taking the two extremal values (left most and right most). Similarly for f_2 ($\boldsymbol{RoIEdgef_2}$).

- **Low Imaginary S/N case**: no calculation is performed and $\boldsymbol{RoIEdgef_1}$=$RoIEdgeRealf_1$, $\boldsymbol{RoIEdgef_2}$= $RoIEdgeRealf_2$.

In the low Imaginary S/N case some form of filtering would often be beneficial and a number of tests have indeed been carried out to reduce the background influence in the imaginary component of the received signal, as detailed in A6.1. "Standard" techniques to deal with this aspect in the case of frequency domain systems do often consist in some form of bandpass or highpass filtering, relying on the fact that the target signal does usually change over a much shorter distance than the background. The very low frequency signal components are therefore associated with the background signal fluctuations. Wavelet based filtering has been trialled as well.

In the case of the signals we looked at their spectral position did actually represent a problem, as the low frequency signal components and the background fluctuations did often fall into the same spectral region. This is also due to the fact that the signals are already differential in nature, the background having already been reduced to first order.

Finding a filtering scheme which is valid in most circumstances, i.e. that can guarantee a sufficient level of robustness, turned therefore out to be quite difficult. We have thus chosen to present results considering signals over the chosen RoIs without additional filtering, possibly having subtracted the corresponding background files.

69. There can be some cases in which the f_iIMAG (i=1 or 2) signal is wider than the corresponding f_iREAL (e.g. a PMN close to the detector). In this case the S/N estimation as defined above is not entirely correct and will be lower than in reality, because a portion of the IMAG target signal will be counted as background. The algorithm will therefore probably use the *RoIEdgeRealfi* limits also for f_iIMAG, thereby effectively cutting a portion of the tails.

6.2. Feature Definition and Extraction

We will define in the following a number of features, i.e. characteristic quantities, and propose ways to calculate them in practice from the experimental data sets available[70]. The features will either be directly derived from the data (e.g. the phase angle response), or from combinations of the data (differential quantities or ratios), or from simplified target models (e.g. *L/R*). Where possible the physics of the problem has been taken into account, for example in the definition of the differential quantities.

Ideal features have a high resolution capability, that is are capable of well separating objects belonging to different classes. It will however be sometimes necessary, in particular in presence of background fluctuations, to trade resolution power for applicability and rely on less discriminating features.

6.2.1. Phase Response

In order to associate a phase angle, or more than one if necessary, to the signal at f_1 and f_2 we have chosen to look at the peaks in the corresponding phase angle distribution, using the following algorithm:

- **Phase angle definition**: the phase angles are calculated using the inverse tangent (arctangent, MATLAB "atan" function) as in Eq. (6.5), and therefore over –90 to +90° (angles in the 2nd quadrant are flipped into the 4th, angles in the 3rd into the 1st) [LOC02].

$$\varphi_i = \text{atan}\left(\frac{Im(f_i)}{Re(f_i)}\right) \quad , \ \text{i=1,2} \tag{6.5}$$

  This definition has the advantage of usually increasing the histogram S/N and reducing the number of peaks; the disadvantage with respect to working over –180° to +180° (e.g. using the MATLAB "angle" function) is a loss of resolution for asymmetric signals.

- **Histogramming**: build a histogram of the phase angles at each frequency over *NB* bins.

  We have set *NB*=45.

- **Peak Finding**: select the *N* highest peaks at f_1 and at f_2, where at least M bins have to separate one peak from the next (same algorithm as previously described).

  We have taken *N*=5 and *M*=3.

- **Select peaks above threshold**: in addition we imposed a threshold, *histoPeakThresh,* defined as a fixed fraction of the highest peak amplitude, independently at f_1 and f*2*. This *relative threshold* implies that high S/N histograms return only one, maximum two peaks. Lower S/N histogram or the response of composite objects such as a PMN mine result on the other hand in more peaks.

  We have taken *histoPeakThresh*=0.1 (i.e. 10% of the highest peak amplitude).

Examples of the input signals in the complex plane and the corresponding phase angle distributions and selected peaks are shown in the first rows of Figure 6.3 and Figure 6.4; other examples are reported in A6.2.

Note that the phase angle values depend on the correct choice of the reference (origin of coordinate system) and that a different number of peaks can be returned at f_1 and f_2. Also, peak selection is usually eased by a correct choice of the RoI. The phase angle calculation could also be made somewhat more precise by weighing each peak with its two neighbours, or by using a histogram fitting scheme; it was however sufficient for our purposes.

70. References to [LOC02] mean that the corresponding idea has been derived there, although not necessarily tested on large scale.

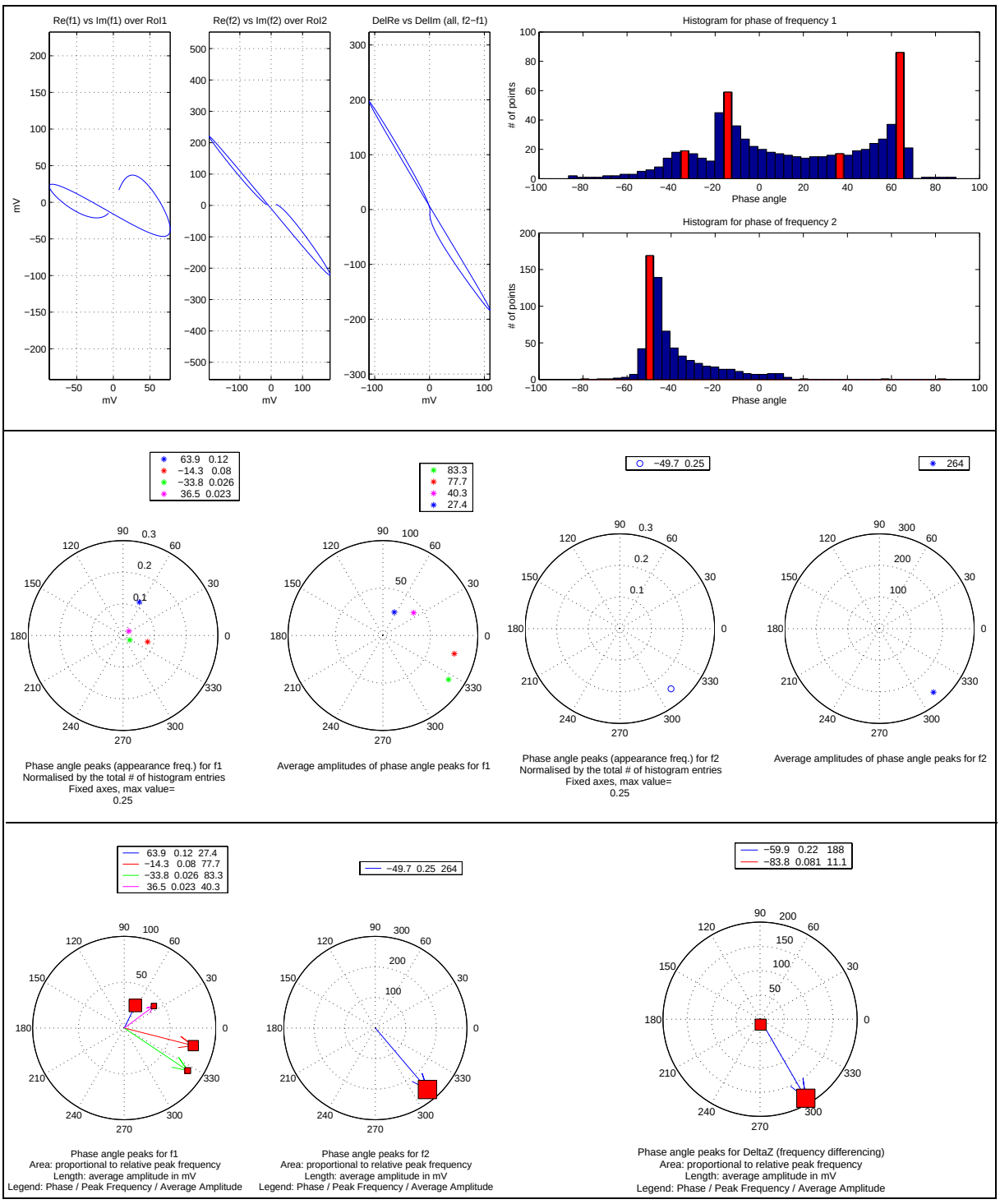

Figure 6.3: Phase response calculation and phase angle peak representation for a **pmnVUB**, complete mine@ 5 cm, PAR1 orientation (composite object). *First row*: complex plane plot and phase histograms. *Second row*: phase angle peaks for f_1 (left) and f_2 (right). *Third row*: "combined interface" at f_1 and f_2 (left) and for DeltaZ (right)

Alternative phase response definitions are obviously possible, such as the phase calculated using the highest amplitude peaks ("peak to peak"), or a straight line fit in the complex plane, which would not be sensitive to the choice of the correct origin.

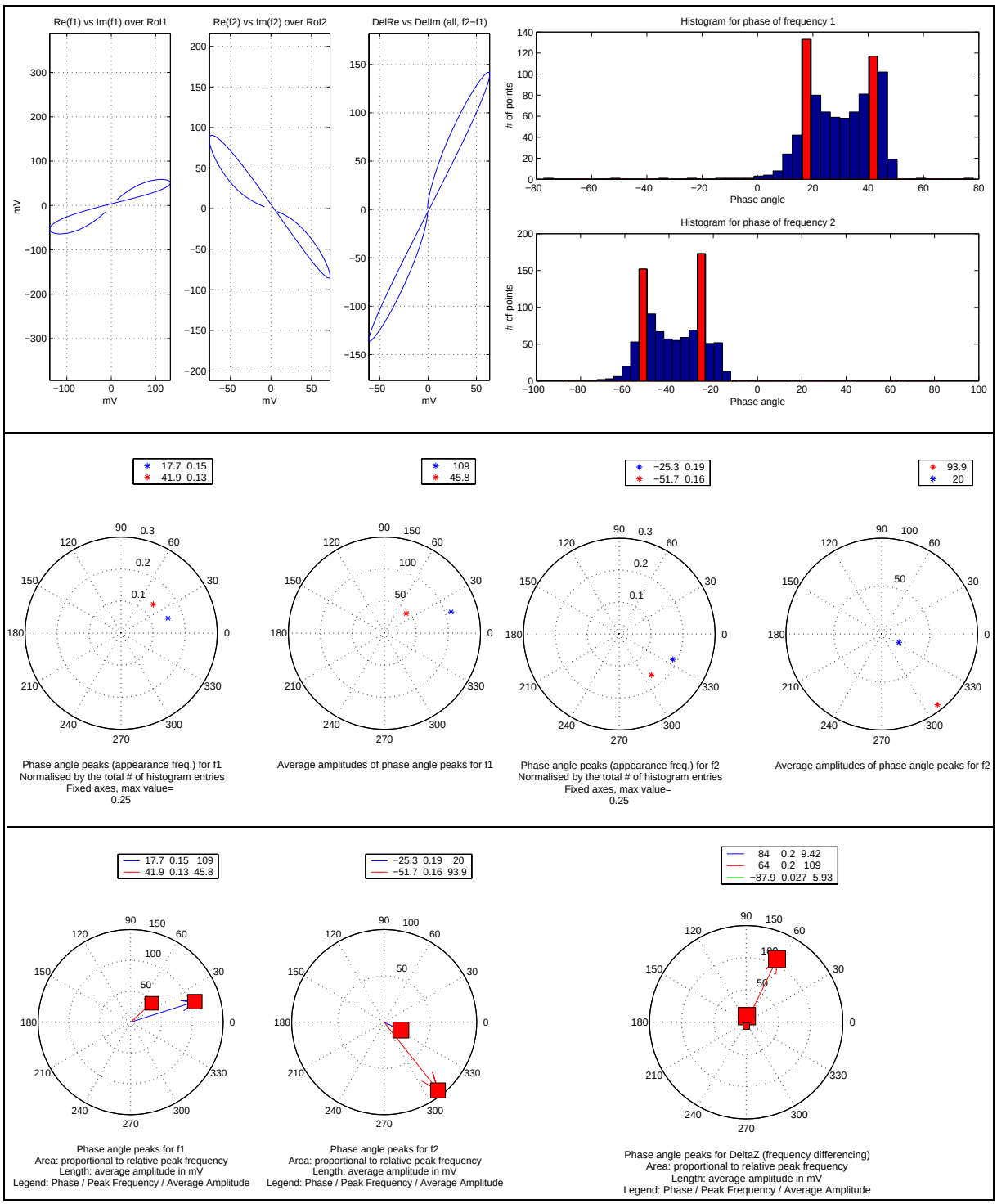

Figure 6.4: Phase response calculation and phase angle peak representation for a **PMR-2A** (stake mine, example of large cylindrical ferromagnetic object) placed vertically.

Average Amplitude Definition

For each of the selected peaks an **average amplitude** is then calculated by adding the amplitudes of all points having a phase value falling in the same histogram bin as the one of the chosen peak [LOC02].

This has the effect of reducing noise influence (samples with low signal amplitudes) and partially enhancing the phase peaks containing data points close to the amplitude maxima, which are usually associated with positions close to the target's centre (where the primary magnetic field is predominantly vertical).

Combined Interface

The second row of Figure 6.3 and Figure 6.4 illustrates the "*developer's interface*" used during the development of the algorithm: the first polar plot features the angular position of the peaks in degrees and their relative peak height ("appearance frequency"), normalized to 1, as radial distance; the second plot features each peaks' angular position and average amplitude in mV as radial distance. Two plots are available at each frequency [LOC02].

The third row of Figure 6.3 and Figure 6.4 illustrates a "*combined interface*" in which all information at a given frequency is represented in one polar plot: the average amplitude is represented as radial distance (arrow length) whereas each rectangle's area corresponds to the relative peak height. These plots do basically represent a simplified version of the complex plane trajectories. As said, other examples are reported in A6.2.

We note that more complex scenarios arise for ferromagnetic and/or composite objects. Ferromagnetic ones are usually not of interest in treasure hunting, but they obviously are to us.

We conclude with a list of possible improvements to the algorithm which has just been illustrated:

- Eliminate data in a small window around 90° (to reduce background effects when these are dominated by the imaginary part of the received signals);
- Introduce a non-linear spacing of the bins in the phase histograms, possibly logarithmically, to better reflect the behaviour of the phase response;
- Exploit the fact that the primary magnetic field is mostly vertical over the object, whereas it has a significant horizontal component far from it, as already discussed in the previous chapter. One could envisage to define a "near" and a "far" set of points and extract the relevant phase response from them. For a non-ferromagnetic objects the phase behaviour is likely to be quite similar, whereas important differences are likely to arise for elongated ferromagnetic objects.

  This is similar to what is done in a dipole model to extract the response along the object's principal axes (§3.6.1).

6.2.2. Absolute Amplitude Ratio

Additional features can be extracted from the signal, in particular the ratio of the absolute values ("Amplitude Ratio"). We have decided to calculate it in two ways, namely as the ratio of the means of the absolute values at f_1 and f_2:

$$AR1 = \frac{\overline{|V_1|}}{\overline{|V_2|}} \quad , \quad \overline{|V_i|} = \left(\sum_{k=1}^{totSamples} |V_i(k)| \right) / (totSamples) \tag{6.6}$$

as well as directly in the complex plane, whereby we first calculate at each frequency the sum of the distances of the two farthest points (taking the sum of the two highest peaks *max1* and *max2* of the absolute value |V1| at f_1, and similarly at f_2), and then take their ratio:

$$AR2 = \frac{max1(|V_1|) + max2(|V_1|)}{max1(|V_2|) + max2(|V_2|)} \tag{6.7}$$

The two values usually coincide to 5-10%, with exceptions in the case of irregular curves in the complex plane, or for low S/N cases. Examples are shown in Figure 6.8, Figure 6.10 and in A6.3

We also define an *average* amplitude ratio *AR* as:

$$AR = \frac{AR1 + AR2}{2} \tag{6.8}$$

For a description of the corresponding modelling results see §6.2.6.

6.2.3. Real Part Ratio

As we have seen the real component of the received signal is quite unaffected by the background in our experimental conditions and in general for non-conductive soils. It is therefore tempting to use the ratio of the real components at f_1 and f_2 (*ReRatio*) as additional feature. We have decided to calculate it as the ratio of their peak to peak value at the two frequencies:

$$ReRatio = \frac{max(Re(f_1)) - min(Re(f_1))}{max(Re(f_2)) - min(Re(f_2))} \tag{6.9}$$

We have used *ReRatio* over the whole range of points, working over RoI only might bring some S/N improvement for weak signals. Examples are shown in Figure 6.9 and Figure 6.10.

For a description of the corresponding modelling results see again §6.2.6.

6.2.4. L/R (Simple Circuit Model)

The response of a simple circuit model, in which the (non-ferromagnetic) target object is modelled as an isolated conductive circuit with a lumped resistance R and inductance L, has already been discussed in detail in §3.1. Overall its response is characterized by single pole at R/L and a zero located at the origin. The *L/R* ratio is therefore characteristic of the target, and from Eq. (3.3) and Eq. (3.4) it can be shown that:

$$L/R|_{f_i} = -\frac{1}{\omega_i}\left(\frac{Im(f_i)}{Re(f_i)}\right) = -\frac{1}{\omega_i}\tan\varphi_i \ , \ i=1,2 \tag{6.10}$$

where $\omega_i=2\pi f_i$ as usual and φ_i is the phase response at the frequency f_i (i=1,2 in our case).

We normalize in the following to $\omega_1=1$ and use the tangent of the highest phase angle peak, $PeakAnglef_i(1)$, as an approximation to the phase response[71]:

$$L/R|_{f_1} = -\tan(PeakAnglef_1(1)) \ , \ L/R|_{f_2} = -\frac{1}{freqRatio}\tan(PeakAnglef_2(1)) \tag{6.11}$$

with $freqRatio=f_2/f_1=\omega_2/\omega_1=8$ for the Förster Minex.

The *L/R* ratio can actually also be calculated using frequency differencing techniques (see §4.3), which should result in a more robust value in presence of background. Adapting the [PAT99] results to our measured signals, *Re* and *Im* (which are already scaled as in Eq. (5.1)), and introducing a weighted difference of the real components, *DeltaReWeighted,* as in Eq. (6.12), we arrive at the following expression[72]:

71. It might actually be better to take the phase angle peak with the highest average amplitude.
72. We replaced the frequency *f* used in [PAT99] by ω and assumed that the FI1 and FR1 coefficients used therein to multiply the imaginary and real target response at f_1 are equal (and therefore phase preserving).

$$L/R|_{\Delta Weighted} = \frac{1}{\omega_1}\frac{DeltaReWeighted}{DeltaIm} = \frac{1}{\omega_1}\frac{(Re(f_2)/freqRatio - Re(f_1))}{Im(f_2) - Im(f_1)} \quad (6.12)$$

The differences are designed to eliminate a constant Imaginary contribution (magnetic soils), as already discussed, and a Real component proportional to frequency (typical of conductive soils, see also §4.3.1).

We normalize again at ω_1=1 and use the peak to peak values of *DeltaReWeighted* and *DeltaIm*, where both signals have been taken over all points, rather than over a RoI only, in the assumption that the real signal is practically not perturbed by the background. There are however some situations in which the signals are quite weak (e.g. **deb22-24**) and errors introduced, resulting in an incorrect value in amplitude and/or sign[73] as evident in Figure 6.11. This method should nevertheless be more robust than $L/R|_{f1}$ and $L/R|_{f2}$ previously described.

6.2.5. DeltaZ (Differential Signal)

We also explored the possibility of using a simple differential signal *DeltaZ* defined as:

$$Real(DeltaZ) = Re(f_2) - Re(f_1) \;,\; Imag(DeltaZ) = DeltaIm = Im(f_2) - Im(f_1) \quad (6.13)$$

which is insensitive to fluctuations in the imaginary components. The resulting signal is however basically the vector difference of the response at f_1 and f_2, and therefore depends heavily on the individual signal amplitudes. It could however still be useful in selected scenarios.

The *DeltaZ* phase response is calculated as for f_1 and f_2, i.e. via a histogram peak finding procedure, but we looked only at the distribution of the phase angle peak with the highest average amplitude. Examples are shown in Figure 6.3, Figure 6.4 and in A6.2.

We have used *DeltaZ* over the whole range of points, working over RoI only might bring some S/N improvement for weak signals. Other definitions are also possible, for instance using *DeltaReWeighted* introduced in Eq. (6.12).

6.2.6. Modelling Results for AR and ReRatio

Modelling results for *AR* and *ReRatio*[74] in the case of a sphere and an infinite cylinder transversal to a uniform magnetic field are shown in Figure 6.5, for *freqRatio*=f_2/f_1=8 typical of the Förster Minex and different permeability values.

ReRatio grows monotonically, reaching about 2.8 at the inductive limit in both cases. *AR* for permeable objects features one peak above and one below the *AR*=1 line, at about the same height for the permeability values shown. The value of the highest peak is of about 1.9 for the sphere and 1.6 for the cylinder, of the lowest about 0.7 for the sphere and 0.65 for the cylinder.

It is in particular impossible to have a situation, for the cylinder, in which both *AR* and *ReRatio* are larger than 1. This is however possible for a permeable sphere over a restricted range of induction parameter values.

The behaviour at larger permeability values is similar to the one shown. It is however different for *low permeability values* (<2 say), as could be the case for some stainless steels: both *AR* peaks get smaller, the first moves towards 1 and gets much less pronounced, the second moves towards 0 and becomes de facto the curve's dip.

73. In principle *DeltaReWeighted* should always have the same sign, at least for the sphere model.
74. Labelled *ImRatio* in the plots, as they show the behaviour of the response function rather than of the measured data.

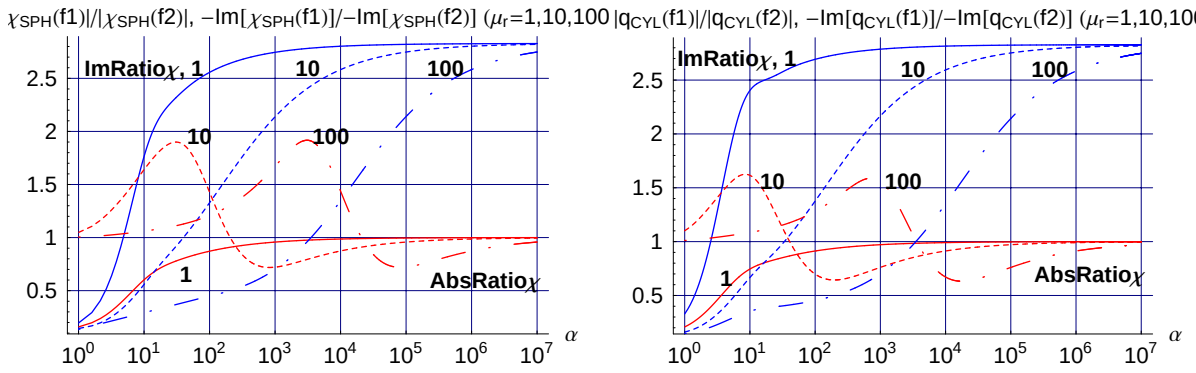

Figure 6.5: Ratios of the imaginary part (*ImRatio,* blue) and absolute value (*AbsRatio,* red) of the response function at $f_2=8f_1$ (Förster Minex params) for a non-ferromagnetic ($\mu_r=1$, continuous) and ferromagnetic objects ($\mu_r=10$: dashed, $\mu_r=100$: dot-dashed). *Left*: sphere (χ_{SPH}), *Right*: transversal infinite cylinder (q_{CYL}).

6.2.7. Comparison of some Results with Model Expectations

Results from some of the test objects, in particular cylinders, have been compared with what is expected from the models (sphere and infinite transversal cylinder). In general agreement is quite good, with obvious exceptions for ferromagnetic cylinders when aligned along the primary magnetic field. The object codes have been described in A5.4.

- **Cylinder in perpendicular setup** (compared with infinite cylinder in perpendicular magnetic field model):

  `coc2` data (phase angles), including *AR* and *ReRatio*, is well reproduced using the conductivity value in Table 3.4. The same is true for **`coc1`**.

  `msc2` PER data is well reproduced (all quantities) using $\sigma=0.63\cdot10^7$ S/m and $\mu_r=100$. In this case *AR*=1.34 and *ReRatio*~0.5. **`msc1`** PER is also well fitted, and *AR*=1.18, *ReRatio*=0.51. Note that in both cases *ReRatio* is well below 1, *AR* above.

- **Sphere** (dipole approximation):

  `sts2`, **`sts4`**: reasonable agreement. **`sts4`** has *AR*=1.8, *ReRatio*=0.81.

- **Cylinders in parallel setup:**

  `msc2` PAR features *AR*=1.83, *ReRatio*: 1.23 >1, with values slightly decreasing with distance.

  `msc1` PAR features *AR*= 1.96, *ReRatio*: 1.48 >1.

  As previously discussed in §6.2.6, such values are not compatible with the model of a cylinder in a perpendicular magnetic field (neither the fact that AR>1.6, nor that both values are >1). They can be qualitatively explained using the *demagnetization effects* already discussed in §3.5.2 and the corresponding deformation of the response function, which bears then similarities with the one of an infinite cylinder in a solenoidal magnetic field (compare with Figure 3.17, in which it is clear that a situation with AR>1 and *ReRatio*>1 is possible).

  Quantitative results for ferromagnetic ellipsoids have been recently presented in [BRA01].

- **Cylinders in vertical setup:**

  `msc2` VER features *AR*=2.42, *ReRatio*: 1.5 >1, constant with lateral displacement.

  `msc2` VER (different setup) features *AR*=2.08, *ReRatio*: 1.32, constant with distance.

  This setup does obviously resemble to the PAR one (longitudinal magnetic field component prevails), with even larger *AR* values.

- **Cylinders at other orientations in the horizontal plane:**

  `msc2` oriented along QU1 and QU4 have *ReRatio* < 1 (although slightly).

6.3. Classification Opportunities

In the following we will analyse the distribution of the previously defined features and discuss the resulting object classification opportunities, that is the possibility of attributing a measurement to a specific object class.

The actual values of some features are obviously dependent on the parameters used for their extraction, such as the minimum distance between peaks in the phase angle histograms or the various thresholds; they are also specific of the Förster Minex operating parameters. The results should nevertheless still be of general interest and it should not be too difficult to extrapolate them to other operating conditions.

"Small" vs. "Large" Objects

The features we are looking at are basically derived from the target's response function and as such do depend on its *response parameter*[75] (or induction number), as discussed in §3.1 and §3.3. The latter is usually a product of permeability, conductivity and the square of an average linear dimension of the target, thereby putting a particular weight on its size.

In the following we will therefore often refer to an *object size* using terms such as "*small*" and "*large*"; *strictly speaking we are however discriminating on the full response parameter rather than on its physical size only.*

6.3.1. Phase Angle Peaks and Amplitude Ratio Distribution

We analyse the distribution of the phase angle peaks and of the (average) amplitude ratio *AR* using 3D scatter plots, each phase angle peak φ_j being represented as a point in 3D space with the following cylindrical coordinates (θ,ρ,z):

- $\theta = \varphi_j$ and $\rho=1$;
- $z=AR$. If there are two or more peaks for a given entry all of them are associated to the same value of *AR*.

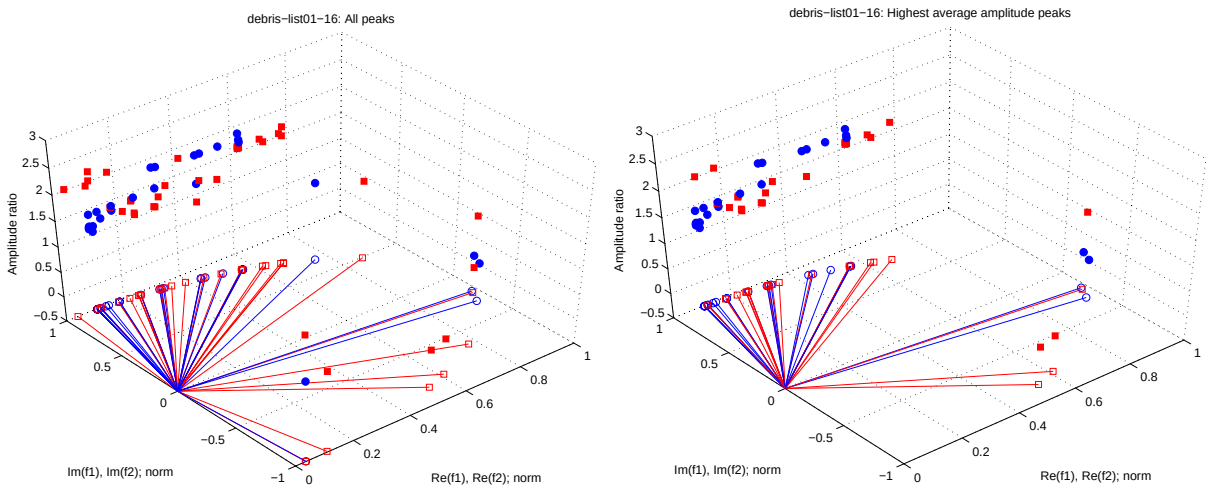

Figure 6.6: Phase angle peaks (left: all, right: highest average amplitude only) vs. average amplitude ratio for **`deb01-14&16`** (blue circles: values at f_1, red squares: values at f_2). Attention, scale(x)=1/2scale(y).

In addition we plot for each point its projection on the x-y plane and connect it with a line to the origin[76], to make it easier to determine each point's phase. Examples are shown in Figure 6.6, the

75. And on its orientation (influence of the demagnetization factor) for most ferromagnetic objects.
76. Actually on a plane at $z = -0.5$, for graphical reasons only.

left plot containing all phase angle peaks, the right one only the highest average amplitude peaks. Points at f_1 are shown with blue dots, at f_2 with red squares. Note that the scale along *x* is 1/2 of the scale along *y*. The corresponding *AR* distribution is shown in Figure 6.8 (*AR*>1 for all ferromagnetic objects, *AR*<1 for the two non-ferromagnetic ones).

The resulting distributions of the phase angle peaks only, i.e. the projections on the x-y plane, *confirm in a quantitative way the qualitative results detailed in the previous chapter.*

In addition the complete distributions (i.e. considering *AR* as well) detail how different object categories, in particular debris, can form *clusters* in the chosen 3D space. Examples are shown in Figure 6.7, the non-ferromagnetic foils **`deb20-26`** in the top left corner (very low *AR*), the ferromagnetic foils **`deb30-37&39`** in the top right corner (*AR*~1), and all ferromagnetic debris (1<*AR*<2.2 with a couple of exceptions) in the bottom half. Note in particular the trend, in this last case, of decreasing phase angle with increasing amplitude ratio.

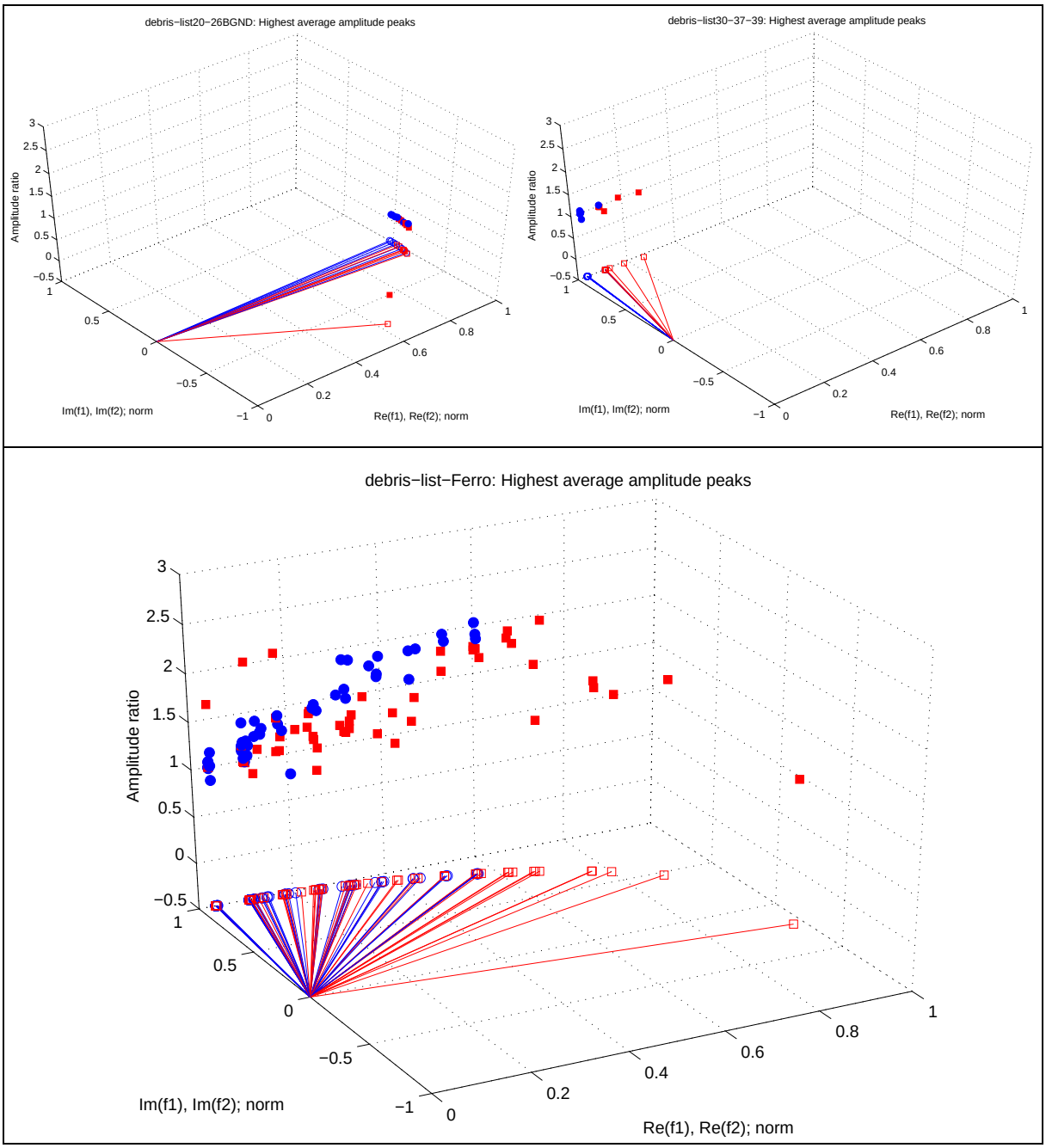

Figure 6.7: Phase angle peaks (highest average amplitude only) vs. average amplitude ratio for **`deb20-26`** (non-ferromag. foils, background subtracted), **`deb30-37&39`** (ferromag. foils), and **`all ferromag. debris`**.

Amplitude Ratio Distribution

The amplitude ratio distribution is detailed in Figure 6.8 to Figure 6.10 (and Figure 6.18) and commented thereafter.

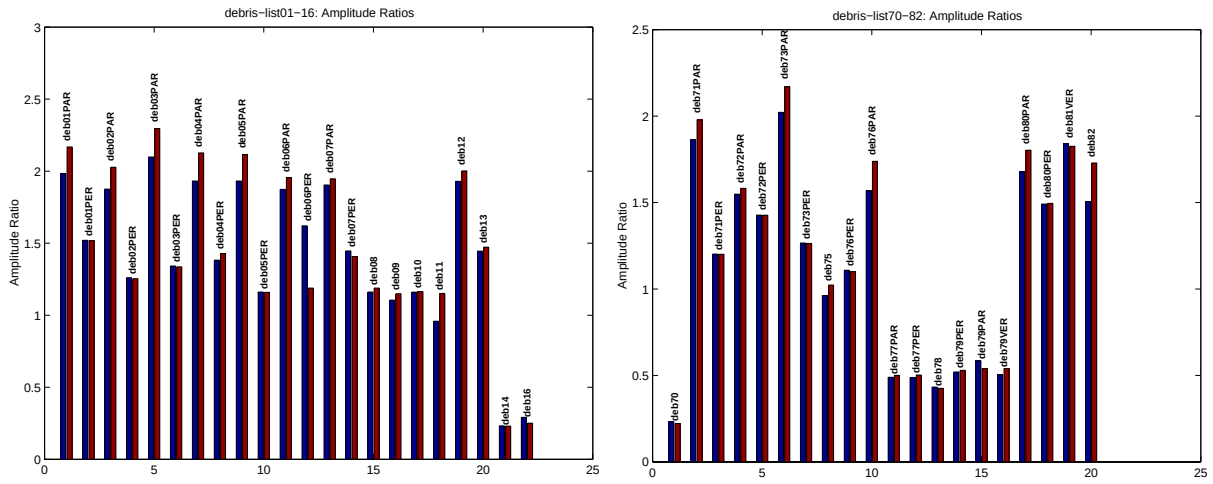

Figure 6.8: Amplitude Ratio distribution (*AR1*,*AR2*) for **`deb01-14&16`** and **`deb70-82.`** First column of each bin: *AR1*, Second column: *AR2*.

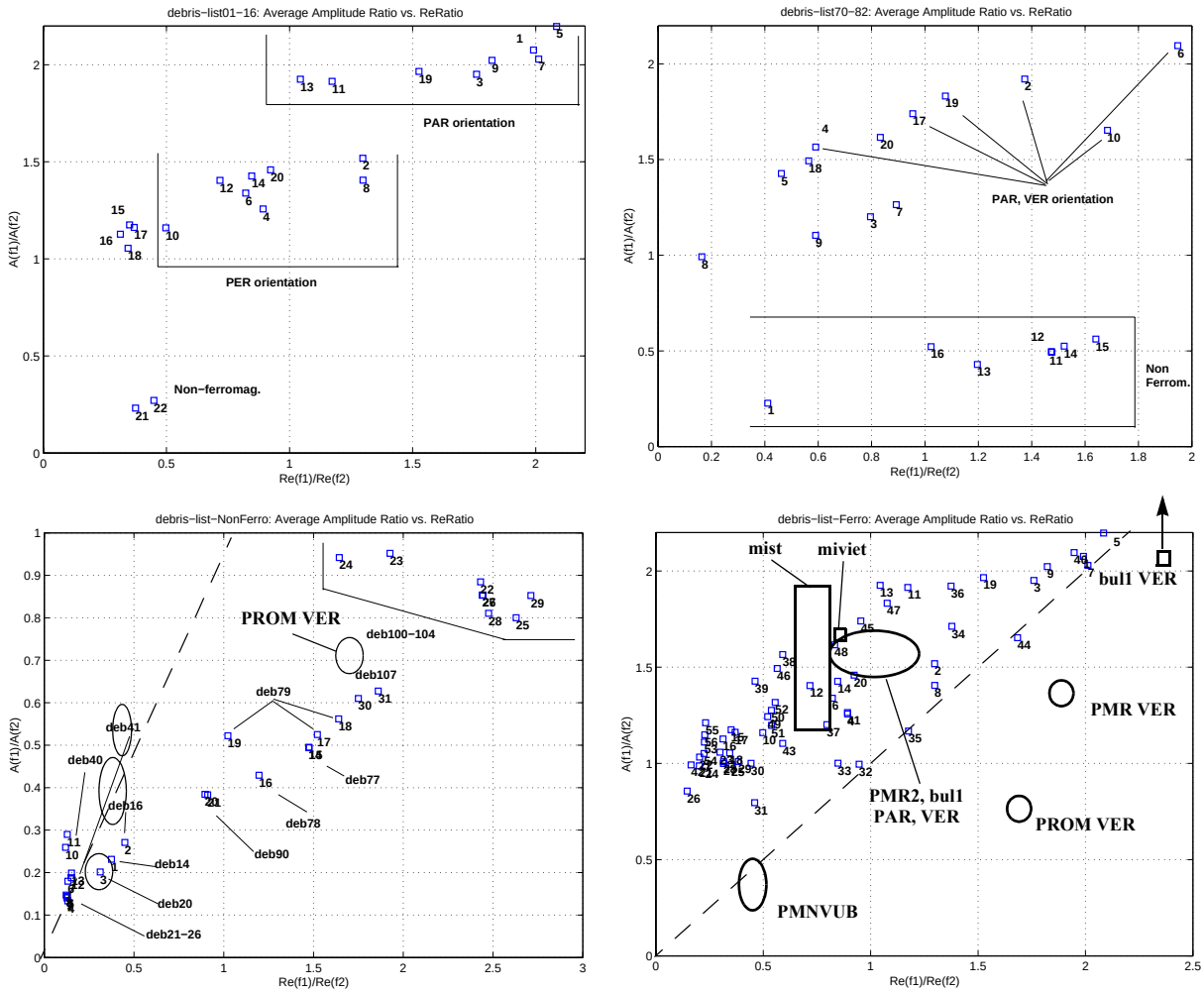

Figure 6.9: Average amplitude ratio *AR* vs. *ReRatio*. *Top left*: **`deb01-14&16`** (object indexing as in Figure 6.8, left), *Top right*: **`deb70-82`** (indexing as in Figure 6.8, right), *Bottom left*: **`all non-ferromag. debris`** (indexing as in Figure 6.11), *Bottom right*: **`all ferromag. debris`** (indexing as in Figure 6.18).

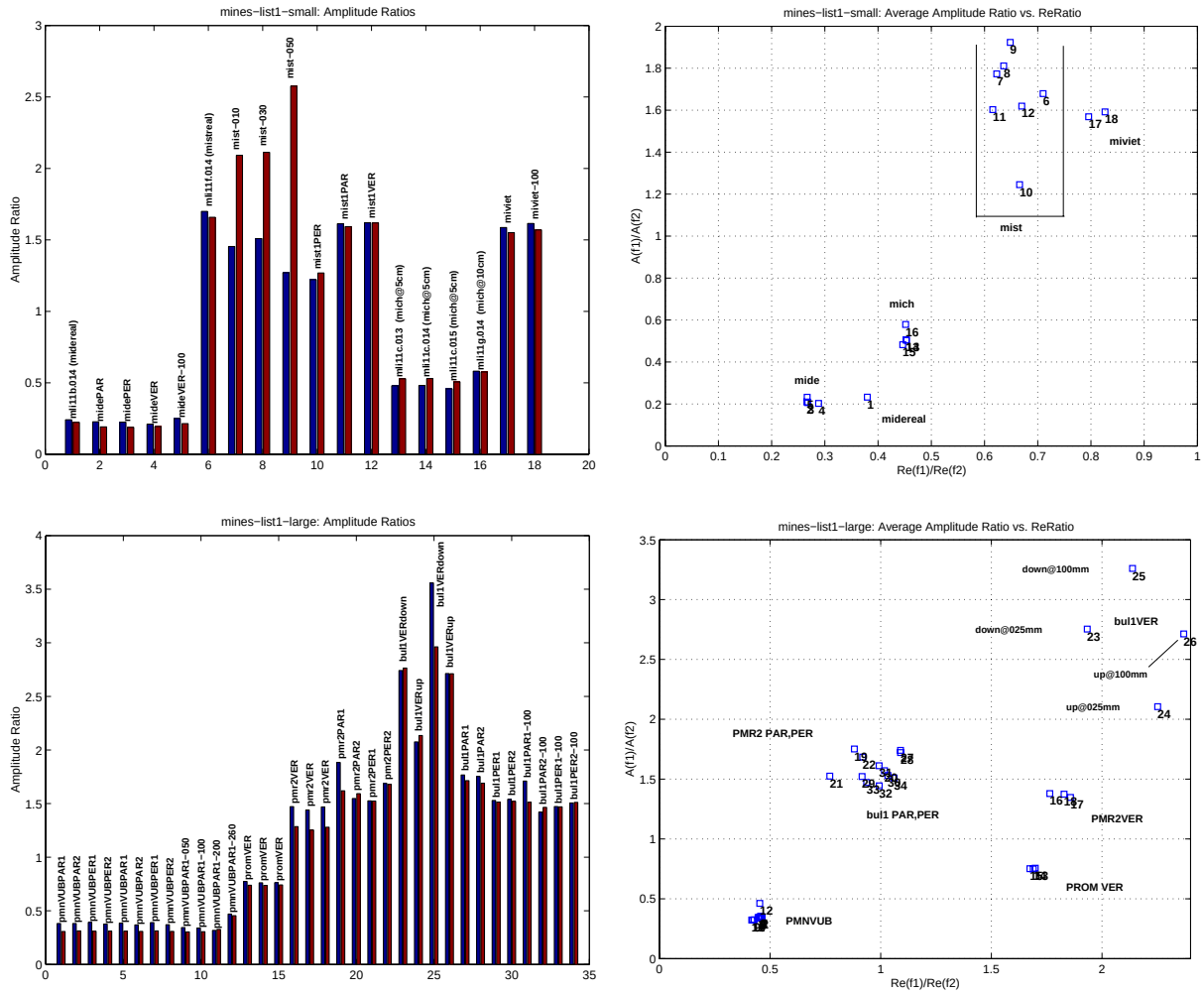

Figure 6.10: Amplitude Ratio distribution (*AR1,AR2*) and Average amplitude ratio *AR* vs. *ReRatio*. *First row*: **`low metal`** content mines and their components, *Second row*: **`PMN`** and **`large metallic mines/UXO.`**

Its main characteristics are:

- ***AR*>1** typical of **ferromagnetic** objects with few exceptions, usually due to very weak or irregular signals.
- ***AR*~1-1.2** for **flat ferromagnetic** objects;
- ***AR*>1.5** typical of **elongated ferromagnetic** objects when there is a significant component of the magnetic field along the symmetry axis (e.g. PAR, VER orientations).

  In general: *AR*(PAR, VER orientations) > *AR*(PER orientation) for a given elongated object, and similarly for ReRatio.
- ***AR*<0.2-0.3** typical of **small non-ferromagnetic** objects (e.g. foils);
- **0.7<*AR*<1** typical of **large** non-ferromagnetic objects (e.g. **`deb100-104`**, Figure 6.9) or large ferromagnetic ones (e.g. **`PROM`**, Figure 6.10).

These results are in general in good agreement with model expectations. Note that a maximum value of about 1.9 is foreseen for a sphere and of 1.6 for a transversal (infinite) cylinder using the Förster Minex operating parameters (see the corresponding plots in Figure 6.5).

Stainless steel cylinders with a small residual permeability represent special cases (see the discussion in §6.2.6).

6.3.2. Amplitude Ratio and Real Part Ratio Distribution

Examples of the average amplitude ratio *AR* vs. *ReRatio* distribution are shown in Figure 6.9 and Figure 6.10. It is evident that the two features are correlated: the higher *AR*, the higher *ReRatio*, with some exception for very large ferromagnetic objects. This corresponds to a trend from small objects in the lower left corner (all *non-ferromagnetic* debris plot) to large ones in the upper right corner, i.e. when moving from the resistive to the inductive limit.

This implies that for non-ferromagnetic objects one can extrapolate to a certain extent the size from the *AR* vs. *ReRatio* plot, which is generally not true for ferromagnetic objects without some a priori knowledge of target type and/or orientation.

In the case of the *debris* most non-ferromagnetic objects are *below* the *AR=ReRatio* line (dashed line in the bottom plots of Figure 6.9), as correctly predicted by the sphere and cylinder model, whereas all ferromagnetic *debris* is *above* it. The models also foresee a maximum *ReRatio* of about 2.8, which is experimentally well verified.

It is interesting to note that some very large ferromagnetic objects could be distinguished on the basis of their (*AR,ReRatio*) values alone, for example a vertical **`PMR-2A`** or **`bull`**.

In general however only a partial target discrimination seems possible using the (AR,ReRatio) values alone, as evident from the bottom plots in Figure 6.9, on which the distribution of several classes of targets of interest – extracted from Figure 6.10 – has been superposed. The residual ambiguity can be resolved in a number of cases using the phase response information.

ReRatio Distribution

The *ReRatio* distribution by itself presents the following characteristics:

- ***ReRatio*<0.2-0.3** typical of small non-ferromagnetic objects such as foils or wire strands. This is mostly true also for similar ferromagnetic objects;
- ***ReRatio*>2.0-2.5** typical of large non-ferromagnetic objects.
- **In general: *ReRatio*(PAR, VER orientations) > *ReRatio*(PER orientation) for a given elongated ferromagnetic object**, similarly to the *AR* behaviour.

ReRatio works therefore well to discriminate very large or very small non-ferromagnetic objects. It does however not seem to be sufficiently robust, used by itself, for ferromagnetic objects (too much influence of permeability and demagnetization factor). Some targets could be discriminated on the basis of their *ReRatio* alone, such as the small mine components, however likely at the price of a high false alarm ratio.

6.3.3. L/R (Simple Circuit Model)

Results for all non-ferromagnetic debris are shown in Figure 6.11. In most cases there is good agreement between $L/R|_{f1}$, $L/R|_{f2}$ and $L/R|_{\Delta Weighted}$. Errors are apparent for weak signals such as in the case of **`deb21-26`** and **`deb40-41`**, but in these cases there is room for improvement.

The resulting values are also well correlated with object "size" (comparing with the corresponding position in the bottom left plot of Figure 6.9) and phase angle behaviour (not shown). The values for the **`mide`** and **`midereal`** mine detonators (not shown) are in the range 0.13-0.19 and are also in good agreement amongst themselves; as a comparison, they are of the same order as the first three debris items in Figure 6.11.

As expected *L/R* does deliver inconsistent results for ferromagnetic or composite objects.

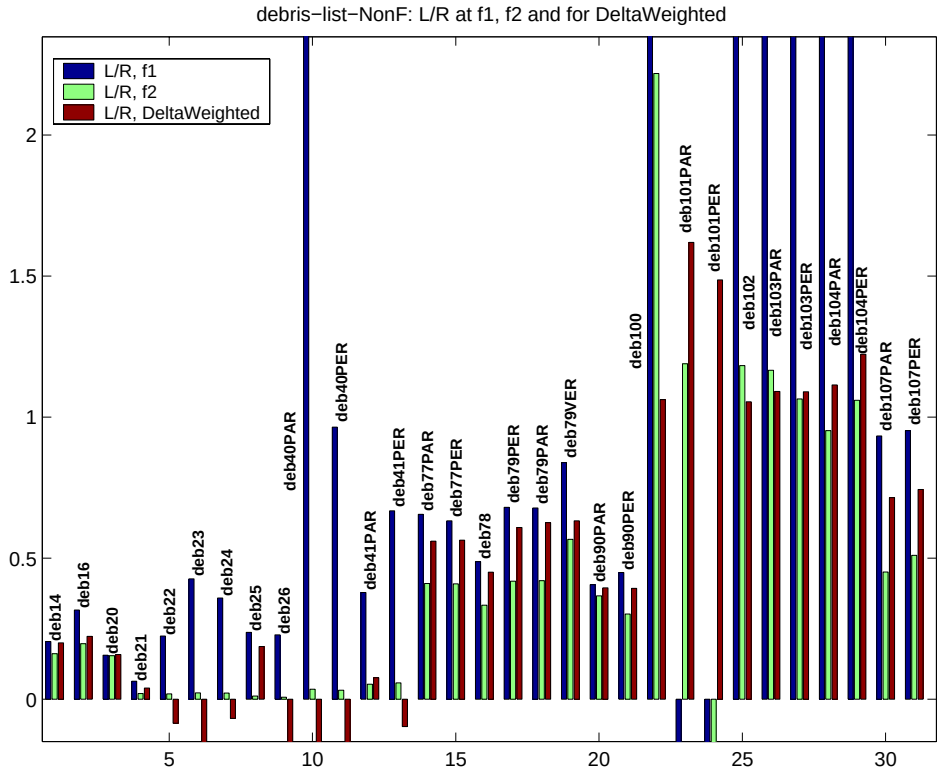

Figure 6.11: *L/R* (simple circuit model) at f_1, at f_2 and using a weighted difference (see text), for **`all non-ferromag. debris`**

6.3.4. Delta Z

Several phase response distributions of the differential signal *DeltaZ* as defined in §6.2.5 are shown in Figure 6.12, having considered only the phase angle peaks with the highest average amplitude. Note that usually positive phase angles result when *ReRatio*>1, negative ones when *ReRatio*<1.

As already hinted at, results depend heavily on the individual signal amplitudes and are as a consequence definitely more variable than other features. From the experimental data it appears in particular that two or more quite different objects can produce a similar *DeltaZ* phase angle, which can therefore in general not be inverted.

Some object categories do however partially *cluster*. For example, the *DeltaZ* phase angle of most foils, whether ferromagnetic or not, is close to the horizontal (0°), probably due to their small *ReRatio* value (see **`deb21-26`** and **`deb30-36`** in Figure 6.12, an exception being the large foil constituting **`deb20`**). Also, a sizeable fraction of small to medium ferromagnetic objects – of the order of 50% – have a *DeltaZ* phase close to the vertical (say in the window +90° to +70° or –90° to –70°, see again Figure 6.12).

DeltaZ could therefore still useful to eliminate foils and some small ferromagnetic pieces – obviously provided the targets have a different behaviour, which was true in the cases we looked at – even in presence of background signal fluctuations.

As an *alternative approach* we note that the phase of *DeltaZ* for the small **`mide`** mine detonator, which does also contain a foil, seems to be quite stable with orientation/distance at around –52° to –60° (–68° for **`midereal`**), a feature which could be exploited if necessary by *discarding objects with different characteristics*, together with its *ReRatio* for example. The small mine striker pin (**`mist`**) does also behave in a similar way. The robustness of such an approach vis-à-vis other mine components has obviously to be checked in detail.

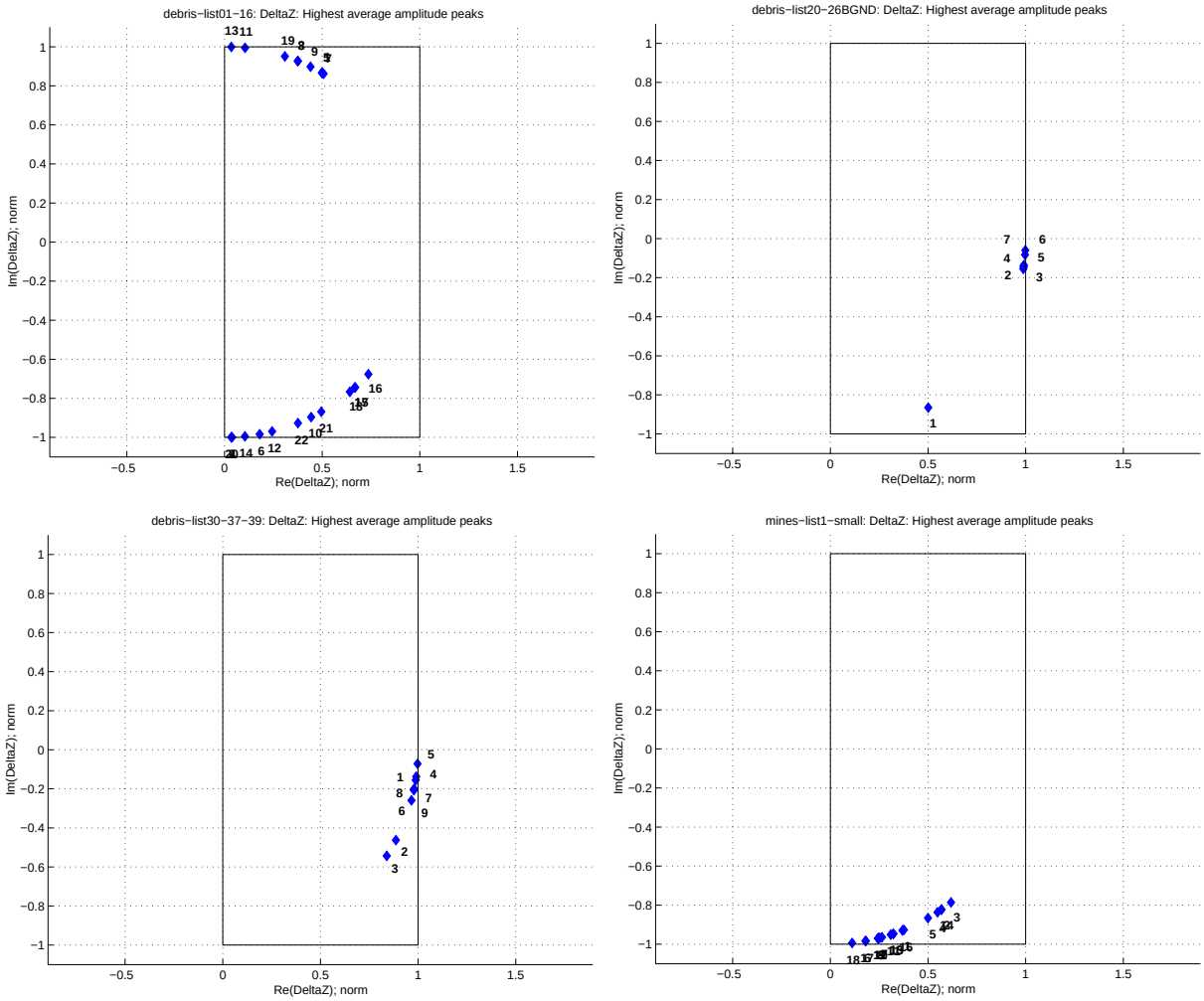

Figure 6.12: *DeltaZ* Phase angle peaks (highest average amplitude only). *Top left*: **`deb01-14&16`**, *Top right*: **`deb20-26`** (non-ferromag. foils, background subtracted), *Bottom left*: **`deb30-37&39`** (ferromag. foils), *Bottom right*: **`low metal`** content mines and their components.

Summarising and simplifying, *DeltaZ* could be used, probably at the price of a higher false alarm rate, when the S/N ratio is too weak and the other features fail, either to discard some objects (e.g. foils) or provided we know what we are looking for.

6.3.5. Ferromagnetic Flag

A "ferromagnetic flag" could be raised when either $AR>1$ (or say $AR>0.9$ with some tolerance), $\varphi_1>0$ or $\varphi_2>0$. This works well for all cases except for very large ferromagnetic objects such as the **`PROM`** mine (§5.9.1). It does not necessarily mean that the whole objects is ferromagnetic, only that it contains a ferromagnetic component.

6.4. Conclusions

Whereas the previous chapter focused more on the qualitative aspects of the phase response behaviour, in this chapter we have defined a number of features, processed the available data and analysed the resulting feature distributions.

6.4.1. Overall Considerations

The peak finding algorithm in particular seems to be working well; this allows to reduce the detailed curves in the complex plane to a coarser information, basically the phase angle peaks and their average amplitudes. Multiple peaks are usually characteristic of composite or ferromagnetic objects, or for low S/N scenarios. One large ferromagnetic peak is usually strongly indicative of a ferromagnetic component.

Most of the information seems to be contained in the phase response. There are however cases in which the use of the amplitude ratio *AR*, and of the *ReRatio*, provides additional information, in particular helping in resolving ambiguities. Examples are the response of a large ferromagnetic item such as the **`PROM`** mine, or of stainless steel objects with a small residual permeability. In general only a partial target discrimination seems possible using the (*AR,ReRatio*) values alone (see §6.3.2 for details).

The models' predictions on the behaviour of *AR* and *ReRatio* are confirmed by the experimental data, similarly to the phase response which we already discussed in the previous chapter. Important demagnetization effects are apparent for elongated ferromagnetic objects, for which *AR*(PAR, VER orientations) > *AR*(PER orientation), and similarly for *ReRatio*.

6.4.2. Main Conclusions

We conclude by *A)* first commenting on the possibility of a coarse object classification based on the *object size* and permeability (ferromagnetic or not), *B)* moving then to the possibility of discriminating large objects (metallic mines, UXO), and finally *C)* mines in general.

A) Coarse Object Classification Possible

A coarse target classification according to the *object size*, as defined at the beginning of §6.3, and permeability (ferromagnetic or not), seems indeed to be possible, at least for scenarios with a sufficient S/N ratio.

The decision could be taken by the user himself relying on a **visual interface** of the type discussed in the last chapter (*complex plane curves*), or using a simplified bidimensional information like the *phase angle peaks*, possibly augmented by an indication of the amplitude ratio if necessary. A simple alternative could be represented by a plot in the *AR* vs. *ReRatio* plane. This type of scenario could apply to a hand-held system, where the user analyses each alarm, and should in any case be very useful for development purposes.

An alternative is represented by an **automated system** with a direct output indicating the most likely *object size* and permeability (ferromagnetic or not). A possible outline of the resulting simplified user interface is sketched in A6.4. This could be combined if necessary with a 2D diagram of the phase response.

Whether these type of approaches are sufficient for actual mine discrimination is discussed in more detail at C).

In the low S/N case detection is still possible but classification gets increasingly difficult (for quantitative considerations on this topic using time domain signals see also [GEN99, TAN01]). Apart from deciding not to attempt classifying a signal with insufficient S/N, when the main

features can not be used reliably any more it should still be possible to exploit features such as *ReRatio*, $L/R|_{\Delta Weighted}$ and *DeltaZ* albeit with reduced discrimination capabilities.

B) Large Metallic Mines/UXO Discrimination

We recall that our initial idea was to discriminate large targets relying on their phase response, for example by imposing a threshold on the phase. The results for some large metallic objects (**PROM**, **PMR**, **bul1**) confirm that this is possible, at least for the object we looked at. Composite objects do definitely deserve a closer look.

It can however be necessary to complement the phase response with *AR* to resolve ambiguities, such as in the case of a **PROM**.

We initially hoped to extend this discrimination approach also to mines with an average metallic content (e.g. **PMN**, **PMN2**). Judging from the experimental results this might be possible for the **PMN** if the signature from the ring is reasonably stable. It looks more difficult for the **PMN2**, which is composed of about 10 pieces (Figure 5.4) of various sizes. This mine delivers a mostly ferromagnetic response, but not equivalent to that of a single larger target; it might however still be possible to distinguish it from non-ferromagnetic and from smaller ferromagnetic items.

C) Mine Discrimination

Discriminating mines from clutter or even different mines among themselves looks feasible; in the end it depends however on the following factors:

- **Which and how many types of mines are present (*a priori* knowledge).**

  Examples: if we are looking for minimum-metal mines containing a detonator similar to the **mide** previously analysed, we could in principle discard all ferromagnetic objects. Similarly, if the target is an object similar to the small nail representing the **mist** mine striker pin one could possibly exclude a number of non-ferromagnetic debris items.

  Too many different types are likely to make a purely visual choice quite difficult.

- **How much one can rely on stable mine signatures**. This influences the tolerance "windows" which will have to be applied around the known targets of interest.

  We can distinguish two aspects here: *differences at the mine component level*, and *differences in the behaviour of a given type of object*.

  The first point has already been discussed in some detail in §5.12. It includes manufacturing differences as well as the use of different components altogether (see also §5.8.3). Along the same lines [DRU00b] discusses differences in the response of a "new" and an "old" PMN mine due to rusting of the cover retaining ring. It is also well known that water can infiltrate into some mines with time, and if ferromagnetic components are present they are likely to rust as well. Similarly, in the case of previous mechanical clearance the mine can be broken and its pieces separated, with a corresponding change in signature. This takes us back to possible *a priori* knowledge.

  The second point relates mostly to changes in the response of ferromagnetic or composite objects for different orientations/distances. They affect the phase response, as discussed in detail in the last chapter, as well as other features as analysed in this chapter.

Note that the fact of having to look at too many different objects and/or of having to use too large windows will probably affect the selectivity of the procedure and the resulting false alarm rate.

- **How representative the debris we had available is, and how often multitarget scenarios are encountered.**
- **How many clutter objects have a sufficient S/N ratio to allow discrimination.**

  Indeed, even provided that one can discriminate mines from clutter, the actual **system effectiveness** will depend on how much the **false alarm rate** can be reduced, i.e. *how many times a clutter item has a sufficient S/N to be identified as such*. In other words, clutter is usually vastly majoritary; therefore, even if we could identify each mine but for example only 10% of the clutter

had a sufficient S/N (i.e. in nearly 90% of the cases we would have to issue an "unknown object type" response), the system would probably not be too useful.

An object's S/N ratio is influenced in particular by its *depth* and *size*. Additionally the soil type does obviously play a crucial role. We will comment in the following on the depth distribution when looking for mines (UXO might be different, as the typical target depths are larger).

It has been reported that most debris is *close to the surface*, which would be beneficial, but we are not aware of large scale quantitative studies in this direction apart from [JOY02][77]. Anecdotal evidence exist on the use by some deminers of small permanent magnets to remove small near surface ferromagnetic items; along the same lines tests have been carried out with large magnets mounted on the rear of vehicles, for example during the vegetation cutting phase, which can only work if most debris is close to the surface.

In order to have some preciser quantitative indications we have gone back to the original results of the Cambodia data collection campaign [GUE97] from which most of the debris we analysed has been derived. All approximate depth indications have been summarised in Table 6.1, for a total of 64 objects; when the depth was within a range of values we have taken the largest one.

The distribution of this limited sample is concentrated in the upper 10 cm, with nearly 3/4 of all targets in the first 5 cm.

Depth (cm)	*0*	*1*	*2*	*3*	*4*	*5*	*6*	*7*	*8*	*9*	*10*	*10+*
# of objects	4	9	10	6	6	12	1	3	4	–	7	2

Table 6.1: Example of debris depth distribution (extracted from [GUE97]; d=0: "on the surface")

From the original notes one can also calculate that *26* objects were clearly *ferromagnetic*, *12* clearly *non-ferromagnetic*, and the remaining 26 of a priori unknown nature. In 3 cases the metallic debris causing the metal detector alarm was too small to be found.

In situations where one can not rely on stable signatures it could still be possible to exclude certain types of clutter (e.g. foils); it remains however to be seen how useful this is.

6.4.3. Additional Considerations on Object Detection

Concerning the Förster Minex detector specifically, it does not seem to be easy, when looking at the detection of metallic object (no classification attempts), to do better than what already implemented without compromising on the robustness side. This might also depend on the fact that we operate on digital signals, i.e. after the A/D conversion, instead of working on the original analogic signals.

There are however a few cases where an amelioration of the detection efficiency might be possible in the case of non-conductive soils[78], relying on the real parts of the received signals as well as on DeltaImag. An example of target objects for which such an approach could be useful are the stainless steel cylinders we analysed, which are probably paramagnetic and whose imaginary part of the received signal is small.

77. During the VAMIDS metal detector array test detailed in §1.3, every piece the hand-held detectors signalled was weighted and inspected, and "most of the false signals were pieces of shrapnel and metal junk like wire and bottle tops that were either on top or in the first 10mm of soil." [JOY02].
78. When the real part of the received signal is mostly background unaffected.

Bibliography

[BRA01] H. Braunisch, C. O. Ao, K. O'Neill, and J. A. Kong, "Magnetoquasistatic Response of Conducting and Permeable Prolate Spheroid Under Axial Excitation", IEEE Transactions on Geoscience and Remote Sensing, v. 39, no.12, pp. 2689-2701, Dec. 2001

[DRU00b] P. Druyts, Y. Yvinec, and L. Merlat, "Signal processing tools for standard metal detectors (Imaging and Signature mode)", in *Proc.* of the *Research on Demining Technologies Joint Workshop*, Joint Research Centre (JRC), Ispra, Italy, 12-14 July 2000.

[FRI01] M. Fritzsche, "Anwendung von Verfahren der Mustererkennung zur Detektion von Landminen mit Georadaren", Forschungsberichte aus dem Institut für Höchstfrequenztechnik und Elektronik der Universität Karlsruhe (TH), Band 30, W. Wiesbeck Ed., Karlsruhe University (Germany), June 2001 (in German). ISSN: 0942-2935.

[GUE97] F. Guerne, description of the DeTeC2 GPR Cambodia data taking, EPFL/DeTeC Website. Available from http://diwww.epfl.ch/lami/detec/

[GEN99] N. Geng, C. E. Baum, and L. Carin, "On the Low-Frequency Natural Response of Conducting and Permeable Targets", IEEE Trans. on Geoscience and Remote Sensing, vol. 37, no. 1, pp. 347-359, Jan. 1999.

[JOY02] Joynt, V. "National Mine Action: Problems and Predictions", Journal of Mine Action, Mine Action Information Center at the James Madison University, Issue 6.1, 2002, pp. 37-41. Available from http://maic.jmu.edu/journal/6.1/index.htm

[LOC02] J. Lochy, "Acquisition and Analysis of Metal Detector Data for Humanitarian Demining Applications", VUB-ETRO-IRIS "Werkkollege" Internal Report, April 2002.

[PAT99] W. Patzwaldt, "Method for the operation and for the evaluation of signals from an eddy current probe and device for performing the method", US Patent #6,005,392, 21 Dec. 1999.

[SAR97] B. I. Saracik, "Improvements in Metal Detection Technology", The University of Western Australia, Dept. of Mechanical and Materials Engineering (supervisor Prof. J. Trevelyan), B. Eng. Thesis, October 1997, 103 pp.

[SIG02] Sigrist, C., and Bruschini, C., "Metal Detectors for Humanitarian Demining: a Patent Search and Analysis", EUDEM2 report, May 2002. Available from http://www.eudem.vub.ac.be/

[SZY98] P. Szyngiera, and A. Wojtasik, "Wavelet Transformation Applied for Eddy-Current Metal Detector Signals Analysis", in *Proc.* of the *Conference of Telecommunication*, Bydgoszcz, Poland, 1998 (Proceedings in Polish).

[TAN01] S. L. Tantum, and L. M. Collins, "A Comparison of Algorithms for Subsurface Target Detection and Identification Using Time-Domain Electromagnetic Induction Data", IEEE Trans. on Geoscience and Remote Sensing, vol. 39, no. 6, pp. 1299-1306, June 2001.

[WAV01] M. Misiti, G. Oppenheim, J.-M. Poggi, and Y. Misiti, "MATLAB® Wavelet Toolbox User's Manual", v. 2.1 (Release 12.1), July 2001.

Appendix A6.

A6.1. Filtering

A number of tests have been carried out to reduce the background influence in the imaginary component of the received signal. "Standard" techniques to deal with this aspect in the case of frequency domain systems do often consist in some form of bandpass or highpass filtering, relying on the fact that the target signal does usually change over a much shorter distance than the background (i.e. that background fluctuations are "slow" – see also §2.3.3.2 and the patents referenced in [SIG02]). The very low frequency signal components are therefore associated with the background signal fluctuations.

In the case of the signals we looked at the spectral position of the signal did actually represent a problem, as the low frequency signal components and the background fluctuations did often fall into the same spectral region. This is also due to the fact that the signals are already differential in nature, the background having already been reduced to first order.

"Classical" Filtering Techniques

Several techniques were tried with partial success in specific cases, but no single robust technique could be identified. Using "classical" filtering techniques the best results were obtained with:

- A highpass filter with a very low frequency pole (e.g. a Chebyshev Type I Infinite Impulse Response minimum order filter);
- The first or second derivative of the signal;
- A lowpass filter with a very large window, 200 samples wide say (corresponding to about 10 cm), to obtain an approximation of the signals' low frequency components. This approximation can then be subtracted from the input quantities;
- The elimination of a linear trend.

Some of the previously mentioned filters, such as taking the derivative, do generate significant signal distortions. This should however not represent a problem when the aim is to calculate the signal's phase and the filter is applied to both the real and imaginary component[79].

"Adaptive" Filters

Partial success was also obtained using the real components as a template for the imaginary ones. The basic idea is that in a number of cases the phase response is quite constant, which means that the real and imaginary component as a function of position, at a given frequency, have the same shape. As the real component is mostly unaffected in non-conductive soils, it can be used as template. DeltaImag could be used as well in a number of situations.

Deconvolution was carried out isolating the relevant portion of the real component at each frequency and using it as deconvolution "kernel" (or Point Spread Function, PSF) of a Wiener filter. The results seem however to be quite dependent on the right choice of the PSF and the noise level present in the data.

79. The use of linear phase filters has been recommended by some authors.

Wavelet Based Filtering

Wavelet transforms have seen an increased use in the past 15 years in signal analysis applied to a number of different domains. We shall provide in the following a brief introduction to the subject, without pretending to be exhaustive; most material has been extracted from [WAV01], which also contains a list of the main references to the subject, and to a lesser extent from [FRI01].

A **wavelet** is a waveform of effectively limited duration – i.e. of compact support – that has an average value of zero, and **wavelet analysis** is a linear technique which can be described as the breaking up of a signal into shifted and scaled versions of the original (or *mother*) wavelet. Wavelet analysis can therefore be described as a windowing technique with variable-sized regions and uses a time-scale region (scale can be connected in a broad sense to frequency).

This has to be compared to Fourier analysis, which consists of breaking up a signal into sine waves of various frequencies and whose main drawback is that transforming to the frequency domain time information is lost[80], or with the Short-Time Fourier Transform (STFT) for example, which maps a signal into a two-dimensional function of time and frequency, using the Fourier transform to analyse only a small section of the signal at a time (using the same window at all frequencies). The STFT does therefore represent a sort of compromise between the time- and frequency-based views of a signal: it provides some information about both when and at what frequencies a signal event occurs.

The **Continuous Wavelet Transform** (**CWT**) is defined as the sum over all time of the signal *f(t)* multiplied by scaled (i.e. stretched or compressed), shifted (i.e. delayed or anticipated) versions $\psi_{a,b}(t)$ of a *mother* wavelet function $\psi(t)$:

$$\psi_{scale,position}(t) = \psi_{a,b}(t) = \frac{1}{\sqrt{a}}\psi\left(\frac{t-b}{a}\right) \tag{6.14}$$

The results are the wavelet coefficients *C(scale,position)=C(a,b)*, $a>0$, which are function of the scale *a* and position *b*, and of the shape of the chosen wavelet obviously:

$$C(scale,position) = C(a,b) = \int_{-\infty}^{\infty} f(t)\frac{1}{\sqrt{a}}\psi\left(\frac{t-b}{a}\right)dt \tag{6.15}$$

The wavelet coefficients basically represent how closely correlated the scaled and shifted wavelet is with the signal under analysis (actually a section of it, given that the wavelet has a limited duration), like for a correlation coefficient. The corresponding plots, in which the *x* axis represents position along the signal (time), the *y* axis represents scale and the colour at each *xy* point represents the magnitude of the wavelet coefficient *C,* are the time-scale view of the signal we referred to earlier. Examples are provided in Figure 6.13.

The higher the scale *a*, the more "stretched" the wavelet, the longer the portion of the signal with which it is being compared, and thus the coarser (slowly changing) the signal features being measured by the wavelet coefficients (*high scale* → *low frequency*).

Unlike the discrete wavelet transform described below, the CWT can operate at every scale; it is also continuous in terms of shifting: during computation, the analysing wavelet is shifted smoothly over the full domain of the analyzed function.

80. When looking at a Fourier transform of a signal, it is impossible to tell when a particular event took place.

The **Discrete Wavelet Transform** (**DWT**) shares the same basic ideas using a only a subset of scales and positions, in particular "*dyadic*" scales and positions (i.e. based on powers of two) for which efficient implementation schemes exist with just as accurate results as the CWT.

Without entering into too many details of the DWT implementation, let us mention that in wavelet analysis one often speaks of **approximations** *A* and **details** *D*. The *approximations* are the *high-scale, low-frequency* components of the signal, the *details* are the *low-scale, high-frequency* components. An input signal might be decomposed in its *A* and *D* components, of same length as the input signal, with an appropriate pair of complementary lowpass/highpass filters.

What happens in practice is that the input signal is *downsampled* after filtering producing two sequences, *cA* containing the DWT approximation coefficients and *cD* containing the DWT detail coefficients, each being about half as long as the input signal. The decomposition process can then be iterated with a cascade of filters (a filter bank), with successive approximation coefficients being decomposed in turn, so that one signal is broken down into many lower resolution components.

This multiple level decomposition is called the *wavelet decomposition tree* and results, at a given level *N*, in one sequence cA_N containing the DWT approximation coefficients at level *N,* and *N* sequences cD_1-cD_N containing the DWT details coefficients:

$$\text{Wavelet decomposition tree result (at level } N\text{): } S \rightarrow cA_N ; cD_1, cD_2, ..., cD_N \tag{6.16}$$

The value of *N* is selected in practice on the basis of the nature of the signal, or on a suitable criterion such as the entropy. The length of the coefficient sequences is decreasing at each level by about a factor of two (at least for the first levels).

In a similar way the DWT coefficients can be used in an inverse process, the **Inverse Discrete Wavelet Transform** (**IDWT**), to reconstruct the original signal without loss of information using appropriate lowpass/highpass reconstruction filters (and signal upsampling), which are not necessarily equal to the decomposition filters[81]. The choice of the filters determines whether perfect reconstruction is possible; in general the wavelet coefficients are modified before reconstruction.

It is in particular also possible to reconstruct the approximations A_i and details D_i themselves, which have the same length as the original signal, from their coefficient vectors[82]. In addition it can be shown that there are actually several ways of reassembling the original signal *S*:

$$S = A_1 + D_1 = A_2 + D_2 + D_1 = A_3 + D_3 + D_2 + D_1 = \ldots = A_N + \sum_{i=1}^{N} D_i \tag{6.17}$$

To construct a wavelet of some practical utility, it usually makes more sense to design the appropriate quadrature mirror filters, and then use them to create the waveform, instead of starting by drawing the waveform first hand. This approach implies that the choice of the filters determines the shape of the wavelet used to perform the analysis, and in general we can not choose an arbitrary wavelet waveform if we want to be able to reconstruct the original signal accurately.

81. The decomposition filters, together with their associated reconstruction filters, form a system called *quadrature mirror filters*.
82. For example at the first level, the coefficient vectors cA_1 and cD_1 have been produced by downsampling and are only half the length of the original signal; they cannot directly be combined to reproduce the signal. It is necessary to *reconstruct* the approximations and details before combining them.

The wavelet function ψ in particular is determined by the highpass filter, which also produces the details of the wavelet decomposition. There is an additional *scaling* function ϕ associated with some, but not all wavelets; it very similar to the wavelet function and is determined by the lowpass quadrature mirror filters, and thus associated with the approximations of the wavelet decomposition.

Finally, it has to be noted that the DWT is not a time-invariant (translation invariant) transform.

Denoising is one of the classical applications of wavelet analysis and represents an alternative to techniques such as lowpass filtering.

Wavelet based denoising is efficient, at least in its basic implementation, for families of functions that have only a few non zero wavelet coefficients, i.e. having a sparse wavelet representation, such as a function which is smooth almost everywhere[83] [WAV01]. It basically consists in carrying out a wavelet decomposition at a given level *N*, and applying for each level a threshold to the details coefficients. Several threshold selection rules exist, as well as the possibility of applying local (time-dependent) thresholds.

The filtered signal is then calculated with an inverse transform using the original approximation coefficients of level *N* and the modified details coefficients of levels 1 to *N*. Note that such a "traditional" wavelet based de-noising on channels affected by drift (low frequency trends) does not eliminate the drift itself.

An example of an application to metal detector laboratory data is provided in [SZY98]. We have also carried out tests using wavelet based denoising, however without apparent improvement with respect to standard lowpass filtering.

Additional tests were therefore carried out with a different aim, namely **signal detrending**, i.e. reducing the mostly low frequency component present in the imaginary part of the signal due to background (soil) fluctuations. The basic idea is to exploit the fact that wavelets ψ can be found whose first *M+1* moments are vanishing:

$$\int_{-\infty}^{\infty} t^p \psi(t)(dt)dt \;=\; 0 \quad \text{for} \quad 0 \le p \le M \tag{6.18}$$

If the analysed signal *S* is a polynomial of degree *M*, then the coefficients *C(a,b)* = 0 for all *a* and all *b*. In other words, such wavelets automatically suppress the polynomials. The degree of *S* can vary with time, provided that it remains less than *M*. If *S* is a polynomial of degree *M* on segment $[\alpha,\beta]$, then *C(a,b)* = 0 as long as the support of the function $(1/\sqrt{a})\psi((t-b)/a)$ is included in $[\alpha,\beta]$. The suppression is local and effects appear on the edges of the segment.

As a consequence the details are also zero. In practice this means that the details obtained with a wavelet of sufficiently high order should not be sensitive to constant, linear, quadratic etc. components. We have tried to exploit this property together with the fact that we have in first approximation reference channels, f_1REAL and f_2REAL (and possibly DeltaImag), which indicate where the signal is concentrated and which form it has. Overall this seems only partly successful.

83. Thinking of the original signal to be retrieved, i.e. not yet affected by noise.

Continuous Wavelet Transform (CWT) Results

Continuous analysis is often easier to interpret, since its redundancy tends to reinforce the traits and makes all information more visible. Thus, the analysis gains in "readability" and in ease of interpretation what it loses in terms of saving space [WAV01].

We will therefore first show selected examples using the Continuous Wavelets Transform, to illustrate data processing improvement possibilities. We have concentrated on *Gaussian derivative wavelets* $\psi^{(N)}(t)$, which have a form similar to the signal we are looking for; this should lead to a reduced number of coefficients with significant amplitude (i.e. a maximum of information is concentrated in a reduced number of coefficients [FRI01]). Log Gabor wavelets have been preferred in [SAR97], where the aim was to retrieve the depth information.

Gaussian derivative wavelets (**`gausN`**) are derivatives of the Gaussian probability density function (Eq. (6.19)), where C_N is such that the 2-norm of $\psi^{(N)}(t)$ is 1. **`gausN`** has N vanishing moments.

$$\psi^{(N)}(t) = C_N \frac{d^N}{dx^N} e^{-x^2} \tag{6.19}$$

We have chosen to work using scale values a of 1 to 128 in increments of 2. For each given scale a the wavelet coefficients $C(a,b)$ are computed for a position b = 1 to ls=length(S). The results about to be shown do therefore correspond to a coefficient matrix C(1:2:128, ls). Two types of scenarios have been investigated:

- **Enhancing the detection of weak signals not affected by background fluctuations** (f_1REAL, f_2REAL and DeltaImag):

  Results using **`gaus1`** are shown in Figure 6.13 in the form of copies of the Matlab Wavelet Toolbox graphical user interface images. The topmost section of each plot shows the signal being analysed (already lowpass filtered, scale in mV), the second the absolute value of the CWT coefficients (coloured by scale), the third one line of coefficients at a given intermediate scale (a=63), the fourth a plot of local maxima of coefficients across scales.

  The peaks correspond to the position of the centre of the signal (i.e. the zero crossing) and allow to find and reshape it. They could also be used to find the coefficients of interest for the filtering of f_1IMAG, f_2IMAG.

  The first plot features f_1REAL in a "high" S/N case; the clear peak at position 500 across all scales corresponds to the signal's zero crossing.

  The bottom plots feature f_1REAL and f_2REAL respectively in a low S/N case (weak signals). The coefficient's structure is still clearly visible and similar to the previous case, the peak around 500-520 corresponding to the signal's zero crossing.

- **Filtering signals affected by background fluctuations** (f_1IMAG, f_2IMAG):

  Results using **`gaus2`** are shown in Figure 6.14: the peaks correspond now to the position of the signal's peaks (i.e. maximum and minimum) and should allow to remove linear trends (# vanishing moments(**`gaus2`**)–1=1). To remove higher order trends it would be necessary to move to **`gaus3`**, etc., or to other higher order wavelets.

  The left plot features f_1IMAG in a low S/N case. The coefficient's structure is however still clearly visible, with peaks at 400-420 and 590 (compare with Figure 6.13, top), and does not show the trend of original signal any more. In this case **`gaus1`** could also work. Qualitatively similar results are obtained using **`db2`** (Daubechies wavelet of order 2).

  The right plot features f_2IMAG in the same setup, with an even poorer S/N; the weak original signal is very strongly background affected. In this case **`gaus1`** would not work well. The coefficients do not show the trend of original signal any more, are however quite weak in the area of interest.

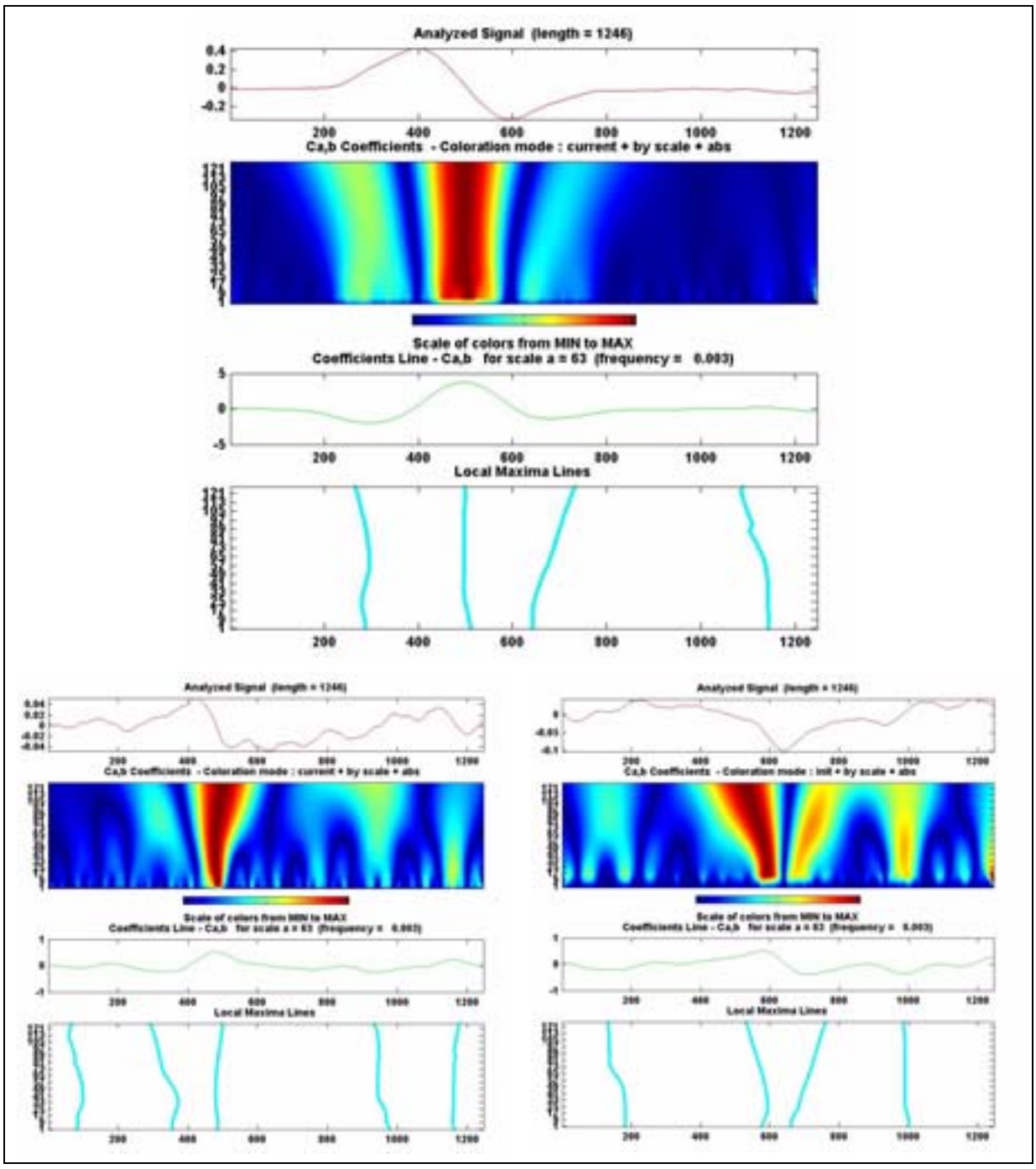

Figure 6.13: Continuous Wavelet Transform (**CWT**) results using **`gaus1`** for **`mist`** flush (mine w/o detonator). *Top*: f_1REAL, detector@80mm; *Bottom left*: f_1REAL, det.@160mm; *Bottom right*: f_2REAL, det.@160mm.

Discrete Wavelet Transform (DWT) Results

Selected examples using the Discrete Wavelet Transform (**DWT**) are shown in Figure 6.15. In this case we have used compactly supported *biorthogonal spline wavelets* (**`bior`** of order *Nr.Nd*, where *r* stands for reconstruction and *d* for decomposition[84]), in particular **`bior3.3`** and to a lesser extent **`bior3.1`**. In the second case the reconstruction wavelet is quite similar to a Gaussian, in the first it is similar to the derivative of a Gaussian. The number of vanishing moments for the decomposition wavelet is *Nr*–1.

84. In this case two wavelets are indeed used, one for decomposition and another for reconstruction.

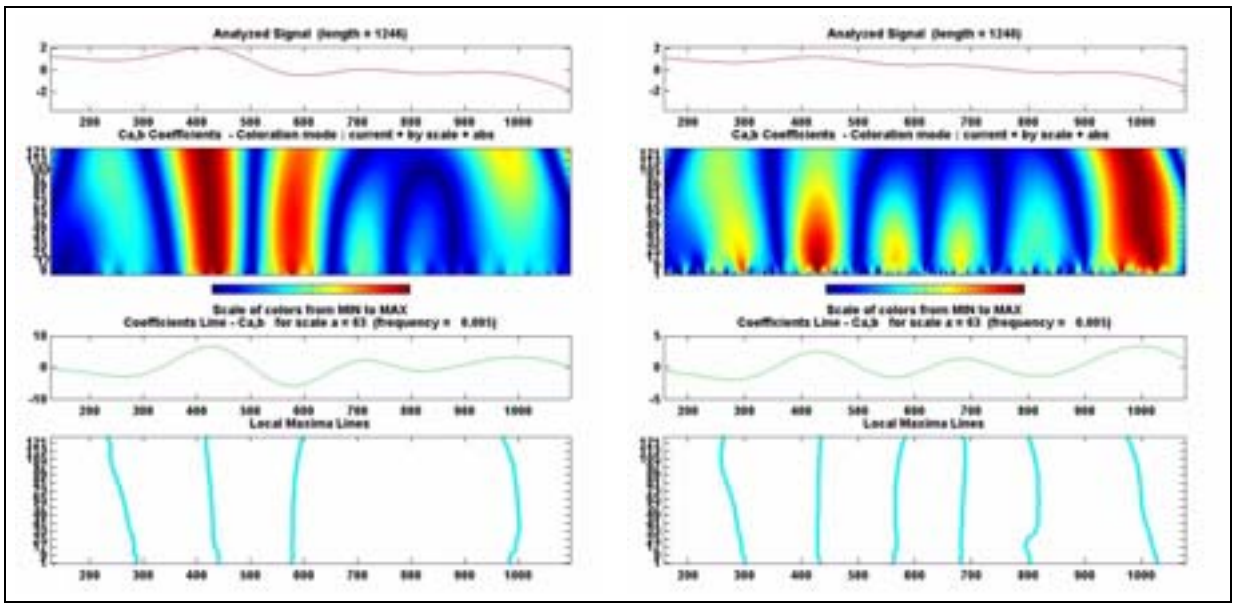

Figure 6.14: Continuous Wavelet Transform (**CWT**) results using **`gaus2`** for **`mist`** flush (mine without detonator). *Left*: f_1IMAG, detector@80mm; *Right*: f_2IMAG, detector.@80mm.

We have again investigated the possibility of filtering signals affected by background fluctuations, partly relying on the insensitivity of the details to low order polynomials when using wavelets with a sufficient number of vanishing moments.

We define a *Reference* signal, f_1REAL or f_2REAL, and a *Target* signal, f_1IMAG or f_2IMAG respectively, and decompose them via DWT up to a level N, which results in two sets of approximation coefficients cA_N and details coefficients cD_1 to cD_N. We then choose, for one of the two signals (usually the *Reference*, but we also tried to inverse the roles in **`S3`**,**`S4`**), the first *maxRetainedCoeff* coefficients with the highest absolute values according to a strategy defined below, and retain the same coefficients of the other signal; all other coefficients are zeroed. The resulting IDWT reconstructed signals are then plotted.

The following coefficient selection strategies **`S1`** to **`S4`** have been trialled, with results displayed in Figure 6.15 for *maxRetainedCoeff* = 5, 7 and 10, *Reference*=f_1REAL and *Target*= f_1IMAG (original signals dashed):

- **`S1`**: Consider ALL coefficients (cA_N, cD_1-cD_N), and base the choice of those to retain on the *Reference* signal.

  This is a simplified form of the "traditional" wavelet based de-noising schemes.

  The basic idea is to use the "clean" channel (no background fluctuations) as *Reference*, identify its most important coefficients and use the corresponding ones of the *Target* for its reconstruction. The hope is that the coefficients which contain the "drift" contribution in the *Target* decomposition will not be selected.

  Two examples are shown in the top row of Figure 6.15: the *Reference* is well fitted, whereas we tend to select "only" the portion of the initial *Target* signal which is in correspondence with the significant parts of the reference signal; this is only moderately useful.

- **`S2`**: Consider the DETAILS coefficients only (cD_1-cD_N), and base the choice on the *Reference* signal (its approximation coefficients cA_N are explicitly zeroed; the *Target* approximation coefficients are therefore automatically zeroed as well).

  As we are not considering the approximation it is necessary to use the higher levels (starting from 8-9 say) to get some meaningful results; examples are shown in the middle row of Figure 6.15. The background fluctuation are indeed attenuated, other fluctuations are however introduced; it is not straightforward to assess their importance.

- **`S3`**: Consider ALL coefficients (cA_N, cD_1-cD_N), but base the choice on the *Target* signal directly.

  Examples are shown in the bottom row of Figure 6.15. If we take a sufficiently high decomposition level (ex. 8, 9) and number of coefficients (~10), we basically retain the approximation coefficients and the reconstructed signal approximates the drift. At a lower level (ex. 5, 6) the details definitely play a marginal role, we are basically selecting only the largest approximation coefficients. This type of strategy does therefore not seem to work.

- **`S4`**: Consider the DETAILS coefficients only (cD_1-cD_N), and base the choice on the *Target* signal directly (its approximation coefficients cA_N are explicitly zeroed; the *Reference* approximation coefficients are therefore automatically zeroed as well).

  Results are similar to those of **`S2`**. The reconstruction seems however to work best for the file whose coefficients are used for the choice (in this case the *Target* file, for **`S2`** the *Reference* file).

Overall **`S1`** and **`S2`** seem to work best, but tuning of the coefficient selection and choice of the appropriate decomposition level are not straightforward and need to be guided by a preciser quantitative analysis.

[SZY98] does use a DWT version without decimation (downsampling), also called Discrete *Stationary* Wavelet Transform, for metal detector data instead of the standard DWT, which according to the authors would introduce phase angle distortions. The aim is denoising rather than detrending (no significant background fluctuations are visible in the data), the argument might however still be valid.

`mist` flush (mine w/o detonator), det.@80mm **S1, Level7**

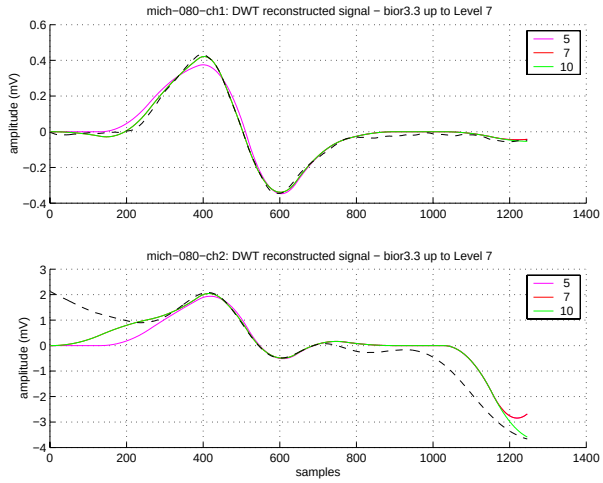

`mist` flush (mine w/o detonator), det.@160mm **S1, Level8**

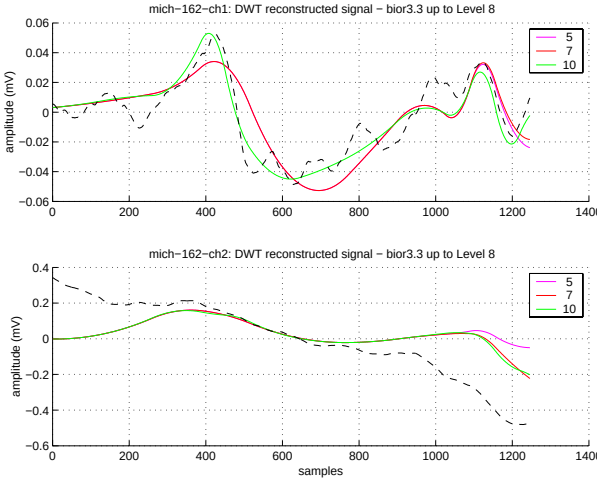

`mide` VER flush (mine detonator), det.@25mm **S2, Level8**

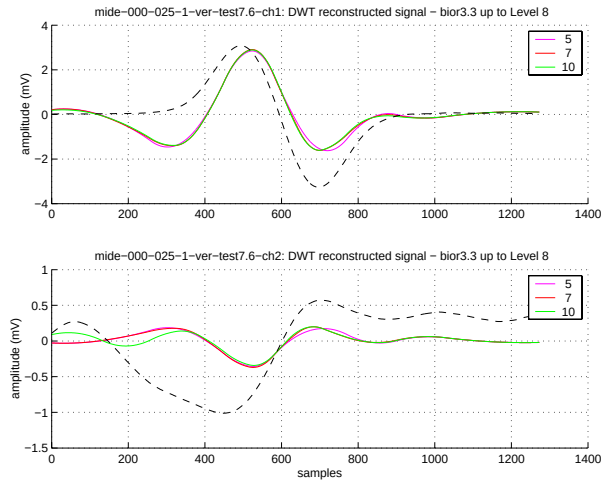

`mist` flush (mine w/o detonator), det.@80mm **S2, Level10**

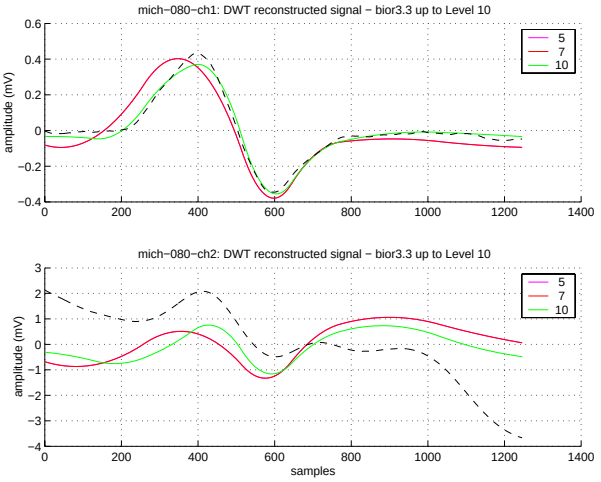

`mist` flush (mine w/o detonator), det.@80mm **S3, Level8**

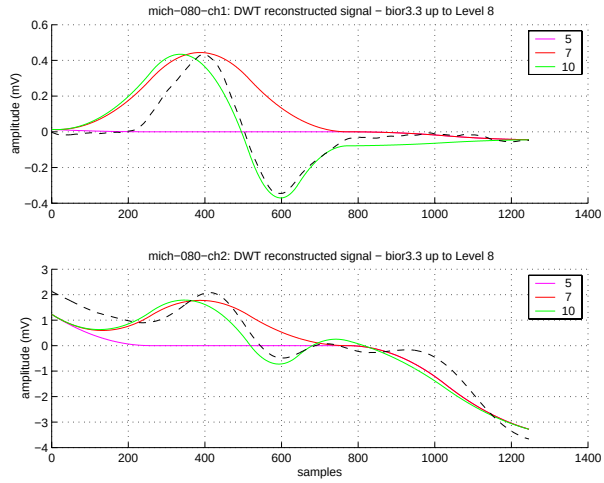

`mide` VER flush (mine detonator), det.@25mm **S3, Level6**

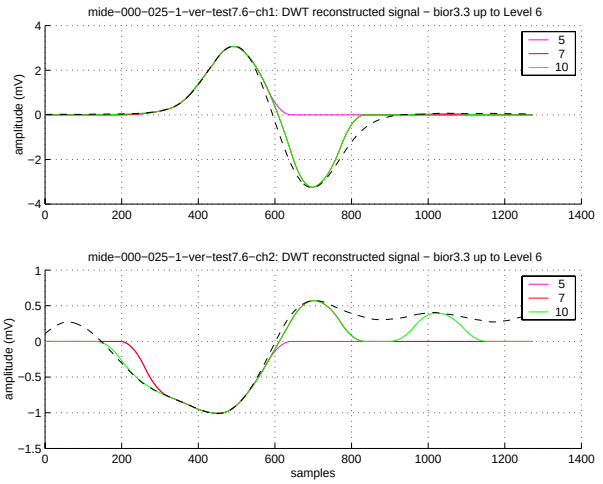

Figure 6.15: Discrete Wavelet Transform (**DWT**) results using **`bior3.3`** for different coefficient selection strategies **`S1-S3`** and decomposition levels *N*. *Top*: **`S1`**, left: N=7, right: N=8; *Middle*: **`S2`**, left: N=8, right: N=10; *Bottom:* **`S3`**, left: N=8, right: N=6. In all cases: Ch1=f_1REAL, Ch2= f_1IMAG, original signal dashed.

A6.2. Feature Definition and Extraction – Additional Examples

Phase Response

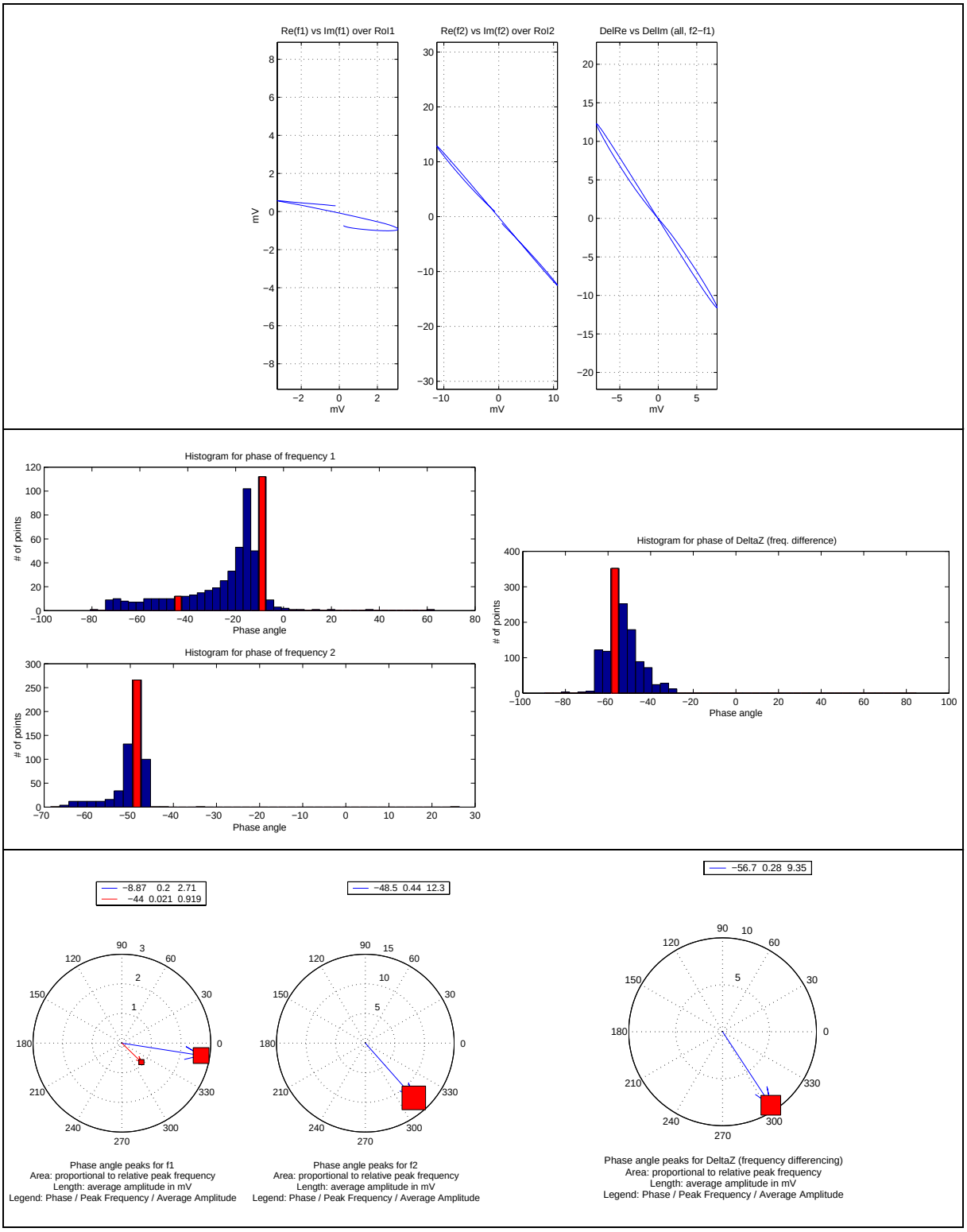

Figure 6.16: Phase response calculation and phase angle peak representation for a minimum-metal mine detonator replica (**`mide`**; example of small non-ferromagnetic object), vertical, flush.

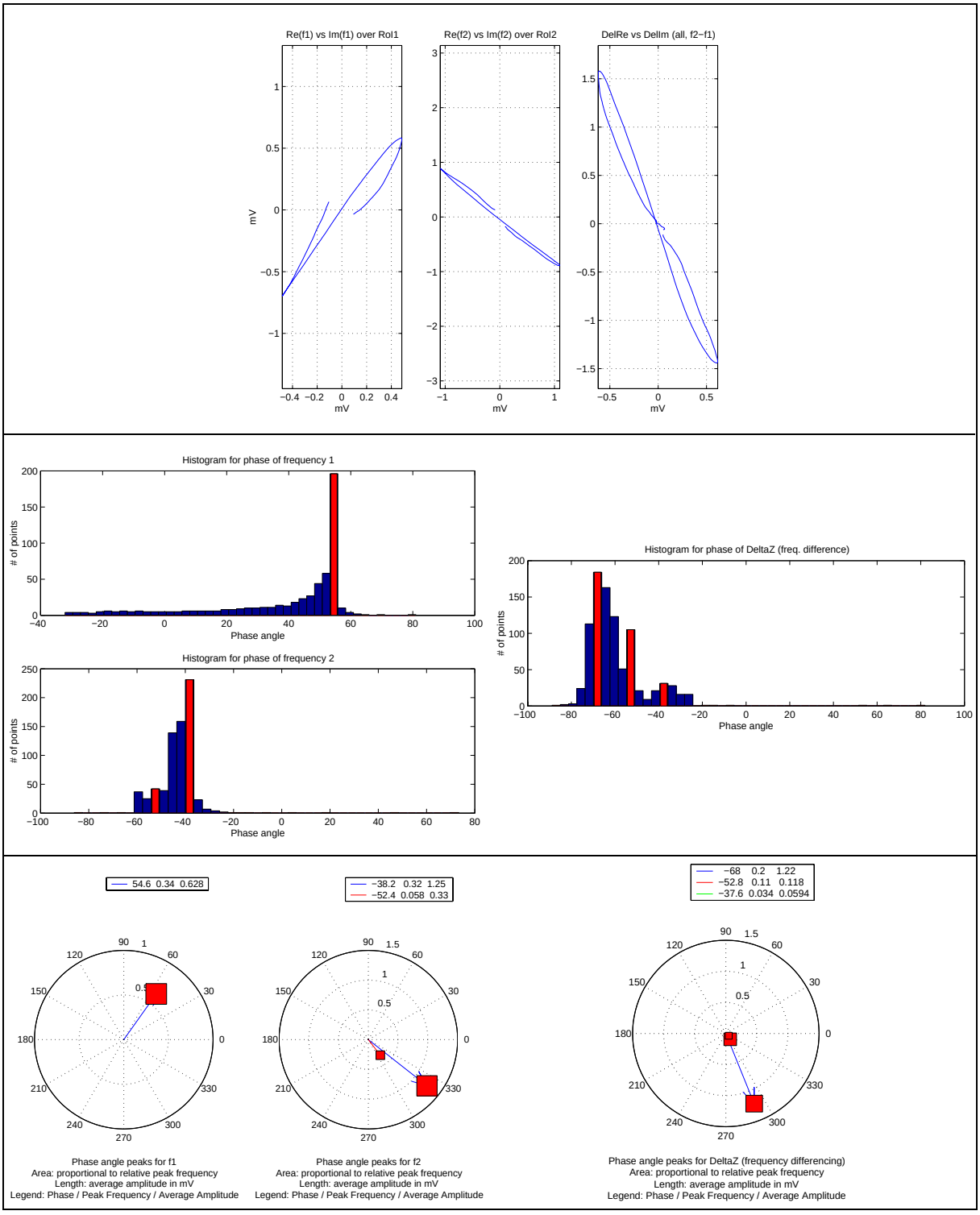

Figure 6.17: Phase response calculation and phase angle peak representation for a real (live) minimum-metal mine (**`mich`**; example of composite object), flush with detector at 5 cm. [mli11g]

A6.3. Classification Opportunities – Additional Examples

Amplitude Ratio Distribution

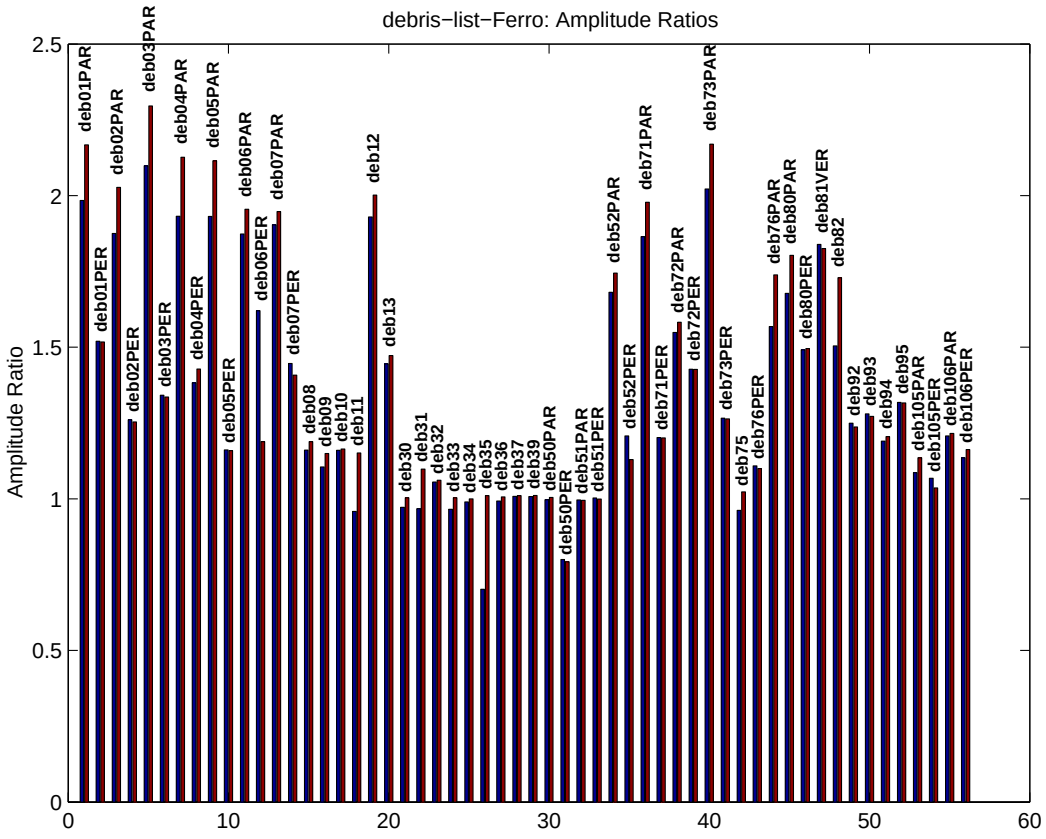

Figure 6.18: Amplitude Ratio distribution (*AR1,AR2*) for **`all ferromagnetic debris`**. First column of each bin: *AR1*, Second column: *AR2*.

A6.4. Example of Simplified User Interface & *Object Size* Classification Scheme

Figure 6.19 reproduces the possible outline of the simplified user interface mentioned in §6.4.2, where the individual *object sizes* correspond to the coarse target classification discussed therein. We have added two categories, UNKNOWN corresponding to targets with either too weak S/N ratio or not fitting any category (e.g. situations with some composite object, or very irregular responses, or multitarget scenarios), and DANGER, triggered when the target resembles either a large object in the case of UXO, or one of a given set of mines (or mine components).

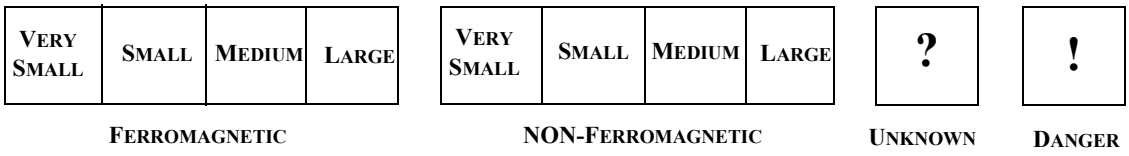

Figure 6.19: Classification opportunities: possible outline of simplified user interface with coarse *object size/type* classification

This interface could be combined if necessary with a 2D diagram of the phase response, either continuous or already with phase angle peaks and average amplitudes, at least during the development phase.

An object could well be associated to different (neighbouring) sizes, or perhaps to all ferromagnetic sizes if it clear that its nature is ferromagnetic but it is impossible to say more.

A possible *object size classification scheme* based on three parameters, the phase angle response at f_1 and f_2, φ_1 and φ_2 respectively, and the amplitude ratio *AR*, is proposed in Table 6.2. It is mostly based on the observation of the response of the debris items, taking certain categories as representative of a size, for example (NF: non-ferromagnetic, F: ferromagnetic):

- **Very small**: NF: **`deb21-26`** (foils), F: **`deb30-39`** (foils);
- **Small**: NF: **`deb20`** (foil), **`deb40-41`**, F: **`deb01-07`** (PER), **`deb92-95`** (fragments);
- **Medium**: NF: **`deb90`** (spent cartridge), F: **`deb80-82`** (shell fragments);
- **Large**: NF: **`deb100-104`**, F: **`PMR`** (stake mine).

	Object Size, Non-Ferromagnetic				*Object Size, Ferromagnetic*			
Feature	*Very Small*	*Small*	*Medium*	*Large*	*Very Small*	*Small*	*Medium*	*Large*
AR	<0.2	0.2:0.5	0.3:0.7	0.7:1	0.9:1.1	0.9:1.5	>1.5	0.5:1.5?
φ_1	0:–5	–10:–20	–20:–60	<–60	90:85	85:75	75:55	55:0
φ_2	0:–10	–10:–50	–50:–70	<–70	90:80	80:60	60:45	$<\varphi_1$

Table 6.2: Possible object classification scheme. All phase angles are in degrees; the phase angle ranges are indicated as (upper limit):(lower limit), the opposite for *AR*.

The phase angle ranges are indicated as (upper limit):(lower limit), which is somewhat natural given that the phase angles normally decrease with increasing *object size*. The lower *AR* end for ferromagnetic objects for the first classes has been taken as 0.9 instead of 1 to cope with some measurement uncertainties.

The choice of the different classes is obviously somewhat *fuzzy*, and is complicated by the orientation dependence of the response for a number of ferromagnetic targets, in particular the elongated ones (demagnetization effects). Other features could be included as well, such as multiple phase angle peaks; we have implicitly relied on one phase angle peak per frequency, the one with largest average amplitude. The phase angle ranges have been taken here as non-overlapping, different choices are again possible, and probably required in order to cope with special cases such as very large ferromagnetic objects (e.g. **PROM** metallic mine).

7.
Metal Detector Near Field Imaging

An approach which is complementary to the one described in the previous chapter consists in providing information on the object's size and shape, which could be useful in discriminating in certain circumstances mines and/or UXO from clutter. "Conventional" metal detectors can indeed be used to generate images of buried metallic objects with varying levels of resolution.

After a brief look at the electromagnetic near field properties we will review a number of existing systems and approaches, to concentrate then on two portable high resolution applications which exploit the geometrical properties of the near field. The first features a commercial multisensor system designed for NdT applications in civil engineering, the second concentrates on the application of image deblurring techniques (deconvolution) to bidimensional data obtained with a commercially available sensor, the Förster Minex metal detector.

7.1. Low Frequency Electromagnetic Near Field Properties

It is often asked how it is possible, using metal detectors, to detect and/or image objects with a resolution of several (tens of) centimetres when the wavelengths of the applied low frequency electromagnetic fields are orders of magnitude larger. The response lies in the fact that the sensors are operated in the near field – all interactions between the field and scatterers occur in the near field of the probe – rather than in the far field as for "classical" imaging applications for example (for which the attainable spatial resolution R is indeed about half of the source wavelength[85], $R=\lambda/2$ – Rayleigh's criterion, the resolution is wavelength limited).

The coupling is then by evanescent waves, whose amplitude decreases exponentially along the direction of propagation, as well as propagating waves in the spectrum of the antennas, and geometrical properties such as the sensor footprint, scanning pattern and object distance can and do play a primary role. In the near field the resolution depends on the degree to which the evanescent waves can actually be measured [GUO98 and references contained therein]. As in our case the source dimension and the source to detector distance are much smaller than the wavelength in the soil, the ultimate resolution is in fact determined, similarly to what happens for the imaging of flaws in NdT, by the quasi-static nature of the EM fields that both illuminate the target and are scattered by it [BAH88] (see also §3.4.2).

The role that evanescent electromagnetic waves can play is discussed on the basis of a simple analytical model in [SMI99] for example. The authors also point to the interesting analogy between the use of evanescent waves to image a mine and what is done in near field scanning optical microscopy (NSOM), where evanescent waves are introduced to increase the resolution beyond what is possible with a traditional microscope relying only on propagating waves.

It makes therefore sense to measure the induced magnetic field, or its gradient, scanning a single sensor or using arrays (several combinations of sensing elements are possible), which can be scanned as well, and build a bidimensional image of the measured signal amplitudes[86]. The latter

85. The attainable resolution R is in general related to the maximum spatial frequency of the field as $R=\pi/k_{max}$. Usually $k_{max}=2\pi/\lambda$ [GUO98].
86. A metal detector does not give directly any depth indication, contrary for example to radar equipment.

can then be processed using image processing techniques which rely to variable levels on the knowledge of the underlying physics. In certain cases 3D or *pseudo*-3D images can be reconstructed as well, or at least some 3D related information recovered (e.g. object depth), exploiting for example multifrequency techniques or the fact that the spatial field behaviour in a horizontal plane is influenced by the object depth.

7.2. Metal Detector Imaging Systems and Applications

A number of different methodologies and systems have been proposed for the "imaging" of buried metallic objects of interest to us (mine components, metal mines or UXO), whereby the precise target application and type of image can be quite different, although emphasis is usually on larger targets. Systems range from arrays composed of individual sensors to innovative sensors, sensor geometries and/or processing techniques. Most of them are vehicle based, but a few are designed to be portable.

We will briefly review the most significant ones, as well as holographic techniques in NdT (the deconvolution approach will be detailed separately in §7.4):

- ***Scanning Systems:***

  ODIS (Ordnance Detection and Identification System) is a vehicular system using one or more differential sensors attached to a rotating arm to scan a path as the sensor platform moves forward. ODIS was conceived to provide the user with quantitative information (relying on database supported inversion) on shallowly buried ordnance and to deliver unprocessed images (not deconvolved) [BOR96, ODIS96]. The latter are very useful to spatially localize the single objects, which is essential in a real-time constrained vehicular operation. However, by themselves, these images probably do not allow because of their resolution to distinguish one object from another, except for "large" objects" (i.e. of size comparable to the detector's dimensions). Additional details are available in the corresponding patents [ESC96,TRI96].

- ***Metal Detector Arrays:***

  Arrays of metal detectors have also been built, to quickly scan a large path for example, such as the Schiebel VAMIDS system [RUS99]. Figure 7.1 shows an image corresponding to data taken on a dirt road at DRES [McF96]. Each of the 9 wide strips represents the full width of the array as the detector moves along the road at uniform speed; the scanning is therefore obtained here by the forward motion of the vehicle alone. Strongly positive signals are white, strongly negative signals are black. A number of mines are detected, as well as a number of nuisance items and false alarms (courtesy Dr. John McFee, Defence Research Establishment Suffield (DRES), Defence Research and Development Branch, Canada).

Figure 7.1: Schiebel VAMIDS "image" (McFee, DRES [McF96])

Figure 7.2 (D. Brown, SAIC [BRO96]) shows an image corresponding to data from the scan of a Field Calibration lane (low metal clutter) during tests at Ft. A. P. Hill, VA, Nov. 95, using a 2 meter array mounted on the multi-sensor VMDT vehicle (Vehicular Mine Detection Testbed) [BRO96]. The large signals are due to metallic mines and the smaller ones to shallowly buried APs. It is evident that some form of discrimination based on the size of a spot is possible.

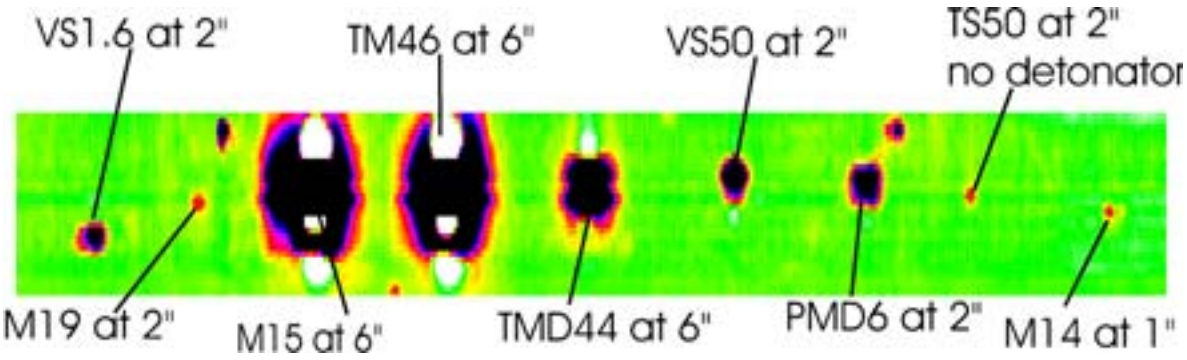

Figure 7.2: VAMIDS image from VMDT vehicle (D. Brown, SAIC [BRO96])

Although VAMIDS was not conceived as an imaging detector, the data it produces can be viewed as low resolution images and existing image processing techniques applied to them. Domain-specific knowledge of metal detector arrays was indeed used and peak detection algorithms suitably modified, allowing realtime operation. Details are reported in [RUS99], which refers to [DAS90] for the modelling aspects used to analyse the features of the spatial response of the array (replacing the target with an equivalent magnetic dipole induced by the transmit field, and using the principle of reciprocity to calculate the voltage induced in a receive coil). This allowed for example to explain why in a number of instances a white (positive) spot is accompanied by two black (negative) spots on each side, as can be seen looking attentively at Figure 7.1.

- ***Special Coil Configurations (spatial periodicity):***

  Another interesting and unconventional application is represented by the Meandering Winding Magnetometer (MWM) described in [MIT96]. The device, a "planar transformer", has the characteristic of using a square wave winding conductor in order to generate a spatially periodic electromagnetic field, whose spatial wavelength depends only on the primary winding spatial periodicity and is the principal reason which allows to model it with accuracy. It can, in principle, detect several characteristics of a buried metallic object (size, shape, etc.) based on a modelled response to the spatial wavelength and has spatial imaging capability. Its application to humanitarian demining has been envisaged, in particular the characterisation of UXO such as unexploded bomblets [GOL98,GOL99].

- ***Other Sensor Arrays:***

  A portable, low power array of giant magnetoresistive (GMR) sensors has been developed, which can also be used for imaging applications [CHA00]. The sensors are arranged in a checkerboard configuration (2D array) such that axes of sensitivity of alternate GMR sensors are orthogonally oriented; other sensor configurations have also been proposed. The preferred target application is UXO remediation via a reduction of the false alarm rate by rapidly distinguishing between buried ordnance and other ferrous items.

  A similar system featuring a different type of magnetoresistive sensors, of the spin dependent tunnelling type (SDT), is described in [WOL99]. In this case the authors have incorporated the data analysis algorithms into the design process, with the goal of recovering the target object parameters – its geometric and material properties – by inverting the measured data using physical models of the target (the recovered parameters will then be compared to collections of model parameters for known targets in a database). The theoretical model used to solve this inverse problem is based on the simplest possible limiting form of the mean field scattering theory, which is according to the authors computationally fast and captures the essential physics in high-contrast scattering; the theory has been specialised for a few canonical shapes.

- ***Holographic Techniques:***

  We have already discussed in §3.4.2 the fact that in the ground the wave equations for the electric and magnetic fields reduce, when displacement currents can be neglected, to diffusion equations. Measurement ranges are usually much less than a wavelength and the corresponding phase delay related to the spatial variations of the waves is therefore usually negligible (it is too small to be used to measure an object's range and shape or to distinguish multiple objects [GUO98]). The magnitude of the electromagnetic field is however very sensitive, as we know, to the distance from the object and to the characteristics of the buried target.

  Near field electromagnetic "holographic" methods have therefore been devised to achieve an imaging resolution not limited by the wavelength resolution limit as in traditional holography[87], with the aim of localizing and possibly resolving near-surface buried metallic (i.e. highly conductive) objects such as UXO and mines [GUO96,GUO98,GUO00].

  These methods basically rely on the properties of the evanescent waves as already discussed in §7.1. We actually already know that using metal detectors for detection applications it is possible to achieve a high spatial resolution and are implicitly always working way beyond the wavelength resolution limit. The interesting point here is the reconstruction of the magnetic field distribution in the horizontal plane at various depths in the ground. This is achieved by propagating the measured (magnetic) field back to the source plane starting from the measured field above or on the ground, and relies on the principle that the back-propagated object field will converge at the object's true location.

  In practice this is achieved with a custom designed pulse metal detector, recording the signal at grid points on a horizontal plane and Fourier transforming it into the frequency domain (amplitude and phase information). The spatial distribution of the magnetic field at a particular frequency is then Fourier transformed in two dimensions to form a spatial frequency spectrum. This spectrum is multiplied by a propagation function to back-propagate it to a desired depth d, and the result is then inverse Fourier transformed (2D) to produce the reconstructed image at the depth d.

  The experimentally achieved resolution was estimated at 10^{-3} of the wavelength in the conducting medium (objects located as close as 1 m could be resolved and individually localised with fairly good accuracy by reconstructing the field images at level planes). It is however not entirely clear how much the results depend on the electrical ground parameters and their variations (inhomogeneities).

- ***Holographic Techniques in NdT:***

  Holographic techniques have also been applied in Non-Destructive Testing (NdT) for the reconstruction of volumetric scatterers within conducting materials. In this case one interprets the eddy currents induced in a conductor as penetrating waves, also called "skin waves", which are strongly damped due to the skin effect; their wavelength is a factor 2π longer than their penetration depth (skin depth). The peculiarity of NdT applications is that due to the presence of good conductors the distances involved are much closer to the skin depth – and therefore to the wavelength – than in applications of interest to us; as a consequence phase shifts in the probe field can be exploited.

  Studies are reported in [HIP90,HIP93] on imaging using broadband holography, in which a coil is moved along a surface (synthetic aperture like process) whilst scanning a given frequency range. In this case depth resolution is obtained by the use of more than one frequency (single frequency operation is detailed for example in [COL84]). A cross-sectional image is generated and its depth resolution increased by phase multiplication of the received multifrequency signals, equivalent to a fictitious reduction of wavelength[88]. The target application was the imaging of volume scatterers, for example flaws, under a conducting surface. Such volume defects cause localized

87. In traditional holography the hologram is in general recorded several wavelengths away from the source and the evanescent waves play a negligible role.
88. Thus avoiding the need of operating at higher frequencies, which would result in an increase in resolution but at the price of a smaller skin depth, and therefore of a reduced penetration in the conductor.

conductivity and/or permeability changes in a conductive material, which can be assimilated to a conductive half-space. Typical frequencies are in the range of several tens to hundreds of kHz, with typical spatial dimensions (eddy current probe and associated field) of the order of one mm.

The presence of high phase shifts in the probe field does usually favour the application of this type of technique. These are however the conditions which are usually avoided in the applications of interest to us, apart from specific scenarios such as the presence of minimum-metal mines in very conductive soils or close to sea shores for example, working towards higher frequencies (where the skin depth could be of the order of the object depth, see Table 3.2). It is therefore not immediately clear if such a technique could be transposed with success to demining applications.

Of all the systems discussed, metal detector arrays are probably the most mature ones (see §2.3.2.3 for more details, with description of systems other than VAMIDS). They are in use, mostly as components of multi-sensor vehicle based systems.

The other systems seem to often neglect the soil response, which as we know is correct to first approximation only, and which can represent a particular problem when looking at small and/or deep objects, or in presence of magnetic soil. Their state of maturity is not known with precision.

7.3. High Resolution Imaging with a Multisensor Visualising System

We will report in the following on high resolution imaging with a commercial multisensor metal detector, designed for NdT applications in civil engineering, with the aim of assessing its potentialities and understanding in a broader sense if such systems, possibly in a modified form, could be useful to tackle some aspects of the humanitarian demining problem along the lines[89] proposed in [EBL96]. The latter include the detection of non minimum-metal mines and shallowly buried Unexploded Ordnance (UXO). In fact, given that spatial resolution and depth penetration constitute conflicting requirements, we do not expect them to be applicable to humanitarian demining "as is".

Results could be a priori expected for "larger" metallic objects of regular size which have to be differentiated from metallic debris often consisting of small metallic pieces scattered around. Examples are mines with an appreciable metallic content (some grams) such as the Russian PMN or PMN2, or shallowly buried Unexploded Ordnance (UXO) such as "bomblets" which still plague some areas (e.g. Laos). Minimum-metal mines such as the Chinese Type 72 contain less than a gram of metal and seem much less likely to profit from such a system alone, in the sense that an image of a pointlike object would be of help to the deminer, but in itself probably insufficient to take a yes/no decision.

The following sections follow closely [BRU97b,BRU98c,BRU00a].

7.3.1. NdT Applications in Civil Engineering

Reinforcing bars are widely employed in civil engineering. They are mostly made of steel, cylindrical, with diameter between 6 mm and 50 mm, and usually located from just underneath the surface to 18 cm maximum in depth (the shallow location being more frequent).

Rebars in concrete can be detected and characterised using metal detectors, whose task is definitely eased by the rebars' ferromagnetic nature. Simple instruments are only able to locate the rebars, whereas more advanced ones can also calculate the distance ("cover") from the surface to a rebar of known size and characteristics (this allows to precalibricate the instruments), usually operating by direct contact on a flat surface. Precision on cover measurement can attain some percent of cover, down to about one mm in the most favourable cases.

The most recent instruments are also able to estimate both cover and rebar size (diameter) by taking at least two measurements of the same rebar under different conditions. Several techniques are available [BRU00a].

Different head sizes are sometimes proposed by the manufacturers, and are normally much smaller than the ones employed in humanitarian demining. They are therefore more accurate at shallow depths (increased spatial resolution) and able to resolve closely spaced objects, which is especially useful in "congested" situations, but lack in depth of penetration given that the detection range is strongly related to the coil dimensions.

Such systems, especially when applied as imaging tools, can indeed exploit the fact that rebars are shallowly placed regular structures composed of ferromagnetic objects, usually lying in a plane, whereas the humanitarian demining world is obviously much more complex (small and irregular objects, ground inhomogeneities, large number of varying scenarios, etc.). The rejection of the background signal, for example due to moisture, is therefore also somewhat less problematic in civil engineering applications.

89. "First generation equipment [] could provide the deminer with a visual image of shape and size of the metal signature."

7.3.2. Imaging Systems for NdT Applications

Work on "imaging" devices is indeed in progress, with at least a couple of systems on the market. Note that single sensors have normally to be scanned on the area of interest, which can be time consuming; devising a simple and accurate tracking and positioning system is also far from trivial. Multi-sensor systems can ease the task at the price of higher cost and somewhat increased complexity; these considerations are valid for humanitarian demining applications as well. Example of developments include the following:

- The University of Kassel has been working on an imaging inductive rebar locator, which uses IR sensors for accurate position measurements (0.5 mm) on a 2D grid of lines [GER96,RIC95]. Priority moved then to data analysis and sensor optimization[90] more than on imaging aspects (although, concerning the latter, interest in a high resolution tracking system remains).
- The University of Manchester is working on inductive rebar locators and on image processing (enhancement) techniques, such as deconvolution (Figure 7.3 left, *c,d*) using an accurately modelled response function, to sharpen the response. This might require the knowledge of the object's depth. Their first generation laboratory prototype used a high resolution positioning frame and a sensor which is physically much smaller than a "conventional" metal detector (Figure 7.3 left, *a*), to improve spatial resolution [GAY94,GAY95]. Recent developments on the sensors as well as on the signal processing side are detailed in [FER00,GAY00]; the development of a multi-array sensor with a new sensor head has also been pursued.

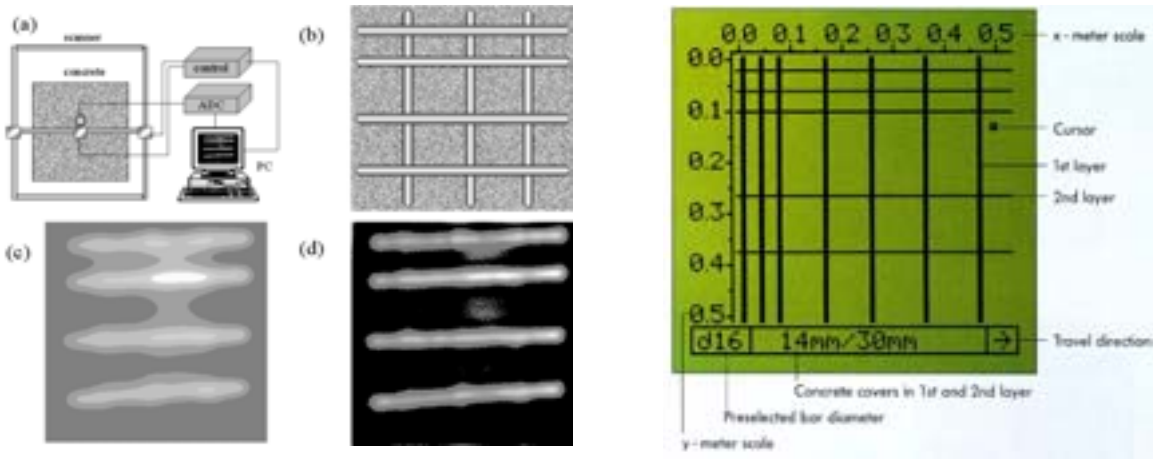

Figure 7.3: *Left*: First generation high resolution imaging metal detector (F. Gaydecki, Manchester [GAY95]). *Right*: Profometer4 rebar display (example over 50×50 cm).

- The Profomoter4 cover meter developed by Proceq. In addition to the usual functions it is possible to fit its probe with a path measuring device and, after scanning a surface along the x and y direction, rebars can be located and displayed on a LCD monitor as shown in Figure 7.3, right.
- The Ferroscan system, developed by the HILTI Corporation, which will be detailed below.

We recall that the response curve of a sensor depends on its intrinsic resolution as well as on the object's depth, and that it will tend to broaden with increasing depth, which can considerably affect the images if left untreated. Figure 7.4 shows examples taken with the Förster Minex.

90. W. Ricken, *Private Communication*, 9/1997.

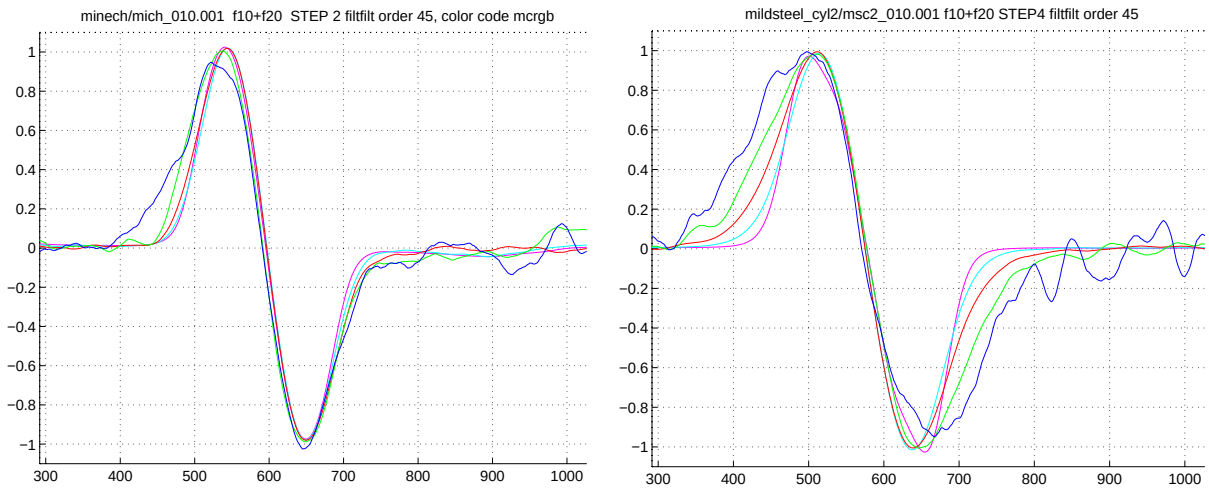

Figure 7.4: Normalized response at five increasing detector heights starting from 1 cm, innermost: shallow; flush objects. *Left*: minimum-metal mine, striker pin only (**`mist`**), 2 cm increments, *Right*: **`msc2`**, PER orientation, 4 cm increments (colour code: magenta, cyan, red, green, blue). Horizontal scale in mm.

7.3.3. The Ferroscan System[91]

Ferroscan, manufactured by the HILTI Corporation (Schaan, Liechtenstein), has appeared on the market at the beginning of the '90s and is targeted at the visualization of steel rebars in concrete.

System Components

The heart of the system is represented by the RS 10 multi-sensor scanner (Figure 7.5, right), of size 230×140×140 mm and weight 1 kg, which is able to scan a width of 15 cm.

Results are displayed on the RV 10 monitor (Figure 7.5, left), of size 270×200×80 mm and weight 2.2 kg (accumulators included). Its backlight LCD works on 320×240 pixels using 9 grey levels. The monitor can be interfaced to a PC via a standard serial RS 232 interface to download the acquired data, with a maximum of 42 raw data files, each one corresponding to a full acquisition (i.e. up to 42 images can be stored). A PC version of the data processing software running on the monitor's 16 bit microprocessor is also available [HIL94].

Scanning Procedure

The maximum area which can be covered and analysed in a single image is 60×60 cm and has to be crossed horizontally and vertically, for a total of eight scans (four in each direction, see Figure 7.6).

This because the system, due to its differential nature, is not able to find objects located parallel to the scanning direction. The latter is in fact strictly true only for rebars somewhat longer than the scan, in the sense that any object shorter than the scan length will produce at least a signal at its beginning and at its end; this will have some interesting implications on the objects of interest to us. Note that diagonally lying objects are displayed with slightly worsened resolution (fuzzier image).

The maximum scanning speed is 0.5 m/s, which looks quite sufficient for hand-held operation; a complete scan is therefore obtained rather quickly. Note that the area of interest can be smaller if necessary, but only sections containing both horizontal and vertical data are actually displayed and analysed [HIL97a].

91. Note: the signature of a Non Disclosure Agreement with the Hilti Corporation was necessary in order to have access to the system's raw data. As a consequence it is not possible to enter into more detail than what reported below.

Figure 7.5: Ferroscan RV 10 monitor (left) and RS 10 scanner (right) (ruler length: 30 cm)

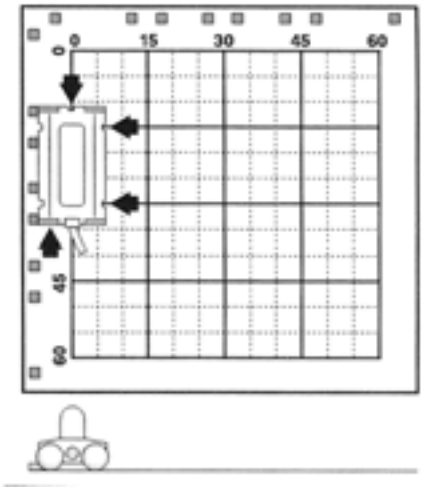

Figure 7.6: Ferroscan scanning procedure, lengths in cm (from [HIL97a])

The distance is measured along the track by odometry, using an optical encoder, given that the surface used is almost always flat. One set of two wheels is placed at each end of the scanner, the four wheels moving together to guarantee displacements as parallel as possible along the scanning direction.

Technical Details

From the Ferroscan patent [KOU94] we know that the system is of multi-sensor and differential nature, basically measuring (an approximation of) the horizontal gradient, along the scanning direction, of the vertical component of the induced magnetic field.

Given that such a system is targeted primarily at steel objects it can be built, in principle, either using a permanent magnet or an electromagnet as in conventional metal detectors used for humanitarian demining, in both cases spanning the scanner width. Corresponding sensors include field plates such as magnetically controlled resistors, or more conventional copper coils. A two dimensional arrangement of the sensors is in principle possible.

Data Processing

The sensor is obviously the central part of the system, but simple and elegant real-time data processing represents an important contribution to system performance too.

Using a differential sensor eases rebar localization, which can be obtained for example by looking for zero crossings in the received signals, or by further differentiation. The differentiated signal curves can then be used to produce, starting from the horizontal and vertical scans, a composite bidimensional grey scale image such as Figure 7.7, bottom right [KOU94].

The latter can then be further processed to look at different depth slices, as depicted in the first three images of Figure 7.7 (but always starting from 0, e.g. 0 to 20 mm or 0 to 35 mm etc.), using a simple and efficient menu driven interface and pushbuttons at the side of the screen [HIL97b]. Note that these images are binary (black/white). These impressive processing steps rely probably in a clever way on the characteristics of the rebars' response, which depends much more on its depth than on its size; as such they are not very likely, in their present form, to be generalized easily to other metallic objects.

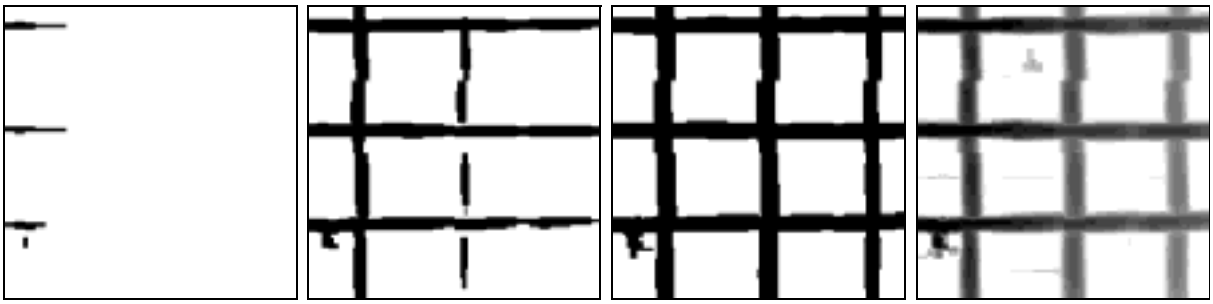

Figure 7.7: Typical Ferroscan B/W rebar images at increasing depth range (0-20 mm, 0-35 mm, 0-50 mm), and overall grey scale image (all depths); 60×60 cm

It is well known that the signals received by metal detectors decay very rapidly with distance, spanning several orders of magnitude. Representing with a few grey levels an image of rebars at different depths requires therefore some form of nonlinear transformation to preserve the system dynamics. This has again implications on the visualization of objects of interest to us, especially small isolated ones. Adequate filtering is also necessary, especially for weak signals.

Note that we did have full access to the system's raw data thanks to the collaboration of HILTI, but that we did not know the exact details of the algorithm implemented in Ferroscan. We have therefore tried to reproduce it as simply as possible along the basic lines described above for the purposes of this study.

Data Analysis

Rebars of 6 mm diameter can be displayed nominally down to 130 mm, and those of 36 mm down to 180 mm. Indication of their depth and size is given only when reliable, which happens for somewhat smaller values of depth. Sensor resolution is such that two rebars should be distinguishable when their distance d is greater than their depth (cover) T ($d/T \geq 1$).

Note that processing is tuned to ferromagnetic objects; non-ferromagnetic ones, e.g. aluminium or copper, do also produce signals, which can however not be evaluated. The corresponding images look somewhat like "negatives" of the expected ones. This does usually not represent a problem given that the analysis of such objects is not the primary goal of the system, and that they appear rarely in the context in which Ferroscan is used.

Note also that the magnetic field induced in the bar, or any other (linear) structure, radiates from its ends in all directions and is often detected in more than one sensor, which contributes to making the final image fuzzier [HIL97b]. This effect complements the one described in the *Scanning Procedure* paragraph.

7.3.4. Ferroscan Results and Discussion

A number of objects were tested during 1997 in a "sandbox" at different depths. For this purpose we put a wooden plate directly on the flattened sand surface and moved the sensor over the plate in much the same way as would be done while scanning a standard wall (as described before). We do obviously NOT suggest here that this experimental practice is applicable "as is" to the detection of ordnance or landmines. On the contrary, as for other detectors which have to be scanned in a precise way over the object of interest, an adequate tracking system would have to be given careful attention and its implementation is far from trivial.

The objects under analysis include (see the corresponding images on the following pages):

- *Small submunition*, steel (ferromagnetic), slight ellipsoidal shape (31×36 mm), 63 grams, internally prefragmented.
- *PMN* "like" AP mine[92] (origin: Cambodia): a "classical" AP mine, diameter 11 cm, height 5 cm, with cover retaining ring (ferromagnetic!) placed at about 1.5 cm from the top (height 5 mm, thickness about 2 mm, double i.e. bent twice). This mine has *usually* a steel striker composed essentially of two cylinders joined one to the other, the first of 19 mm length and 9 mm diameter, the second of 39 mm length and 5 mm diameter. This striker is located horizontally somewhat above the bottom. The one in our possession had in fact a slightly smaller, non-ferromagnetic (alloy?) striker.
- *BLU 26 "bomblet"* (blue coloured, probably the training version), round (65 mm diameter), 430 grams. Its body is likely to be non-ferromagnetic (e.g. aluminium), containing ferromagnetic shrapnel. Note that this might be different from the live (all steel?) version[93]. Large quantities of similar UXO are still found in Laos for example.
- *Mortar shell*: of total length 300 mm, its top half is steel (ferromagnetic), while the bottom half is aluminium.
- *20mm Projectile*: cylindrical, 20 mm diameter at the basis, 140 mm length, steel (ferromagnetic) with an aluminium tip.
- *"Rocket"*: cylindrical, aluminium, 32-33 cm length.
- *Debris*: a steel screw (ferromagnetic), about 20 mm long, head 7 mm wide, and a large metallic piece of irregular shape (twisted), 10 mm large and about 3-4 mm thick, probably made of copper (reddish colour).

All of them have been placed flat (horizontally). Further details are available in the next section.

92. It could be a Chinese Type 58 copy (Lyn Haywood, *Private Communication).*
93. Lyn Haywood, Miltra Eng., *Private Communication.*

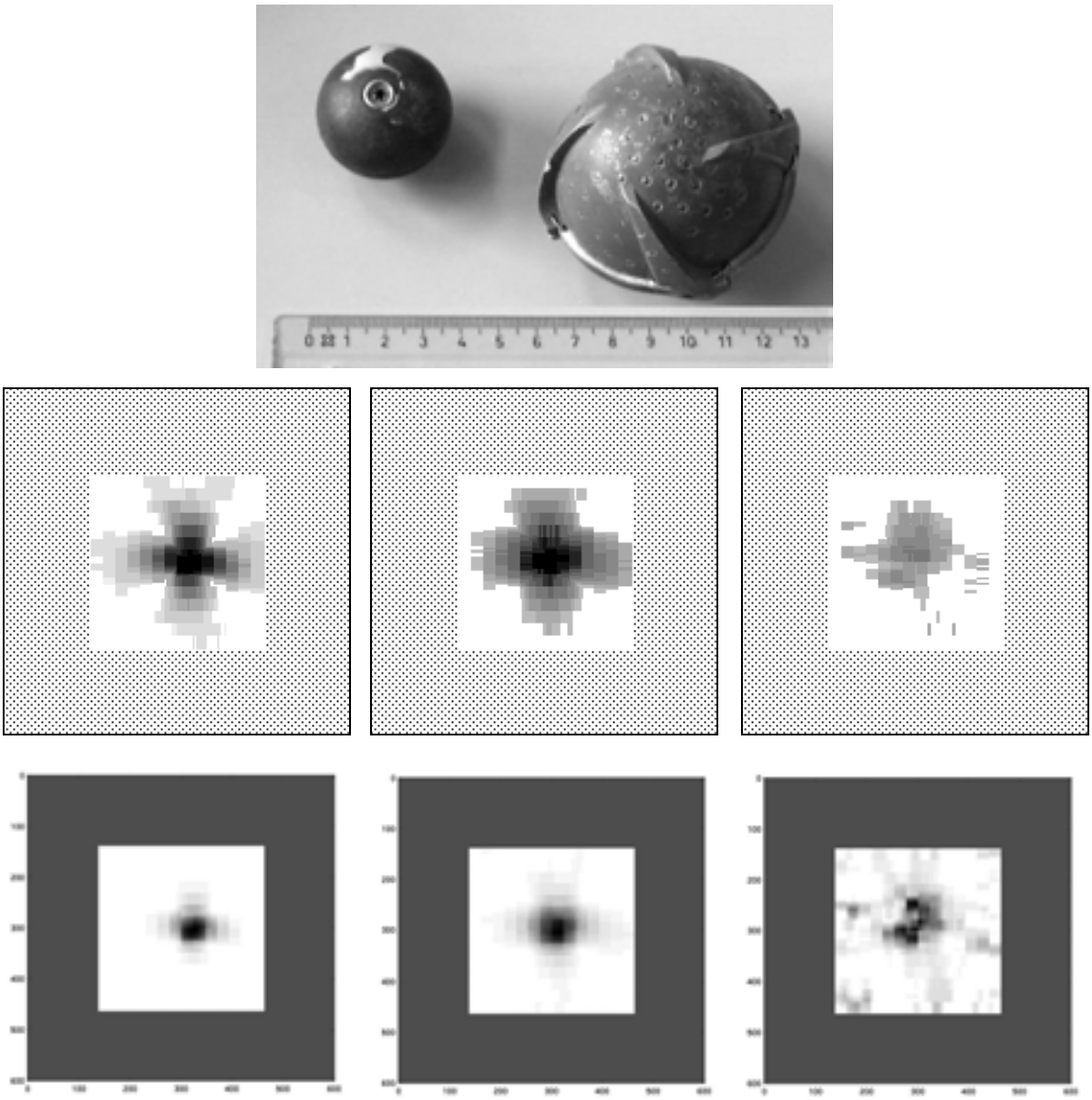

Figure 7.8: ***Small submunition*** **(upper left of photograph)** (visible ruler length: 13 cm). Top row: original FS images. Bottom row: linear scale. Depth: flush (+1.9cm), 5 cm (+1.9cm), 9 cm (+1.9cm). Image size 30×30 cm (central section).

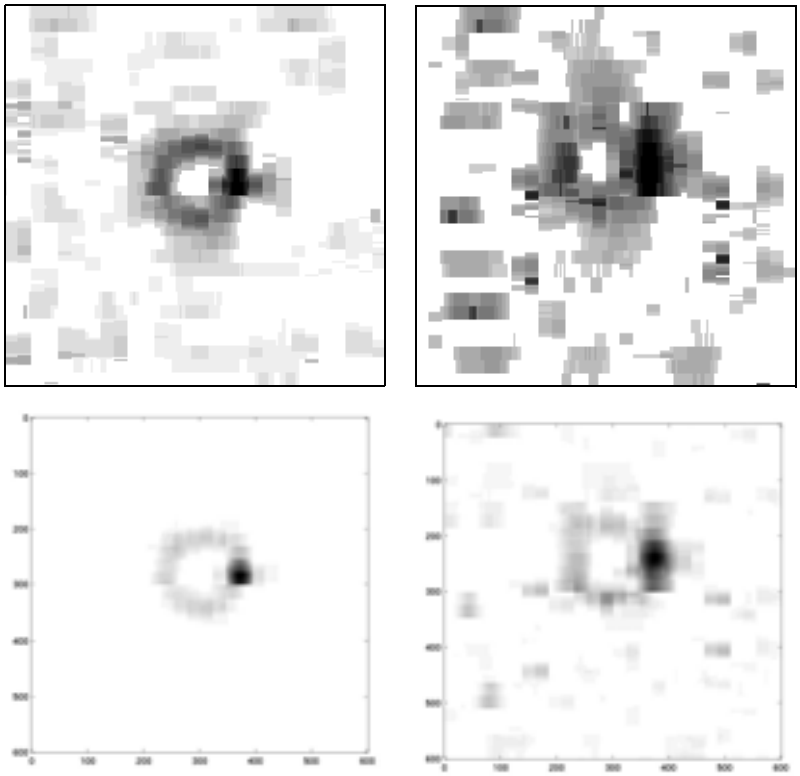

Figure 7.9: ***PMN*** (see also Figure 5.4). Top row: original FS images. Bottom row: linear scale. Depth from left to right: flush (+1.6cm), 3 cm (+1.6cm). Image size 60×60 cm.

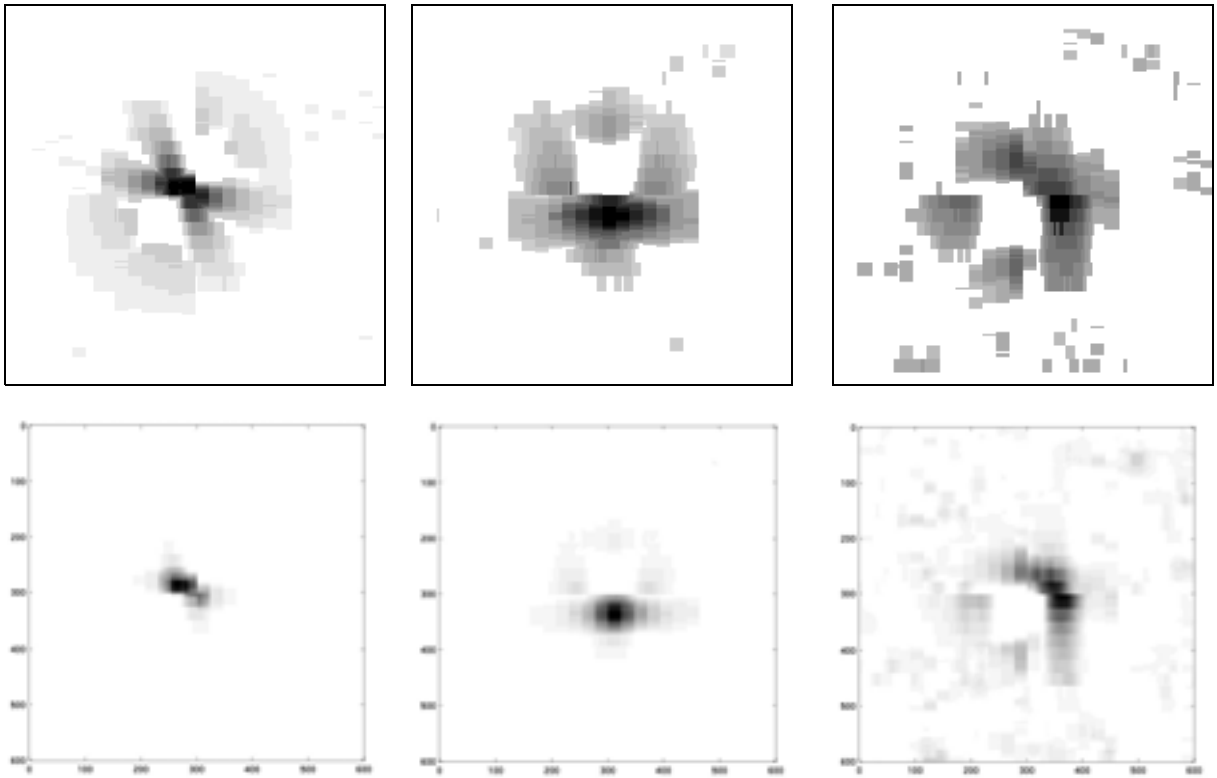

Figure 7.10: ***BLU26 "bomblet"*** **(lower right of photograph** in Figure 7.8). Top row: original FS images. Bottom row: linear scale. Depth: flush (+1.9cm), 3 cm (+1.9cm), 5 cm (+1.9cm). Image size 60×60 cm.

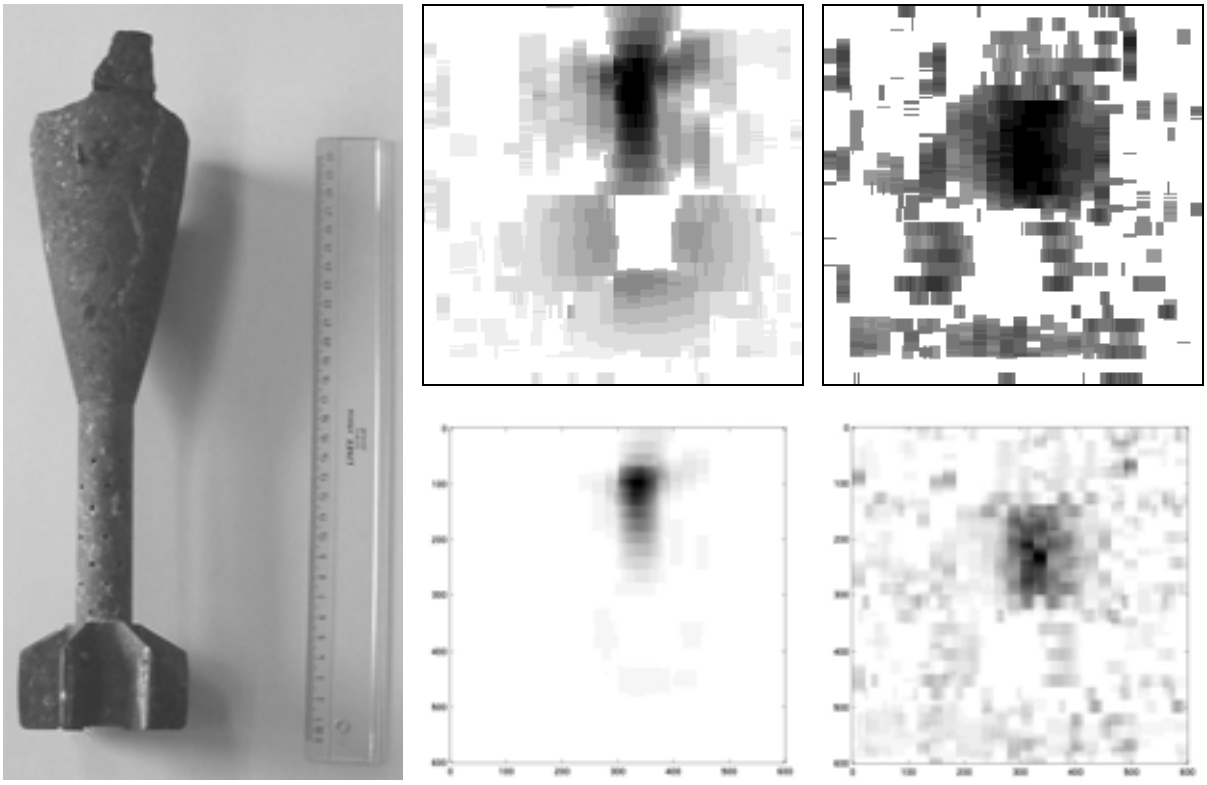

Figure 7.11: ***Mortar shell*** (ruler length: 30 cm). Top row: original FS images. Bottom row: linear scale. Depth (of the uppermost parts) from left to right: 1-2 cm (+1.6cm), 10-12 cm (+1.6cm). Image size 60×60 cm.

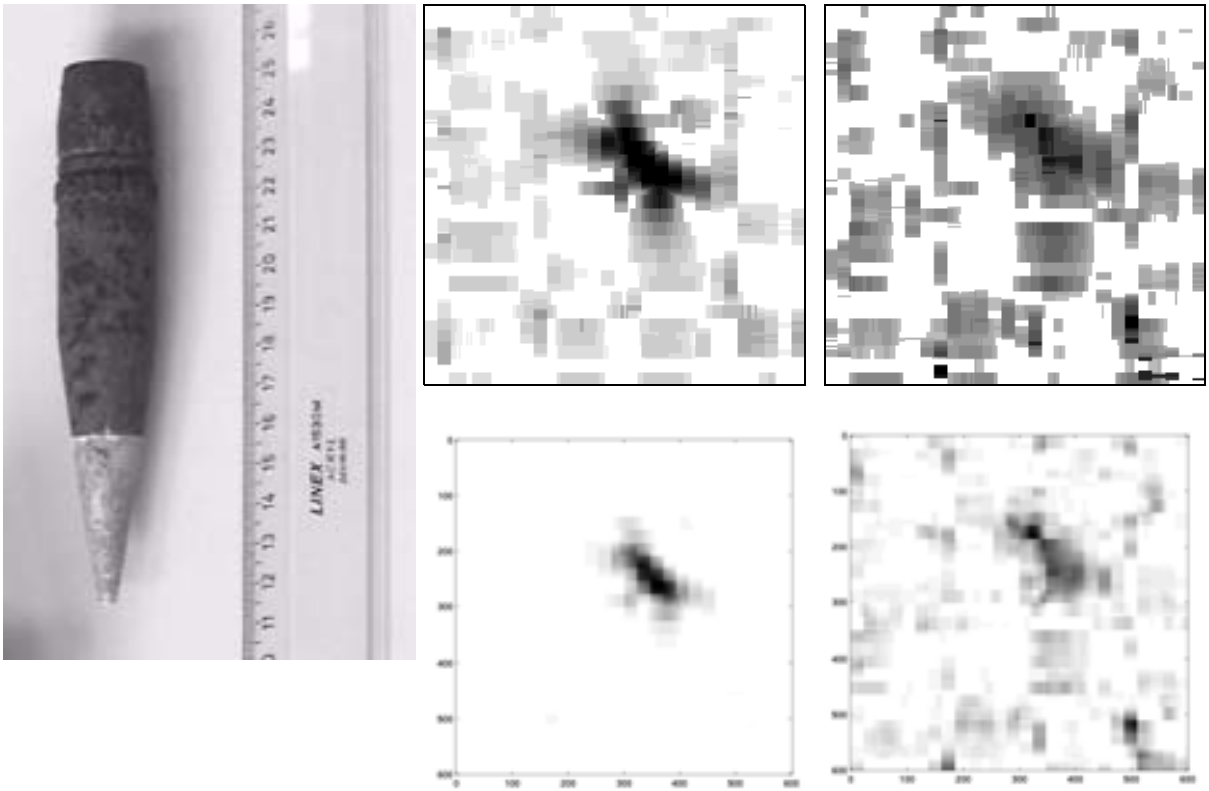

Figure 7.12: ***20mm projectile*** (visible ruler length: 14 cm). Top row: original FS images. Bottom row: linear scale. Depth from left to right: flush (+1.6cm), 6 cm (+1.6cm). Image size 60×60 cm.

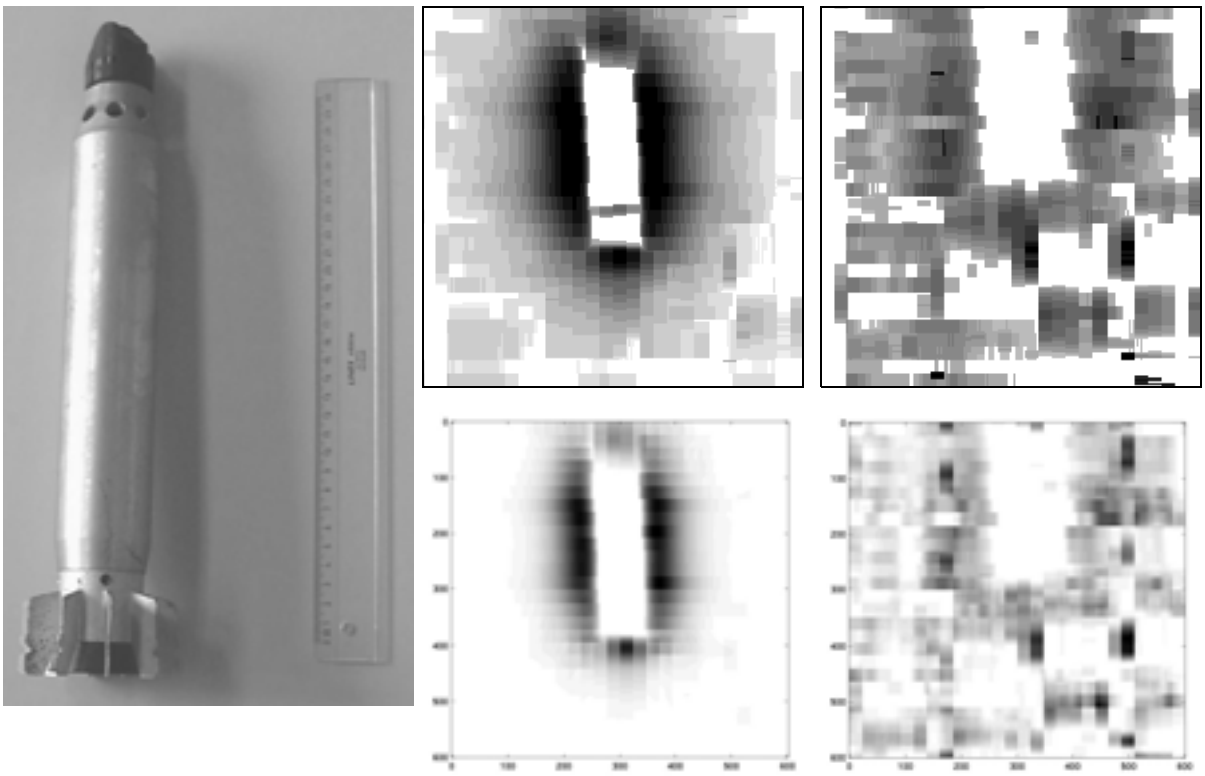

Figure 7.13: (UXO) *Rocket*. Top row: original FS images. Bottom row: linear scale. Depth from left to right: flush (+1.6cm), 8cm (+1.6cm).

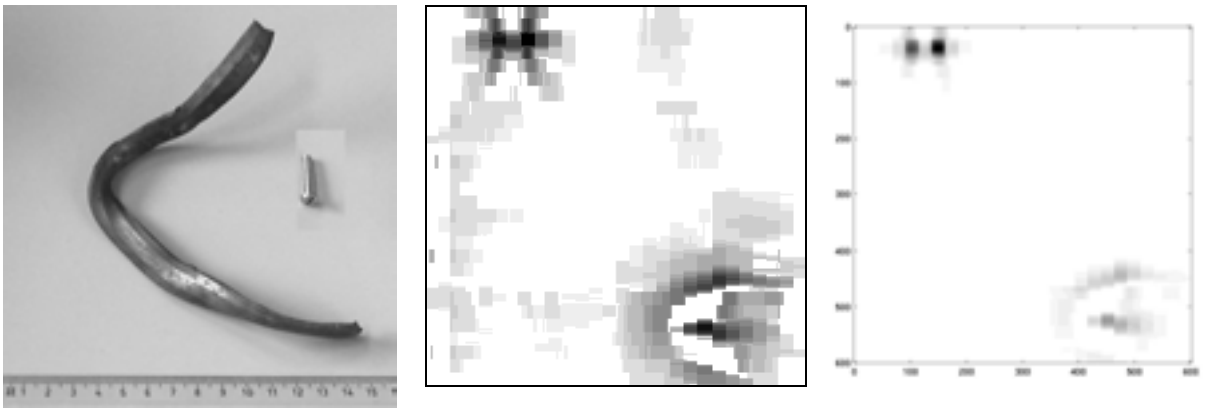

Figure 7.14: *Debris* (large copper, steel screw). Flush (+1.6cm). Left: original Ferroscan image, Right: linear scale. Visible ruler length: 15cm

Discussion

As hinted at before, a wooden plate was placed between the sensor and the sand (thickness 1.6 cm or 1.9 cm, indicated with "+1.6cm" and "+1.9cm" respectively). This thickness has therefore to be added to the depth indicated for each object, measured from its top, to obtain the actual distance from the sensor. "Flush" means (with the top) just underneath the surface level.

Each image is presented as the standard Ferroscan picture (compression of the intensity's dynamic range by default) and as obtained by us using a linear scale. The latter might be more appropriated to reproduce with greater accuracy an (isolated) object's shape.

The objects are represented up to a depth which gives roughly, *with the current hardware and data processing*, reasonable images, but which has not to be taken as a precise indication of the actual sensor performances. Note also that the data has been acquired with two different sensors, with the second one possibly more noisy. All images are taken on the full 60×60 cm except where indicated.

Some of the interesting features of the images presented include the following:

- *Small submunition*: image size 30×30 cm.
- *PMN*: the cover retaining ring is clearly visible, with the darker spot probably corresponding to the area around the pin used to secure the ring (see the front part of the corresponding photograph in Figure 5.4).
- *BLU 26 "bomblet"*: its mixed nature (ferromagnetic and non-ferromagnetic material embedded in the same object) is probably at the origin of some of the complex image details displayed.
- *Mortar shell*: notice the "negative image" (void) corresponding to the bottom non-ferromagnetic part, due to the processing algorithm tuned to enhance ferromagnetic objects and suppress non-ferromagnetic ones.
- *20mm Projectile*: was lying diagonally along the axis NW-SE, which as expected somewhat degrades image quality. A rebar of the same size would be visible, if orthogonal to one of the scanning directions, down to 160 mm.
- *"Rocket"*: this large ferromagnetic object produces again a "negative image" (void).
- *Debris*: notice again the halo of the ferromagnetic object (lower right) and the bizarre shape of the screw (upper left) in the original image. The latter is due to some of the technical and physical features described in the previous paragraphs, enhanced by the compression of the intensity's dynamic range necessary to visualize clearly all objects.

In general an object's image gets larger with increasing depth, as expected.

Concluding Remarks

The Ferroscan system is one of the few commercially available metal detectors capable of providing the user with visual information on the objects under study, in addition to "traditional" indications on depth and diameter. Its images are indeed a precious aid in localizing and interpreting the underlying metallic structure, without pretending to deliver a true representation of it. This task has been solved by employing multi-sensor hardware and, as far as we have been able to judge, simple and elegant data processing software. Imaging has also been "eased" by the fact that the nature of the problem is rather well defined a priori, i.e. mostly cylindrical parallel ferromagnetic objects placed horizontally in standard patterns at shallow depth.

Our tests were targeted at applying this existing system "as is" to the localization, and possibly visualization, of some AP mines with relevant metal content (e.g. PMN) and of shallowly buried UXO, mostly ferromagnetic. The size of such objects can vary rather widely, and they often do come isolated, placed at random.

The multi-sensor arrangement is practical to rapidly scan a large area, and its resolution looks indeed sufficiently high for large or extended objects such as UXO and rebars respectively. On the other hand using more than one sensor, and the differential arrangement itself, have some side effects on the visualization of smaller isolated (ferromagnetic) objects, for which the system was indeed not intended, and in presence of edges. In these cases a single sensor might be scanned in more detail over the object, possibly providing a more accurate image.

In any case, the increased spatial resolution comes obviously at the price of decreased depth penetration, to nobody's surprise.

Summarizing, the images we have obtained demonstrate that some simple, near real-time high resolution imaging (R=2-3 cm for a flush object) is possible for shallowly buried large or extended targets. Depth penetration improvements seem however necessary for practical applications; they could come from the data processing side, for very weak signals for example, and from the sensors, where it has been suggested to use smaller probes, e.g. magnetoresistive or miniature fluxgate elements[94] [CZI96] (as discussed for example in §7.2), or to alter the coil geometry [GAY94] to gain in sensor directivity ("focusing" the magnetic field).

94. Which obviously have to provide the required sensitivity and work at the required frequencies, not at DC as standard magnetometers.

7.4. Shape Determination via Deconvolution

The fact that a raw metal detector "image" is essentially an image of the probe field is well known in non-destructive testing (NdT) [BAH88]. More accurate imaging results can therefore be expected by taking into account the detector's intrinsic response and deconvolving it from the measured data to obtain an approximation of the object's real (2D) shape. This work was inspired by similar R&D in NdT (rebar detection) as already described in §7.3.2 and relies on image processing deblurring techniques.

The simplest approach consists in assuming a linear behaviour, whereby the measured (i.e. degraded) "image" *M(x,y)* can be written in the spatial domain as a convolution of the real (i.e. original, or true) image *R(x,y)* and of the detector's impulse response *P(x,y)*, known in optical image processing theory as "*Point Spread Function*" (*PSF*), as:

$$M(x,y) = R(x,y) \otimes P(x,y) \tag{7.1}$$

In the image processing domain the *PSF* represents a distortion operator which describes the degree to which an optical system blurs (spreads) a point of light [MAT01]. This convolution process is assumed to be correct in most cases in NdT as well [BAH88].

This convolution operation is almost equivalent in the frequency domain to the (element-by-element matrix) multiplication of the corresponding Fourier transforms $\Im$, that is:

$$\Im(M) = \Im(R) \cdot \Im(P) \Rightarrow R = \Im^{-1}\left(\frac{\Im(M)}{\Im(P)}\right) \tag{7.2}$$

The initial image is therefore obtained by applying in the frequency domain the *inverse filter* $1/\Im(P)$ ($\Im(P)$, the *PSF*'s Fourier transform or Optical Transfer Function, describes the alteration of the image's spatial frequencies). This is however true only in an idealized scenario which does not take into account the presence of noise $\eta(x,y)$, usually assumed to be additive:

$$M(x,y) = R(x,y) \otimes P(x,y) + \eta(x,y) \tag{7.3}$$

The inverse filter is therefore in practice not always stable due to noise and low values in $\Im(P)$, and a stabilized version, the *pseudoinverse* filter, is often preferred [JAI89]:

$$P_s = 0 \text{ when } |\Im(P)| < \varepsilon \text{ , } P_s = 1/\Im(P) \text{ otherwise.} \tag{7.4}$$

As image restoration is basically a high-pass operation it is quite important to avoid noise amplification. Alternative filtering technique for deconvolution (deblurring) are therefore often selected, such as the Wiener filter described for example in detail in [THO98,DRU00].

In our case better results were however obtained using the *Lucy-Richardson (LR) maximum-likelihood algorithm*, as implemented in an accelerated version in the MATLAB® **`deconvlucy`** function. The *LR* algorithm is a member of the family of iterative nonlinear constrained methods. The term *nonlinear* refers to the fact that, although Eq. (7.1) is still assumed to be valid, the solution $\hat{R}(x,y)$ (our estimate of the true image) can not be expressed as a linear function of the measured image *M(x,y)*. The use of an *iterative* approach has the advantage of allowing control of spurious fluctuations by interaction with the solution as it evolves. The notion of "constrained" means that the solution is required to be physically possible (*physical-realizability constraints*), and implies in practice that bounds are imposed on it. This is frequently synonymous of positivity (amplitude bounds, the solution can not be negative) as in the case of the *LR* algorithm; spatial bounds are also feasible. Such techniques feature a reduced noise sensitivity with respect to traditional linear methods and have seen an increasing use in the last 20 years or so (for details see [JAN97]).

The *LR* algorithm in particular, well known in optics, astronomy, medical imaging, etc., arises from a maximum-likelihood argument in which the image is modelled with Poisson statistics. Multiple iterations are performed maximizing the likelihood that the resulting image, when convolved with the *PSF*, is an instance of the blurred image [HAN97]; the algorithm converges to the maximum-likelihood solution for Poisson statistics in the data. In practice the result $\hat{R}_k(x, y)$ of each iteration is multiplied by a correction factor that relates to the remaining fitting error in the following way (implying element-by-element division and multiplication as before):

$$\hat{R}_{k+1}(x, y) = \hat{R}_k(x, y)\left(P(-x, -y) \otimes \left[\frac{M(x, y)}{P(x, y) \otimes \hat{R}_k(x, y)}\right]\right) \tag{7.5}$$

where $P(-x, -y)$ is the reflected *PSF*. Note that with a positive initial estimate the successive estimates will automatically be positive as well. Also, the *LR* algorithm conserves the total energy; it can be effective when the *PSF* is known, but little information is available about the additive noise in the corrupted image [MAT01].

In order to avoid overfitting, i.e. fitting statistical fluctuations, it is in fact appropriate to stop the *LR* iterations before the maximum-likelihood solution is reached. An alternative approach to the suppression of noise amplification consists in the use of damping techniques. Note that the number of iterations necessary to achieve a satisfactory result can depend on the application. For example, it has been reported that overfit sets in early when looking at diffuse sources (smooth and extended object), whereas it becomes important only at late iterations for point sources [HAN97]. We have observed a similar behaviour in the metal detector data. Various techniques for the algorithm's acceleration have also been devised.

The Point Spread Function

The quality of the deblurred image is in general mainly determined by the knowledge of the *PSF*. There are basically two approaches to evaluate it: either a set of measurements are taken on small (dipole like) objects, such as spheres, or the detector's response to such objects is calculated (modelling).

A possible modelling approach consists in calculating the magnetic field generated by the transmit coil at the target object position; this would allow to calculate the secondary magnetic field, due to the eddy currents, generated by the target object itself. Integration of the latter on the surface of the receive coil and derivation with respect to time would then lead to the induced voltage in the receive coil. An alternative approach consists in replacing the target object with equivalent electric and magnetic dipoles, and then applying the principle of reciprocity to obtain the voltage induced in the receiver coil [DAS90]. In any case, only in a few cases rigorous analytical solutions are available (for example for spherical objects and rectangular coils, or circular coils on their axis). [BAH88] discusses how to compute the *PSF* for different eddy current probe systems, in order to evaluate their imaging characteristics, and points out that in general more than one *PSF* may be required to characterise a flaw with an eddy current probe, in contrast to optical image processing.

The resulting *PSF* is in general quite extended compared to the size of typical targets, due to the detector footprint which is of the order of its diameter. In our case we have chosen to work with a *PSF* of about 40×40 cm. The image to be deconvolved has also to be large enough to contain the peak of the target's response as well as its tails.

As we realised early on [BRU98b], the *PSF* will actually be a function of the object depth, i.e. be a $P(x,y)_z$ (see again Figure 7.4). A somewhat similar situation arises in optical microscopy [SWE97], although in our case the *PSF* gets broader and flatter with increasing depth and the concept of in-focus plane does not seem to exist as such. An object's image will therefore depend on its depth as well, which we can express by rewriting Eq. (7.1) as follows:

$$M(x, y, \Delta z) = R(x, y) \otimes P(x, y, \Delta z) \tag{7.6}$$

In optical microscopy Δz represents a sample's distance from the in-focus plane, in our case it could represent the object depth with respect to a fixed reference.

One could actually go one step further and notice that again in optical microscopy it is possible to build a three-dimensional image *M(x,y,z)* of a thick specimen (i.e. of a 3D object) by summing images from different focal planes, whereby the resulting measured image is the convolution of the 3D *PSF* with the specimen (represented by *R(x,y,z)* in this case). We could therefore speculate that a similar procedure is applicable to metal detector data by carrying out scans on different horizontal planes, or use coils at different heights.

We will however stick to two dimensional quantities, which already present a sufficient number of challenges, for example the fact that ferromagnetic objects, in particular elongated ones, are likely to induce nonlinear features in the acquired images. Whether this approach will be practically applicable in the field, from the point of view of the resulting resolution, scanning speed and cost for example, remains therefore to be demonstrated.

7.4.1. 2D Data Taking with a Conventional Metal Detector (Förster Minex)

Data was acquired with a Förster Minex metal detector, which as already discussed is of a differential type. In order to reconstruct a complete map of the horizontal gradient of the vertical component of the induced magnetic field we have therefore decided to add two orthogonal projections by carrying out two series of parallel scans along the same lines, once with the metal detector head in the standard position, which we will term *A scans*, and once with the head in the same horizontal plane but rotated by 90° (*B scans*). The use of one projection only, typically the *A* scans, might be sufficient in some scenarios.

Each measurement is composed as usual of a magnitude and a phase, or equivalently of a real and imaginary part (for details see Chapter 5).

The *A* and *B* scan results have been lowpass filtered as usual and offsets removed. An example of the resulting bidimensional data at f_1 for both types of scans is shown in the first row of Figure 7.15, $f_1\text{REAL}|_A$ on the left and $f_1\text{REAL}|_B$ on the right. The differential nature of the signal along both coordinates is evident, as well as the image size being of the order of the detector footprint.

The next step is the composition of the *A* and *B* scans into a vector field representing the horizontal gradient. We have chosen to compose the real parts of the signals at a given frequency f_j (j=1,2), which are less background affected[95], on each point (x,y) of the scanning grid as follows:

$$M_j(x, y) = (f_j REAL|_A(x, y), f_j REAL|_B(x, y)) \tag{7.7}$$

The values of $M_j(x,y)$ are stored as complex numbers representing our measured "image". Examples of the vector field at f_1 and of its amplitude are provided in the second row of Figure 7.15. These images are similar to those obtained with the ODIS system discussed in §7.2.

The distance between the parallel scans has usually been taken as 2 cm, which was assumed to be reproducible even in field applications. The *PSF* has been measured experimentally on a small (point-like) target, the **`mist`** mine striker pin, and is shown in Figure 7.16. The resolution of the *PSF* can however be improved, either working on a finer grid in the across track direction, or via modelling for example.

95. Similarly to what happens in NdT, where in practice the image taken for viewing is the one for which the measurement reference phase has been adjusted to minimise background noise [BAH88].

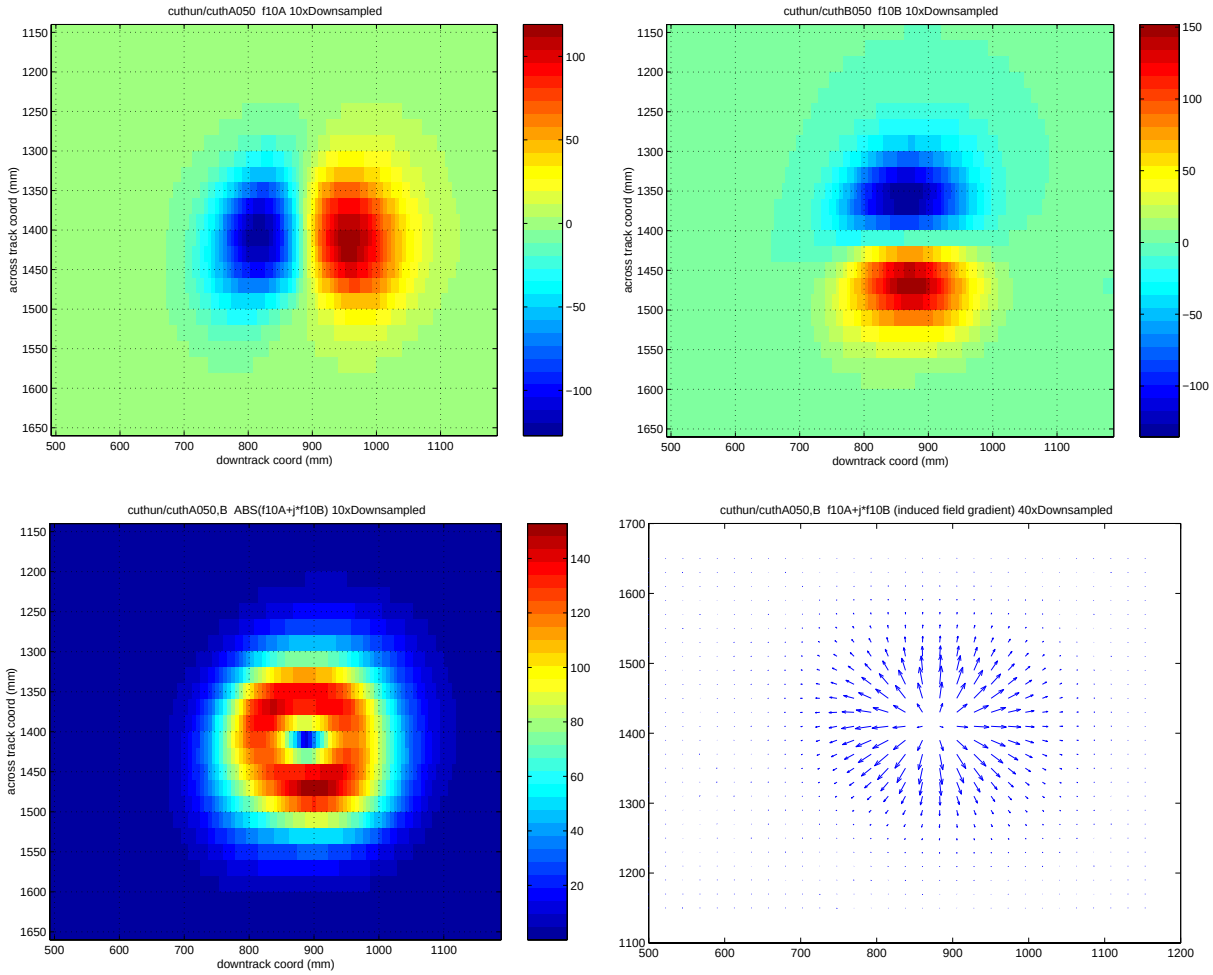

Figure 7.15: "Images" of a large object (copper debris, see Figure 7.14, flush, detector at 5 cm) using the f_1REAL signal. *Top*: values along the *A* and *B* scans. *Bottom*: composed vector field (right) and its absolute value (left).

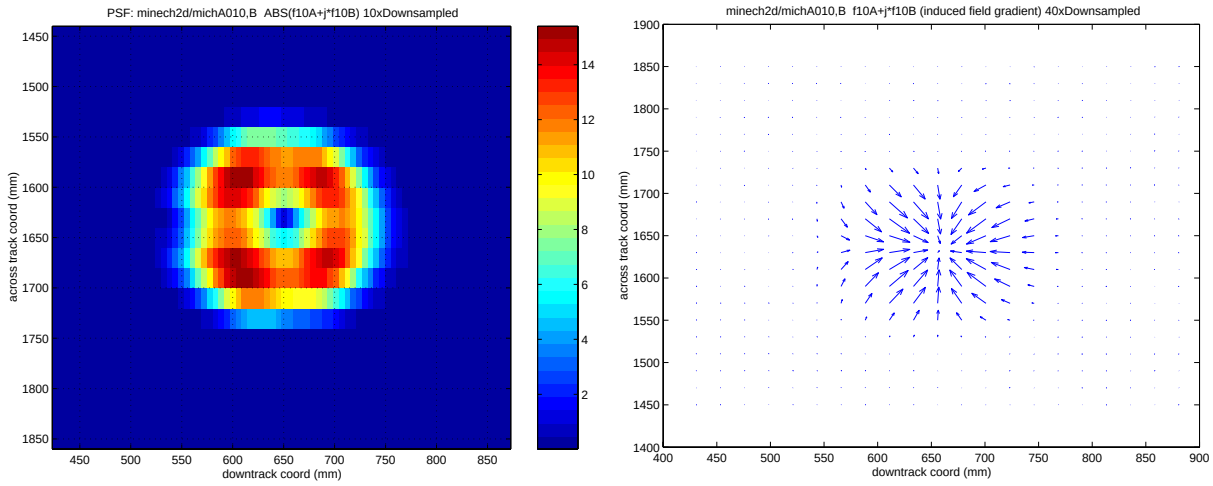

Figure 7.16: *Point Spread Function* (*PSF*), measured on a point-like object (minimum-metal mine buried 1 cm deep, striker pin only (**`mist`**), detector at 2-3 cm): composed vector field (right) and its absolute value (left)

7.4.2. Deconvolution Results and Discussion

Initial tests have been reported in [BRU98a, BRU98b, BRU00c]. A pseudoinverse filter was used as previously described, fixing its threshold with a trial and error procedure, with appropriate extensions of the various matrices involved [JAI89,LOW91]. Additional care could reduce boundary related ringing effects, which can be relevant when working with weak signals as the Discrete Fourier Transform (DFT), used by the deblurring functions, assumes that the frequency pattern of an image is periodic [MAT01].

Typical examples of results are shown in Figure 7.17 and Figure 7.18, together with results from the *LR* algorithm using 10 iterations, no damping and working with the absolute values of the images.

Figure 7.17 shows results for the same point-like object used to define the *PSF*; in this case the deconvolution works quite well at different object depths, although this is certainly favoured by the fact that in this specific case – basically a small vertical steel nail – the target response does not spread out significantly with increasing depth (see Figure 7.4 on the left).

Results are definitely less noisy for the *LR* algorithm, even for less favourable input data such as at 10 cm (last row, pseudoinverse plot not shown). There is quite good agreement between the two filters, although it can be noticed that in the second row the *LR* algorithm has not yet converged to the same across track spatial position as the pseudoinverse one (which is here the correct one). This is one of the cases in which *LR* deconvolution results can be improved using a higher number of iterations.

Figure 7.18 shows results for a couple of realistic, extended objects, the copper debris shown in Figure 7.14, which has an irregular shape and is not flat, and a PMN mine, whose response is dominated by its ring. Larger differences are apparent between the different algorithms, and although it is evident that the object has a structure, it is difficult to appreciate its details. Note also the large halo around the copper debris, which was in fact already present in the initial image (not shown). For these extended objects the *LR* algorithm results depend much more on the number of iterations than for the case of the point-like target.

One example is also shown obtained with a *blind deconvolution* algorithm, as implemented in the MATLAB® **`deconvblind`** function [MAT01], which aims at recovering both the original image and the *PSF*. It has worked in some specialized applications with success, for example when only an imperfect knowledge of the *PSF* is available. The **`deconvblind`** function performs deblurring using an iterative process similar to the Lucy-Richardson maximum-likelihood algorithm previously described. In our case the known *PSF* was provided as initial guess, but results are in general quite inferior to those of the "standard" *LR* algorithm. A possible application could be the refinement of the *PSF* when the target depth is not known, but this might work only by placing much stronger constraints on the properties of the *PSF* itself.

Research along similar lines (image deconvolution) has been carried out at the Royal Military Academy (RMA) in Brussels and is described in [THO98, MER99], with emphasis on Wiener filtering of amplitude data from a single coil Vallon pulse metal detector. Initial results have then been extensively complemented by the development of a number of target models leading to different imaging kernels (*PSF*) and different interpretations of the target function [DRU00a]. The authors have demonstrated that good quality images can be obtained using the right deconvolution kernel, i.e. the right target model and the right object depth, which are however usually not known a priori. Resolution decreases with depth (good results were obtained up to about 10 cm).

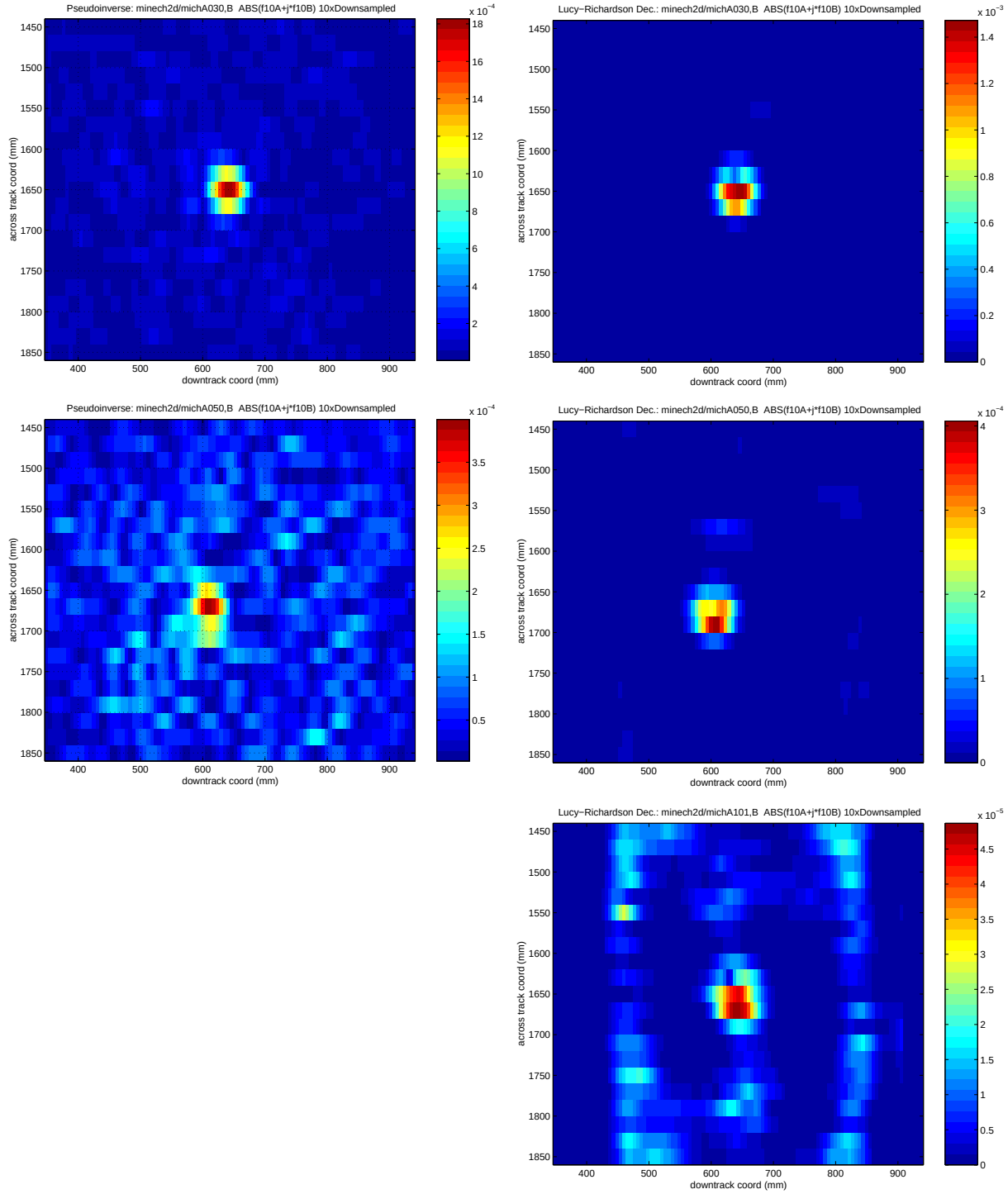

Figure 7.17: Examples of **deconvolved** images for a *point-like object*, a minimum-metal mine buried at 3, 5 and 10 cm (1st, 2nd and 3rd row), striker pin only (**`mist)`** , detector at 2-3 cm. *Left column*: pseudoinverse filter, *Right column*: Lucy-Richardson maximum likelihood algorithm.

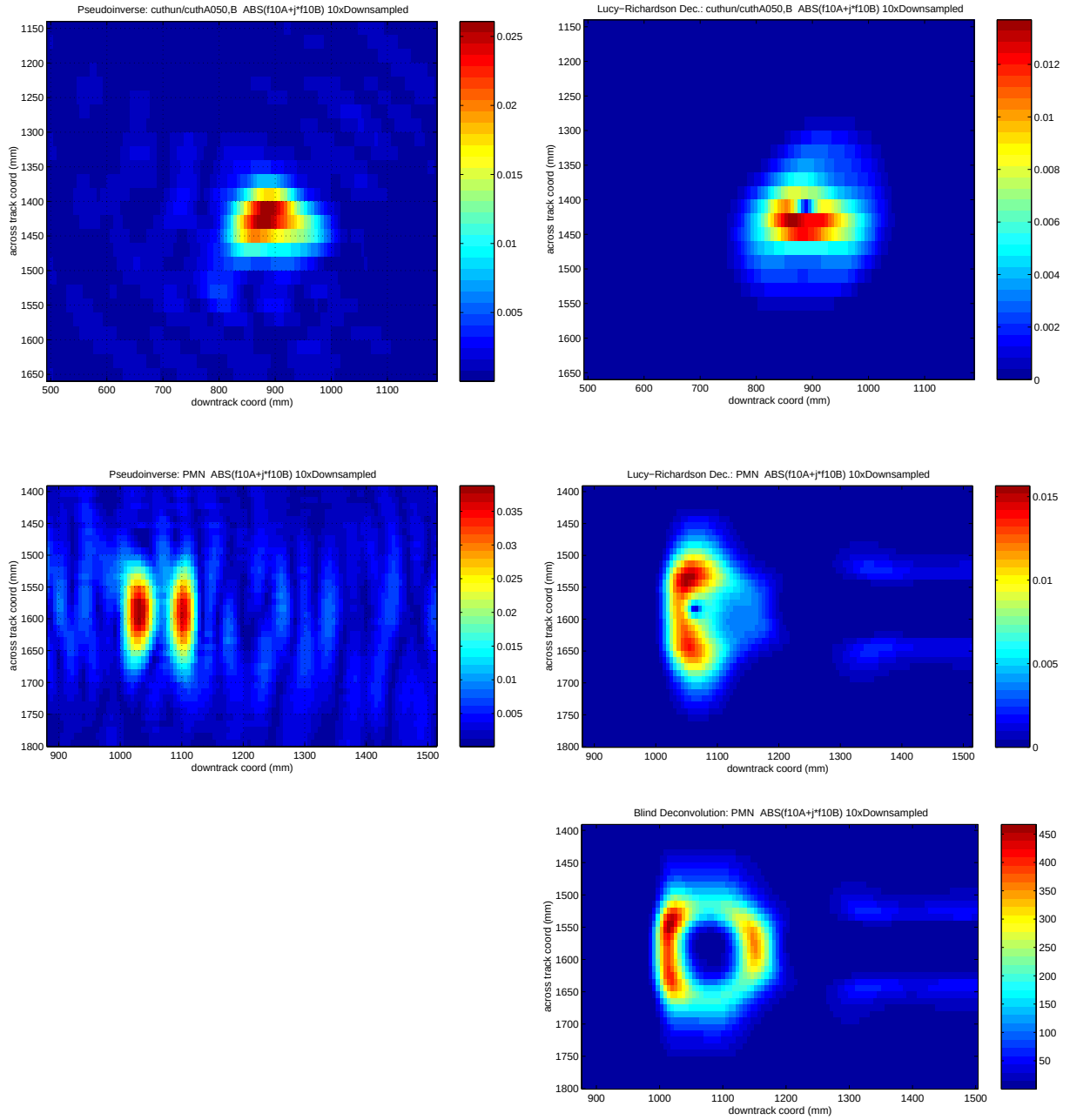

Figure 7.18: Examples of **deconvolved** images for *extended objects:* copper debris (Figure 7.14) placed perpendicular to the scanning direction (flush) and PMN mine (@1 cm); detector at 5 cm. *Left col.*: pseudoinverse filter, *Right col.*: Lucy-Richardson maximum likelihood algorithm (last image: blind deconvolution).

7.4.3. Conclusions

Standard metal detectors have not been conceived as imaging devices. As as consequence unprocessed images are too coarse and unsuitable for direct interpretation, unless large objects are encountered (of the order of the detector diameter).

Image resolution can be enhanced with deblurring (deconvolution) techniques, as demonstrated in the previous figures. The resulting resolution could at present be sufficient to distinguish point-like from extended or composite objects, which could be useful in a number of scenarios. Improvements can come from a finer sampling of the *PSF* in the across track direction for example.

Tuning of the deconvolution algorithms is however not always straightforward, in particular in the presence of noise, and the resulting images can present artifacts. Also, application of the method to a portable device will require the use of a precise scanning pattern (probably with high spatial resolution), if possible controlling in some way the detector distance from the surface. Sampling on an irregular grid will also have to be addressed [DRU00a].

Practical applicability will also have to address two basic issues, namely the *PSF* choice – the use of an "average *PSF*" is far from optimal according to [DRU00a] – and deviations from the linear model assumed in Eq. (7.1), which are likely for ferromagnetic objects.

7.5. Conclusions

As a complementary approach to the one described in the previous chapter we have investigated two portable high resolution applications which exploit the geometrical properties of the near field, with the aim of understanding if such systems could be useful to provide the deminer with a visual image of the shape and size of the metal signature. The first approach features a commercial multisensor systems designed for NdT applications in civil engineering, the second concentrates on the application of image deblurring techniques (deconvolution) to bidimensional data obtained with a commercially available sensor, the Förster Minex metal detector.

Concerning the first approach, to the best of our knowledge the first high resolution 2D near real-time "images" of (ferromagnetic) metallic components of mines with relevant metal content (e.g. PMN) and UXO were obtained. They demonstrate that some simple, near real-time high resolution imaging (R=2-3 cm for a flush object) is possible for shallowly buried large or extended targets. Spatial resolution and depth penetration do nevertheless constitute conflicting requirements, and depth penetration improvements seem necessary for practical applications.

Concerning the second approach, first deconvolved MD images of minelike objects were obtained using bidimensional data taken with a differential metal detector designed for demining applications[96], and we demonstrated that image resolution can be enhanced with deblurring (deconvolution) techniques. However, when looking at realistic, extended objects it is evident that the target has a structure but it is still difficult to appreciate its details. The resulting resolution could therefore at present be sufficient to distinguish point-like from extended or composite objects, which could be useful in a number of scenarios.

This approach has the advantage of using an existing sensor with its well known sensitivity. Tuning of the deconvolution algorithms is however not always straightforward. Also, practical applicability will have to address basic issues such as the *PSF* choice, the use of a precise scanning system, and deviations from the linear model assumed in Eq. (7.1), which are likely for ferromagnetic objects.

Improvements in both techniques are obviously possible and have been detailed in the corresponding paragraphs.

Whether this approach will be practically applicable in the field, from the point of view of the resulting resolution, scanning speed and cost for example, remains to be demonstrated. This will also depend on whether simpler methods, relying for example on the exploitation of the information from traditional metal detectors along the lines described in the previous chapters, will prove to be feasible. In the end it depends therefore on the real added value that such an approach can bring.

96. As already mentioned similar activities started in parallel at the RMA in Brussels and have been developed since.

Bibliography

[BAH88] Bahr, A. J., and Auld, B. A., 1988, An Electromagnetic Model for Eddy-Current Imaging. Journal of Nondestructive Evaluation, v. 7, no. 1/2, p. 71-77.

[BOR96] Borgwardt, C. *High-Precision Mine Detection with Real Time Imaging*. Proceedings SPIE No. 2765, Conference on Detection and Remediation Technologies for Mines and Minelike Targets, Orlando, FL, USA, Apr. 1996, pp. 301-309.

[BRO96] Brown D.R., *et al*., "Multisensor Vehicular Mine Detection Testbed for Humanitarian Demining", in Proc. of the "Technology and the Mine Problem Symposium", Naval Postgraduate School, Monterey, California, 18-21 Nov. 96., pp. 4-73/4-78.

[BRO98] Brooks, J.; Nicoud, J.D. *Applications of GPR Technology to Humanitarian Demining Operations in Cambodia: Some Lessons Learned*. Proceedings of the Third Annual Symposium on Technology and the Mine Problem, Naval Postgraduate School, Monterey, CA, USA, 6-9 Apr. 1998. Available online as ref. Brooks98a at http://diwww.epfl.ch/lami/detec/

[BRU97b]C. Bruschini, "Evaluation of a Commercial Visualizing Metal Detector for UXO/Mine Detection: the HILTI Ferroscan System", SusDem'97 (International Workshop on Sustainable Humanitarian Demining) conference poster, Zagreb (Croatia), 29 September-1 October 1997.

[BRU98a]C. Bruschini, B. Gros, F. Guerne, P.-Y. Pièce, and O. Carmona, "Ground penetrating radar and imaging metal detector for antipersonnel mine detection", *J. of Applied Geophysics* **40**, pp. 59-71, 1998.

[BRU98b]C. Bruschini, "Förster Documentation Overview: Part I: Matlab Algorithms; Signals and Data Acquisition Format (8 pp.); Part II: Metal Detector Test Data (58+6 pp); Part III: 2D Deconvolution Tests (12 pp.)", EPFL-LAMI and VUB-ETRO-IRIS, Internal Note, Lausanne, Switzerland, April 1998.

[BRU98c]C. Bruschini, "*Evaluation of a Commercial Visualizing Metal Detector for UXO/Mine Detection: the HILTI Ferroscan System"*. Published in Sustainable Humanitarian Demining: Trends, Techniques and Technologies, Mid Valley Press, Verona, VA, USA, Dec. 1998, pp. 314-325 (hdic@jmu.edu).

[BRU00a]C. Bruschini, "Metal detectors in civil engineering and humanitarian de-mining: overview and tests of a commercial visualising system", *INSIGHT – Non-Destructive Testing and Condition Monitoring* **42**(2), pp. 89-97, February 2000. Also available from http://diwww.epfl.ch/lami/detec/.

[BRU00c]C. Bruschini, H. Sahli, "Phase angle based clutter reduction and 2D imaging using data from a commercial differential two frequency EMI system", EUROEM2000 Conference (EuroElectromagnetics), Edinburgh, Scotland, 30/5-2/6 2000, Abstract # 66.5, p. 90.

[CHA00] Chaiken, A. *Apparatus and Method for Imaging Metallic Objects using an Array of Giant Magnetoresistive Sensors*. US Patent # 6,124,712, 26 Sept. 2000.

[COL84] H. Dale Collins, J. M. Prince, and T. J. Davis. *Non-Destructive Testing Method and Apparatus Utilizing Phase Multiplication Holography*. US Patent # 4,476,434, 9 Oct. 1984.

[CZI96] Czipott, P.V.; Iwanowski, M.D. *Magnetic sensor technology for detecting mines, UXO, and other concealed security threats*. Proceedings SPIE No. 2933, Conference on Terrorism and Counterterrorism Methods and Technologies, Boston, MA, USA, 20-21 Nov. 1996, pp. 67-76.

[DAS90] Y. Das, J. E. McFee, J. Toews, and G. C. Stuart, "Analysis of an Electromagnetic Induction Detector For Real-Time Location of Buried Objects", IEEE Trans. on Geoscience and Remote Sensing, vol. 28, no. 3, pp. 278-288, May 1990.

[DRU00a]P. Druyts, L. Merlat, and M. Acheroy, "Modeling Considerations for Imaging with a Standard Metal Detector", in *Detection and Remediation Technologies for Mines and Minelike Targets; SPIE Proceedings Vol. 4038*, pp. 1431-1451, Orlando, FLA, USA, April 2000.

[EBL96] Eblagh, K. *Practical Problems in Demining and Their Solutions*. Proceedings, EUREL Int. Conference on The Detection of Abandoned Landmines, Edinburgh, UK, 7-9 Oct. 1996, pp. 1-

5.

[ESC96] Eschner, W.; *et al. Bildgebendes hochauflösendes Sensorsystem zu Detektion, Ortung und Identifizierung von metallischen Objekten* (Sensor System for Detecting, Locating and Identifying Metal Objects). German Patent # DE 44 36 078 A1, 11 Apr. 1996 (in German). See also WO96/11414 (international application published under the Patent Cooperation Treaty).

[FER00] Fernandes, B. T., Silva, I., and Gaydecki, P., 2000, *Vector extraction from digital images of steel bars produced by an inductive scanning system using a differential gradient method combined with a modified Hough transform.* NDT&E International, v. 33, no. 2, March, p. 69-75.

[GAY94] Gaydecki, P.A.; Burdekin, F.M. *An inductive scanning system for two-dimensional imaging of reinforcing components in concrete structures.* Measurement Science and Technology 5, 1994, pp. 1272-1280.

[GAY95] Gaydecki, P.A.; Klossop, K.; Burdekin, F. *A prototype inductive scanning system for two-dimensional imaging of metal reinforcing components in concrete: system design and data visualization.* Proceedings, Int. Symposium on Non-Destructive Testing in Civil Engineering, Berlin, Germany, Sept. 1995, pp. 745-752. Online documentation available at http:// www.in.umist.ac.uk/DIAS/gaydecki.htm.

[GAY00] Gaydecki, P., Silva, I., Fernandes, B. T., and Yu, Z. Z., 2000, *A portable inductive scanning system for imaging steel-reinforcing bars embedded within concrete.* Sensors and Actuators A (Physical), v. A84, no. 1-2, Aug., p. 25-32.

[GER96] Gerhold, T.; Becker, W.-J.; Ricken, W. *Mehrfrequenz-Wirbelstrom-Messverfahren zur Strukturerkennung von Stahlbetonbewehrung bei grösserem Abstand*. Grundlagen der Zerstörungsfreien Prüfung, Berichtsband 55, Fachausschuss Hochschullehrer, Dortmund (MTQ), Germany, 13 Nov.1996 (in German).

[GOL98] Goldfine, N. J.; *et al. Magnetometer and Dielectrometer Detection of Subsurface Objects*. WO98/30921 A2, 6 Jan. 1998 (international application published under the Patent Cooperation Treaty).

[GOL99] Goldfine, N., *et al.*, "New Quasistatic Magnetic and Electric Field Imaging Arrays and Algorithms for Object Detection, Identification, and Discrimination", in *SPIE Proceedings Vol. 3710*, pp. 89-100, Orlando, FLA, April 1999.

[GUO96] Guo, Y.; Nelson, C.V.; White, D.M. *3-D Localization Using A Time-Domain Electromagnetic System*. Presented at the UXO Forum 1996, Williamsburg, VA, USA, 26-28 Mar. 1996.

[GUO98] Guo, Y., Ko, H. W., and White, D. M., 1998, 3-D localization of buried objects by nearfield electromagnetic holography: Geophysics, v. 63, no. 3, May-June, p. 880-889.

[GUO00] Guo, Y., Ko, H. W., and White, D. M. *Imaging Objects in a Dissipative Medium by Nearfield Electromagnetic Holography*. US Patent # 6,084,412, 4 Jul. 2000.

[HAN97] Hanisch, R. J., White, R. L., and Gilliland, R. L., 1997, Deconvolution of Hubble Space Telescope Images and Spectra, in [JAN97], pp. 310-360.

[HIL94] *Ferroscan Product Brochure*. Hilti Corporation, FL-9494 Schaan, Liechtenstein, 1994.

[HIL97a] *Ferroscan System FS 10 Operating Instructions*. Hilti Corporation, FL-9494 Schaan, Liechtenstein, 1997.

[HIL97b] *Ferroscan Data Analysis Software*. Hilti Corporation, FL-9494 Schaan, Liechtenstein, 1997.

[HIP90] Hippler, J. H., Ermert, H., and von Bernus, L., 1990, Über die Nutzung des Skin-Effekts für holographische Abbildungsverfahren zur zerstörungsfreien Prüfung metallischer Materialien und Bauteile (On the utilization of the skin-effect for holographic imaging in nondestructive evaluation of metallic materials and devices): Archiv für Elektronik und Übertragungs-technik (AEÜ), v. 44, no. 4, July-Aug.., p. 257-264 (in German).

[HIP93] Hippler, J. H., Ermert, H., and von Bernus, L., 1993, Broadband holography applied to eddy current imaging by using signals with multiplied phases: Journal of Nondestructive Evaluation, v. 12, no. 3, Sept., p. 153-162.

[JAI89] A. K. Jain, Fundamentals of Digital Signal Image Processing, Prentice-Hall International, 1989,

Ch. 8.

[JAN97] P. A. Jansson, Deconvolution of Images and Spectra, 2nd ed., Academic Press, 1997, 514 pp.

[KOU94] Kousek, K.; *et al. Apparatus for Determining Location of an Element of Magnetizable Material in a Construction Structure*. US Patent # 5,296,807, 22 Mar. 1994.

[LOW91] A. Low, Introductory Computer Vision and Image Processing, McGraw-Hill, 1991, Ch. 14.

[MAT01] "MATLAB® Image Processing Toolbox User's Manual", v. 3.1 (Release 12.1), May 2001.

[KIN96] King C. *Mine Clearance…in the Real World*. Proceedings of the Technology and the Mine Problem Symposium, Naval Postgraduate School, Monterey, CA, USA, 18-21 Nov. 1996, pp. 3-3/3-9.

[McF96] McFee, J.E.; Carruthers, A. *A multisensor mine detector for peacekeeping – Improved Landmine Detector Concept (ILDC)*. Proceedings SPIE No. 2765, Conference on Detection and Remediation Technologies for Mines and Minelike Targets, Orlando, FL, USA, Apr. 1996, pp. 233-248.

[MER99] L. Merlat, M. Acheroy, "Improving quality of information from metal detectors", in Proc. 1999 ARIS Technical Workshop on Ground Survey for Humanitarian Demining, Brest, France, 26-27 Oct. 1999.

[MIT96] Tsipis K., "Report on the Landmine Brainstorming Workshop of Aug. 25-30, Nov. 96", Report #27, Program in Science & Technology for International Security, MIT, Cambridge, MA, USA, 1996.

[ODIS96] *High-Precision Ordnance Detection with the Real-Time Imaging System ODIS*. System Brochure, Dornier, Daimler-Benz Aerospace, 1996.

[RIC95] Ricken, W.; Mehlhorn, G.; Becker, W. *Determining of the concrete cover thickness and the bar diameter in reinforced concrete with a method of eddy current testing*. Proceedings, Int. Symposium on Non-Destructive Testing in Civil Engineering, Berlin, Germany, Sept. 1995, pp. 197-204. Online documentation available at http://www.uni-kassel.de/fb16/ipm/mt/de/forschung/mfid/mfid.ghk.

[RUS99] K. Russell, Y. Das, J. McFee, and R. Chesney, "A realtime target detection technique for metal detector arrays - an image processing approach", in *SPIE Proceedings Vol. 3710*, pp. 887-894, Orlando, FLA, April 1999.

[SMI99] G. S. Smith, R. F. Apfeldorfer, and L. E. Rickard Petersson, "The role of evanescent electromagnetic waves in the detection and identification of buried landmines", in *SPIE Proceedings Vol. 3710*, pp. 101-112, Orlando, FLA, April 1999.

[SWE97] Swedlow, J. R., Sedat, J. W., and Agard, D. A., 1997, Deconvolution in Optical Microscopy, in [JAN97], pp. 284-309.

[THO98] O. Thonnard, "Détecteur de Métaux – Analyse d'un Détecteur de Métaux et Conception d'un Système de Balayage afin de Produire des Images 2-D du Sol" (Metal Detector – Analysis of a Metal Detector and Design of a Scanning System for the Generation of 2-D Soil Images), Signal Image Centre, École Royale Militaire (Royal Military Academy), Brussels, Belgium, 1998 (M.Sc. Thesis, in French).

[TRI96] Trinkhaus, H.-P.; *et al. Verfahren und System zur Altlastendetektion*. German Patent # DE 44 23 623 A1, 1 Nov. 1996 (in German). See also Eschner, W.; *et al. Process for Detecting Metallic Items Including a Search Path Defined by a Linear Movement with a Superimposed Rotational Movement along a Curved Closed Path*. US Patent # 5,719,500, 17 Feb. 1998.

[WOL99] Wold, R. J., *et al.*, "Development of a Hand-held Mine Detection System using a Magnetoresistive Sensor Array", in *SPIE Proceedings Vol. 3710*, pp. 113-123, Orlando, FLA, April 1999.

8.

Conclusions and Outlook

This thesis has detailed an analysis of metal detectors (low frequency EM induction devices) and their use in a number of disciplines (multidisciplinary approach), from the technical point of view as well as looking at the underlying basic physics. Frequency Domain (FD) systems and the operational conditions of interest to humanitarian demining have been emphasized.

An initial look at humanitarian demining and related R&D has allowed to identify needs and opportunities for the study of metal detectors. After a review of their basic principles we have turned our attention to **electromagnetic induction modelling** and to **analytical solutions** to some basic FD problems, with the aim of understanding the direct (forward) problem. This sets the **theoretical framework**. The first chapters have in fact a tutorial nature as well, as for quite some time little scientific information has been available on this subject.

The second half of the thesis focuses on the **analysis of an extensive amount of data**, following a pattern recognition approach. The possibility of target classification is first discussed on a qualitative basis (complex plane plots), then quantitatively (feature definition, extraction and analysis). The experimental data is also compared to theoretical expectations. Finally, we discuss a complementary approach, i.e. shape and size determination via near field imaging.

On the **theoretical side** we emphasized the operating conditions prevailing in humanitarian demining and the *phase response* of FD systems in particular. We have confirmed the possibility of *distinguishing* between different objects and of *identifying* some targets based on their characteristic phase response. In addition, we have indicated the possibility of exploiting the phase shift dependence on the object size to reduce the amount of detected clutter. Finite length permeable cylinders have been considered in a semi-quantitative way and demagnetization effects stressed. Finally, we have also considered some second order effects such as galvanic currents or the influence of a conductive medium or overburden.

The **importance of soil effects** (for FD systems in particular), which are often not sufficiently considered in the existing scientific literature, has been recognized early on, in particular for small or deep targets. Soil effects have been taken into account by studying the response for different soil permeabilities (homogenous half-space model) and by analysing some frequency differencing methods and features which are more robust to variations in ground conditions. Fluctuations in the soil signal are also clearly documented in the experimental data.

On the **experimental side** we have exploited spatial high-resolution scanning to analyse the response from reference objects and targets, ranging from a minimum-metal mine and its components to larger metallic mines and UXO. We have also carried out a detailed clutter (debris) analysis used representative objects. The use of "only" two frequencies is partially compensated by them being placed towards the limits of the frequency band of interest.

A number of theoretical elements of the basic models we looked at have been confirmed, in particular the trends in the phase response with increasing object size and/or conductivity (actually increasing induction number), the difference between ferromagnetic and non-ferromagnetic objects, and important demagnetization effects.

Where we see particular added value for the scientific community is in the **detailed response analysis**, which has allowed to highlight a number of effects such as orientation dependencies or changes due to axial offsets (elongated ferromagnetic targets). Subtle effects have also been

documented, such as the response of composite objects and their variability, or of different versions of a same mine. This has also been achieved thanks to the use of internal signals, whose availability from existing systems was in no way granted at the time this work started.

On the **qualitative side** (signal trajectories in the **complex plane**) we have shown that it is possible to distinguish smaller clutter items from larger objects, and that some mines have quite characteristic responses (e.g. PMN). A "qualitative" (coarse) target classification is therefore possible, at least for situations with a sufficient signal to noise (S/N) ratio.

On the **quantitative side** we have simplified the complex plane curves by extracting a corresponding set of features, resulting in a **combined, simplified user interface**. Additional features have also been proposed and the resulting distributions analysed. Most of the information turns out to be contained in the phase response; there are however situations in which the additional features help in resolving ambiguities.

The resulting **classification opportunities** have then been discussed along three main lines:

- A **coarse target classification** according to the ***object size*** (actually the response parameter, see §6.3), and permeability (ferromagnetic or not), seems indeed to be possible, at least for scenarios with a sufficient S/N ratio. In the low S/N case it should however still be possible to exploit some of the additional features which are more robust to background (soil) fluctuations.
- The results for some **large metallic objects** confirm that it is possible to discriminate them for smaller clutter relying on their phase response. This seems true to a limited extent only for mines with an average metallic content (e.g. **`PMN`**, **`PMN2`**).
- **Discriminating mines from clutter** or among themselves depends in the end on i) which and how many types of mines are present (*a priori* knowledge), ii) how much one can rely on stable mine signatures, iii) how representative the debris we had available is, and in particular on iv) how many clutter objects have a sufficient S/N ratio to allow discrimination.

  Indeed, *the actual system effectiveness will depend on how much the* ***false alarm rate*** *can be reduced,* i.e. *how many times a clutter item has a sufficient S/N to be identified as such*.

Finally, we have shown, to the best of our knowledge, the first high resolution (R=2-3 cm for a flush object) 2D near real-time "**images**" of shallowly buried (ferromagnetic) metallic components of mines with relevant metal content (e.g. **`PMN`**) and UXO. First deconvolved MD images of minelike objects were also obtained, using 2D data taken with a commercial detector designed for demining applications, demonstrating that image resolution can be enhanced with deblurring (deconvolution) techniques. The limits of both approaches are detailed in Chapter 7. Whether they will be practically applicable in the field, from the point of view of the resulting resolution, scanning speed and cost, remains to be demonstrated.

As a final comment we note that although some of these results were already known to the metal detector community, their diffusion has rarely happened, to the best of our knowledge, in a public document and in a coherent way, with the necessary scientific rigour.

Outlook

As a next step along the lines of this work it should not be too difficult to move from the laboratory to the field, in order to acquire data under realistic conditions, learn by looking at the user interface, and collect preciser target statistics, in particular to understand how many (clutter) objects retain a sufficient S/N ratio for their discrimination. Deceptions can be foreseen for difficult ground conditions, but that's part of the learning process. Finally, although emphasis has been put on analytical models it is recognised that it will be beneficial to look at numerical ones to get a more detailed understanding of complex scenarios, to model soil cavities, and possibly to increase imaging resolution.

Other approaches have already been detailed in the previous chapters and will not be repeated here.